



Calhoun: The NPS Institutional Archive
DSpace Repository

Theses and Dissertations

1. Thesis and Dissertation Collection, all items

2014-09

The cold gas-dynamic spray and characterization of microcrystalline austenitic stainless steel

Schiel, Jonathan F.

Monterey, California: Naval Postgraduate School

<http://hdl.handle.net/10945/43994>

This publication is a work of the U.S. Government as defined in Title 17, United States Code, Section 101. Copyright protection is not available for this work in the United States.

Downloaded from NPS Archive: Calhoun



Calhoun is the Naval Postgraduate School's public access digital repository for research materials and institutional publications created by the NPS community. Calhoun is named for Professor of Mathematics Guy K. Calhoun, NPS's first appointed -- and published -- scholarly author.

Dudley Knox Library / Naval Postgraduate School
411 Dyer Road / 1 University Circle
Monterey, California USA 93943

<http://www.nps.edu/library>



NAVAL POSTGRADUATE SCHOOL

MONTEREY, CALIFORNIA

THESIS

**THE COLD GAS-DYNAMIC SPRAY AND
CHARACTERIZATION OF MICROCRYSTALLINE
AUSTENITIC STAINLESS STEEL**

by

Jonathan F. Schiel

September 2014

Thesis Advisor:
Second Reader:

Luke N. Brewer
Sarath K. Menon

Approved for public release; distribution is unlimited

THIS PAGE INTENTIONALLY LEFT BLANK

REPORT DOCUMENTATION PAGE			<i>Form Approved OMB No. 0704-0188</i>	
Public reporting burden for this collection of information is estimated to average 1 hour per response, including the time for reviewing instruction, searching existing data sources, gathering and maintaining the data needed, and completing and reviewing the collection of information. Send comments regarding this burden estimate or any other aspect of this collection of information, including suggestions for reducing this burden, to Washington headquarters Services, Directorate for Information Operations and Reports, 1215 Jefferson Davis Highway, Suite 1204, Arlington, VA 22202-4302, and to the Office of Management and Budget, Paperwork Reduction Project (0704-0188) Washington DC 20503.				
1. AGENCY USE ONLY (Leave blank)		2. REPORT DATE September 2014	3. REPORT TYPE AND DATES COVERED Master's Thesis	
4. TITLE AND SUBTITLE THE COLD GAS-DYNAMIC SPRAY AND CHARACTERIZATION OF MICROCRYSTALLINE AUSTENITIC STAINLESS STEEL			5. FUNDING NUMBERS DWAM31009	
6. AUTHOR(S) Jonathan F. Schiel				
7. PERFORMING ORGANIZATION NAME(S) AND ADDRESS(ES) Naval Postgraduate School Monterey, CA 93943-5000			8. PERFORMING ORGANIZATION REPORT NUMBER	
9. SPONSORING /MONITORING AGENCY NAME(S) AND ADDRESS(ES) Office of the Secretary of Defense Corrosion Policy and Oversight			10. SPONSORING/MONITORING AGENCY REPORT NUMBER	
11. SUPPLEMENTARY NOTES The views expressed in this thesis are those of the author and do not reflect the official policy or position of the Department of Defense or the U.S. Government. IRB Protocol number ____N/A____.				
12a. DISTRIBUTION / AVAILABILITY STATEMENT Approved for public release; distribution is unlimited			12b. DISTRIBUTION CODE	
13. ABSTRACT (maximum 200 words) This thesis presents research on the cold gas-dynamic spray process applied to the deposition of stainless steel coatings. Cold spray deposition is a relatively new process utilized to create corrosion protection coatings and to perform additive repair for large steel structures. This thesis aims to study the effectiveness of the low-pressure cold spray process on four, commercially available, austenitic stainless steel powders by characterizing both the powders and the resultant coatings. Particle velocimetry and fluid dynamics simulation were also utilized to study the in-flight characteristics of the powder. Notably, this thesis presents evidence that austenitic stainless steel can be successfully deposited via the low-pressure cold spray process. Substantial variability was observed in the commercially available austenitic stainless powders, particularly in the phase content, the particle size distribution, and the particle shape. These parameters had a large effect on the particle velocity and subsequent deposition characteristics. In fact, the PG-AMP-10 powder, which possessed the highest ferrite fraction and had irregular particle shapes, achieved much higher velocities and greater deposition efficiency than the phase-pure and spherically-shaped S5001 powder.				
14. SUBJECT TERMS cold spray, stainless steel, particle velocity, laser velocimetry			15. NUMBER OF PAGES 185	
			16. PRICE CODE	
17. SECURITY CLASSIFICATION OF REPORT Unclassified	18. SECURITY CLASSIFICATION OF THIS PAGE Unclassified	19. SECURITY CLASSIFICATION OF ABSTRACT Unclassified	20. LIMITATION OF ABSTRACT UU	

THIS PAGE INTENTIONALLY LEFT BLANK

Approved for public release; distribution is unlimited

**THE COLD GAS-DYNAMIC SPRAY AND CHARACTERIZATION OF
MICROCRYSTALLINE AUSTENITIC STAINLESS STEEL**

Jonathan F. Schiel
Lieutenant Commander, United States Navy
B.S., North Carolina State University, 2003

Submitted in partial fulfillment of the
requirements for the degree of

MECHANICAL ENGINEER

from the

**NAVAL POSTGRADUATE SCHOOL
September 2014**

Author: Jonathan F. Schiel

Approved by: Luke N. Brewer
Thesis Advisor

Sarath K. Menon
Second Reader

Garth V. Hobson
Chair, Department of Mechanical and Aerospace Engineering

THIS PAGE INTENTIONALLY LEFT BLANK

ABSTRACT

This thesis presents research on the cold gas-dynamic spray process applied to the deposition of stainless steel coatings. Cold spray deposition is a relatively new process utilized to create corrosion protection coatings and to perform additive repair for large steel structures. This thesis aims to study the effectiveness of the low-pressure cold spray process on four, commercially available, austenitic stainless steel powders by characterizing both the powders and the resultant coatings. Particle velocimetry and fluid dynamics simulation were also utilized to study the in-flight characteristics of the powder. Notably, this thesis presents evidence that austenitic stainless steel can be successfully deposited via the low-pressure cold spray process. Substantial variability was observed in the commercially available austenitic stainless powders, particularly in the phase content, the particle size distribution, and the particle shape. These parameters had a large effect on the particle velocity and subsequent deposition characteristics. In fact, the PG-AMP-10 powder, which possessed the highest ferrite fraction and had irregular particle shapes, achieved much higher velocities and greater deposition efficiency than the phase-pure and spherically-shaped S5001 powder.

THIS PAGE INTENTIONALLY LEFT BLANK

TABLE OF CONTENTS

I.	INTRODUCTION.....	1
A.	MOTIVATION	1
B.	LITERATURE REVIEW	5
1.	The Cold Spray Deposition Process and Characteristics.....	5
2.	Utilizing Austenitic Stainless Steel Powder in the Cold Spray Deposition Process	9
C.	OBJECTIVES	10
II.	MICROSTRUCTURE-PROCESSING-MICROSTRUCTURE CHARACTERIZATION OF AUSTENITIC STAINLESS STEEL POWDERS AND COATINGS	13
A.	INTRODUCTION.....	13
B.	EXPERIMENTAL METHODS	15
1.	Particle Size Analysis.....	15
2.	Powder and Coating Cross-sectional Samples Metallographic Preparation.....	16
3.	Cold Spray Deposition Experiments	16
4.	Scanning Electron Microscopy of Powders and Coatings.....	17
5.	X-ray Diffraction.....	18
C.	RESULTS	19
1.	Feedstock Powder Characteristics	19
2.	Cold Spray Coating Characteristics.....	29
D.	DISCUSSION	36
1.	The Relationship between Low-Pressure and High-Pressure Cold Spray Deposition of Austenitic Stainless Steel	36
2.	The Effect of the Low-Pressure Cold Spray Deposition Process on the Phase Content and Distribution of the Deposited Coatings	37
3.	The Effect of the Low-Pressure Cold Spray Deposition Process on Crystallite Size of Austenitic Stainless Steel.....	39
III.	PARTICLE VELOCITY OF THE LOW-PRESSURE COLD SPRAY DEPOSITION PROCESS: SIMULATION AND EXPERIMENT.....	41
A.	INTRODUCTION.....	41
1.	Fundamentals of the Laser Particle Velocimetry Process.....	43
a.	Velocity and Diameter Measurement and Calculation	43
b.	Signal Processing, Acceptance Criteria, and Parameter Modification	46
c.	Powder Feed Rate and Substrate Interaction Analysis	47
B.	EXPERIMENTAL METHODS	48
1.	Calibration of the Laser Particle Velocimeter for Austenitic Stainless Steel Powders.....	49
2.	Powder Feed Rate and Substrate Interaction Analysis.....	51

a.	<i>Powder Feed Rate Experiment</i>	51
b.	<i>Substrate Interaction Experiment</i>	52
3.	One-Dimensional MATLAB Simulation of the Centerline (Windsor) SST Model Series C UltiLife Nozzle and Comparison with Laser Velocimetry Nozzle Exit Results	53
4.	Laser Velocimetry for Austenitic Stainless Steel	62
5.	Determination of Critical Velocity for Austenitic Stainless Steel..	63
C.	RESULTS	64
1.	Velocimeter Detector Calibration for PG-AMP-10 and S5001 Austenitic Stainless Steel	64
2.	Nominal Powder Feed Rate and Substrate Interaction.....	71
3.	Simulation of Centerline (Windsor) UltiLife Nozzle	75
4.	Comparison of Laser Velocimetry Measurements Utilizing the One-Dimensional Model Simulation	84
5.	Laser Measured Particle Velocity of S5001 and PG-AMP-10.....	87
6.	Determination of the Critical Velocity for S5001 and PG-AMP-10 Austenitic Stainless Steel	92
D.	DISCUSSION	98
1.	The Effect of Particle Size and Morphology on Particle Velocity and Deposition Efficiency.....	98
2.	Critical Velocity Determination in the Low-Pressure Cold Spray Deposition Process	99
3.	The Effect of Powder Feed Rate and Substrate Interaction on Achieving Statistically Significant and Consistent Particle Velocity Measurements	100
4.	The Effect of Working Gas Type, Pressure, and Temperature on Particle Velocity and Deposition Efficiency	102
IV.	LOW-PRESSURE COLD SPRAY DEPOSITION OF AUSTENITIC STAINLESS STEEL.....	105
A.	INTRODUCTION.....	105
B.	EXPERIMENTAL METHODS	107
C.	RESULTS	110
1.	Deposition Efficiency and Coating Thickness per Pass.....	110
a.	<i>Nitrogen Testing</i>	110
b.	<i>Helium Testing</i>	112
2.	Coating Microstructure.....	118
3.	Hardness	126
D.	DISCUSSION	130
1.	Deposition Efficiency versus Coating Quality.....	130
2.	The Relationship between Porosity and Coating Hardness.....	131
3.	Powder Design	131
V.	CONCLUSION	135
	APPENDIX A: ONE-DIMENSIONAL MODEL SIMULATION MATLAB CODE ...	137
A.	HELIUM EXAMPLE.....	137

B.	NITROGEN PRESSURE RATIO VECTOR.....	142
C.	CREATEFIGURE CODE.....	143
APPENDIX B: SUMMARY TABLES OF VELOCIMETRY EXPERIMENT RESULTS		145
APPENDIX C: SUMMARY RESULTS OF ALL DEPOSITION EXPERIMENTS FROM CHAPTER IV		151
LIST OF REFERENCES.....		153
INITIAL DISTRIBUTION LIST		159

THIS PAGE INTENTIONALLY LEFT BLANK

LIST OF FIGURES

Figure 1.	Comparison of approximate gas temperature and particle velocity ranges for thermal spray techniques, after [1].	3
Figure 2.	Schematic of the cold spray deposition process from [6].	5
Figure 3.	Mean particle velocity versus z-axis position for copper powder indicating the impact of gas molecular weight on particle velocity in the cold spray process, from [15].	8
Figure 4.	Copper particle velocity distributions in the cold spray process and their associated deposition efficiencies with an approximated critical velocity, from [20].	8
Figure 5.	Particle size distributions for the four commercial cold spray stainless steel powders.	20
Figure 6.	Secondary electron images of the four stainless steel powders as-received. A.) S5001, B.) S5002, C.) KM316, D.) PG-AMP-10.	21
Figure 7.	Backscatter electron images of the four stainless steel powder cross-sections. A.) S5001, B.) S5002, C.) KM316, D.) PG-AMP-10.	22
Figure 8.	EDX map for the S5001 powder showing the primary austenite and ferrite stabilizers (Cr, Ni, and Mo) for austenitic stainless steel.	23
Figure 9.	EDX map for the S5002 powder showing the primary austenite and ferrite stabilizers (Cr, Ni, and Mo) for austenitic stainless steel.	23
Figure 10.	EDX map for the KM316 powder showing the primary austenite and ferrite stabilizers (Cr, Ni, and Mo) for austenitic stainless steel.	24
Figure 11.	EDX map for the PG-AMP-10 powder showing the primary austenite and ferrite stabilizers (Cr, Ni, and Mo) for austenitic stainless steel.	24
Figure 12.	Powder X-ray diffraction patterns from the four commercial stainless steel powders taken prior to cold spraying.	25
Figure 13.	EBSD maps for S5001 (304L) stainless steel powder. A.) Inverse pole figure map (with respect to the sample normal) for the austenite phase, B.) Phase map (green-ferrite, red-austenite).	26
Figure 14.	EBSD map for pg-amp-10 stainless steel powder. A.) Phase map (green-ferrite, red-austenite), b.) Inverse pole figure map (with respect to the sample normal) for the austenite phase, c.) Inverse pole figure map (with respect to the sample normal) for the ferrite phase, and d.) Higher magnification view of Figure 14-C.	27
Figure 15.	Grain orientation spread for three stainless steel powders. Red pixels indicate a 20° scalar misorientation from the average crystallite orientation, while blue indicates a 0.1° misorientation. A.) S5001 (austenite phase), B.) KM316 (austenite phase), c.) PG-AMP-10 (ferrite phase), and D.) PG-AMP-10 (austenite phase).	28
Figure 16.	Backscatter electron micrographs of cold sprayed deposited coatings for each of the four commercial stainless steel powders sprayed with helium gas at $T_i = 230^\circ\text{C}$, $P_i = 1.7\text{ MPa}$ (250 psi). Each shows porosity at the	

	particle to particle boundary with KM316 having significant porosity. A.) S5001, B.) S5002, C.) KM316, D.) PG-AMP-10.	30
Figure 17.	Backscatter electron micrographs of cold sprayed deposited coatings showing ultra-fine grain crystallites within the deformed particles. The dark lines represent the prior particle boundaries where finer grains are observed. A.) S5001, B.) PG-AMP-10.	32
Figure 18.	EBSD orientation maps of S5002 (A and B) and KM316 (C and D) coatings. Figures A and C show inverse pole figure maps for the austenite phase with respect to the spray direction (vertical in the image). Dark regions are either from the ferrite phase or from material that could not be indexed. Figures B and D show grain orientation spread (GOS) for the austenite phase.	33
Figure 19.	X-ray diffraction patterns for the S5002 (blue) and PG-AMP-10 (red) coatings after cold spray deposition of the powders with helium gas at $T_i = 230\text{ }^{\circ}\text{C}$, $P_i = 1.7\text{ MPa}$ (250 psi).	35
Figure 20.	EBSD maps of the austenite (FCC-red) and ferrite (BCC-green) phases in the four deposited coatings. A.) S5001, B.) S5002, C.) KM316, D.) PG-AMP-10. Black regions represent regions with unreliable EBSD indexing patterns.	36
Figure 21.	Optical micrograph of etched cross-section of spherical 316L stainless steel powder showing the dendritic structure attained from gas atomization of the particles during manufacturing, from [28].	38
Figure 22.	Chart of austenitic stainless steel crystallite size before cold spray deposition (as-received powders) and after cold spray deposition (cold spray deposited coatings).	40
Figure 23.	Set-up of the optical sensor head, from [52].	44
Figure 24.	Representation of a two-peak signal with different peak heights where TOF = time of flight, from [53].	45
Figure 25.	Experimental set-up for velocimetry experiments. Sensing head is positioned 60 mm from the nozzle centerline. The red dots are the alignment lights that show the width of the measurement zone. A.) Rear view, B.) Side view.	49
Figure 26.	Schematic of the substrate interaction experiment indicating the laser stand-off distance held constant at 20 mm and the substrate stand-off distance starting at 40 mm and reducing to ~21 mm in the direction of motion indicated by the blue arrow.	53
Figure 27.	Schematic of the 120 mm nozzle utilized in the Centerline (Windsor) SST Model Series C cold spray deposition unit. (drawing not to scale)	54
Figure 28.	Screenshot of MATLAB of curve fit process.	64
Figure 29.	Capture depth calibration experiment results plot for S5001 and PG-AMP-10 indicating the optimal capture depth set-point for each at 10 μsec and a reduction of #GOOD/sec for all capture depths greater than 50 μsec . Black (S5001), Red (PG-AMP-10)	65
Figure 30.	Trigger level calibration experiment results plot for Ss5001 and PG-AMP-10 indicating the optimal trigger level set-point for each at 50 and 100 mV	

	and a reduction of #good/sec for all trigger levels greater than 500 mV. Black (S5001), Red (PG-AMP-10).....	67
Figure 31.	Effect of capture depth modification on the measured particle velocity distribution for S5001 showing a higher peak at larger capture depth values indicating more slower particles are being accepted.	68
Figure 32.	Effect of capture depth modification on the measured particle diameter distribution for PG-AMP-10 showing that capture depth has insignificant impact on the diameter distribution.	69
Figure 33.	Effect of trigger level modification on the measured velocity distribution for PG-AMP-10 showing that at higher trigger levels (> 1000 mV) the velocity distributions shifts toward larger, slower particles.	70
Figure 34.	Effect of trigger level modification on the measured diameter distribution for S5001 showing that at higher trigger levels (> 500 mV) the diameter distribution shifts toward larger particles.	71
Figure 35.	Effect of nominal powder feed rate on the consistence of statistical good per second and average particle velocity indicating that the nominal powder feed rate has little impact on both. Black (GOOD/sec), Red (Average particle velocity).	72
Figure 36.	Nominal powder feed rate effect on the measured velocity distribution for S5001 indicating for all nominal powder feed rates the peak occurs at the same particle velocity with a slightly different height.	73
Figure 37.	Effect of substrate interaction on the consistence of statistical good per second and average particle velocity indicating that interference occurs and disrupts the number of good per second at a small stand-off distances (< 5 mm) but the average particle velocity remains constant. Black (GOOD/sec), Red (Average particle velocity).	74
Figure 38.	Substrate interaction effect on the measured velocity distribution for S5001 indicating no effect of the substrate interaction on the particle velocity distribution.	75
Figure 39.	Gas exit pressure as a function of inlet pressure for helium and nitrogen, simulated at $T_i = 300$ °C. Indicates that for the range of operation of the nozzle the gas exit pressure is always above ambient pressure. Red (helium), Black (nitrogen).	76
Figure 40.	Fluid dynamics and particle transport MATLAB® model of the Centerline (Windsor) UltiLife nozzle. Simulated with helium gas at $P_i = 1.7$ Mpa (250 psi), $T_i = 230$ °C and particle size, $D_p = 20$ μ m. A.) nozzle contour radius, B.) gas pressure, C.) gas and particle velocity, D.) gas and particle temperature.	78
Figure 41.	Working gas pressure and temperature profiles along the nozzle for simulated at $T_i = 230$ °C and $P_i = 1.7$ MPa (250 psi) for both nitrogen and helium as the working gases. Indicates that helium expands faster through the nozzle throat causing a larger decrease in both gas temperature and pressure.	79
Figure 42.	Working gas and particle velocity profiles along the nozzle simulated with helium and nitrogen at $T_i = 230$ °C and $P_i = 1.7$ MPa (250 psi).	

	Indicates that helium velocity is much greater than nitrogen velocity due to a much more rapid expansion of the gas in the throat, causing the particle velocity to be greater in helium than nitrogen.	80
Figure 43.	Effect of gas inlet temperature on gas and particle nozzle exit velocities simulated at a constant $P_i = 1.7$ MPa (250 psi), and $D_p = 20$ μ m. Indicates that gas inlet temperature has significant effect on gas exit velocity, but not as significant on particle exit velocity. Red is helium, black is nitrogen, solid is gas, and open symbol is particle.	81
Figure 44.	Effect of gas inlet pressure on the particle nozzle exit velocity (simulated at a constant $T_i = 300$ $^{\circ}$ C, $D_p = 20$ μ m). Indicates that gas inlet pressure has as significant effect on particle exit velocity. Helium (red diamonds), Nitrogen (black circles).....	82
Figure 45.	Effect of particle diameter on particle nozzle exit velocity. Simulated with helium and nitrogen at constant $T_i = 230$ $^{\circ}$ C and $P_i = 1.7$ MPa (250 psi). Indicates that as particle size increase, particle velocity decreases, but as particle size increases the effect on velocity decreases. Indicates that nitrogen driven particles are less affected by particle size differences than helium driven ones. Black (nitrogen-driven), Red (helium-driven).	83
Figure 46.	Effect of particle morphology on particle exit velocity. Simulated at $T_i = 230$ $^{\circ}$ C, $P_i = 1.7$ MPa (250 psi), and $D_p = 20$ μ m. Indicates that as particle becomes less spherical (coefficient of drag increase), the particle exit velocity increases. Suggests that helium-driven particles are more affected by this than nitrogen-driven ones. Red (helium), Black (nitrogen).	84
Figure 47.	Comparison of simulated (red) and measured (black) particle velocity distributions utilizing nitrogen gas with inlet conditions of $T_i = 450^{\circ}$ C and $P_i = 1.7$ MPa (250psi). Indicates approximately the same particle velocity at the peak and the same shape for each. Measured particle velocity shows a long tail toward higher velocities and more lower velocity values suggesting that the particle size bins did not show all available particle diameters.	86
Figure 48.	Comparison of simulated (red) and measured (black) particle velocity distributions utilizing helium gas with inlet conditions of $T_i = 325$ $^{\circ}$ C and $P_i = 1.2$ MPa (175psi). Indicates approximately the same particle velocity at the peak and the same shape for each.	87
Figure 49.	Effect of working gas type on particle velocity distribution for PG-AMP-10 sprayed at $T_i = 230$ $^{\circ}$ C, $P_i = 1.7$ MPa (250 psi), and SOD = 10 mm. Indicates that helium entrained particles travel at higher velocities for the same gas conditions.	88
Figure 50.	Effect of gas inlet temperature on the measured particle velocity distribution for S5001 sprayed with helium gas at a constant $P_i = 1.7$ MPa (250 psi) and stand-off distance of 10 mm. Indicates that at all temperatures the peak is at the approximately the same particle velocity. Suggests that gas inlet temperature has very little impact on particle velocity distribution.	89

Figure 51.	Effect of gas inlet pressure on the measured particle velocity distribution for PG-AMP-10 sprayed with helium gas at a constant $T_i = 230\text{ }^{\circ}\text{C}$ and stand-off distance of 20 mm. Indicates a significant shift to higher velocities at higher pressure suggesting gas inlet pressure has a significant impact on particle velocity.....	90
Figure 52.	Effect of particle size and particle morphology on the measured particle velocity distribution. S5001 (black) and PG-AMP-10 (red) sprayed with helium at $T_i = 325\text{ }^{\circ}\text{C}$, $P_i = 1.2\text{ MPa}$ (175 psi), and SOD = 10 mm. Indicates, in conjunction with the characterization data for both powders that larger particles move at lower velocities and less spherical particles accelerate to higher velocities.....	91
Figure 53.	Effect of stand-off distance on the measured particle velocity distribution for S5001 powder sprayed with helium at $T_i = 230\text{ }^{\circ}\text{C}$ and $P_i = 1.7\text{ MPa}$ (250 psi). Indicates that particle velocity increases from a stand-off distance of 10 mm (black) to 20 mm (red) to 40 mm (blue).....	92
Figure 54.	Qualitative approximation of critical velocity utilizing velocity distribution curves. PG-AMP-10 sprayed with helium at SOD = 10 mm. Indicates a critical velocity of approximately 650 m/sec fits the observed data well.....	94
Figure 55.	Average particle velocity versus deposition efficiency for PG-AMP-10 sprayed with helium at various gas inlet parameters. Suggests that for a given stand-off distance as the average particle velocity increases, the deposition efficiency increases.....	95
Figure 56.	Average particle velocity versus deposition efficiency for S5001 sprayed with helium at various gas inlet parameters. Suggests that for a given stand-off distance as the average particle velocity increases, the deposition efficiency increases.....	96
Figure 57.	Critical velocity versus gas inlet temperature for S5001 (black) and PG-AMP-10 (red) sprayed with helium gas at a constant $P_i = 1.2\text{ MPa}$ (175 psi) and SOD = 10 mm. Indicates that critical velocity is a function of gas inlet temperature, and powder.....	97
Figure 58.	Deposition efficiency and average particle velocity as a function of stand-off distance for S5001 sprayed with helium at $T_i = 230\text{ }^{\circ}\text{C}$, $P_i = 1.7\text{ MPa}$ (250 psi). Suggests that average particle velocity increases as stand-off distance increases, but deposition efficiency decreases.....	98
Figure 59.	Effect of powder feed rate on mean particle velocity, after [20]. Red boxed area indicates the range over which S5001 experimentation was conducted.....	101
Figure 60.	Mean particle velocity versus temperature plot for spray of $22\text{ }\mu\text{m}$ copper powder at constant inlet pressures, $P_i = 2.0\text{ MPa}$ (300 psi) with helium or air as the driving gas, after [20]. Red boxed area represents range of austenitic stainless steel research conducted in this research showing minor increase in particle velocity due to temperature increase.....	103

Figure 61.	Current low temperature-low pressure stainless steel cold spray research compared against previous low pressure cold spray research. Current work (blue) is at much lower pressure and temperature.	106
Figure 62.	Sample plot of correction accomplished on nano-indentation powder hardness. Shows the uncorrected (red) and corrected (black), with the corrected being flat. The area of interest for the hardness measurement averaging was 100 – 200 nm into the surface of the powder.	110
Figure 63.	Photograph of S5002 sprayed with helium at $T_i = 230\text{ }^{\circ}\text{C}$, $P_i = 1.2\text{ MPa}$, and SOD = 16 mm. The spray pattern is 25 mm by 40 mm. This photograph shows that the second pass completely removed the first with the exception of a few flakes of metal that remained.	115
Figure 64.	Effect of gas inlet pressure on deposition efficiency. Indicates all four powders deposition were immeasurable at the 0.7 MPa condition and increased in deposition efficiency as gas inlet pressure was increased from 0.7 MPa to 1.7 MPa. (with the exception of S5002 at 1.2 MPa).	115
Figure 65.	Effect of gas inlet pressure on coating thickness per pass. Indicates all four powders coating thickness was immeasurable at the 0.7 MPa condition and increased in thickness as gas inlet pressure was increased from 0.7 MPa to 1.7 MPa. (with the exception of S5002 at 1.2 MPa).	116
Figure 66.	Effect of gas inlet temperature on deposition efficiency. Indicates an increase in deposition efficiency as gas inlet temperature is increased for all powders. Low inlet pressure was utilized to have enough comparison points and therefore deposition efficiency is low.	117
Figure 67.	Effect of gas inlet temperature on coating thickness per pass. Indicates all four powders coating thickness increased as gas inlet temperature was increased from 230 – 600 $^{\circ}\text{C}$. Shows PG-AMP-10 powder achieved the largest coating thickness at 0.08 mm, doubling or more all the other powders.	118
Figure 68.	Low magnification optical microscopy images of coating cross-sections of all four powders sprayed with helium at $T_i = 230\text{ }^{\circ}\text{C}$, $P_i = 250\text{ psi}$ and SOD = 16 mm. Qualitatively more porosity in the KM316 and PG-AMP-10 coatings. Crack through the thickness of the S5001. A.) S5001, B.) S5002, C.) KM316, D.) PG-AMP-10.	119
Figure 69.	High magnification (200x) cross-section optical microscopy images of all four powders' coatings sprayed with helium at $T_i = 230\text{ }^{\circ}\text{C}$, $P_i = 250\text{ psi}$ and SOD = 16 mm. S5001 and S5002 have limited porosity. Different phases are observable in S5002 and PG-AMP-10. PG-AMP-10 has large amounts of porosity at the particle-particle boundary. A.) S5001, B.) S5002, C.) KM316, D.) PG-AMP-10.	120
Figure 70.	High magnification (200x) optical microscopy images of particle-substrate boundary for all four commercial powders sprayed with helium at $T_i = 230\text{ }^{\circ}\text{C}$, $P_i = 250\text{ psi}$ and SOD = 16 mm onto grey cast iron. Cracking observable in S5001 and PG-AMP-10 near the particle-substrate boundary (boxed in red) that is not prevalent in the main coating microstructure. A.) S5001, B.) S5002, C.) KM316, D.) PG-AMP-10.	121

Figure 71.	PG-AMP-10 low magnification optical microscopy images of the coating and particle-substrate boundary at varying stand-off distances, sprayed with helium at $T_i = 230\text{ }^{\circ}\text{C}$, $P_i = 250\text{ psi}$. Suggests that stand-off distance has no significant effect on coating porosity, but does have an effect on particle-substrate boundary porosity and bond. As stand-off distance increased from 10 mm to 40 mm the boundary porosity reduced significantly. A.) SOD = 10 mm, B.) SOD = 20 mm, C.) SOD = 40 mm....	122
Figure 72.	PG-AMP-10 high magnification optical microscopy images of the particle-substrate boundary at varying stand-off distances, sprayed with helium at $T_i = 230\text{ }^{\circ}\text{C}$, $P_i = 250\text{ psi}$. Suggests that stand-off distance does have an effect on particle-substrate boundary porosity and bond. As stand-off distance increased from 10 mm to 40 mm the boundary porosity reduced significantly. A.) SOD = 10 mm, B.) SOD = 20 mm, C.) SOD = 40 mm.	123
Figure 73.	Gas inlet temperature effect on PG-AMP-10 coating microstructure indicating that as temperature is increased the coating porosity is reduced and the particle-substrate boundary porosity is reduced. Also shows that the second pass at higher temperature is less porous than the first. Sprayed with helium at $P_i = 1.2\text{ MPa}$ (175 psi) and SOD = 10 mm. A.) $T_i = 275\text{ }^{\circ}\text{C}$, B.) $T_i = 325\text{ }^{\circ}\text{C}$	124
Figure 74.	Gas inlet temperature effect on particle-substrate boundary porosity and bond. Indicates that as gas inlet temperature is increased the boundary porosity decreases and bond quality increases. PG-AMP-10 sprayed with helium at constant $P_i = 1.2\text{ MPa}$ (175 psi) and SOD = 10 mm. A.) $T_i = 230\text{ }^{\circ}\text{C}$, B.) $T_i = 275\text{ }^{\circ}\text{C}$, C.) $T_i = 325\text{ }^{\circ}\text{C}$. (red boxed area is the particle-substrate interface).....	125
Figure 75.	PG-AMP-10 optical microscopy images, sprayed with helium at $T_i = 230\text{ }^{\circ}\text{C}$ and SOD = 10 mm. Suggest pressure has limited effect on improving coating quality, but may have a minor effect on improving the particle-substrate bond quality. A.) $P_i = 1.2\text{ MPa}$ (175 psi), B.) $P_i = 1.7\text{ MPa}$ (250 psi).....	126
Figure 76.	Powder hardness as corrected from nano-indentation measurements. S5002 is hardest with small variability. KM316 is the softest but with vary large variability.....	127
Figure 77.	Inter-splat cracking of S5001 coating as a result of taking Vicker's microhardness indents. Suggests that the coatings, and in particular the particle-particle boundaries are brittle.	128
Figure 78.	Gas inlet temperature effect on coating hardness. S5001 and PG-AMP-10 sprayed with helium at constant $P_i = 1.2\text{ MPa}$ (175 psi) and varying temperature. Suggests that increasing gas inlet temperature may have reduced coating hardness but due to scatter in the results it is difficult to definitely say.....	129

THIS PAGE INTENTIONALLY LEFT BLANK

LIST OF TABLES

Table 1.	Commercial powder nominal composition summary (all elemental contributions given in weight percent).....	15
Table 2.	Summary of cold spray deposition conditions.....	17
Table 3.	Commercial cold spray stainless steel powder particle size characteristics.	20
Table 4.	Summary of commercial stainless steel powder characteristics.	29
Table 5.	Summary of cold spray coating characteristics for four commercial powders sprayed with helium gas at $T_i = 230\text{ }^{\circ}\text{C}$, $P_i = 1.7\text{ MPa}$ (250 psi). † denotes collection via X-ray diffraction. * denotes the ferrite crystallite size.	34
Table 6.	Summary of the capture depth and trigger level set-points utilized in the powder calibration experimentation for S5001 and PG-AMP-10	50
Table 7.	Summary of experimental conditions for the powder feed rate limitation experiment. (highlight indicates the powder nominal feed rate % modification).....	52
Table 8.	Summary of the experimental conditions for the substrate-laser stand-off distance interaction experiment. (highlight indicates the stand-off distance modification accomplished).....	53
Table 9.	Summary of simulation experiments and associated parameters for the study of fluid dynamics and particle transport properties. (highlighted values represent the parameter modified and the range over which it was modified in each experiment)	60
Table 10.	Working gas initial conditions and properties utilized in nozzle simulation...	61
Table 11.	S5001 particle initial conditions and properties utilized in nozzle simulation.....	61
Table 12.	Summary of helium inlet condition combinations utilized in the laser velocimetry experimentation.	62
Table 13.	One-dimensional model validation results indicating model is correctly simulating the isentropic compressible flow of helium and nitrogen through the nozzle.....	76
Table 14.	Summary of S5001 average particle velocity, critical velocity, and deposition efficiency. Sprayed with helium gas at stand-off distance of 10 mm.	93
Table 15.	Summary of PG-AMP-10 average particle velocity, critical velocity, and deposition efficiency. Sprayed with helium gas at stand-off distance of 10 mm.	93
Table 16.	Matrix of entrainment gas conditions utilized for complete comparison of cold spray deposition effect on austenitic stainless steel.....	108
Table 17.	Automatic robot parameters utilized on the Centerline (Windsor) SST Model Series C.....	108
Table 18.	Parameters utilized for nano-indentation measurements of feedstock powder hardness.....	109

Table 19.	Summary of nitrogen cold spray deposition results. Indicates that S5001 and S5002 did not successfully deposit and achieve both a measurable deposition efficiency and coating thickness. Shows that KM316 deposited the best in terms of deposition efficiency but PG-AMP-10 deposited the best in terms of coating thickness per pass. (highlights: yellow = gas parameters, green = measureable depositions, red = unmeasurable depositions).....	111
Table 20.	Summary of deposition efficiency and coating thickness per pass results for all four powders at $T_i = 230\text{ }^{\circ}\text{C}$, $P_i = 1.7\text{ MPa}$ (250 psi), and SOD = 16 mm. This condition provided the best overall deposition efficiency and coating thickness per pass. All powders achieved greater than 10 % deposition efficiency. (highlight indicates the measured DE and coating thickness measurements)	113
Table 21.	Summary of deposition efficiency and coating thickness per pass results for all four powders at $T_i = 230\text{ }^{\circ}\text{C}$, $P_i = 0.7\text{ MPa}$ (100 psi), and SOD = 16 mm. This condition provided the least overall deposition efficiency and coating thickness per pass. All powders, with the exception of S5002, did not achieve measurable deposition. (highlight indicates the measured DE and coating thickness measurements).....	113
Table 22.	Summary of deposition efficiency and coating thickness per pass results for all four powders at $T_i = 325\text{ }^{\circ}\text{C}$, $P_i = 1.2\text{ MPa}$ (175 psi), and SOD = 16 mm. This condition provided the second best overall deposition efficiency and coating thickness per pass. All powders achieved greater than 2 % deposition efficiency. KM316 and PG-AMP-10 both achieved greater than 20 % deposition efficiency. (highlight indicates the measured DE and coating thickness measurements).....	114
Table 23.	Vicker's micro-hardness results of all four commercial powder coatings sprayed with helium at $T_i = 230\text{ }^{\circ}\text{C}$, $P_i = 250\text{ psi}$, SOD = 16 mm. PG-AMP-10 had the lowest hardness.	128
Table 24.	Vicker's micro-hardness results for S5001 and PG-AMP-10 as a function of gas inlet pressure. Sprayed with helium at constant $T_i = 230\text{ }^{\circ}\text{C}$. Suggest gas inlet pressure has no significant effect on coating hardness.	130
Table 25.	S5001 capture depth calibration results (highlight indicates the capture depth modification and resultant #good/sec).	145
Table 26.	PG-AMP-10 capture depth calibration results (highlight indicates the capture depth modification and resultant #good/sec).	145
Table 27.	S5001 trigger level calibration results (highlight indicates the trigger level modification and resultant #good/sec).	146
Table 28.	PG-AMP-10 trigger level calibration results (highlight indicates the trigger level modification and resultant #good/sec).	147
Table 29.	Summary of results of the nominal powder feed rate experiment (highlighted values indicate the parameter changed, powder nominal feed rate, and the resultant statistical measure and average particle velocity.....	147

Table 30.	Summary of results of the substrate interaction experiment. Highlighted values indicate the parameter changed (substrate stand-off distance) and the resultant statistical measure and average particle velocity.	148
Table 31.	Summary of all laser velocimetry, critical velocity, deposition efficiency, and coating thickness per pass results for S5001, from Chapter III.	149
Table 32.	Summary of all laser velocimetry, critical velocity, deposition efficiency, and coating thickness per pass results for PG-AMP-10, from Chapter III. ...	150
Table 33.	Summary of helium spray deposition results for S5001 powder.....	151
Table 34.	Summary of helium spray deposition results for S5002 powder.....	151
Table 35.	Summary of helium spray deposition results for KM316 powder.....	151
Table 36.	Summary of helium spray deposition results for PG-AMP-10 powder.....	152

THIS PAGE INTENTIONALLY LEFT BLANK

ACKNOWLEDGMENTS

I would like to thank Dr. Dong Jin Woo, formerly of the Naval Postgraduate School, for his tutelage and expertise on all the equipment used in the conduct of my research. He was instrumental in helping me learn how to operate the Centerline Cold spray equipment, the Horiba particle size analyzer, the Tecnar particle velocimeter, and the Agilent Technologies nano-indenter. He dedicated numerous morning, afternoon, and weekend hours in support of my research, and surely without his aid this research would not have completed.

Additionally, I am indebted to Dr. Sarath Menon and Dr. Muguru Chandrasekhara, both of the Naval Postgraduate School (NPS). Dr. Menon provided excellent guidance and foresight throughout the course of my thesis. He provided not only great knowledge and insight, but also more hours than I can count aiding me in the preparation and characterization of materials on the Zeiss scanning electron microscope and its ancillary equipment, the powder X-ray diffractometer, and the optical microscope. Likewise Dr. Chandra shared numerous insights into the fluid dynamics and particle velocity aspects of this thesis. His superior knowledge in the field of fluids not only aided me in ensuring my simulation was functioning properly, but also helped me interpret the results of my experimentation. Without that support the fluid dynamics portion of this work would have never finished.

Likewise, I would like to extend my extreme gratitude to Professor Luke N. Brewer, also of the Naval Postgraduate School. His constant support throughout my graduate studies, as a professor and thesis advisor, has surely made me a stronger critical thinker and academic mind, and most importantly, a more well-rounded asset to the Navy and the engineering duty officer community. His dedication to his thesis students and his work at the NPS are surpassed only by the care he possesses for each and every one of our successes.

We are very grateful for funding for this research from Mr. Richard Hays of the OSD Office of Corrosion Policy and Oversight. This research was supported as a part of

the Technical Corrosion Collaboration. Likewise, we are grateful to Dr. Ken Ho of the Expeditionary Warfare Center for supporting this research and bringing the problem of low-pressure cold spray for repair of iron and steel structures to our attention.

Lastly, but certainly not least, I would like to thank my family members, especially my wife. Without her support and hard work keeping the home front operating smoothly and the kids happy, I couldn't have accomplished any of this.

I. INTRODUCTION

A. MOTIVATION

In the Navy, there are two failure types that occur on a more regular basis than any others—mechanical failure and corrosion. Due to this, there is an enormous amount of research time and funding dedicated to the prevention and repair of these two failure drivers. The design of a new component, or structure, or redesign of an old one either attempts to prevent the mechanical failure, or increase the component's lifetime. The use of techniques, such as painting and cathodic protection, attempts to prevent corrosion from occurring. Despite all the efforts placed toward preventing mechanical failure and corrosion, they both still occur, and therefore there is a definite need for the ability to repair these items and restore them to a normal operating condition. Current maintenance repair methods, however, rely heavily on the complete removal of damaged and replacement of new material. Another common approach is the use of thermal spray techniques, such as plasma spray, flame spray, or high velocity oxygen fuel (HVOF) spray, to build the material back up dimensionally to a usable condition.

Traditional thermal spray techniques have both advantages and disadvantages to their use. The advantages are aspects such as high deposition rates, spray capability of a wide range of materials or composites, and the ability to spray on numerous different suitable substrate surfaces. These techniques, however, also possess some important disadvantages, such as porosity and oxidation inclusion in the deposited coating [1]. One major disadvantage to traditional thermal spray techniques is the fact that the metal powders are heated above their melting point, thus altering their properties. The substrate to which the particles are deposited is also heated to varying degrees, depending upon the technique used and the time it is used for, further altering its properties [1]. Materials science and engineering spends an ever-increasing amount of money to process metals and their alloys to exact mechanical property and microstructural standards, such as yield strength, hardness, fatigue strength, ductility, porosity, and phase content, which are needed for specific physical applications. Therefore the use of traditional thermal spray techniques causes changes in the physical, microstructural, and in some cases the

electrochemical properties of the material deposited and the substrate. Cold spray, an emerging coating and additive manufacturing technology, has been found to combat the limitations of traditional thermal spray technologies by eliminating the thermally and microstructurally induced property changes [1].

Cold spray is conducted at much lower temperatures and higher particle velocities than traditional thermal spray techniques (Figure 1), therefore leading to denser (less porous) coatings. This increase in density is due to the lack of splashing effect that occurs with molten particles in other traditional thermal spray techniques. In addition, the high particle velocity of cold spray results in a peening effect that causes plastic deformation to fill the porous gaps [1]. Another effect of conducting this technique at lower temperature is that there are less thermally induced property changes to both the powders and the substrate. Specifically, there are no oxide impurities introduced into the material, limited thermal gradients and residual stresses, and limited property changes of the underlying substrate generated [1]. There is also no loss of volatile elements during the process such as the loss of high vapor pressure elements such as zinc and magnesium, which occur during traditional thermal spray techniques and welding [1]. Because of these benefits, cold spray can be used as both a coating application technique and an additive manufacturing (or repair) technique.

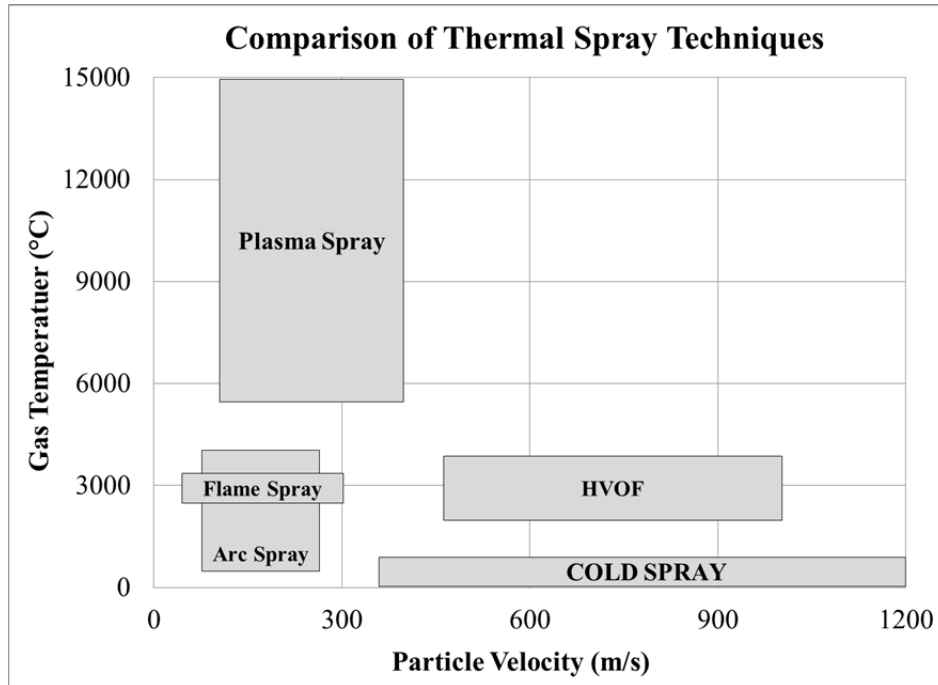


Figure 1. Comparison of approximate gas temperature and particle velocity ranges for thermal spray techniques, after [1].

The coating application potential of cold spray deposition can serve numerous purposes, but the most important one is the application of the cold spray deposition process in the creation of a corrosion resistant coating to electrochemically protect the underlying material. Because of its wide use in the Department of Defense, and aerospace and automotive industries, the corrosion protection of magnesium alloys has been a major focus of research. In 2010, Spencer and Zhang explored the application of 316L stainless steel coatings on a magnesium alloy, AZ91E, substrate [2]. They concluded that the stainless steel coating substantially reduced corrosion potential as compared to the magnesium substrate alone. Thicker coatings were observed to be more effective. Also in 2010, Tao et al. demonstrated the corrosion protection effectiveness of a cold sprayed aluminum coating on AZ91D, a magnesium alloy. Their findings suggested that the aluminum coating demonstrated increased pitting corrosion protection for the magnesium alloy [3]. In 2011 DeForce et al. successfully demonstrated that the use of Al-5 wt. % Mg coatings produced via cold spray deposition successfully inhibited the corrosion potential of an otherwise active magnesium alloy, ZE41A-T5 [4]. As AL-

Mangour et al. demonstrated in 2012, corrosion protection through cold sprayed coatings is not just limited to the use of aluminum powder and the protection of magnesium alloys. They demonstrated that a Co-Cr coating produced by cold spray and deposited on 316L stainless steel enhanced the corrosion resistance of the 316L material considerably [5]. Cold spray deposition is certainly a viable option for providing a protective, corrosion resistant layer, but it also has another potential application in the repair of damaged structures.

A second major application of the cold spray deposition process is repair of damaged mechanical components. Whether this damage comes from corrosion damage, wear, or cracks in mechanical parts, it has been shown that cold spray can be utilized to replace lost material and allow that component to be returned to normal operation vice scrapping and replacing with new. This approach benefits not only the budget aspects of repair, but also could have a major impact on the operational availability of the component, both of which are major concerns in the Navy today. P.F. Leyman and V.K. Champagne have conclusively demonstrated the ability of cold spray deposition to repair aluminum mast supports utilized in U.S. Army rotorcraft. They did so by removing the mast support, utilizing cold spray to refill the damaged portions of the rotor mast, and having the mast machined back to original specification [6]. This process has led to the successful recovery of over 50 mast supports that would otherwise have been scrapped and replaced with new ones because they had pitting corrosion or mechanical damage in them. Likewise other cold spray repair of aircraft components, accomplished by Villafuerte and Wright, has been accomplished with aluminum alloys meeting all FAA requirements for service [7]. It should be noted that these aircraft repair are for dimensional restoration and not structural (load-bearing) repair. The use of cold spray repair for structural repairs is a currently active area of research [8, 9].

The Navy, being in a constant struggle with budget and operational tempo, is on a constant search for new and innovative techniques to save money and reduce downtime of equipment. Cold spray deposition, having already proven to be a viable repair option for aluminum structures, may prove a viable field repair option for steel Naval structures

and vessels. With all the advantages of the cold spray deposition process, it is clear that the Navy and its contractors could benefit from its use.

B. LITERATURE REVIEW

1. The Cold Spray Deposition Process and Characteristics

Cold gas dynamic spray is a relatively new technology in which metal powder particles are accelerated in a supersonic jet of gas (known as the entrainment or working gas) to velocities in the 500-1200 m/sec range. These particles are bonded to a substrate by way of extensive plastic deformation [2, 10–17]. A general schematic of the process is depicted in Figure 2. The supersonic jet of gas is generated by expanding a pressurized, preheated gas (commonly nitrogen or helium) through a converging-diverging, de Laval, nozzle. During this expansion of the gas, the pressure and temperature both decrease, the temperature decreasing to levels less than 100°C, thus naming the process “cold spray” [17]. In reality, the term “cold” really refers to the fact that the particles remain in the solid state throughout the process, unlike the melting of particles found in most thermal spray processes. The metal powders utilized in the process generally have a diameter of 5-50 μm and are injected into the high velocity gas stream either prior to or immediately following the throat of the nozzle.

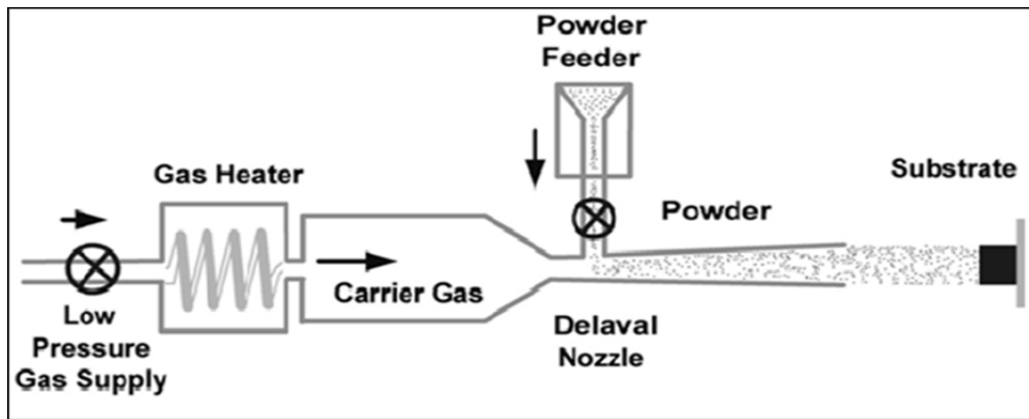


Figure 2. Schematic of the cold spray deposition process from [6].

The metal powders are accelerated in the gas stream and once they achieve a particular velocity, adhere to the substrate via adiabatic shear deformation [18]. This

finite velocity is referred to as the critical velocity and is one of the most important pieces of information for both the experimental and practical use of the cold spray. All particles traveling greater than or equal to this velocity will adhere to the substrate, and those traveling slower than it will bounce off. Therefore a way to predict (through modeling) and measure (through laser velocimetry) the particle velocity is of critical importance.

The particle velocity can be predicted by many methods such as fluid dynamics modeling of the gas flow and particle transport through the nozzle. A simple one-dimensional model (Equations 1 and 2) can be utilized, where (1) describes the gas velocity through the length of the nozzle (with the pressure, temperature, and gas type being the drivers), and (2) describes the gas-particle interaction and subsequent acceleration of the particle through the nozzle (where the particle size, morphology, material type, and gas type are the influential parameters) [19].

$$U_{g_x} = \sqrt{2 \left(\frac{\gamma}{\gamma - 1} \right) R T_{g_i} \left[1 - \left(\frac{P_x}{P_i} \right)^{\frac{(\gamma-1)}{\gamma}} \right] + U_{g_i}^2} \quad (1)$$

$$\frac{dU_{p_x}}{dt} = \frac{3}{4} \frac{C_d}{D_p} \frac{\rho_{g_x}}{\rho_p} (U_{g_x} - U_{p_x}) |U_{g_x} - U_{p_x}| \quad (2)$$

where:

U_{g_x} : the gas velocity at any point, x, along the nozzle

R: the gas specific constant

T_{g_i} : the inlet temperature of the working gas

P_x : the gas pressure at any point x along the nozzle

P_i : the inlet gas pressure

γ : the specific heat ratio of the working gas

U_{g_i} : the inlet gas velocity

U_{p_x} : the particle velocity at any point, x, along the axis of the nozzle

C_d : the drag coefficient for a sphere function of Reynolds number

D_p : the particle diameter

ρ_{g_x} : the gas density which varies along the nozzle with the temperature and pressure of the gas.

ρ_p : the particle density

It should be noted, however, that there are a number of assumptions made in the derivation of these equations and the equations are valid only for the length of the nozzle up to the nozzle exit whereas coating deposition is performed at varying stand-off distances from the nozzle exit. Due to the assumptions and limitations of the modeling, there is a need for actual in-flight particle velocity measurements to garner that knowledge. Gilmore et al. successfully measured copper particle velocity utilizing laser velocimetry and studied the influence of gas parameters and particle parameters on the particle velocity [20]. They demonstrated the effect of both helium and air (two different molecular weight gases) and their transport properties on the average velocity of cold sprayed copper particles (Figure 3), showing that helium effectively accelerated the particles to higher velocities than air. They also investigated the effects of gas pressure and temperature on particle velocity and found that increasing gas temperature and pressure increased the particle velocity. They also suggest that by comparing the deposition efficiency with the velocity distribution attained from laser particle velocimetry, a quantitative representation of the critical velocity can be attained (Figure 4). The figure shows that for the condition with zero deposition efficiency almost no particles attain that velocity according to the measured velocity distribution. For the 53 % deposition efficiency conditions approximately half of the particle velocities measured lie above that velocity, and for the 95 % condition almost the entire velocity distribution lies above the critical velocity.

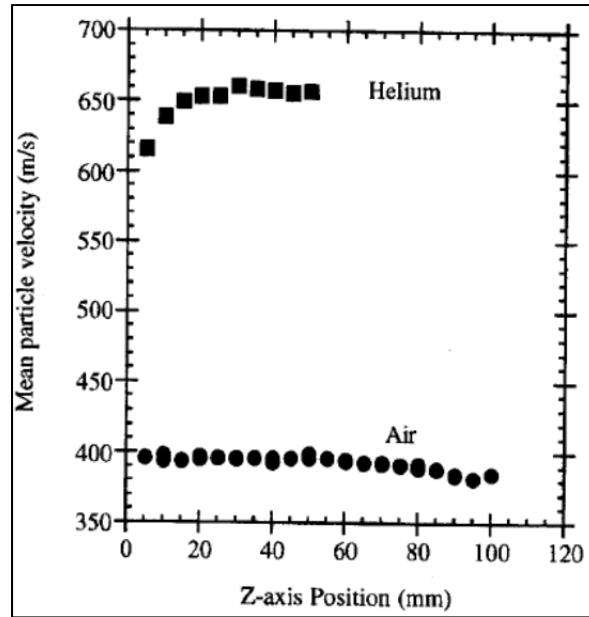


Figure 3. Mean particle velocity versus z-axis position for copper powder indicating the impact of gas molecular weight on particle velocity in the cold spray process, from [15].

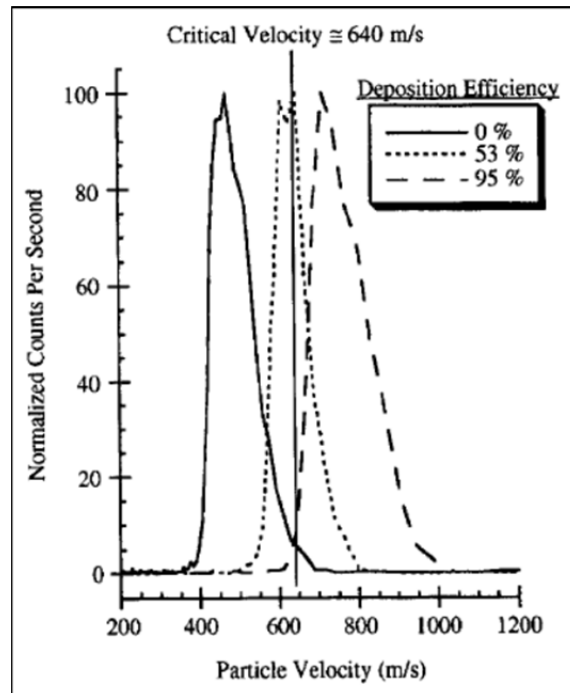


Figure 4. Copper particle velocity distributions in the cold spray process and their associated deposition efficiencies with an approximated critical velocity, from [20].

It is important to note also that although particle velocity knowledge is of critical importance there are numerous other parameters that affect the deposition characteristics of the cold spray process. All of these properties and parameters (including the gas and particle ones discussed) can generally be grouped into a four broad categories:

- Entraining gas properties: molecular weight, pressure, and temperature
- Physical process parameters: nozzle design, distance from the nozzle exit to the substrate (stand-off distance), and robot or manual parameters such as traverse speed and pass overlap
- Feedstock powder properties: material, size, morphology, hardness, and phase content.
- Substrate properties: material type, hardness, and surface finish (smooth or grit-blasted)

Most of these parameters have been investigated and their effects on the cold spray deposition process are reviewed in Champagne's book, *The Cold Spray Materials Deposition Process: Fundamentals and Applications* [21]. For instance, if gas pressure and/or temperature are increased, the subsequent particle velocity and deposition efficiency are also increased. For spherical particles, if the diameter is made smaller, the particle velocity increases. If traverse speed of the process is decreased or powder feed rate is increased, the coating thickness per pass will increase. It has also been shown that grit blasting the substrate surface prior to cold spray tends to increase deposition efficiency over smooth-finish surfaces.

2. Utilizing Austenitic Stainless Steel Powder in the Cold Spray Deposition Process

Cold spray deposition might provide a solution for field repair of naval steel structures. In particular, cold spray deposition of austenitic stainless steels could provide dimensional restoration, structural repair, and corrosion prevention for corroded and/or damaged steel structures. Cold spray deposition of austenitic stainless steel has been recently explored as a means of providing a corrosion resistant coating on magnesium alloys [2, 15], aluminum components [22], and biomedical implants [5, 23]. A number of investigators have demonstrated successful cold spray deposition of austenitic stainless steels, i.e. SS304 and SS316, over a range of gas inlet conditions ($P_i = 2.5 - 4$ MPa and

$T_i = 400 - 1000\text{ }^{\circ}\text{C}$) [2, 12, 15, 23–26]. However, all of these studies have either used high pressure cold spray deposition or the related technique, kinetic metallization, neither of which is particularly well-suited to a portable field repair option. Low-pressure cold spray deposition (pressure generally less than 2.0 MPa) is generally more portable and can be used for in field repairs. To date, successful, low-pressure cold spray deposition of austenitic stainless steels has not been investigated. Furthermore, almost nothing is known about the microstructures of the austenitic stainless steel feedstock powders or the coatings that they produce. As mechanical and corrosion behavior are strongly determined by microstructure, it is essential that we understand the processing-microstructure-property relationships for low pressure cold sprayed austenitic stainless steel coatings.

As critical to understanding the processing-microstructure-property relationships is for utilizing cold spray deposition of austenitic stainless steel as a field repair technique, so too is the particle-velocity relationship. Gilmore et al. provides a thorough review of the effects of different gas parameters and powder properties, but that is for copper powder [20]. Huang et al. studied the in-flight velocity of austenitic stainless steel powder with a high pressure-high temperature deposition system [26]. While they report nearly 100 % deposition efficiency, they did not measure the critical velocity - a key material parameter that varies with powder characteristics and temperature, and therefore leaves the question of what is the critical velocity for cold spray deposition of austenitic stainless steel, and what conditions need to be used to achieve certain deposition efficiencies. This piece of information is critical to the foreknowledge and planning for repairs in determining the type and amount of gas and amount powder needed to conduct the repairs.

C. OBJECTIVES

This thesis is organized around three main technical objectives:

- 1. Investigate the Powder Microstructure–Processing–Coating Microstructure Relationships of Cold Sprayed Austenitic Stainless Steel**

Successful deposition of austenitic stainless steel has been demonstrated in previous research, but there is a lack of understanding of both the feedstock powder and deposited coating microstructures. In this research, we will present a thorough characterization of commercially available austenitic stainless steel powders, including particle size, shape, phase content, and grain structure. We will also present a complete as-deposited characterization in order to fully analyze the effects of the cold spray deposition process on the microstructure of the deposited coating.

2. Use Laser Particle Velocimetry to Determine the Critical Velocity of Austenitic Stainless Steel Powder for Cold Spray Application

This research will be the first at Naval Postgraduate School to implement the laser particle velocimetry process and to measure the velocity of in-flight particles in the cold spray process. Because it is new to the research here we will highlight important operating characteristics of the laser system, show how to successfully measure particle velocity utilizing the system, and utilize the velocity data measured to determine if there exists a critical velocity necessary for the successful deposition of austenitic stainless steel, and if it does exist, is it the same for different austenitic stainless steel powders. We will also numerically model the fluid dynamics in the cold spray nozzle in an attempt to predict particle velocity and to validate the current experimental measurements.

3. Investigate the Processing Parameter Space for Low-Pressure Cold Spray of Austenitic Stainless Steel

In this study, we will assess the full parameter space that controls the low-pressure cold spray deposition of austenitic stainless steel. We will modify parameters such as temperature, pressure, the type of the working gas, and the stand-off distance during cold spray deposition. This parameter study will allow us to correlate the initial microstructure, particle morphology, and phase content of austenitic stainless steel powders to the low pressure cold spray deposited coating properties such as deposition efficiency, coating thickness per pass, porosity, and hardness.

THIS PAGE INTENTIONALLY LEFT BLANK

II. MICROSTRUCTURE-PROCESSING-MICROSTRUCTURE CHARACTERIZATION OF AUSTENITIC STAINLESS STEEL POWDERS AND COATINGS

This chapter will explore the connections between the microstructures of starting austenitic stainless steel powders with their respective microstructures after low-pressure cold spray deposition. The microstructure, composition, phase distribution, and particle size of the as-received powders were all characterized utilizing electron microscopy, X-ray diffraction, and laser particle size analysis. One low-pressure cold spray condition was utilized to create the coatings in which the microstructure and phase distribution were further investigated. A literature review of recent stainless steel cold spray deposition work is discussed in Section A. The experimental methods used for characterization of both the powders and coatings, and the methods used for the creation of the coatings are discussed in Section B. The experiment results and discussions are contained in Section C and D respectively.

A. INTRODUCTION

Austenitic stainless steel powders have been successfully deposited onto magnesium alloys [2, 15], aluminum components [22], and biomedical implants [5, 23]. These depositions have occurred over a range of spray temperature (320-1000°C), pressure (0.6-4MPa), and gas types (nitrogen and helium). The lower pressure experiments were performed using the kinetic metallization process, a similar, but subsonic, spray deposition process [27]. The reported deposition efficiencies ranged from nineteen [28] to nearly one-hundred percent [26]. The deposition efficiency was increased by the use of mixed particle sizes [2], the addition of aluminum oxide powders [2], and increases in the temperature and pressure of the entrainment gas during spray deposition, causing an increase in the particle velocity [25, 26, 28]. Huang et al. measured particle velocities at higher temperatures and pressures in the range of 625-800 m/s using nitrogen as the entrainment gas [26]. The higher particle velocities correlated directly to increased deposition efficiencies and increased coating densities.

The mechanical properties of these coatings were varied and have been connected primarily to the inter-particle porosity of the coatings. The hardness of the cold sprayed coatings was generally much greater than the underlying substrate, presumably from the intense strain hardening experienced by the particles upon impact. In contrast to the assumption that elastic modulus trends with hardness, Han et al., measured the elastic modulus of a SS304 coating in three point bending and found it to be approximately 117 GPa, as opposed to the nominal value of 200 GPa for stainless steel indicating a reduction in elastic modulus vice an increase. This substantial reduction in modulus was accredited to the inter-particle, or splat, porosity in the coating [10]. Meng et al reported very low (<4%) values of elongation to fracture under tensile loading for cold sprayed SS304 coatings even after annealing at 950°C for one hour [12]. The inter-particle porosity has also been linked to unfavorable fatigue performance [23], and reduction in elongation to fracture.

While the basic mechanical properties have been surveyed in previous literature, there is a need for more information about the microstructures of these materials. All of the previous studies have shown optical or scanning electron microscopy (SEM) images of the coating microstructure. While the inter-particle porosity can be seen in these images, the crystallite, or grain, structure is unclear. No crystallite size measurements have been reported. Different observations have been made as to the phase content of the powders and resultant coatings. Borchers et al. stated that ferrite was observed in the starting powders but with very little to none in the deposited coatings [29]. Spencer et al. also observed delta ferrite in the starting powders via X-ray diffraction, but its presence in the deposited coatings was not mentioned [15]. Han et al. report the presence of ferrite in the SS304 cold spray coatings, but they do not mention if there was ferrite present in the starting powders [30]. Recently, Villa et al. clearly showed X-ray diffraction data from SS316L powders that were single phase austenitic both before and after cold spray deposition [28]. In addition, authors have noted that the particles are quite deformed after spraying, but there has been no measurement of deformation texture or dislocation density.

This chapter examines the microstructures of both the starting commercial powders and the resultant cold spray deposits. It provides microstructural information such as crystallite size, phase content, and level of plastic deformation with the goal of providing connections between the powder microstructure and the coating microstructure for cold sprayed austenitic stainless steel.

B. EXPERIMENTAL METHODS

Four commercial powders were used for these characterization and cold spray deposition experiments: Centerline S5001 (SS304L), Centerline S5002 (SS316L), Inovati KM316 (SS316), and Plasma Giken PG-AMP-10 (SS316L). Table 1 summarizes the powders and the nominal compositions as provided by the manufacturer. Each of these powders was analyzed and used as-received without further modification or heat treatment.

Powder	Fe	Cr	Ni	Mn	Mo	Si	C
S5001 (304L)	68.4	19	10.9	0.97	-	0.6	0.017
S5002 (316L)	65.5	17.2	13	1.5	2.2	0.5	0.014
KM 316 (316)	68.2	16.8	10.8	1.3	2.1	0.6	0.02
PG-AMP-10 (316L)	69	17	12	-	2	-	-

Table 1. Commercial powder nominal composition summary
(all elemental contributions given in weight percent).

1. Particle Size Analysis

The size distribution of each of the four commercial powders was measured utilizing the Horiba Laser Scattering Particle Size Analyzer (LA-950V2) equipped with a 650 nm wavelength laser. Approximately 500 mg of each powder was dispersed in isopropanol and inserted into an analytic glass cell. The refractive index used for stainless steel was 2.757 [31].

2. Powder and Coating Cross-sectional Samples Metallographic Preparation

To analyze the internal structure and chemistry of the stainless steel powders, they were mixed with Buehler KonductoMet epoxy powders and hot compression mounted. Standard metallographic preparation techniques were utilized for grinding and polishing of the powders and coating cross-sectional samples of the cold sprayed stainless steel deposited coatings. Grinding was accomplished utilizing different grit paper up to 1200 grit, and initial polishing was accomplished with 1 μm and 0.25 μm diamond. Final polishing was conducted utilizing 0.05 μm colloidal silica suspension using a VibroMet2 Buehler vibratory polisher.

3. Cold Spray Deposition Experiments

The cold spray deposition experiments were performed using the Centerline (Windsor, Ontario) SST Model Series C low-pressure cold spray deposition system utilizing a tungsten carbide nozzle with a 2 mm throat and 120 mm divergent barrel section and a stand-off distance of 16 mm. The carrier gas used was helium at a temperature and pressure of 230 °C and 1.7 MPa (250 psi), respectively. The grey cast iron substrate was initially machine milled and then grit-blast prior to deposition. Grit-blasting was conducted utilizing Centerline SST-G002, alumina grit powder, nitrogen gas at $T_i = 250^\circ\text{C}$, $P_i = 1.4 \text{ MPa}$ (200 psi), a nominal powder feed rate of 20%, and a stand-off distance of 15 mm. During deposition, the spray gun was manipulated by a robot at a traverse speed of 40 mm/s and step over per pass of 1.2 mm. The powder feed rate was set nominally on the Centerline unit at 40%, which caused a range of actual feed rates of powder from 20 to 60 g/min depending on the feeding properties of the individual powder. The spray condition data is summarized in Table 2.

Powder Material	S5001, S5002, KM316, PG-AMP-10
Gas	Helium
Substrate Material	Grey Cast Iron
Gun Type	Automatic
Nozzle	WC
Gas Temperature (°C)	230
Gas Pressure (MPa)	1.7 (250psi)
Nominal Powder Feed Rate (%)	40
Gun Stand-off Distance (mm)	16
Gun Traverse Speed (mm/s)	40
Gun Step Over per Pass (mm)	1.2

Table 2. Summary of cold spray deposition conditions.

During the experiment, the deposition efficiency (DE) and coating thickness per pass were measured. DE of the deposit was found by taking the ratio of the mass of the deposit to the mass of the sprayed powder, Equations 3 and 4.

$$DE(\%) = \frac{Mass_{Deposit}}{Mass_{Sprayed Powder}} \times 100\% \quad (3)$$

$$Mass_{Deposit} = Mass_{Substrate+Deposit} - Mass_{Substrate} \quad (4)$$

The mass of the substrate was measured with a digital balance before and after each experiment. The mass of the sprayed powder was attained by measuring the amount of powder inserted into the cold spray unit initially and then measuring how much was left after the experiment was completed. Coating thickness per pass was measured with a digital micrometer at the thickest cross section of the deposit. The balance and digital micrometer are accurate to 0.1 grams and 0.01 mm, respectively.

4. Scanning Electron Microscopy of Powders and Coatings

Secondary electron (SE) and backscatter electron (BSE) images of the microstructure of each powder were taken using a Zeiss Neon 40 FIB-SEM at 20 keV with a 60 µm objective aperture and a nominal electron probe current of approximately 1320 pA at numerous magnifications from 250x to 10000x. The composition of each

powder was mapped using an EDAX Pegasus energy dispersive X-ray spectroscopy (EDX) system with a silicon drift detector (10 mm² area). The crystallite size of each powder was measured using electron backscatter diffraction (EBSD) on the Zeiss Neon 40 instrument. The EDAX OIM 6.0 EBSD system was used with a Hikari, high-speed EBSD detector. The nominal electron probe current was increased to 1-2 nA for all EDX and EBSD experiments. The EBSD data was collected with the SEM operated at 20 keV using a 60 µm objective aperture. EBSD patterns were indexed for both the austenite (FCC) and ferrite (BCC) phases simultaneously using a minimum of five detected bands. Orientation maps were collected using a range of step sizes, 40-150 nm, in the x and y directions over a variety of map size ranges depending upon the exact microstructure in the field of view. After collection, the EBSD data was treated with a de-noising routine consisting of one iteration of confidence index (CI) standardization and one iteration of dilation. Only data points with a CI ≥ 0.2 were analyzed and included in the maps. The amount of plastic deformation was visualized using a measurement of intragranular misorientation. For these results, the grain orientation spread (GOS) was used to quantify intragranular misorientation. The GOS algorithm first calculates the mean orientation of each identified grain and then calculates the mean, scalar misorientation between this orientation and every other pixel in the grain. This technique and its comparisons with other algorithms are detailed in the book chapter by Brewer and Fields [32].

5. X-ray Diffraction

The bulk crystalline phases in the powders and coatings were determined using X-ray powder diffraction. The X-ray diffraction was conducted using a Panalytical PW_830 X-ray diffractometer with a Cu K α radiation source at a powder of 35 kV and 30 mA with a graphite monochromator on the diffracted beam side. A step size of $2\theta=0.02^\circ$ and a dwell time of 2 seconds/step were used in all acquisitions. An approximate determination of the volume fractions of ferrite in the as-received powders was made from the relative integrated intensities of the $\{111\}_\gamma$ and the $\{110\}_\alpha$ peaks. A simple calculation was performed using the approach by Cullity [33], Equation 5:

$$\frac{I_{\gamma}}{I_{\alpha}} = \frac{R_{\gamma}}{R_{\alpha}} \frac{v_{\gamma}}{v_{\alpha}} \quad (5)$$

where I_i is the integrated X-ray intensity and v_i is the volume fraction of the phase and R_i is given by Equation 6:

$$R_i = |F|^2 p \frac{(1 + \cos^2 2\theta)}{(\sin^2 \theta \cos \theta)} \quad (6)$$

where F is the structure factor for each phase, p is the multiplicity factor, and θ is the Bragg angle. Here f is assumed to be the same for both the austenite and ferrite phases and thus $|F|^2$ can be taken as $16f^2$ and $4f^2$ for the $\{111\}_{\gamma}$ and the $\{110\}_{\alpha}$ reflections, respectively, with multiplicity values of 8 and 12 neglecting errors associated with the compositional differences of the ferrite and austenite phases. Combining the above equation with the condition that only austenite and ferrite are present, i.e. $v_{\gamma} + v_{\alpha} = 1$, the ferrite volume fractions can be conveniently determined. Note that errors due to X-ray fluorescence, extinction, fine grain size, and strain were not addressed in these calculations.

C. RESULTS

1. Feedstock Powder Characteristics

The particle size distributions showed a substantial variation in the powders. The mean particle size varied by more than a factor of two (Figure 5). All of the powders possessed a distribution with a tail towards larger particle sizes as would be expected. The S5001 and KM316 powders exhibited relatively symmetric, unimodal distributions peaked at approximately 20 μm and 12 μm , respectively. The S5002 and PG-AMP-10 powders displayed a distinct second hump in their distribution at larger ($>100 \mu\text{m}$) particle sizes. The PG-AMP-10 powder possessed at least ten percent of particles with diameters larger than 160 μm . The KM316 powder showed a distribution of particles at larger sizes but with a less pronounced hump in the distribution as compared to the PG-AMP-10. This range of particle sizes was also visible in the SEM images (Figure 6).

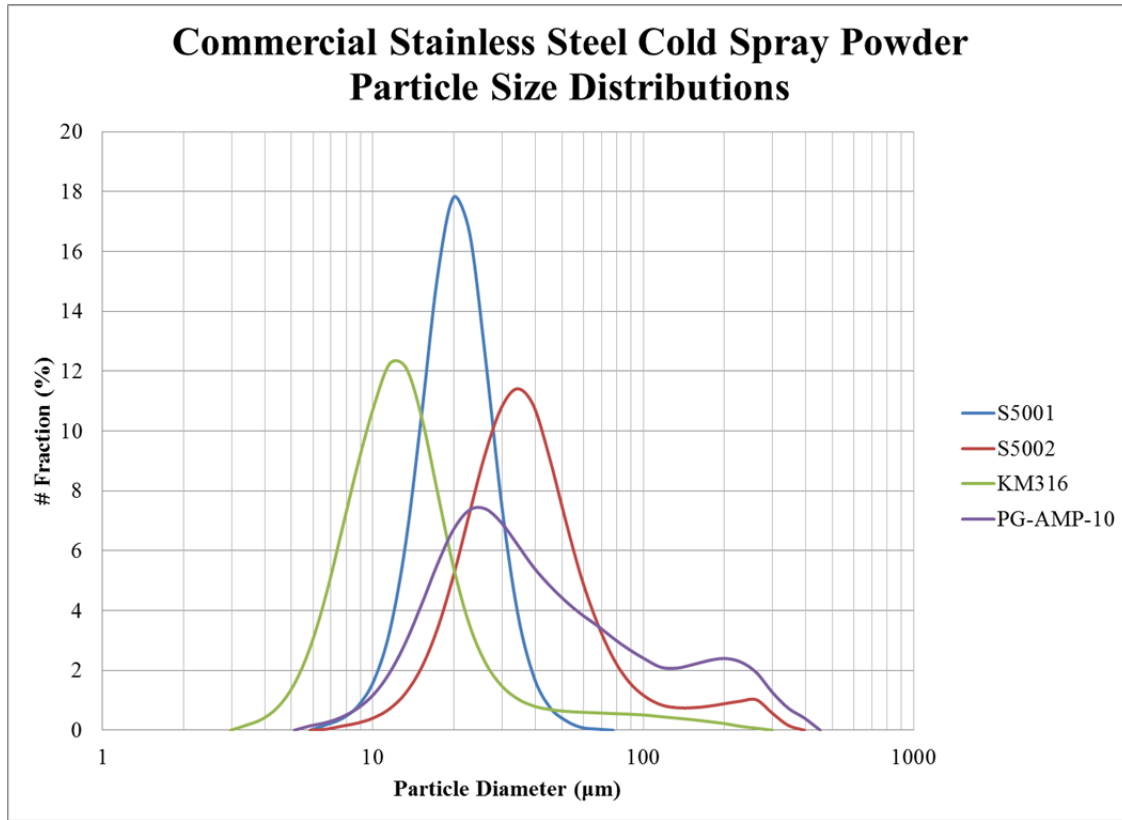


Figure 5. Particle size distributions for the four commercial cold spray stainless steel powders.

Powder	Mean Size (μm)	D10 (μm)	D90 (μm)
S5001 (304L)	19.9	12.5	28.4
S5002 (316L)	45.6	18.1	75.2
KM 316 (316)	17.2	6.7	25.5
PG-AMP-10 (316L)	61.3	14.3	164.8

Table 3. Commercial cold spray stainless steel powder particle size characteristics.

The morphologies and shapes of the powder particles were consistent with particles that had been produced through gas atomization but with some post-processing (Figure 6). The external shapes of the S5001, S5002, and KM316 were fairly spherical, which is typical for powders produced through gas atomization [2, 28]. The particle surface roughness also varied considerably, with the surfaces of the S5002 particles being quite smooth while the surfaces of the S5001 particles were quite rough as shown in

Figure 6. The shapes of the PG-AMP-10 powders were irregular with visible bonding between the smaller and larger particles.

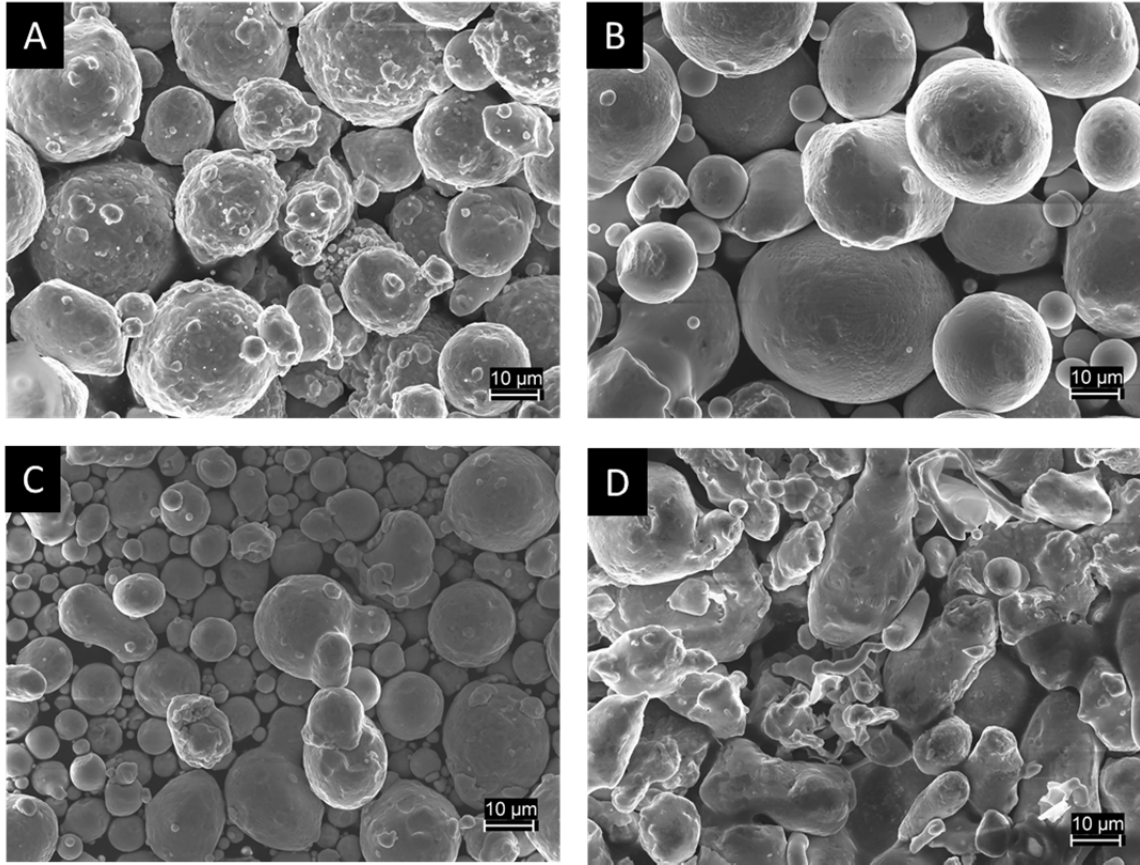


Figure 6. Secondary electron images of the four stainless steel powders as-received. A.) S5001, B.) S5002, C.) KM316, D.) PG-AMP-10.

The internal shapes and morphologies of the particles, provided through SEM images of the cross-section, showed several distinct differences (Figure 7). The S5001, S5002, and KM316 powder particles were more irregular in shape, than as evidenced by the external topographical view, with only the smallest particles being truly spherical in shape. All of the powders possessed fine, sub-micron, internal porosity. The KM316 powder displayed strong backscatter contrast typically observed in deformed metallic structures. The cross-sectional images of the PG-AMP-10 powder clearly showed sintering or diffusion bonding between smaller particles to effectively make up larger particles. None of the particles exhibited the dendritic/cellular microstructure expected

for a rapidly solidified, gas atomized powder [24, 28, 34]; suggesting that all of these powders received post-atomization processing.

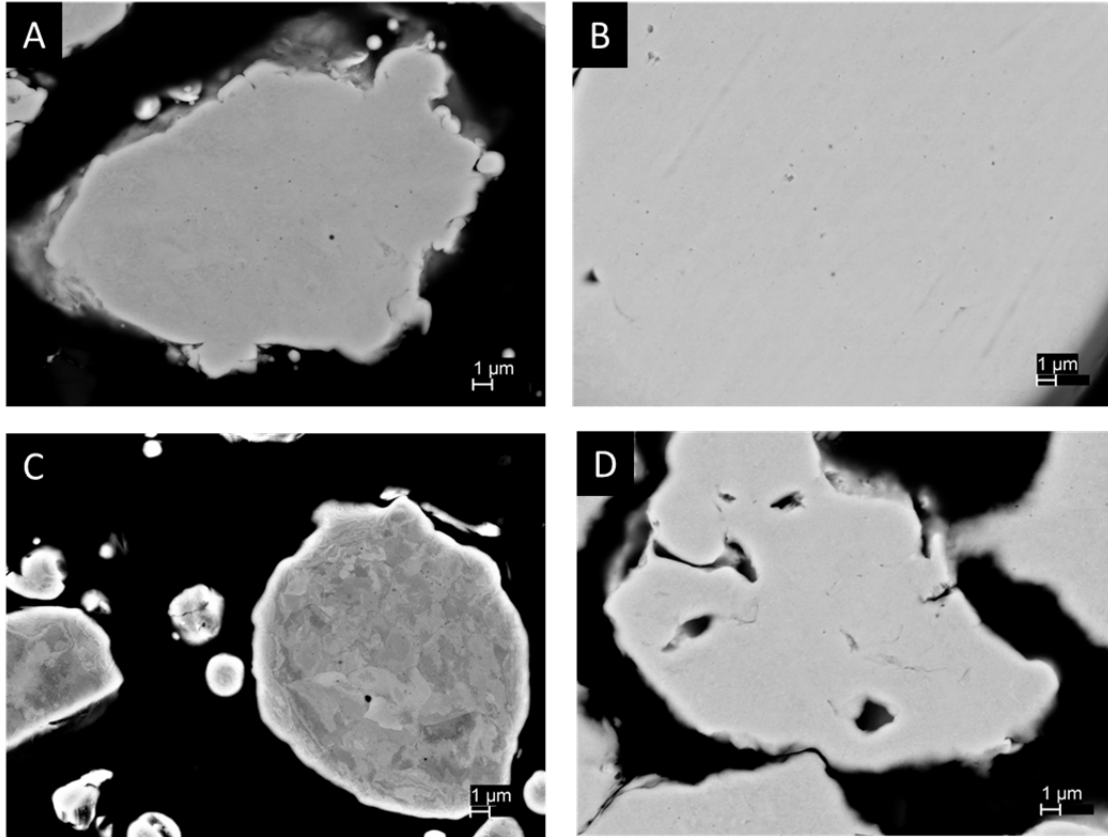


Figure 7. Backscatter electron images of the four stainless steel powder cross-sections. A.) S5001, B.) S5002, C.) KM316, D.) PG-AMP-10.

EDX maps for each powder showed a relatively uniform distribution of all the primary elements (Figure 8 - 11). The key austenite and ferrite stabilizers, Ni, Mn, Cr, and Mo, were all uniformly distributed throughout the powder particles, for all four stainless steel powders. Small silicates, approximately 1 μm in size, were observed in each mount, outside of the powder particles. In addition, small aluminum and titanium containing particles were observed between primary powder particles.

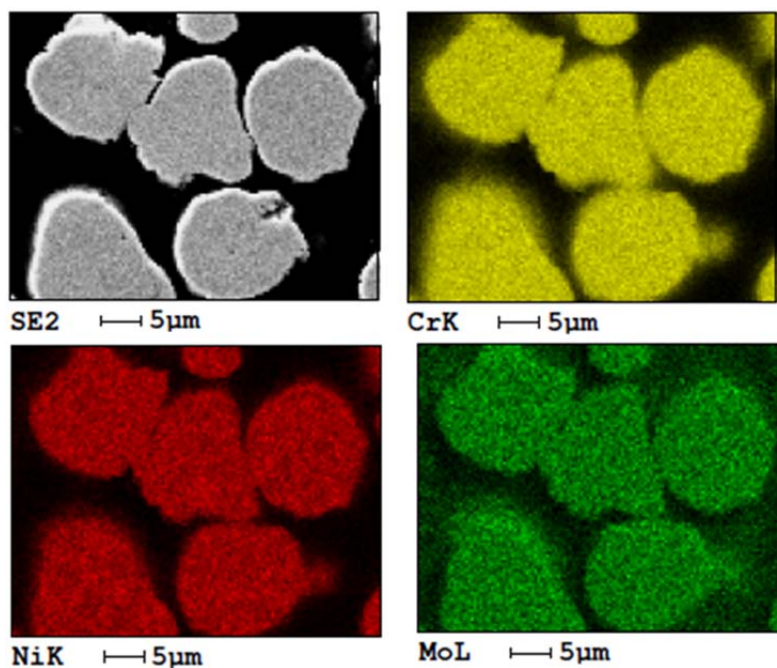


Figure 8. EDX map for the S5001 powder showing the primary austenite and ferrite stabilizers (Cr, Ni, and Mo) for austenitic stainless steel.

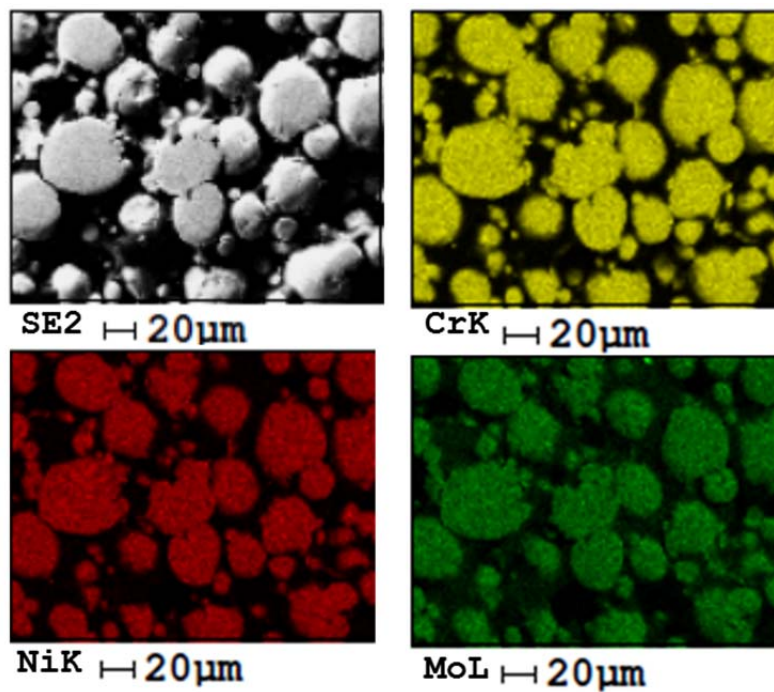


Figure 9. EDX map for the S5002 powder showing the primary austenite and ferrite stabilizers (Cr, Ni, and Mo) for austenitic stainless steel.

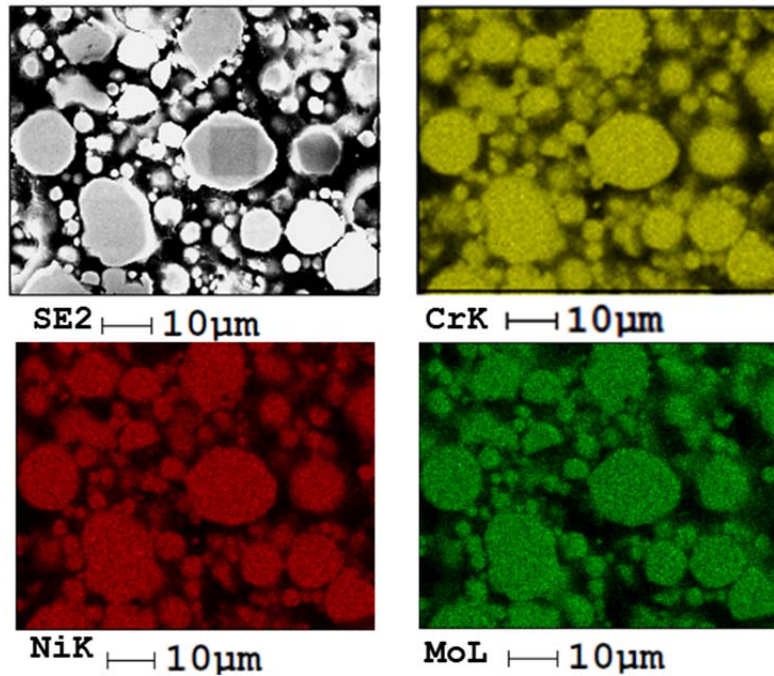


Figure 10. EDX map for the KM316 powder showing the primary austenite and ferrite stabilizers (Cr, Ni, and Mo) for austenitic stainless steel.

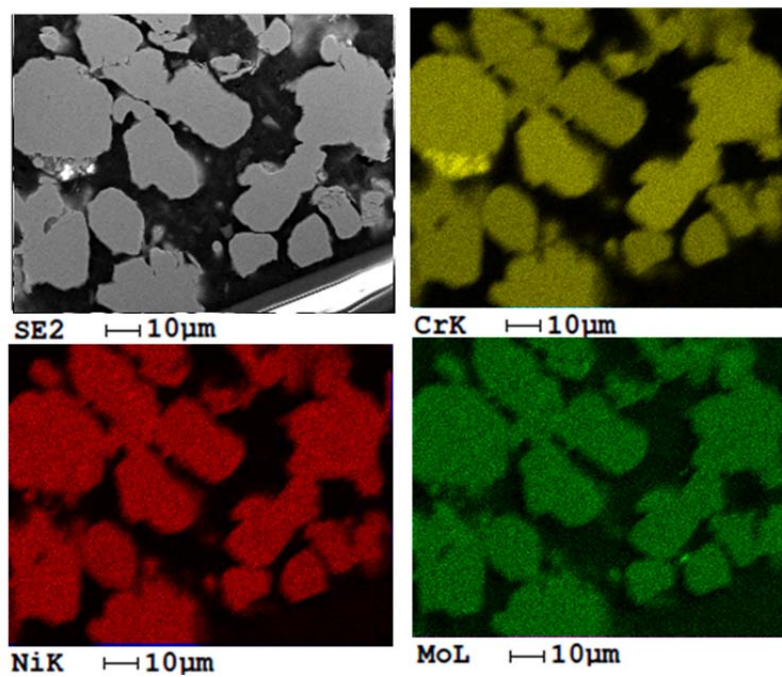


Figure 11. EDX map for the PG-AMP-10 powder showing the primary austenite and ferrite stabilizers (Cr, Ni, and Mo) for austenitic stainless steel.

Powder X-ray diffraction indicated that three of the four commercial powders had both austenite (FCC) and ferrite (BCC) phases present before spraying (Figure 12), with the SS304L, S5001 powder being the only as-received that powder that showed no presence of a ferrite peak. For the PG-AMP-10 and S5002 powders the $\{110\}$, $\{200\}$, and $\{211\}$ reflections for the ferrite phase were easily observable above the background. The KM316 powder had an easily observable $\{110\}$ reflection while the other two reflections were not clearly visible. The calculated percent ferrite volume fractions for the three powders containing ferrite ranged from 20–50 volume percent (Table 4). No diffraction peaks from any other phases were observed in this X-ray diffraction data.

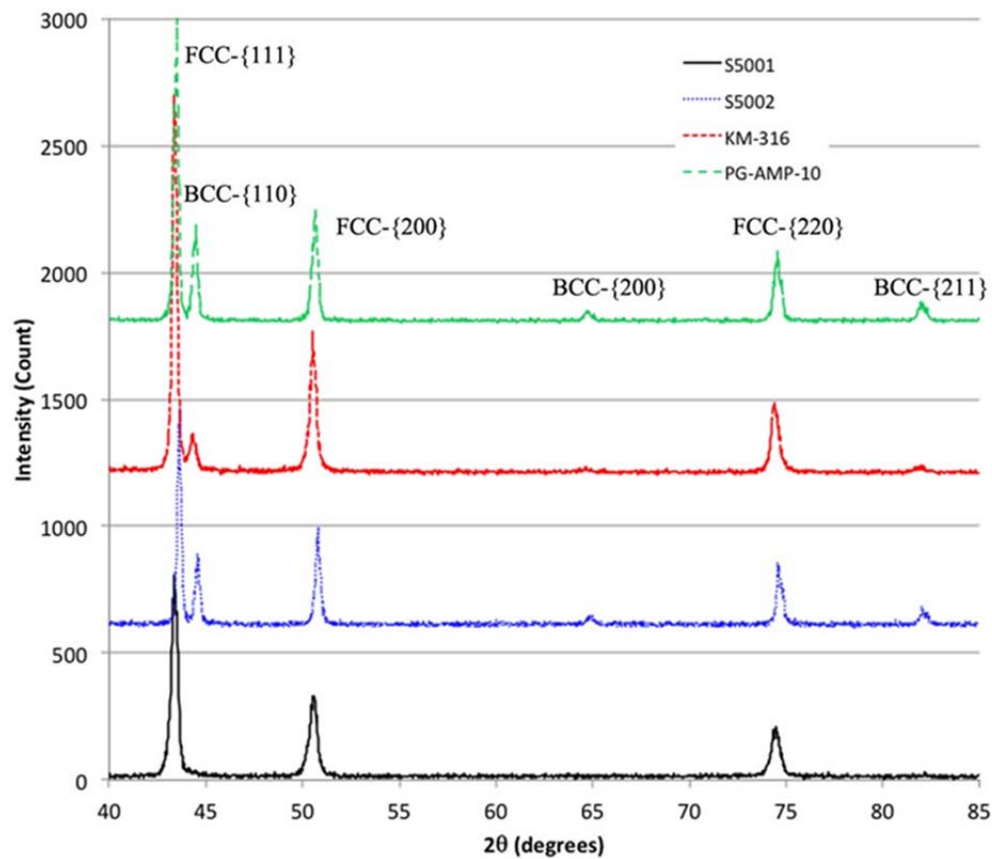


Figure 12. Powder X-ray diffraction patterns from the four commercial stainless steel powders taken prior to cold spraying.

Electron backscatter diffraction (EBSD) data showed important differences between the powders as well. The relative fractions of the austenite (FCC) and ferrite (BCC) phases varied depending upon the powder. For the S5001 (304L) and KM316 (316L) powders, the ferrite content was less than five percent of the total area examined and was observed primarily on the exterior of the particles (green phase in Figure 13 and Figure 14). In the PG-AMP-10 (316L); however, the ferrite content ranged from 50-75 percent of the cross-sectional area examined (Figure 14). The crystallite sizes, of the austenite phase, were also determined from EBSD orientation mapping, and they varied from 2-6 μm for the four powders. It should be noted that the ferrite phase of the PG-AMP-10 particles showed a much finer crystallite size with a mean size of less than one micron.

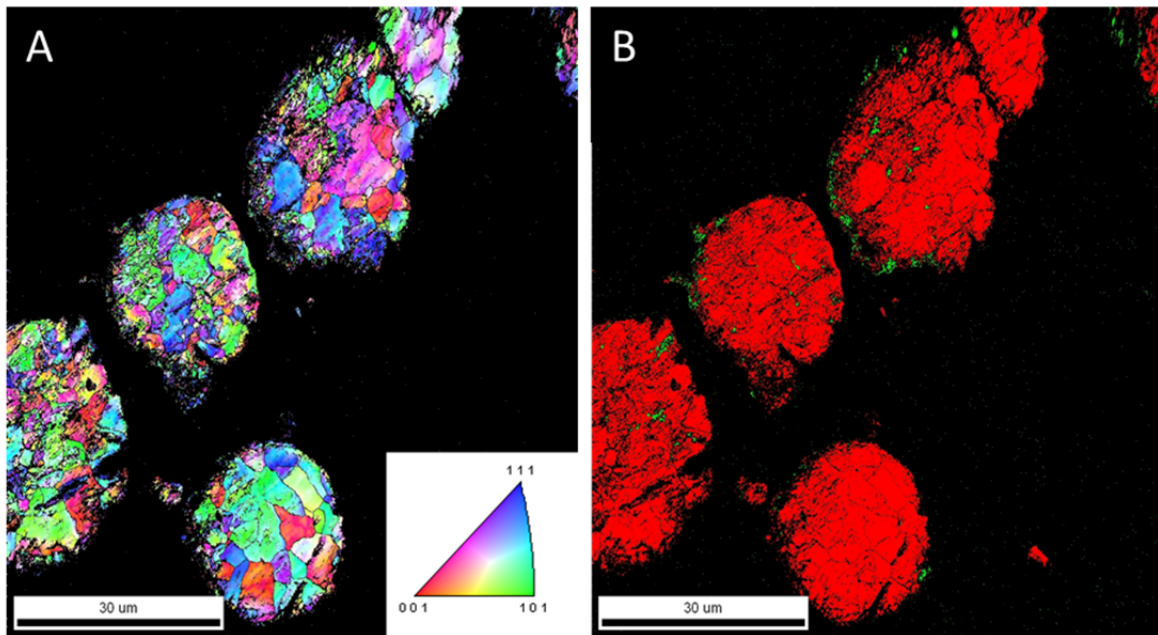


Figure 13. EBSD maps for S5001 (304L) stainless steel powder. A.) Inverse pole figure map (with respect to the sample normal) for the austenite phase, B.) Phase map (green-ferrite, red-austenite)

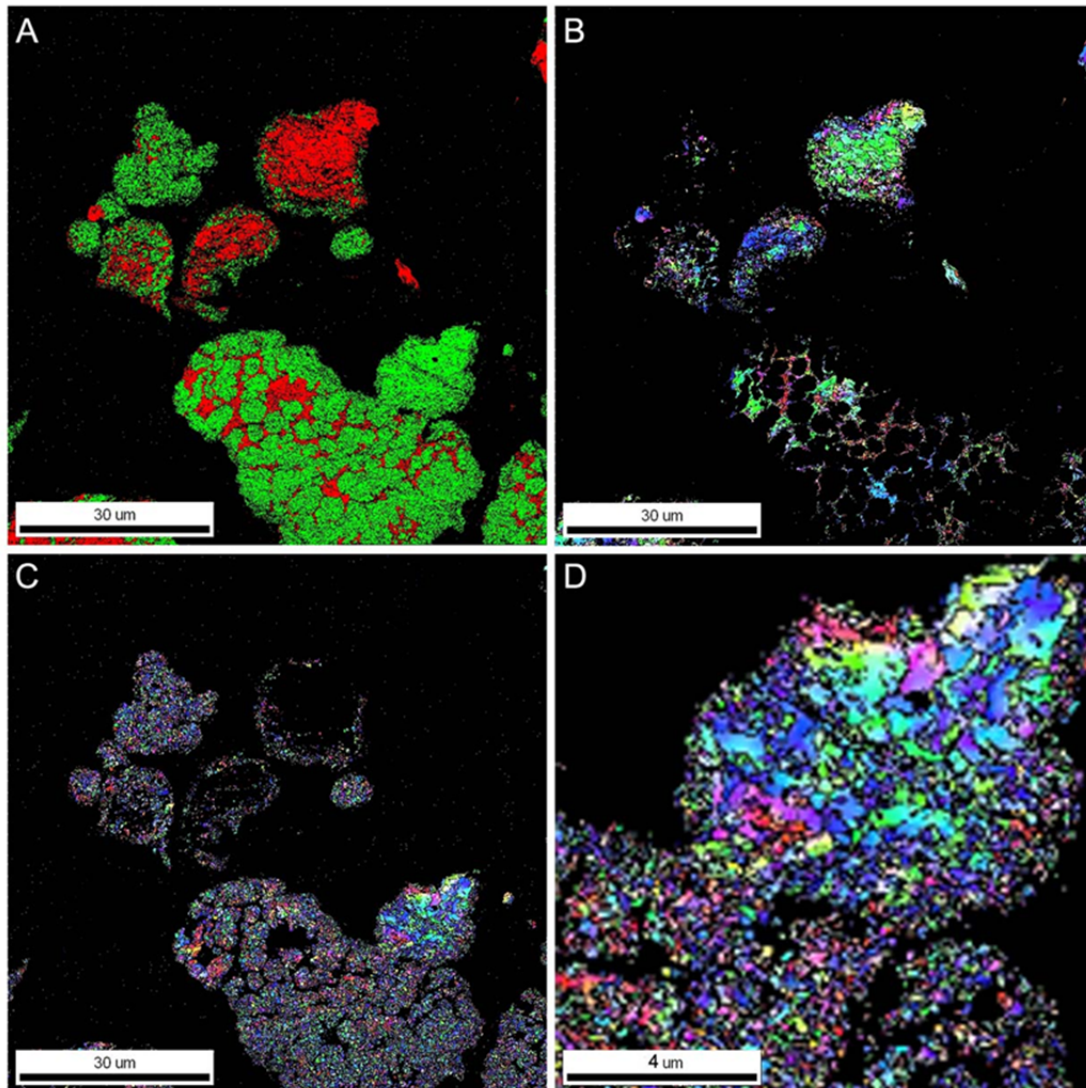


Figure 14. EBSD map for pg-amp-10 stainless steel powder. A.) Phase map (green-ferrite, red-austenite), b.) Inverse pole figure map (with respect to the sample normal) for the austenite phase, c.) Inverse pole figure map (with respect to the sample normal) for the ferrite phase, and d.) Higher magnification view of Figure 14-C.

The relative amount of plastic deformation was quantified by examining the intragranular orientation spread. In Figure 15, the grain orientation spread (GOS) maps show the relative amount of plastic deformation for the powder particles. For an annealed, deformation-free, crystallite, a GOS value of $0.1\text{-}0.3^\circ$ would be expected [32]. All of the powders show GOS values ranging from $1.6\text{-}2.4^\circ$ which is indicative of substantial plastic deformation in the particles. Both the S5001 (Figure 15-A) and

KM316 (Figure 15-B) show substantial amounts of intragranular misorientation in the austenite phase as would be expected of powders that were mechanically milled. The GOS values for the ferrite phase in the PG-AMP-10 powder (Figure 15-C) are much lower and suggest that this material may be recrystallized. In contrast, the GOS values for the austenite phase (Figure 15-D) for this same powder are similar to those of the other two powders.

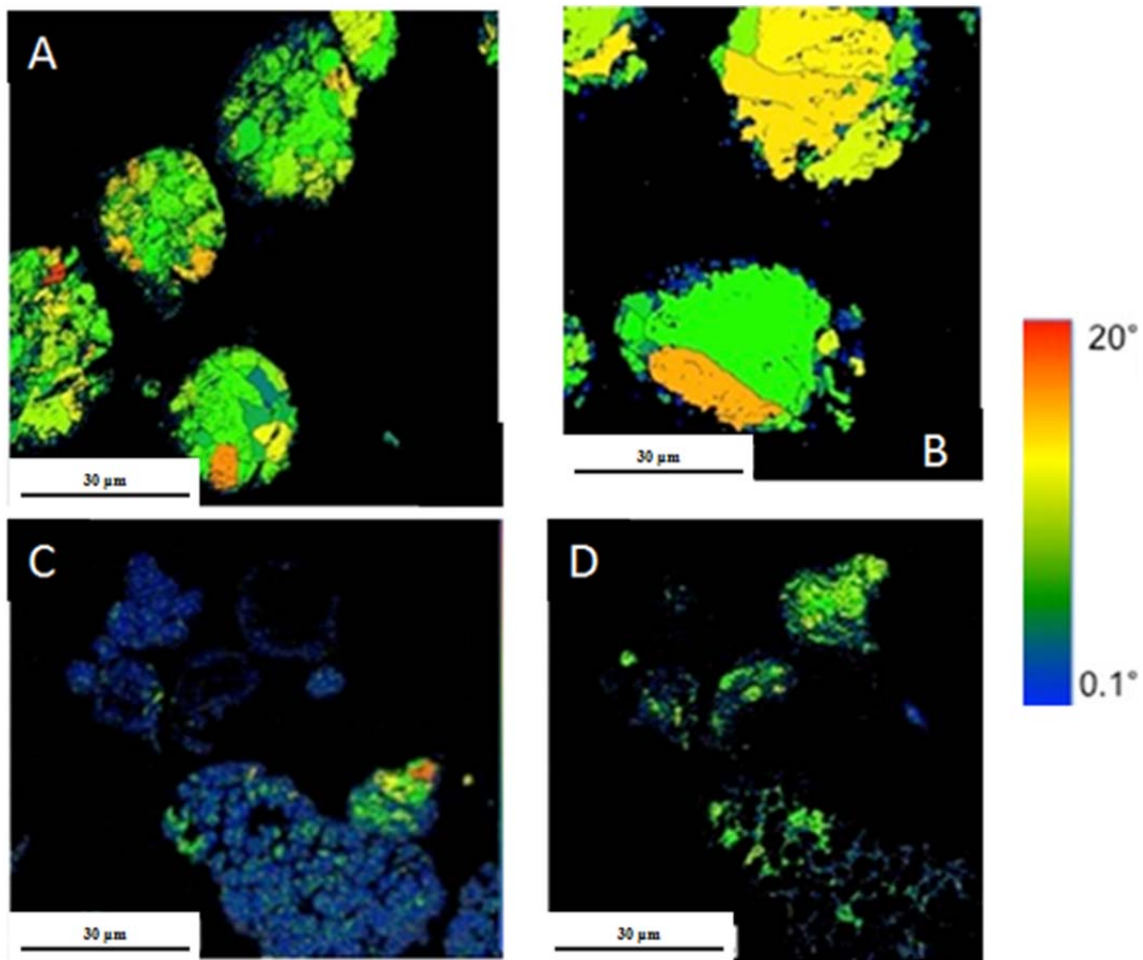


Figure 15. Grain orientation spread for three stainless steel powders. Red pixels indicate a 20° scalar misorientation from the average crystallite orientation, while blue indicates a 0.1° misorientation. A.) S5001 (austenite phase), B.) KM316 (austenite phase), c.) PG-AMP-10 (ferrite phase), and D.) PG-AMP-10 (austenite phase).

A summary of the characteristics for the as-received four commercial stainless steel powders including: mean particle size (obtained from the laser scattering data), the volume percent ferrite (obtained from the X-ray diffraction data), the crystallite size, and average GOS (obtained from the austenite phase of the EBSD orientation maps) is shown in Table 4.

Powder	Mean Size (μm)	% Ferrite (XRD)	Crystallite Size (μm)	Average GOS ($^\circ$)
S5001 (304L)	19.9	~0	2.7	1.8
S5002 (316L)	45.6	50	6.4	2.4
KM 316 (316)	17.2	23	4.1	2.4
PG-AMP-10 (316L)	61.3	46	6	1.6

Table 4. Summary of commercial stainless steel powder characteristics.

2. Cold Spray Coating Characteristics

The deposition performances for the four powders were distinctly different from each other for the single cold spray condition analyzed in this chapter (helium entrainment gas, $T_i = 230^\circ\text{C}$, $P_i = 1.7 \text{ MPa}$). All four powders exhibited reasonably high (>10%) deposition efficiency using low-pressure cold spray deposition with helium as the working gas. The actual DE values for each powder are summarized in Table 5. The KM316 and PG-AMP-10 powders demonstrated particularly high deposition efficiencies for these spray conditions. It should be noted however that the thickness per pass was significantly different. The thickness per pass is an absolute measurement of how much material (by volume or thickness) was actually deposited for a given pass of the nozzle. It is both a product of the mass deposition efficiency (the fraction of powder that “sticks” to the substrate) and the actual mass flow rate of the powder through the nozzle. All four powders were sprayed with the same *nominal* feed rate, while the thickness per pass is more sensitive to the *actual* feed rate through the system, which is highly deposition system dependent. The thickness per pass for a given powder would likely be different on different cold spray deposition systems. Only the S5001 and S5002 powders were actually designed to be used on the Centerline cold spray deposition system.

Most of the coatings were dense with some limited porosity located primarily at the prior particle boundaries as shown in Figure 16. The KM316 coating had fairly uniform porosity, or lack of bonding, between powder particles. The S5001 coating was qualitatively the densest of the coatings.

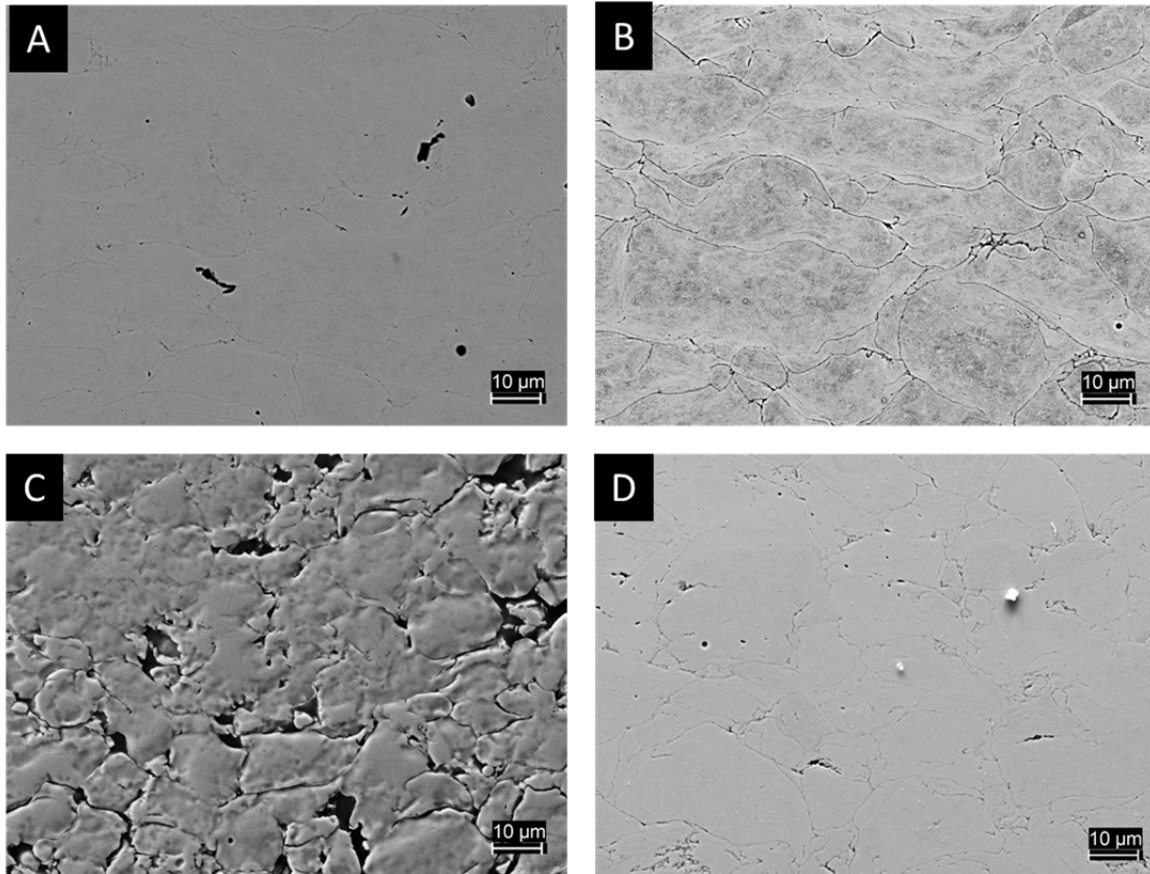


Figure 16. Backscatter electron micrographs of cold sprayed deposited coatings for each of the four commercial stainless steel powders sprayed with helium gas at $T_i = 230\text{ }^{\circ}\text{C}$, $P_i = 1.7\text{ MPa}$ (250 psi). Each shows porosity at the particle to particle boundary with KM316 having significant porosity. A.) S5001, B.) S5002, C.) KM316, D.) PG-AMP-10.

The crystallite size of all of the four stainless steel powders was greatly reduced after cold spray deposition (S5001 and PG-AMP-10 are depicted in Figure 17). All four powders created coatings with ultra-fine grain/crystallite sizes throughout the coating. The crystallite size reduction was particularly notable near the prior particle boundaries. The crystallite size was quantified through the use of EBSD orientation mapping. The

average austenite crystallite size was between 250-400 nm for all four powder deposits. The ferrite crystallite size observed in the coatings was also sub-micron. The austenite crystallite size was not uniform as can be seen in Figure 18. The centers of the prior particles had a notably larger crystallite size (multiple microns) than the regions in between deposited particles. In fact, the crystallite size was so small and the level of plastic deformation was so high in some inter-particle regions that high quality EBSD data could not be collected. These regions correspond to much of the black colored area in Figure 18, particularly for the KM316 coating.

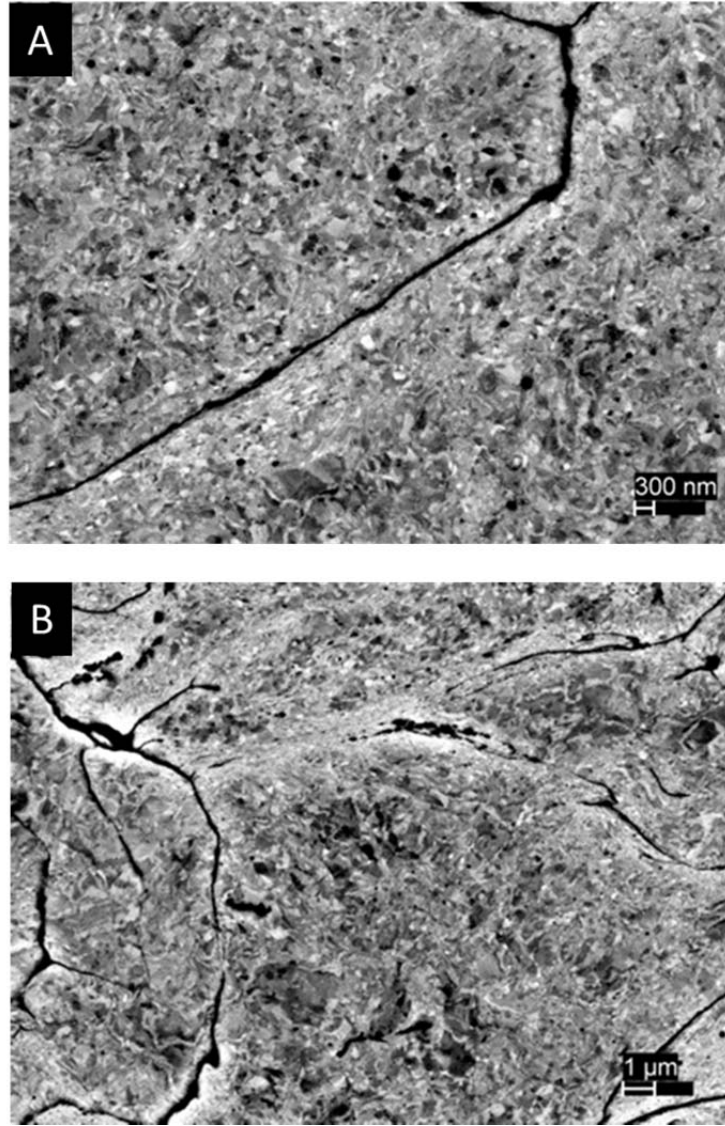


Figure 17. Backscatter electron micrographs of cold sprayed deposited coatings showing ultra-fine grain crystallites within the deformed particles. The dark lines represent the prior particle boundaries where finer grains are observed. A.) S5001, B.) PG-AMP-10.

The evolution of intragranular misorientation after cold spray deposition was highly powder dependent and is summarized in Table 5. Due to the extensive plastic deformation that occurs during the cold spray deposition process, the average GOS values for the austenite phase in the S5001 and PG-AMP-10 coatings both increased, as expected. This relationship did not however hold true for the S5002 and KM316 powders. The average GOS value for the KM316 coating did not measurably change

from the powder to the coating, but there were regions with grains possessing a lower GOS (blue) that can be seen in the interparticle regions (Figure 18-D). For the S5002 coating, the average GOS value actually decreased from 2.4° to 1.7° after cold spray deposition. This reduction was actually a redistribution of the plastic deformation in the microstructure. As seen in Figure 18-B, the GOS values in the austenite crystallites at the centers of the prior particles are quite large (yellow-red), while the interparticle regions have much finer crystallites with low values of GOS (blue). This data suggests that the interparticle regions recrystallize during the cold spray deposition process.

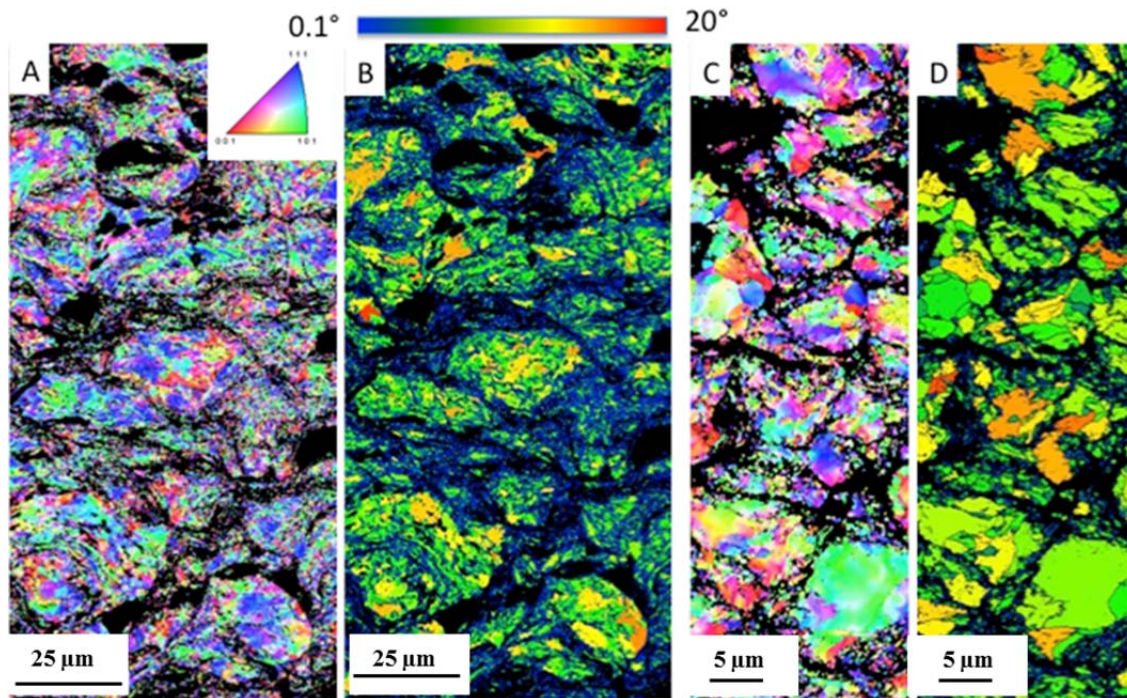


Figure 18. EBSD orientation maps of S5002 (A and B) and KM316 (C and D) coatings. Figures A and C show inverse pole figure maps for the austenite phase with respect to the spray direction (vertical in the image). Dark regions are either from the ferrite phase or from material that could not be indexed. Figures B and D show grain orientation spread (GOS) for the austenite phase.

Powder	DE (%)	Thickness per Pass (mm)	% Ferrite (EBSD/XRD)	Crystallite Size (μm)	Average GOS ($^{\circ}$)
S5001 (304L)	11.8	0.67	1	0.22	2.3
S5002 (316L)	12.3	0.71	19/48 [†]	0.38	1.7
KM 316 (316)	41.8	0.15	1	0.33	2.4
PG-AMP-10 (316L)	29.4	0.93	27/58 [†]	0.33	2.2/1.3 [*]

Table 5. Summary of cold spray coating characteristics for four commercial powders sprayed with helium gas at $T_i = 230\text{ }^{\circ}\text{C}$, $P_i = 1.7\text{ MPa}$ (250 psi). [†] denotes collection via X-ray diffraction. ^{*} denotes the ferrite crystallite size.

The phase distributions in the deposited coating were largely consistent with that observed in the starting powders. X-ray diffraction from the S5002 and PG-AMP-10 coatings showed both the austenite and ferrite phases after cold spray deposition (Figure 15). The peaks were broader than in the powders due to the plastic deformation induced during cold spray deposition. The signal to noise ratio was lower for these diffraction measurements as there was no monochromator present on the 4-circle goniometer used for diffraction measurement of the coatings. A rough quantification of the ferrite content in these coatings estimated a 48 % ferrite content for the S5002 coating and a 58 % ferrite content for PG-AMP-10 coating (Table 5). The ferrite content for the S5002 was almost identical to that measured in the starting powder. The ferrite content of the PG-AMP-10 powder was higher than the powder, but the difference was due to the quality of the diffraction data. On the microstructural scale, EBSD data for both the S5001 and KM316 coatings exhibited small but measurable amounts of ferrite, about one percent by area (Figure 20). The amount of ferrite was not qualitatively different from the starting powder for S5001. It should also be noted that for the S5002 powder, the particles are either primarily austenite or primarily ferrite, while the PG-AMP-10 exhibits particles that are a mixture of austenite and ferrite. It was also observed that the smaller particles tend to be primarily ferrite, which is consistent with the formation of primary ferrite during the powder formation process due to a higher cooling rate in the smaller particles.

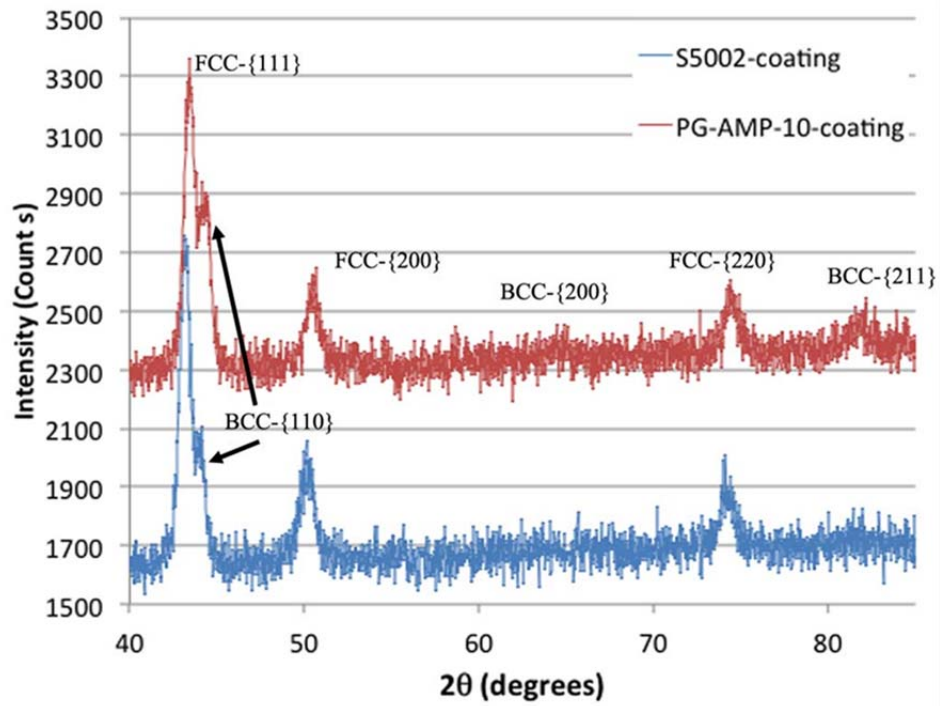


Figure 19. X-ray diffraction patterns for the S5002 (blue) and PG-AMP-10 (red) coatings after cold spray deposition of the powders with helium gas at $T_i = 230^\circ\text{C}$, $P_i = 1.7\text{ MPa}$ (250 psi).

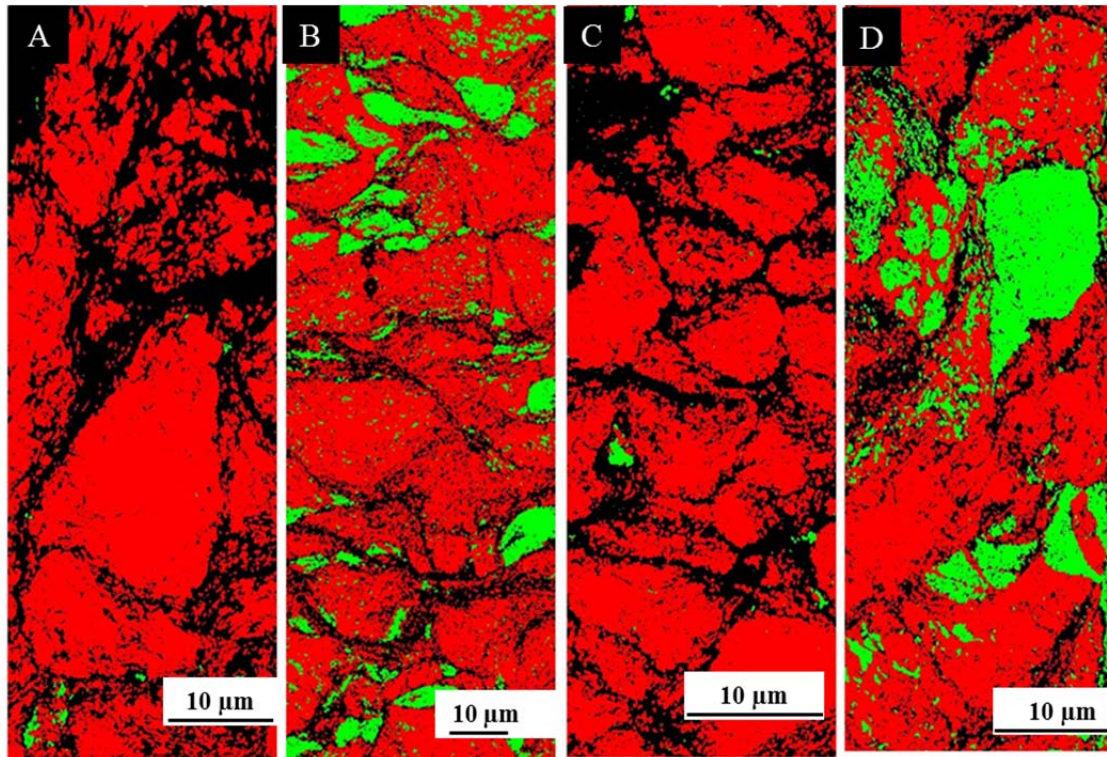


Figure 20. EBSD maps of the austenite (FCC-red) and ferrite (BCC-green) phases in the four deposited coatings. A.) S5001, B.) S5002, C.) KM316, D.) PG-AMP-10. Black regions represent regions with unreliable EBSD indexing patterns.

D. DISCUSSION

1. The Relationship between Low-Pressure and High-Pressure Cold Spray Deposition of Austenitic Stainless Steel

Low-pressure cold spray deposition is able to create austenitic cold spray coatings, albeit at a lower deposition efficiency than higher-pressure cold spray deposition. The definition between low and high pressure systems is somewhat arbitrary, but a pressure of approximately 2 MPa is at the upper end for the low-pressure systems. The deposition efficiencies in this work ranged from 12-40 percent when using helium gas at 230°C and 1.7 MPa (250 psi). Much higher deposition efficiencies (50- > 95%) have been reported by Huang et al. and Villa et al. using nitrogen gas but with temperatures between 600-1000°C and at pressures between 2-4 MPa [26, 28]. The direct comparison can be misleading as pressure, temperature, and gas type all affect the

particle velocity, which is the most important parameter for determining deposition efficiency. Low-pressure cold spray systems can be made more effective by using helium gas instead of nitrogen, although at a greater cost. Spencer and Zhang, reported similar DE values for austenitic stainless steel at even lower pressure, 0.62 MPa, at 320°C using helium as the entrainment gas [2]; however, these deposition experiments were performed using the kinetic metallization technique, which successfully sprays particles at sub-sonic velocities [35].

2. The Effect of the Low-Pressure Cold Spray Deposition Process on the Phase Content and Distribution of the Deposited Coatings

The ferrite content of stainless steel powder for cold spray deposition can vary considerably and is highly process dependent. Several other authors have observed ferrite content in the starting cold spray powders [2, 24, 30]. Borchers et al. noted that the amount of ferrite in the starting powder depended upon the particle size examined, with ferrite present in the smallest particle size (~22 μm) [24]. The presence of ferrite in gas atomized, 304 stainless steel powders has been documented in the work of Wright et al. [34]. These authors demonstrated that the ferrite content is both a function of the type of gas atomization used to produce the powder and the particle size examined. For the particle sizes of the 304 stainless steel examined in this work, 10-15 percent ferrite would be predicted for powders produced by vacuum gas atomization. Centrifugal gas atomization, for the same particle size range, would produce primarily ferrite powder. Interestingly, Villa's recent work on 316L stainless steel powder showed presence of only the austenite phase both before and after cold spray deposition [28]. This powder was produced by Sandvik-Osprey, seemingly by gas atomization given the spherical particle shape.

The microstructural distribution of the austenite and ferrite phases varied considerably with the powder type. In this study, ferrite was observed both as a minority portion of the primarily austenite particles and as the majority phase of other particles. For the S5001 and KM316 powders, the ferrite phase observed was primarily towards the exterior of the austenite powder particles with a smaller amount present between the austenite crystallites in the particle interior. For the S5002 powder, the particles seemed

to be comprised primarily of either austenite or ferrite with the ferrite particles being of smaller diameter, a similar finding to other authors. The major exception was for the PG-AMP-10 powders in which many particles were found that were primarily ferrite with minority austenite regions. The dendritic or cellular structure that might be expected from gas atomized powder was not observed in these commercial powders. For comparison, the powders of Villa [28], Borchers et al. [24], and Wright [34] clearly show a cellular/dendritic solidification structure as produced by gas atomization (Figure 21).

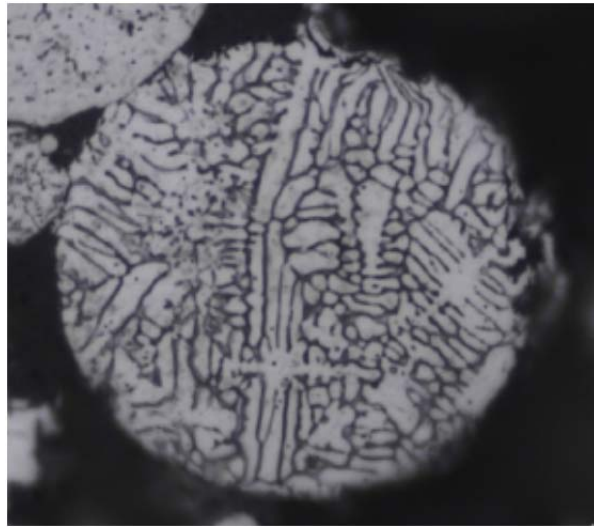


Figure 21. Optical micrograph of etched cross-section of spherical 316L stainless steel powder showing the dendritic structure attained from gas atomization of the particles during manufacturing, from [28].

The results of this study and of other related literature clearly demonstrate that a range of austenite-ferrite microstructures are possible in the feed stock powder for cold spray deposition. It is essential for practitioners of cold spray deposition of austenitic stainless steels to work closely with powder suppliers and to perform careful powder characterization to fully understand the phase content and distribution of the starting powders. The distribution of ferrite in the coatings after cold spray deposition seems closely related to the deformation process involved. The duplex, austenite-ferrite microstructure produced by dendritic solidification is still apparent after cold spray deposition in the microstructures reported by Borchers et al., Villa, and Meng [25, 28,

29]. In this work, small amounts of ferrite were observed in the interparticle regions for the S5001 and KM316 coatings (Figure 20). For the S5002 coating, deformed ferrite particles were deposited in between primarily austenite particles. The ferrite distribution in the PG-AMP-10 coatings is much more complex just as it was in the feedstock powder (Figure 20). Deformed particles that were primarily austenite, primarily ferrite, and even a mixture of the two phases were observed in the coating microstructure. It should be noted that all of these coatings were observed in the as-deposited state without further heat treatment. From this data, it seems that for low-pressure cold spray deposition, the phase composition and distribution of the coatings may simply be determined by the deformation bonding during the spray process. Cold spray experiments at high temperatures (e.g. $> 700^{\circ}\text{C}$) may result in further phase evolution during the deposition process.

3. The Effect of the Low-Pressure Cold Spray Deposition Process on Crystallite Size of Austenitic Stainless Steel

The cold spray deposition process consistently reduced the crystallite size of the deposited material to the sub-micron range for all four commercial austenitic stainless steel powders (Figure 22). The austenite phase crystallite size in the starting powders ranged from 2-6 μm for the starting powders, and all were reduced by $>90\%$. It should be noted that for the primary ferrite particles observed in the PG-AMP-10 powder, the ferrite crystallite size was approximately 500 nm prior to spraying. After cold spray deposition, the crystallites near the prior-particle boundaries were consistently in the range of 100-300 nm for all coatings. This range of crystallite size was observed for both the austenite and ferrite phases. Borchers et al. observed a crystallite of 10-50 nm within 500 nm of the interface of 316L stainless steel prior-particle boundaries [29]. In this work, the crystallite size right at the prior-particle boundaries was too fine for measurement by EBSD, even with a step size of 40 nm. The EBSD orientation maps (Figure 18) did show that the crystallite size was larger in the centers of the prior particles and much finer at the particle to particle boundaries.

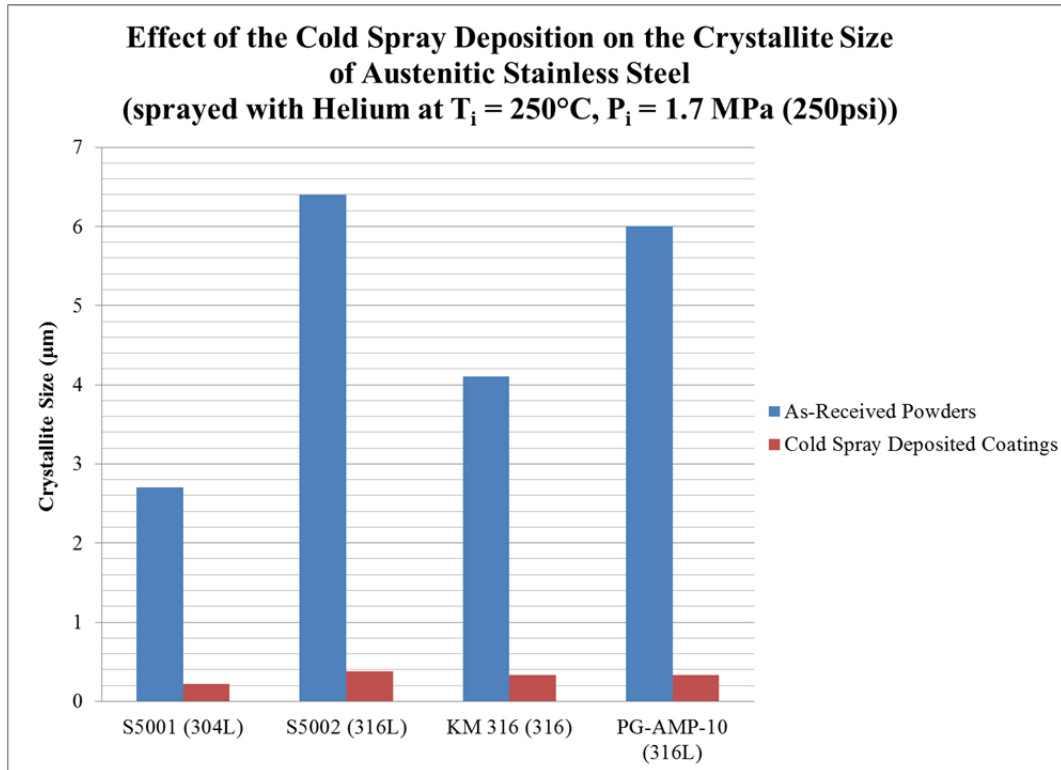


Figure 22. Chart of austenitic stainless steel crystallite size before cold spray deposition (as-received powders) and after cold spray deposition (cold spray deposited coatings).

This reduction in crystallite size after cold spray deposition has previously been observed for aluminum [36-38] and titanium [39, 40], alloys. The change in crystallite size is often attributed to the severe plastic deformation experienced by the particles during impact. In fact, an increase in the grain refinement is observed in initially high dislocation density or highly cold worked materials [37]. In the limit, cryo-milling or ball-milling of cold spray powders has been used to achieve fully nanocrystalline coatings in aluminum [37, 41], nickel [42], and copper [43].

III. PARTICLE VELOCITY OF THE LOW-PRESSURE COLD SPRAY DEPOSITION PROCESS: SIMULATION AND EXPERIMENT

This chapter discusses the in-flight particle velocity of a cold spray plume. This chapter will discuss the fundamentals of laser velocimetry and investigate the basic parameters (both of the laser and the physical experimental set-up). We will also model the Centerline (Windsor) SST Model Series C UltiLife nozzle utilized for experimentation in an attempt to study the fluid dynamics and particle transport properties of the low pressure cold-gas dynamic process. This model will investigate the effects of gas type, pressure, and temperature on the fluid dynamics and resultant particle velocity profiles. This approach predicts the particle velocity at the exit of the nozzle and can be used to validate the laser velocimetry experiments. Section A contains a review of both the relevant literature the fundamentals of the laser velocimetry process. Section B contains the experimental methods, which includes a study of the laser set-points and laser detection calibration process, a study of the physical experimental parameters of feed rate and substrate interaction. It also includes a one-dimensional model of the fluid dynamics and particle transport properties of the nozzle and laser velocimetry experimentation for austenitic stainless steel. In conjunction with the velocity experimentation, deposition experiments were performed in an attempt to determine the critical velocity for austenitic stainless steel. Section C and Section D delineate the results of the experimentation and discussion respectively.

A. INTRODUCTION

Key to the low-pressure cold gas dynamic deposition process is the particle velocity at the time of particle impact with the substrate. Acceleration of the metallic particles to supersonic velocities occurs through the use of an entrainment gas such as nitrogen or helium, and a converging-diverging nozzle such as a de Laval nozzle. It is well studied and documented that particles in this process must attain a critical velocity prior to their deposition onto a substrate surface, [44–46] and if the particles fail to be

accelerated to the critical velocity then they will simply rebound off the surface and not deposit, or have an abrasive effect on the substrate itself.

The fluid dynamics of a gas flowing through a nozzle has been thoroughly studied and numerous simulation, numerical studies, and experiments have been conducted in an attempt to optimize the nozzle design and/or optimize the entrainment gas properties (temperature and pressure) to attain the best deposition efficiency [47–51]. Pattison et al.'s investigated the bow shock phenomenon that occurs as a result of supersonic gas impingement on a surface [47]. The bow shock causes flow irregularities that tend to cause drag and slow down the particles prior to impact on the substrate. Park et al. further this work, by conducting a numerical simulation using computational fluid dynamics to characterize and optimize the performance of supersonic nozzle flows by varying the nozzle design and stand-off distance of the substrate, in an attempt to eliminate shockwave fluctuations and create more uniform coatings [48]. Their findings suggest that designing a nozzle such that the nozzle exit pressure is equal to the ambient pressure is essential to reducing the shock formation and creating a more uniform coating. Huang et al. studied the effect of entrainment gas pressure and temperature on the particle velocity and deposition efficiency of commercially available 316L stainless steel powders and found that utilizing a high-pressure, high-temperature cold spray system with pressures ranging from 2-3 MPa, and temperatures ranging from 600-1000°C, that as temperature and/or pressure of the working gas was increased, so therefore was the particle velocity, reporting velocities over the range of 400 to 1100 m/sec, with the majority of particles between 625 to 800 m/sec [26]. They reported obtaining nearly 100% deposition efficiency with their system at the highest temperature and pressure combinations. It should also be noted that they used laser particle velocimetry, similar to the work in this thesis, to measure the particle velocity rather than numerical simulation or estimation as have most others. Since critical velocity is one of the most important parameters in the cold spray process a number of studies have also been conducted in attempt to experimentally find, or analytically predict the critical velocity for certain materials.

Gilmore et al. found through the use of laser velocimetry that copper's critical velocity is approximately 640 m/sec when using helium at 300°C [20]. Li et al. studied the effect of oxygen content on deposition efficiency, and estimated the critical velocity of stainless steel (with a low oxygen content of 0.086 wt. %) to be approximately 580 m/sec [46]. It should be noted however that this study was not conducted with laser velocimetry, and no in-flight particle velocity measurements were taken. The particle velocity was estimated through numerical relationship of the gas parameters and the particle diameter.

The experiments in this thesis aim to determine if a critical velocity for austenitic stainless steel exists for the low-pressure cold gas deposition process. In particular, it is important to determine if this velocity is the same for different stainless steel powders. It should be noted that the laser particle velocimetry process is new to cold spray deposition research conducted at the Naval Postgraduate School and thus warrants a review of the experimental fundamentals and a study of the limitations of its operation.

1. Fundamentals of the Laser Particle Velocimetry Process

a. Velocity and Diameter Measurement and Calculation

The TECNAR Automation (Saint-Bruno, Quebec) CSM eVOLUTION was utilized throughout the laser particle velocimetry experimentation and thus the details of that system's fundamentals of operation are discussed in this section. The system consists of three main components: an optical sensor head, a detection module, and a control module [52]. The optical sensor head houses the optical fiber (laser) and a two-slit mask utilized in the measurement of particle velocity (Figure 23) [52].

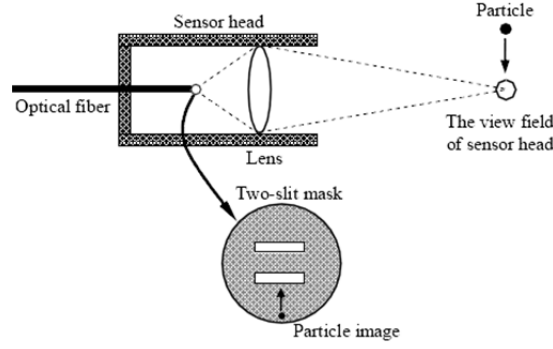


Figure 23. Set-up of the optical sensor head, from [52]

The CSM eVOLUTION utilizes a higher-power diode laser with a power density of 6.57 W/cm^2 and a wavelength of 810 nm laser to measure the particle velocity and particle diameter during the cold spray process. A laser is utilized in the cold spray velocimetry process because the particles, being generally cold, do not emit sufficient black body radiation for thermal imaging. This approach, in turn, means that in order to capture the particle velocity and diameter, laser light must be scattered off the particles and recaptured for measurement. The system measures the particle velocity by taking a ratio of the known distance between the slits in the two-slit mask to the time of flight for a particle to pass through those two slits, multiplied by a magnification factor for the lens (Equation 7) [53].

$$U_p = \frac{s}{TOF} \times OML \quad (7)$$

where U_p is the particle velocity, s is the distance between the slits in the two slit mask (known to a $1 \text{ } \mu\text{m}$ precision), TOF is the time of flight of a particle to pass through the two slits, and OML is the optical magnification of the lens. TECNAR reports the precision on the velocity measurement to be on the order of 0.5%.

The particle diameter (Equation 8) is found through the use of Planck's Law and two hypotheses: (1) the intensity of the reflected signal is proportional to the square of the particle's diameter, and (2) the particle shape is spherical.

$$D_p = \sqrt{\frac{E(\lambda_i)}{DC}} \quad (8)$$

where D_p is the particle diameter, $E(\lambda_i)$ is photon intensity of the signal ($i = 1$ or 2 depending on which slit the measurement is coming from), and DC is a diameter coefficient that is found during calibration of the system. It should be noted that $E(\lambda_i)$ is corrected in the system for different peak heights which may occur due to a particle's trajectory not being completely perpendicular to the slits and some particles may not be completely seen in both slits. A representation of the signal received in this case is shown in Figure 24. If this correction was not made, the particle diameter would systematically always be underestimated. TECNAR reports that once calibration is completed properly, the precision of the measured diameter is between 7-15 %, but this precision is also greatly dependent on the validity of hypothesis of the particles being spherical in shape.

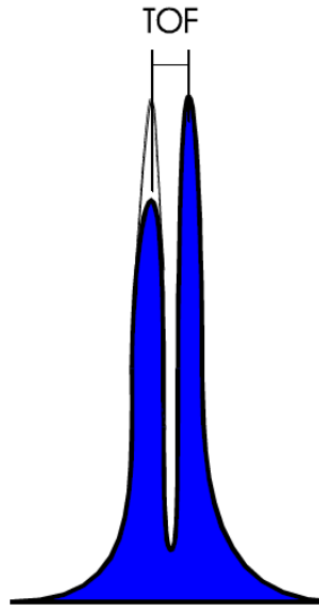


Figure 24. Representation of a two-peak signal with different peak heights where TOF = time of flight, from [53].

b. Signal Processing, Acceptance Criteria, and Parameter Modification

The previous section discusses the mathematical theory of how the laser velocimetry process works to measure particle velocity and diameter when a particle passes through the sensing head's view field and is processed by the control module. It is important to note however that not all of the particles that pass through the sensing field are evaluated. In fact, a majority of particles that pass by the sensing equipment are rejected for a number of different reasons; and therefore, no velocity or diameter data is stored for those particles during the experiment. The particles that do pass all the established criteria are categorized as "good", while the ones that do not pass are categorized into a number of different categories. The number of accepted particles needs to be maximized in order to increase the statistical sampling of the particle velocity distribution and to obtain the most accurate depiction of the spray process particle velocity. Below are some of the major categories of "bad" or rejected particles while the full list can be found in the TECNAR manual [53].

- No first peak
- No valley
- No second peak
- Missing quiet zone

A number of the rejection categories have parameters that can be modified to increase the number of good particles obtained, however Huang et al. discussed the parameters in detail and conducted an experiment adjusting one parameter at a time to determine its effect on the number of good particles accepted per time and measured velocity distributions of those good particles [52]. They found that most of the parameters involved could be set at the manufactures recommended level without any substantial effect on the velocity distribution or decrease in the number of good particles measured. They did, however, find that modifying the trigger level and capture depth parameters had the greatest impact on the number of good particles measured per unit time and the accuracy of the velocity distribution measured, as these two parameters directly relate to the material and the process involved.

Trigger level directly correlates to the intensity of the reflected light that is required for the system to recognize the particle above noise and must be determined for each powder utilized. If the trigger level is set too low, the system will trigger on noise and not count the particles for one of the previous rejection criteria, likely no quiet zone or no first peak. If it is set too high, the system will miss a significant portion of the smaller particles (i.e., the particles that reflect less light). Capture depth is also particle and process dependent. Capture depth is the size of the time window allotted for a particle to pass between the slits of the two-slit mask and be acquired by the system. It is particle and process dependent because if set too low then the velocity distribution will be shifted toward the smaller/faster particles and will eliminate the slower particles that do not make it into the time window allotted. If the acquisition window is set too high, then there lies the possibility of more than one particle being in the acquisition window at once; and because of the software limitations, only the first particle is counted and therefore lowering the number of good particles per unit time that are measured and reducing the statistical accuracy of the results. These two parameters were calibrated for each of the powders used in this study.

c. Powder Feed Rate and Substrate Interaction Analysis

In order to fully understand and ensure that the velocimetry experiments were being conducted with all the proper parameters (electronically and physically), there was also a need to conduct some physical parameter testing, such as the effect of powder feed rate and the effect of introducing a substrate into the gas-particle flow on the consistency and accuracy of the measurements.

Nominal powder feed rates utilized in velocimetry and deposition experiments can range anywhere from 2–100 %. Due to this wide range of usable feed rates, an experiment was conducted to investigate the impact that powder feed rate may have on the measured velocity distribution. This impact could be on the statistical significance (how many good particles per second are we measuring?) or the consistency of the results (do the average velocities or velocity distributions significantly change?).

Second, the research and industry standard is to measure the particle velocity without the presence of a substrate. It is known however that having a substrate (or flow interrupter) in the path of the gas-particle flow can affect that flow, causing shock waves and flow fluctuations, thus slowing down the particles due to air friction [47]. It would therefore be ideal to measure the particle velocity at the substrate interface so that any shock wave effects could be measured and a representation of the actual particle velocity upon impact could be measured. An experiment was designed in order to identify if the possibility exists of placing a substrate into the flow, measuring the particle velocity at that flow-substrate interface, and attain statistically significant and consistent results for the particle velocity.

B. EXPERIMENTAL METHODS

Two stainless steel powders, S5001 and PG-AMP-10 were used throughout the velocimetry experiments described in this section. The characteristics of these powders were described in detail in section II of this thesis. Due to its spherical shape, S5001 was utilized for the powder feed rate and substrate interaction experiments, as well as the nozzle exit velocimetry measurements to be compared with the simulation. A one-dimensional MATLAB simulation was created in an attempt to model the existing nozzle to compare against the measured results. For all the velocimetry experiments the velocimeter was calibrated to the mean particle size of the powder being used. The sensing head was positioned 60 mm from the nozzle centerline and perpendicular to the spray plume (Figure 25).

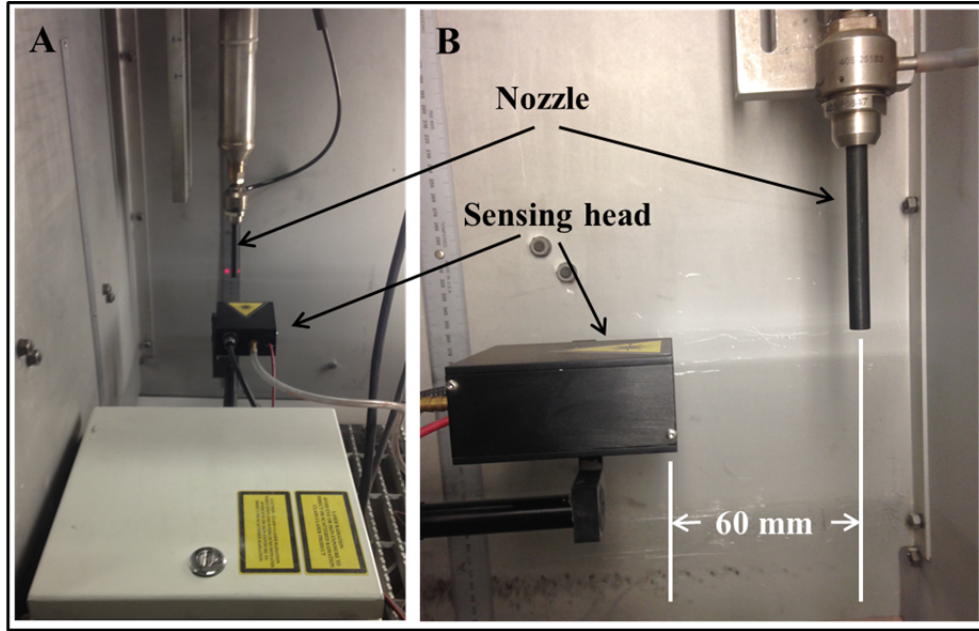


Figure 25. Experimental set-up for velocimetry experiments. Sensing head is positioned 60 mm from the nozzle centerline. The red dots are the alignment lights that show the width of the measurement zone. A.) Rear view, B.) Side view.

1. Calibration of the Laser Particle Velocimeter for Austenitic Stainless Steel Powders

In order to ensure that the results of the laser particle velocimetry experiments for the stainless steel powders were statistically accurate, the velocimeter detector had to be calibrated in much the same way as the process that Huang et al. followed [52] in their analysis of the effect of the laser parameters on the statistical accuracy and consistency in the velocity distribution obtained. Their findings reported that the two major parameters affecting the results obtained were the capture depth and trigger level, and thus those two parameters were systematically modified in this experiment to find the optimal parameter values for future experiments with the austenitic stainless steel powders. These experiments were accomplished for both the S5001 and PG-AMP-10 powders because as previously shown in Section II, the powders exhibited significantly different morphologies and thus would have different in-flight and laser intensity reflection characteristics, and those two powders were chosen for the particle velocimetry process to determine the critical velocity of austenitic stainless steels.

The trigger level and capture depth calibration experiments were conducted with helium gas at 250 °C and 1.03 MPa (150 psi), with a nominal feed rate of 40%. The laser stand-off distance for all the experiments was held constant at 20 mm. During these experiments the trigger level was held constant at 200 mV and the capture depth was adjusted from 10 – 500 μ sec for a total of five experiments (each with a higher capture depth than the previous). The trigger level experiment was accomplished in much the same fashion. During the trigger level experiment, the capture depth was held constant at 20 μ sec and the trigger level was adjusted from 50 – 2000 mV for a total of eight experiments (each with a higher trigger level than the previous). Table 6 summarizes the laser set-points of trigger level and capture depth utilized in the calibration experiments.

Capture Depth Calibration	
Trigger Level (mV)	Capture Depth (μsec)
200	5
	10
	20
	50
	250
	500
Trigger Level Calibration	
Trigger Level (mV)	Capture Depth (μsec)
50	20
100	
150	
200	
250	
500	
1000	
2000	

Table 6. Summary of the capture depth and trigger level set-points utilized in the powder calibration experimentation for S5001 and PG-AMP-10

The particle velocimetry data extracted consisted of the particle velocity, diameter, and time acquired. This data was analyzed to determine the number of “good” (acceptable) particles per second, and the velocity and diameter distributions, where the velocity and diameter distributions were binned into 100 m/sec and 10 μm sized bins, respectively. It should be noted that the CSM pre-bins the velocity and diameter into its own histogram values. The choice of 100 m/sec and 10 μm sized bins was done in an attempt to normalize the bins (as the CSM bins were different for each experiment) and provide the best fit to the data without reducing the precision of the results. Smaller bins fluctuated the data erratically indicating that it was not correlating well to the original CSM bins.

2. Powder Feed Rate and Substrate Interaction Analysis

These experiments were designed to study the effects of powder feed rate and the introduction of a substrate into the gas-particle flow on the statistical significance and consistency of the measured velocity. The feed rate experiment was conducted and analyzed first in order to use those results in the substrate interaction experiment because if the feed rate could be minimized then there would be less particle reflection and coating deposit interference in the substrate interaction experiment. For both experiments the S5001 austenitic stainless steel powder was sprayed with nitrogen gas at 450°C and 1.7 MPa (250 psi). The laser unit was calibrated to the mean particle size of the powder, 20 μm , and the capture depth and trigger level were set at 10 μsec and 100 mV, respectively. These values were determined based upon the results of the calibration experiments.

a. Powder Feed Rate Experiment

During the powder feed rate experiment the nominal powder feed rate was set on the portable Centerline spray unit and ranged from 2-80 %. The laser stand-off distance was held constant at 20 mm from the nozzle exit. Table 7 summarizes the conditions used for the experiment.

Test No.	1	2	3	4	5	6
Powder Material	S5001	S5001	S5001	S5001	S5001	S5001
Gas (N2 or He)	N2	N2	N2	N2	N2	N2
Gas Temperature (°C)	450	450	450	450	450	450
Gas Pressure (Mpa)	1.7	1.7	1.7	1.7	1.7	1.7
Powder Nominal Feed Rate (%)	2	5	10	20	40	80
Laser Stand-Off Distance (mm)	20	20	20	20	20	20

Table 7. Summary of experimental conditions for the powder feed rate limitation experiment. (highlight indicates the powder nominal feed rate % modification)

The data extracted from the CSM eVOLUTION control module consisted of a measure of the particle velocity and diameter along with its respective time of capture during the experiment. From this data the number of good particles per unit time, a measure of the statistical significance of the measurement, an average of the particle velocities for each condition, and a particle velocity distribution for each condition was found by binning the number of particles measured into 100 m/sec velocity bins.

b. Substrate Interaction Experiment

During the substrate interaction experiment the nominal feed rate was held constant at 40% for all spray conditions. For this experiment, the laser stand-off distance was held constant at 20 mm from the nozzle exit while the substrate, made of 316 stainless steel, was raised starting from a stand-off distance of 40 mm to ~21 mm just below the laser stand-off distance (Figure 26). Table 8 summarizes the conditions utilized in this experimental set-up. Similar data to the previous experiment was extracted to analyze each condition.

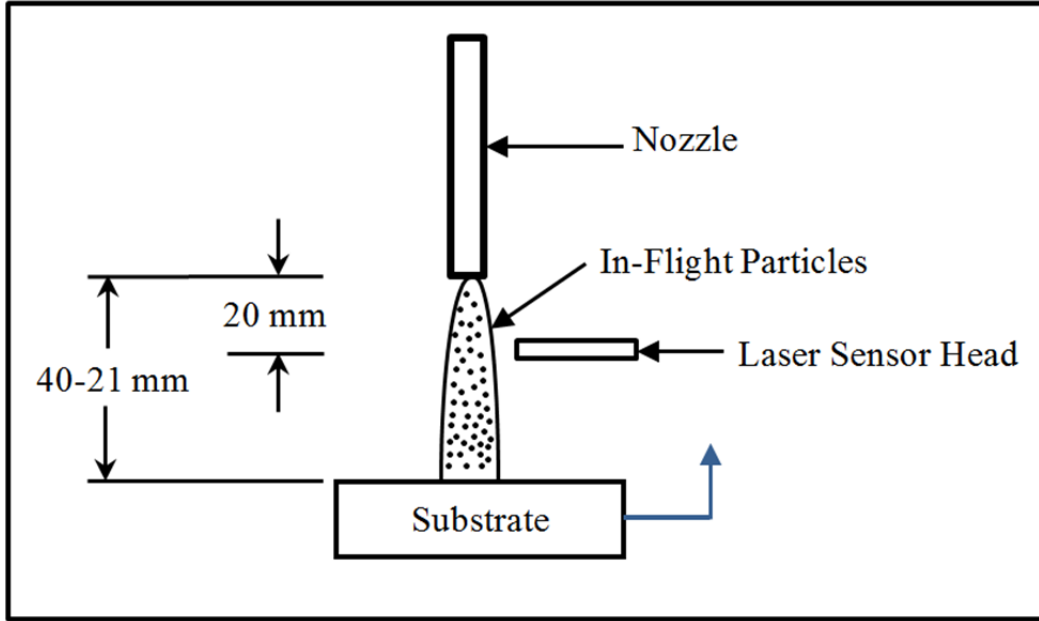


Figure 26. Schematic of the substrate interaction experiment indicating the laser stand-off distance held constant at 20 mm and the substrate stand-off distance starting at 40 mm and reducing to ~21 mm in the direction of motion indicated by the blue arrow.

Test No.	1	2	3	4	5
Powder Material	S5001	S5001	S5001	S5001	S5002
Gas (N2 or He)	N2	N2	N2	N2	N3
Substrate Material	316SS	316SS	316SS	316SS	316SS
Gas Temperature (°C)	450	450	450	450	450
Gas Pressure (MPa)	1.7	1.7	1.7	1.7	1.7
Powder Nominal Feed Rate (%)	40	40	40	40	40
Substrate Stand-Off Distance (mm)	40	30	25	22.5	~21
Laser Stand-Off Distance (mm)	20	20	20	20	20

Table 8. Summary of the experimental conditions for the substrate-laser stand-off distance interaction experiment. (highlight indicates the stand-off distance modification accomplished).

3. One-Dimensional MATLAB Simulation of the Centerline (Windsor) SST Model Series C UltiLife Nozzle and Comparison with Laser Velocimetry Nozzle Exit Results

A one-dimensional MATLAB simulation model (code in Appendix A) of the UltiLife nozzle utilized during all experiments was created in an attempt to study the

fluid dynamics and particle transport properties of the cold gas-dynamic process. It was also utilized to validate the laser velocimetry measured particle velocities.

The nozzle was a converging-diverging, de Laval type, nozzle with a 2 mm throat diameter, 5 mm convergent section, 120 mm divergent section length, and 6.3 mm exit diameter. The powder particles were injected into the flow 1 mm after the throat. A schematic of the nozzle is represented in Figure 27.

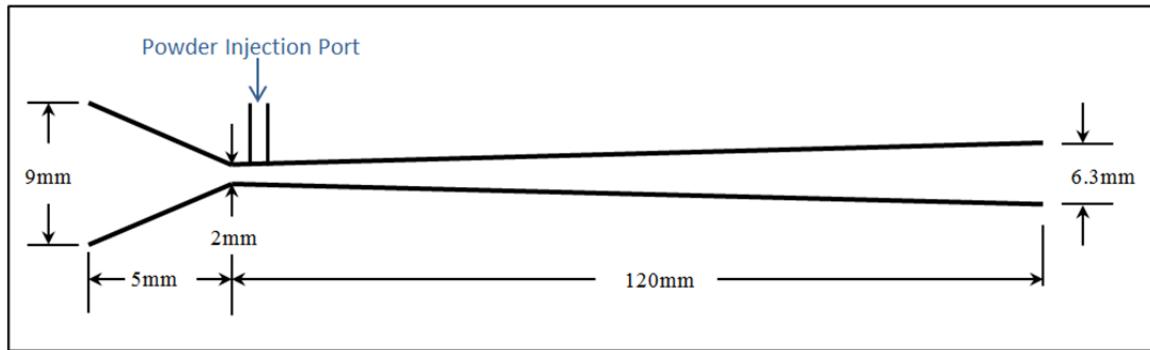


Figure 27. Schematic of the 120 mm nozzle utilized in the Centerline (Windsor) SST Model Series C cold spray deposition unit. (drawing not to scale)

The numerical simulation of the model was created utilizing the same assumptions and equations as in Sakaki's previous research [19]. The assumptions utilized to determine the fluid dynamics of the gas flow through the nozzle were:

- Flow through the nozzle is a quasi-one-dimensional isentropic flow of a semi-perfect gas with zero friction and boundary layer development on the walls of the nozzle.
- Parameters of the intake of the nozzle: initial gas velocity, $U_{gi} = 0$ m/sec, the inlet temperature, T_{gi} , and the inlet pressure, P_i of the gas flow were assumed to be the nominal values set on the Centerline unit.

Utilizing these assumptions, the following equation of compressible one-dimensional fluid flow can be utilized to calculate the pressure at any point along the nozzle (Equation 9).

$$\frac{A_x}{A_t} = \sqrt{\left(\frac{\gamma-1}{2}\right)\left(\frac{2}{\gamma+1}\right)^{\frac{(\gamma+1)}{(\gamma-1)}} \left[\left(\frac{P_x}{P_i}\right)^{\frac{2}{\gamma}} - \left(\frac{P_x}{P_i}\right)^{\frac{(\gamma+1)}{\gamma}} \right]} \quad (9)$$

where A_x is the area at any point x along the nozzle, A_t is the area of the nozzle at the throat, P_x is the gas pressure at any point x along the nozzle, P_i is the inlet gas pressure, and γ is the specific heat ratio of the working gas.

Once P_x is known at all points along the nozzle, and P_i is known, the following two equations can be utilized to find the temperature (Equation 10) and velocity (Equation 11) of the working gas.

$$T_{g_x} = T_{g_i} \left(\frac{P_x}{P_i} \right)^{\frac{(\gamma-1)}{\gamma}} \quad (10)$$

where T_{gx} is the temperature of the working gas at any point x along the nozzle, T_{gi} is the inlet temperature of the working gas.

$$U_{g_x} = \sqrt{2 \left(\frac{\gamma}{\gamma-1} \right) R T_{g_i} \left[1 - \left(\frac{P_x}{P_i} \right)^{\frac{(\gamma-1)}{\gamma}} \right] + U_{g_i}^2} \quad (11)$$

where U_{gx} is the gas velocity at any point, x , along the nozzle, R is the gas specific constant, and U_{gi} is the inlet gas velocity.

The particle flow behavior within the nozzle was also modeled utilizing the assumptions and equation as outlined by Sakaki [19]. The assumptions utilized in modeling the particle behavior are as follows:

- The particle is spherical and the particle temperature is constant throughout its volume.
- The particle specific heat is constant and independent of temperature. (i.e. is a property of the material only)

- Interaction between particles is ignored and no gravitational effect is used as the acceleration of the particle due to working gas has significantly higher impact.
- Acceleration and heating of the particle is assumed to have negligible effect on the gas energy.

Utilizing the above assumptions, the velocity of the particle can be found by numerically integrating the acceleration. The acceleration of the particle can be described at any point along the nozzle, x , with the following equation:

$$\frac{dU_{p_x}}{dt} = \frac{3}{4} \frac{C_d}{D_p} \frac{\rho_{g_x}}{\rho_p} (U_{g_x} - U_{p_x}) |U_{g_x} - U_{p_x}| \quad (12)$$

where U_{p_x} is the particle velocity at any point, x , along the axis of the nozzle, C_d (Equation 13) is the drag coefficient for a sphere [54] and is a function of Reynolds number (Equation 14), D_p is the particle diameter, ρ_{g_x} and ρ_p are the gas and particle densities, respectively, where the gas density varies along the nozzle with the temperature and pressure of the gas.

$$C_d = \left[2.25 \text{Re}_x^{-0.31} + 0.36 \text{Re}_x^{0.06} \right]^{3.45} \quad (13)$$

$$\text{Re}_x = \frac{\rho_{g_x} D_p}{\mu_x} (U_{g_x} - U_{p_x}) \quad (14)$$

where Re_x is the Reynolds number at any point, x , along the nozzle, and μ_x is the gas viscosity at any point, x , along the nozzle. The drag coefficient is assumed accurate to 5% in the range of $10^{-2} < \text{Re} < 3 \times 10^5$ [54].

The temperature of the particle (Equation 15) in the gas flow was found utilizing the same equation as Champagne [19].

$$\frac{dT_{p_x}}{dt} = (T_{g_x} - T_{p_x}) \frac{6h}{c_p \rho_p D_p} \quad (15)$$

where T_{p_x} is the temperature of the particle at any point, x , along the nozzle, h is the heat transfer coefficient (Equation 17) is a function of the Nusselt number, given by the Ranz-Marshall correlation [55] (Equation 16) and c_p is the specific heat of the particle.

$$\overline{Nu}_x = 2 + 0.6 Re_x^{0.5} Pr_x^{1/3} \quad (16)$$

where Nu_x is the Nusselt number at any point, x , along the nozzle, and Pr_x is the Prandtl number and is a function of the working gas temperature at any point, x , along the nozzle.

$$h_x = \frac{\overline{Nu}_x k_x}{D_p} \quad (17)$$

where k_x is the thermal conductivity of the working gas and is a function of the temperature at any location, x , along the nozzle.

The Prandtl number, viscosity, and thermal conductivity of the gas were all found as a function of gas temperature by linearly interpolating the working gas properties (nitrogen or helium) from the National Institute of Standards and Technology (NIST) tables of gas data [56]

Prior to using the simulation to investigate the fluid dynamics and particle transport properties of the nozzle, it was necessary to ensure the model was implemented correctly. In order to verify this, key isentropic compressible flow relationships were calculated and then compared to the simulation output. Those relationships for isentropic compressible flow are the pressure, temperature, and density of the gas at the exit as compared to the inlet [57]. The exit pressure, Equation 18 is given by:

$$P_{g_e} = P_{g_i} \left\{ \left[1 + \frac{1}{2}(\gamma - 1) Ma_e^2 \right]^{\gamma/(\gamma - 1)} \right\}^{-1} \quad (18)$$

where P_{g_e} is the exit gas pressure, P_{g_i} is the inlet gas pressure, γ is the specific heat ratio, and Ma_e is the exit Mach number, given by Equation 19.

$$Ma_e = \frac{U_{g_e}}{a} = \frac{U_{g_e}}{\sqrt{\gamma R T_{g_e}}} \quad (19)$$

where U_{ge} is the exit velocity of the gas, a is the speed of sound in the gas, γ is the specific heat ratio, R is the specific gas constant, and T_{ge} is the exit temperature as found in Equation 10.

The gas exit temperature isentropic relationship, Equation 20, is given by:

$$T_{ge} = T_{gi} \left[1 + \frac{\gamma - 1}{2} Ma_e^2 \right]^{-1} \quad (20)$$

where T_{ge} is the exit gas temperature and T_{gi} is the inlet temperature, γ is the specific heat ratio, and Ma_e is the exit Mach number.

The exit gas density, Equation 21, is given by:

$$\rho_{ge} = \rho_{gi} \left\{ \left[1 + \frac{1}{2} (\gamma - 1) Ma_e^2 \right]^{\frac{1}{\gamma - 1}} \right\}^{-1} \quad (21)$$

where ρ_{ge} is the exit density, ρ_{gi} is the inlet density, γ is the specific heat ratio, and Ma_e is the exit Mach number.

One final piece to ensuring the model is accurately representing the fluid dynamics is to ensure that over the range of operation, the gas exit pressure is greater than the ambient pressure of the cabinet. This ensures that there will be no shock wave inside the nozzle caused by backpressure.

A number of different conditions of gas type, gas pressure, gas temperature, and particle size and morphology were simulated to investigate the fluid dynamics and particle transport properties of the system and are summarized in Table 9. In particular, the effect of gas type, helium or nitrogen, on the fluid dynamics was studied by running the simulation utilizing the same inlet gas conditions of pressure and temperature, 1.7 MPa (250 psi) and 230 °C, respectively, for both working gases. The next simulation was conducted to investigate the fluid dynamics and particle transport properties of each gas type by simulating the same pressure and temperature conditions as above, with the addition of a 20 μ m diameter particle into the flow. To investigate the effect of gas inlet temperature on gas and particle exit velocity, a simulation was conducted, for both gas types, with a constant inlet pressure of 1.7 MPa (250 psi) and particle diameter of 20 μ m.

Temperature was varied over the range of the system from 100 to 600 °C. The next simulation was conducted to investigate the effect of gas inlet pressure on gas and particle exit velocity. Gas inlet pressure was varied from 0.34 to 2.0 MPa (50 to 300 psi), in 0.34 MPa (50 psi) increments, while inlet temperature and particle diameter were held constant at 300 °C and 20 μm , respectively. To study the effect of particle size and morphology on the exit particle velocity, two simulations were conducted at 230 °C and 1.7 MPa (250 psi), for both helium and nitrogen. In the particle size simulation, particle diameter was varied from 10 to 100 μm . In the particle morphology simulation, particle size was held constant at 20 μm while the drag coefficient was varied from 0.5 to 2.0, equation roughly to a sphere to a flat-plate or cube-like particle in the flow.

Parameters	Value or Range
Fluid Dynamics	
Gas Type	He, N2
Gas Inlet Pressure (MPa)	1.7
Gas Inlet Temperature (°C)	230
Particle Velocity	
Gas Type	He, N2
Gas Inlet Pressure (MPa)	1.7
Gas Inlet Temperature (°C)	230
Particle Diameter (µm)	20
Effect of Gas Inlet Temperature	
Gas Type	He, N2
Gas Inlet Pressure (MPa)	1.7
Gas Inlet Temperature (°C)	100 - 600
Particle Diameter (µm)	20
Effect of Gas Inlet Pressure	
Gas Type	He, N2
Gas Inlet Pressure (MPa)	0.3 - 2.0
Gas Inlet Temperature (°C)	300
Particle Diameter (µm)	20
Effect of Particle Size	
Gas Type	He, N2
Gas Inlet Pressure (MPa)	1.7
Gas Inlet Temperature (°C)	230
Particle Diameter (µm)	10 - 100
Effect of Particle Morphology	
Gas Type	He, N2
Gas Inlet Pressure (MPa)	1.7
Gas Inlet Temperature (°C)	230
Particle Diameter (µm)	20
Drag Coefficient	0.5 - 2.0

Table 9. Summary of simulation experiments and associated parameters for the study of fluid dynamics and particle transport properties. (highlighted values represent the parameter modified and the range over which it was modified in each experiment)

The final two simulations were conducted to compare the simulation exit particle velocities to the laser measured particle velocities at the nozzle exit. Nitrogen at $T_i = 450^\circ\text{C}$, $P_i = 1.7 \text{ MPa}$ (250psi) and helium at $T_i = 325^\circ\text{C}$ $P_i = 1.2 \text{ MPa}$ (175psi), were utilized in the simulation and the laser velocimetry experiments. S5001 powder was utilized for the laser measured velocities and the laser stand-off distance was approximately 1 mm from the nozzle exit. The particle diameters utilized in the simulation ranged from approximately 7-68 μm . The actual diameter values were chosen based upon the Horiba particle size analysis results from Section II. These values were chosen because there was a known particle fraction for each particle diameter and thus the information could easily be plotted (as particle fraction versus particle velocity) for comparison purposes. S5001 was chosen as the validation powder because it is spherically shaped and thus fits the assumptions utilized in the derivation of the simulation equations. Table 10 and Table 11 summarize the gas and particle properties, respectively, that were utilized in the nozzle exit velocity simulation and experimentation.

Type	Gas Inlet Temperature ($^\circ\text{C}$)	Gas Inlet Pressure (Mpa)	Gas Inlet Velocity (m/sec)	Specific heat ratio	Gas Constant (kJ/kgK)
Nitrogen	450	1.7	0	1.4	0.2969
Helium	325	1.75	0	1.66	2.0772

Table 10. Working gas initial conditions and properties utilized in nozzle simulation

Powder	Initial Velocity (m/s)	Initial Temperature (K)	Particle Diameter (μm)	Density (kg/m^3)	Specific Heat (J/kgK)
S5001	1	300	7-68	8000	502

Table 11. S5001 particle initial conditions and properties utilized in nozzle simulation

4. Laser Velocimetry for Austenitic Stainless Steel

The effects of gas type and inlet conditions, stand-off distance, and particle size and morphology were investigated utilizing PG-AMP-10 and S5001 powders via laser velocimetry. Nitrogen and helium were both utilized as working gases to measure average particle velocity and obtain particle velocity distributions at different pressure, temperature, and stand-off distance combinations. Nitrogen testing was accomplished at one condition to examine the effect of gas type on the velocity distribution, $T_i = 230^\circ\text{C}$, $P_i = 1.7 \text{ MPa}$ (250psi) at a stand-off distance of 10 mm. The helium testing was accomplished at a total of six different working gas conditions with values of temperature ranging from 200 to 450 °C and pressure ranging from 0.7 to 1.7 MPa (100 – 250 psi). The specific combinations (Table 12) were chosen based on previous deposition efficiency experiments and limitations of the cold spray unit. The helium experiments were conducted at three different stand-off distances, 10 mm, 20 mm, and 40 mm. All experiments were conducted with a nominal feed rate of 40%. A summary of the conditions is provided in Table 12, which also depicts all the helium working gas temperature and pressure combinations used.

Helium Inlet Conditions	
Temperature (°C)	Pressure (MPa)
230	1.7
200	1.7
230	1.7
230	1.2
275	1.2
325	1.2
450	0.7

Table 12. Summary of helium inlet condition combinations utilized in the laser velocimetry experimentation.

The laser particle velocimetry process was conducted in much the same manner as previous experiments. The capture depth and trigger level, 10 µsec and 100 mV

respectively, were used for both the PG-AMP-10 and S5001 powders. These values were chosen based upon the results of the powder calibration experiment. The particle velocity measurements from each condition were analyzed to determine the average velocity, were binned into 100 m/sec velocity bins to visualize the particle velocity distribution, and were plotted to investigate the effects of all the parameters on measured particle velocity.

5. Determination of Critical Velocity for Austenitic Stainless Steel

S5001 and PG-AMP-10 austenitic stainless steel powders were utilized in these experiments in an attempt to determine the critical velocity of austenitic stainless steel for the low pressure cold spray deposition process. The powders were deposited onto 316 stainless steel substrates utilizing the same gas pressure, gas temperature (as detailed in Table 12), and stand-off conditions (10, 20, and 40 mm) utilized during the laser velocimetry experiments. Deposition efficiency and coating thickness per pass were measured for each experimental condition in the same manner as detailed in Chapter I.

Critical velocity was determined by fitting a Gaussian curve (Equation 22) with one or two terms to the scatter plot data acquired from the laser velocimetry.

$$f(U_p) = \sum a_i e^{-((U_p - b_i)/c_i)^2} \quad (22)$$

where a_i , b_i , and c_i are coefficients given by the MATLAB curve fitting tool and $i = 1$ or 2 . All the curve fits attained a minimum of 0.98 RMS. The particle fraction curve was numerically integrated from the maximum velocity measured back towards lower velocities until the area under the curve matched the acquired deposition efficiency. The velocity at which the area under the curved matched the measured deposition efficiency was taken to be the critical velocity. This approach assumes that all particles traveling faster than that velocity contributed equally to the mass of the deposit. Figure 28 provides a screenshot of the curve fit for S5001 powder sprayed with helium at $T_i = 450$ °C, $P_i = 1.7$ MPa (250 psi) at a stand-off distance of 20 mm. A visual representation of the backward integration process can be seen in Figure 54 of the results section which

overlays three curves and backward integrates all three to find the critical velocity associated with them.

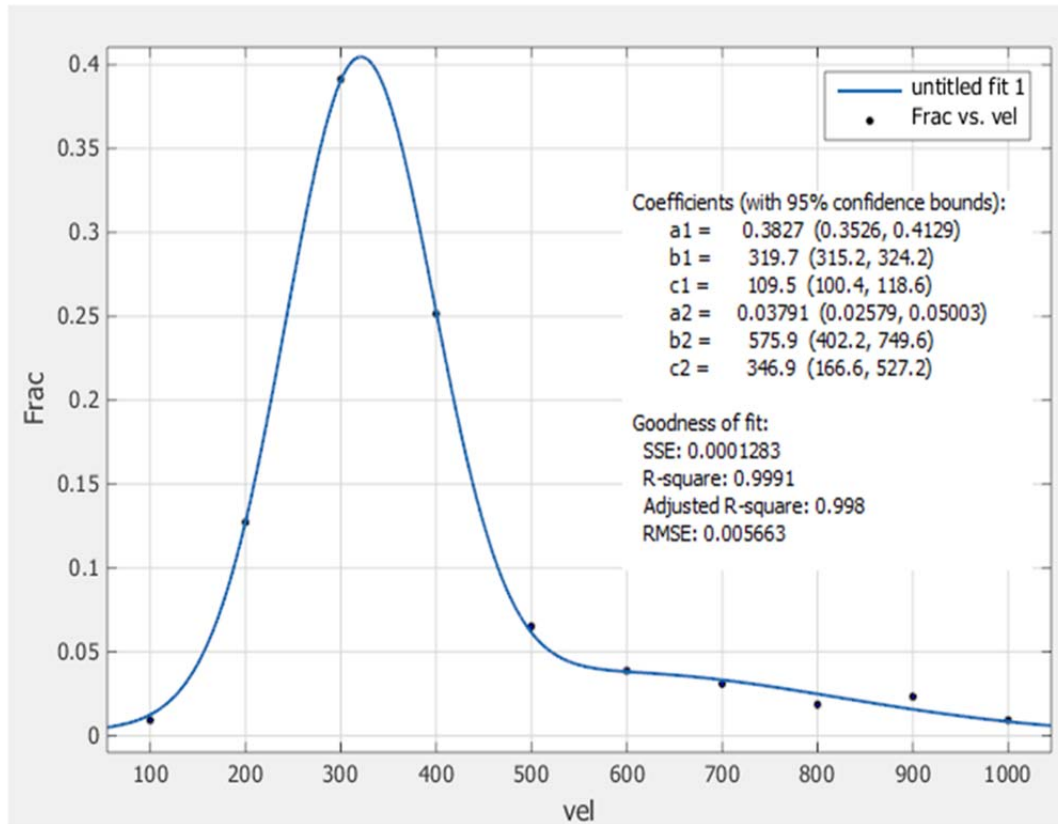


Figure 28. Screenshot of MATLAB of curve fit process.

C. RESULTS

1. Velocimeter Detector Calibration for PG-AMP-10 and S5001 Austenitic Stainless Steel

The optimal capture depth for both powders was determined to be 10 μ sec, Figure 29. This capture depth value resulted in the highest number of “good” particle measurements per second. At capture depth values higher than 50 μ sec, both the S5001 and PG-AMP-10 powders continuously reduced in the number of good particles measured. The reduction of number of acceptable measurements per second at the higher capture depth values indicates that the capture window was too large. Because the window was too large multiple peaks appeared in it at once, but because the software

counted only the first peak, the rest were rejected. It should also be noticed that there exists no maximum on the curve indicating that for these powders the smaller capture depths work well. Figure 29 also shows a large difference in the number of good particles measured between the two powders. This is likely indicative of the choice of trigger level, 200 mV, utilized during the experiment. Due to the size disparity of the S5001 and PG-AMP-10 particles (20 μm versus 60 μm average particle size), the larger particles of the PG-AMP-10 tended to be counted more for the higher trigger level used.

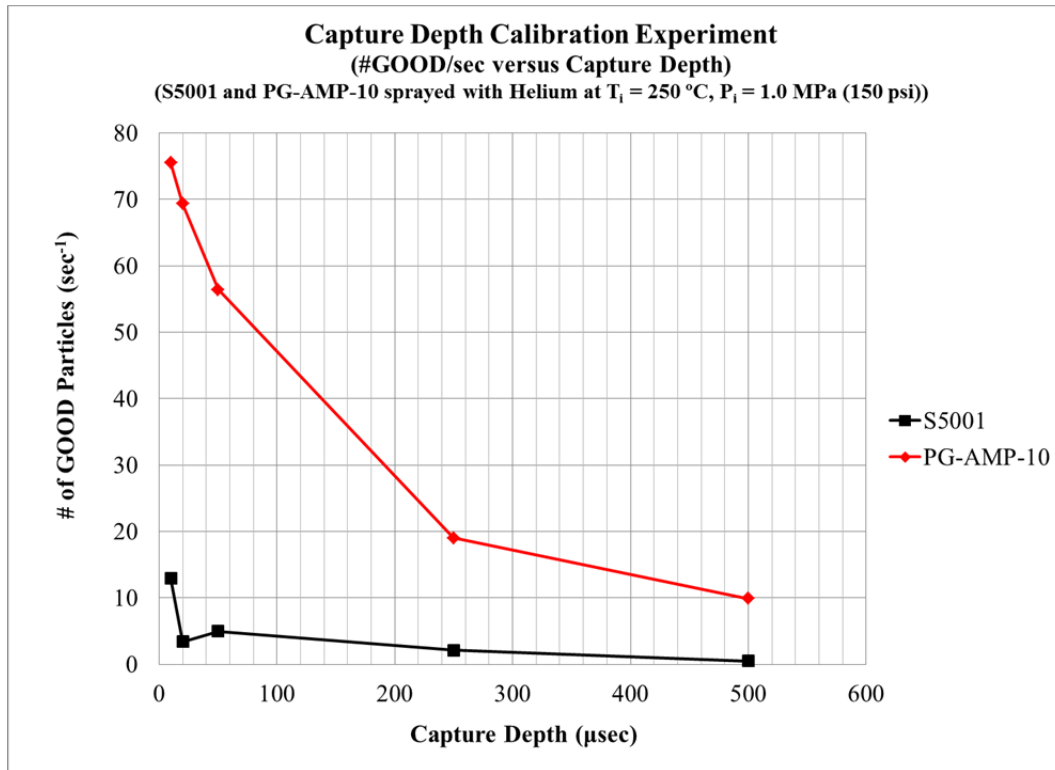


Figure 29. Capture depth calibration experiment results plot for S5001 and PG-AMP-10 indicating the optimal capture depth set-point for each at 10 μsec and a reduction of #GOOD/sec for all capture depths greater than 50 μsec . Black (S5001), Red (PG-AMP-10)

The results of the trigger level calibration experiment indicate that for the parameters used in this calibration step, an optimal trigger level to utilize for S5001 and PG-AMP-10 was 100 mV and 50 mV, respectively, Figure 30. These values resulted in the highest number of good particles per second measured. During the subsequent

velocimetry experiments; however, 100 mV was chosen for PG-AMP-10 as well because the reduction in the number of acceptable particle measurements per unit time was minute. This allowed both powders to be measured utilizing the same capture depth and trigger level values. Again there is a noticeable difference between the number of good particles per second measured for the S5001 as compared to the PG-AMP-10. This is once again likely due to the value that was held constant (capture depth) during the experiment. The previous results already showed that the optimal value should have been 10 μ sec vice the 20 μ sec used in this experiment. It should also be noticed that the effect of trigger level on the number of good particles per second measured initially causes a reduction as trigger level is increased, but then both the S5001 and PG-AMP-10 tend to increase again at 250 mV. They never attain the higher values achieved at lower trigger levels, and once trigger level is increased above 500 mV both show a significant reduction in the number of good particles measured per second. This is likely due to the fact that both of these powders exhibit a second smaller hump in their particle size distributions. As trigger level was increased, the return intensity was from the larger particles, but because there are a larger number of smaller particles, the second peak was not as high as the first. It should be noted however that the PG-AMP-10 powder consistently achieved better statistical measures than the S5001 powder during these and the follow-on velocimetry experiments.

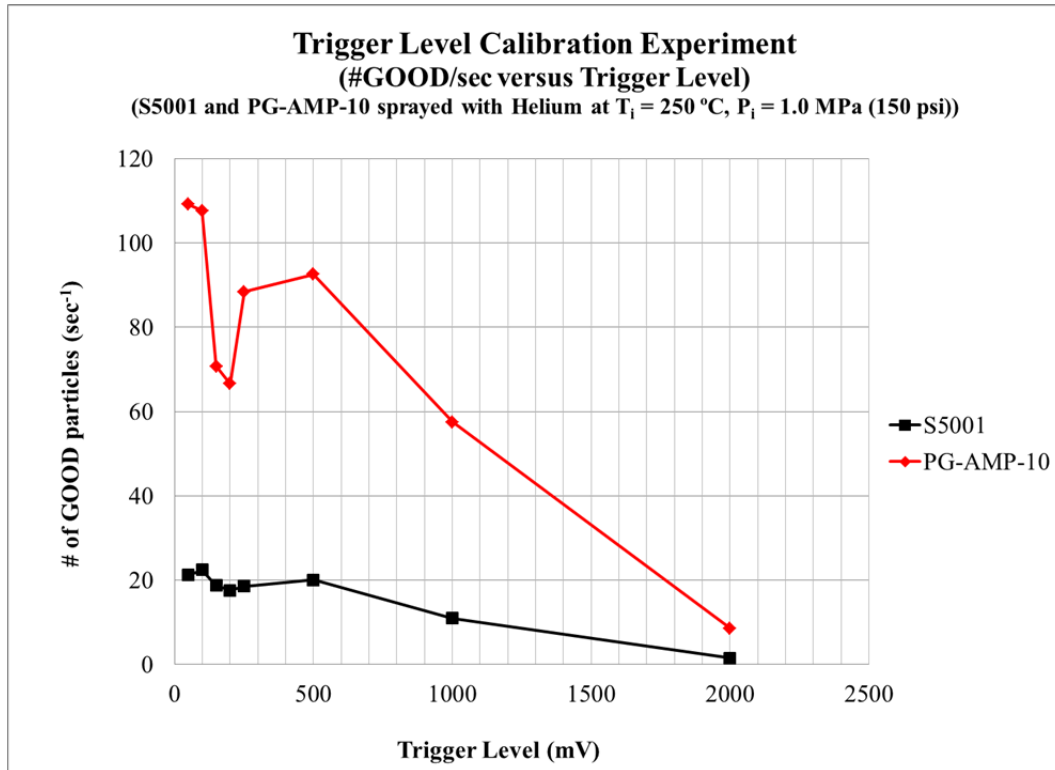


Figure 30. Trigger level calibration experiment results plot for Ss5001 and PG-AMP-10 indicating the optimal trigger level set-point for each at 50 and 100 mV and a reduction of #good/sec for all trigger levels greater than 500 mV. Black (S5001), Red (PG-AMP-10).

Capture depth and trigger level also have a significant impact on the measured velocity and diameter distributions attained during laser velocimetry. For both the S5001 (Figure 31) and the PG-AMP-10, capture depth did not have a strong effect on the velocity distribution attained during measurement. It can be seen that for all the capture depths less than 500 μsec , the velocity distributions were approximately the same, peaking at approximately 400 m/sec with 40 % of the particles. At 500 μsec the peak still existed at 400 m/sec but the peak significantly jumped to over 60 % of the particles measured. This is indicative of the larger capture window counting more of the slower particles (where only one peak would be in the window because they are slower) while the faster ones resulted in more peaks in the window at one time and only the first peak was counted. The capture depth modification had very little effect on the diameter distribution of the particles with the shifts in the distribution being caused by binning

only. Figure 32 shows the effect the capture depth on the diameter distribution for PG-AMP-10. At all capture depths the peak tended to be approximately the mean size of the particles (60 μm) with slight variations due to binning in 10 μm bins.

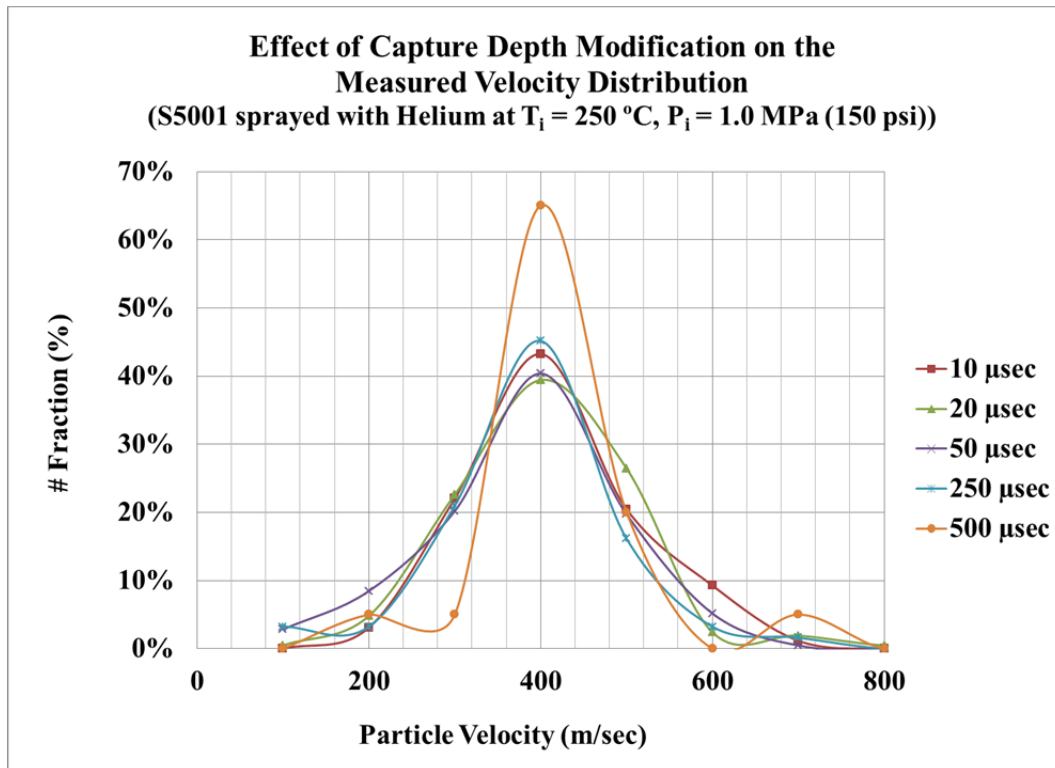


Figure 31. Effect of capture depth modification on the measured particle velocity distribution for S5001 showing a higher peak at larger capture depth values indicating more slower particles are being accepted.

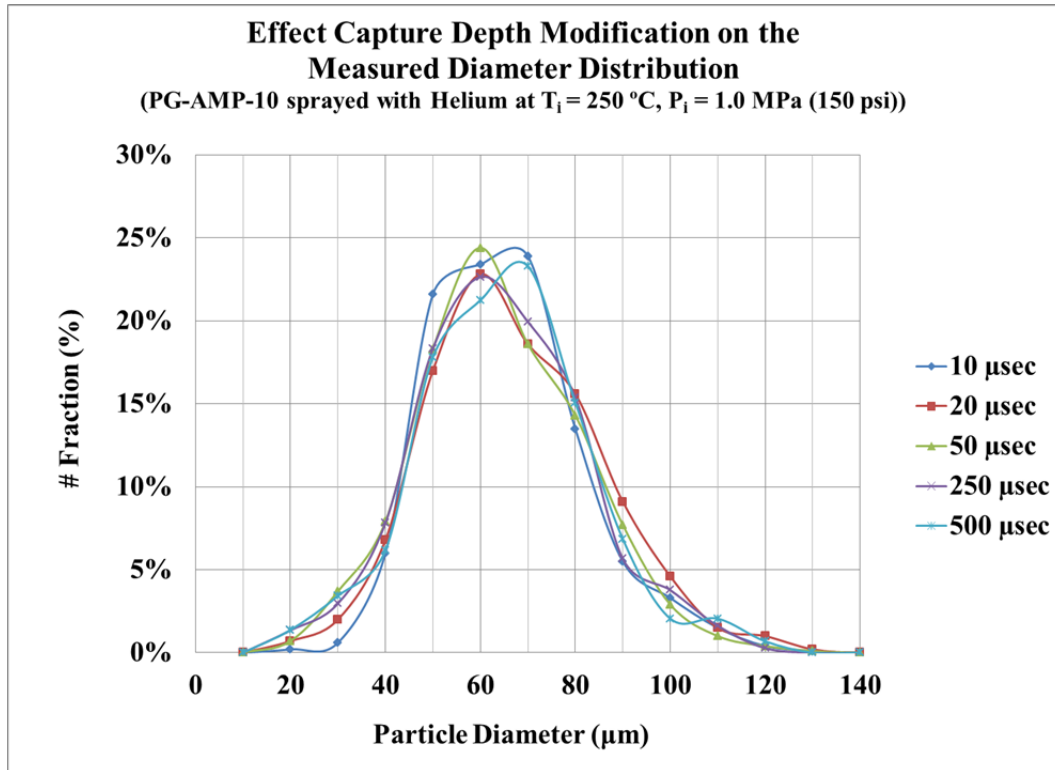


Figure 32. Effect of capture depth modification on the measured particle diameter distribution for PG-AMP-10 showing that capture depth has insignificant impact on the diameter distribution.

Trigger level, however, had an impact on both the velocity and diameter distributions of the measurements. Both S5001 and PG-AMP-10 showed a similar effect to the velocity distribution as trigger level was systematically increased during the calibration experiment. For the PG-AMP-10 powder (Figure 33), there is a shift in the particle velocity distribution toward slower particles velocities (i.e. bigger particles) consistent with what would be expected with an increase in trigger level as increasing trigger level means that a higher intensity (i.e. bigger particle) signal is needed to pass the acceptance criteria. Similar to the velocity trend of accepting larger particles, the diameter distributions also shifted toward larger particles for both S5001 (Figure 34) and PG-AMP-10. As seen, for values less than 250 mV the particle diameter distributions were approximately the same, but once above that threshold value the distributions began shifting to the right and peaking at higher particle diameters.

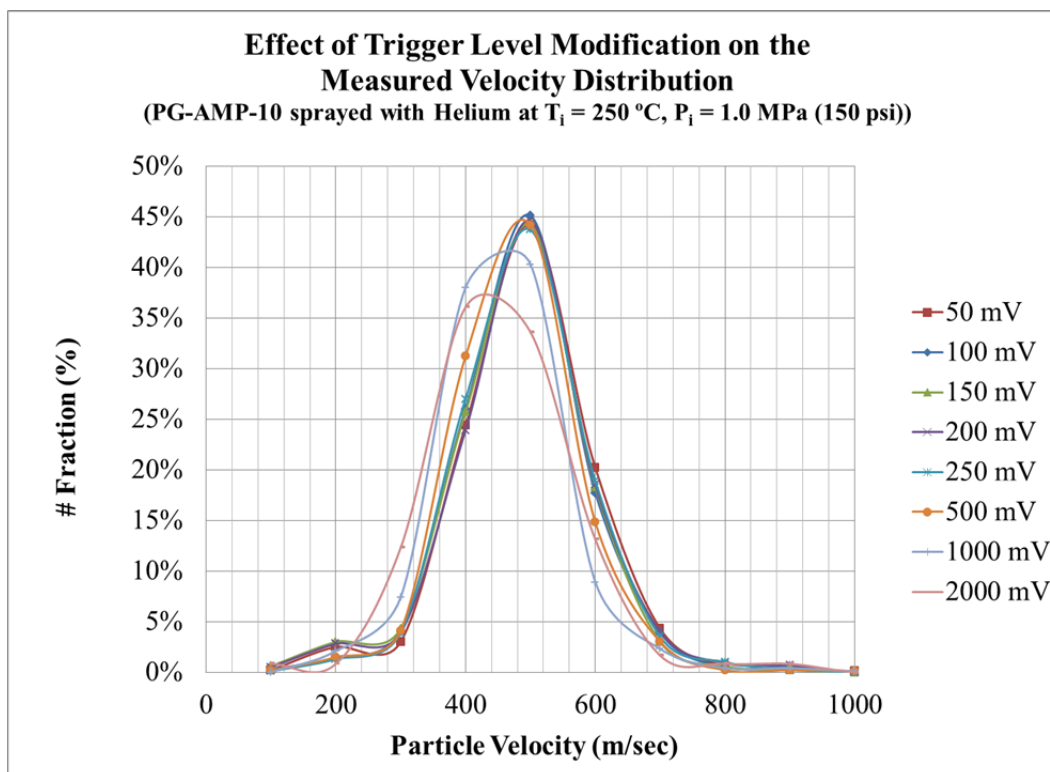


Figure 33. Effect of trigger level modification on the measured velocity distribution for PG-AMP-10 showing that at higher trigger levels ($> 1000\text{ mV}$) the velocity distributions shifts toward larger, slower particles.

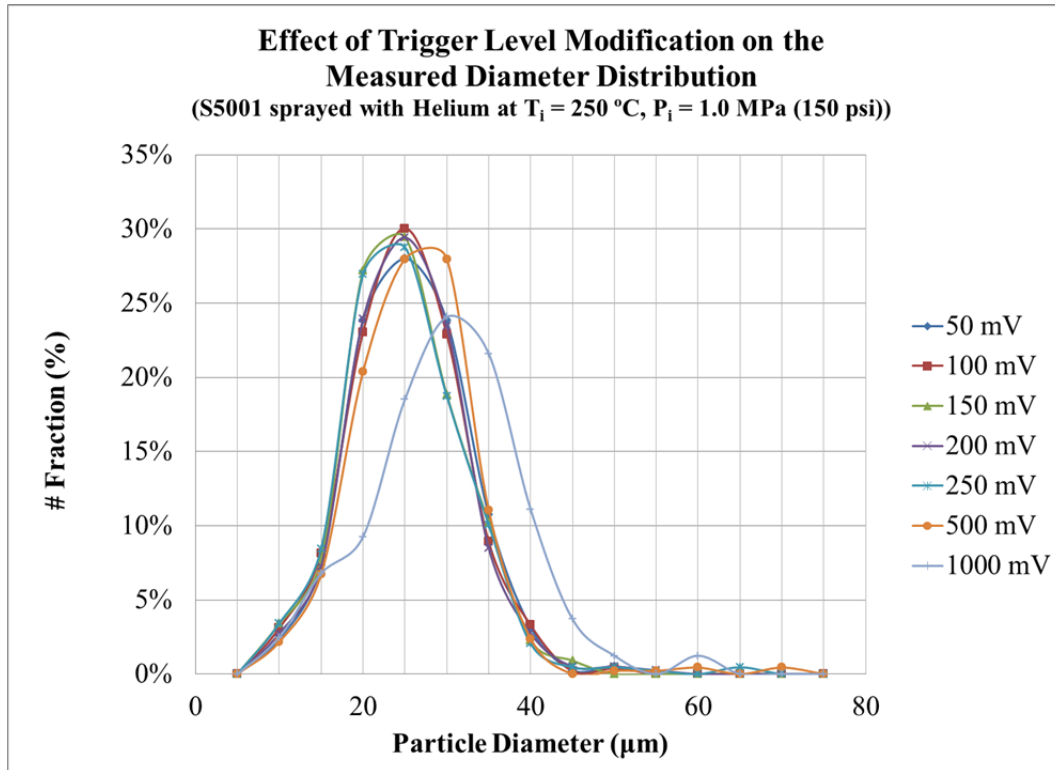


Figure 34. Effect of trigger level modification on the measured diameter distribution for S5001 showing that at higher trigger levels ($> 500\text{ mV}$) the diameter distribution shifts toward larger particles.

2. Nominal Powder Feed Rate and Substrate Interaction

The nominal powder feed rate experiment, conducted with S5001, was accomplished to investigate if changes in powder feed rate would significantly alter the measured velocity results for both statistics (the number of good particles measured per second) and consistency (average particle velocity and velocity distribution remain constant). Figure 35 shows the statistical trend and average velocity trend, both of which are practically constant, for the nominal powder feed rate experiment as feed rate increases from 2 – 80 %. Although there is some experimental fluctuation in the values, the number of good particles measurements per second were all approximately 40 and within 10 % of each other. The average particle velocity also fluctuated but centered at approximately 410 m/sec and all values were within 10% of each other.

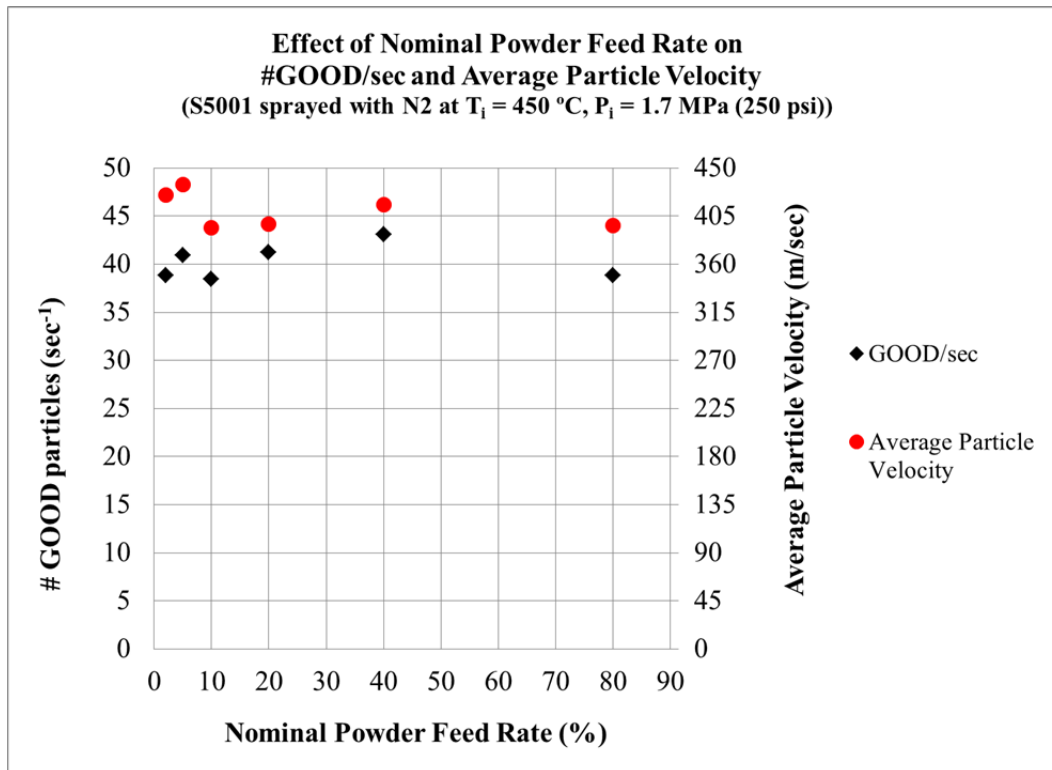


Figure 35. Effect of nominal powder feed rate on the consistence of statistical good per second and average particle velocity indicating that the nominal powder feed rate has little impact on both. Black (GOOD/sec), Red (Average particle velocity).

The nominal powder feed rate effect on the velocity distribution is depicted in Figure 36. The plot shows that regardless of the nominal feed rate percentage, for S5001, the velocity distributions all peak at approximately 400 m/sec with slightly different peak heights which correlates to the average velocity data centering on the same velocity with slight (< 10 %) fluctuations above and below the overall average velocity. Based on these results, we should be able to safely assume that the velocity measurements are not sensitive to the powder feed rate during the experiment.

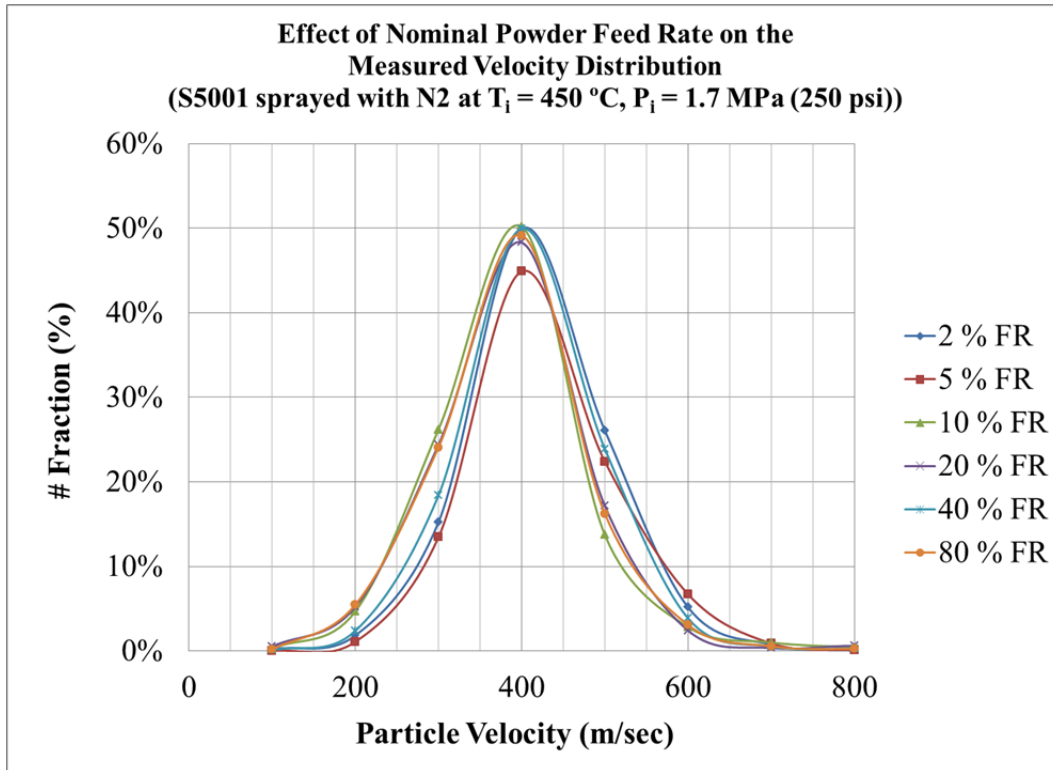


Figure 36. Nominal powder feed rate effect on the measured velocity distribution for S5001 indicating for all nominal powder feed rates the peak occurs at the same particle velocity with a slightly different height.

The substrate interaction experiment, also conducted with S5001, was accomplished to investigate the feasibility of measuring particle velocity at the point of impact with the substrate. Again the statistical consistency, average particle velocity, and velocity distributions were utilized to characterize the results. Figure 37 shows the statistical trend and average velocity trend. There is an observable drop in the number of good particles per second achieved once the substrate is introduced and brought to within 5 mm of the laser indicating that there is interference caused by the particles bouncing back off the substrate and passing through the laser again. It should however be noted that although this reduction in the statistical consistency occurs, the average particle velocity remains relatively constant at approximately 430 m/sec, and all the values are within 5 % of each other indicating that the measurement of velocity is remaining constant even with the interference. It can also be assumed that because the average

velocity remains constant even as the measurement is taken at the substrate interface that for these conditions there is no bow shock effect on the particles.

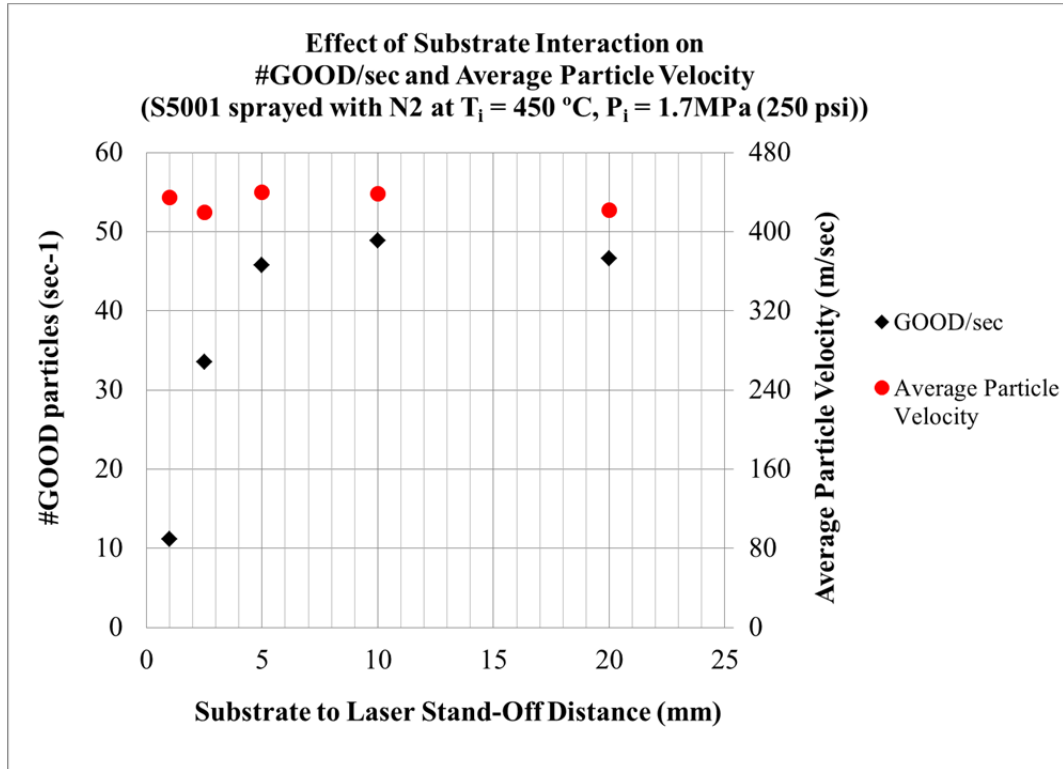


Figure 37. Effect of substrate interaction on the consistence of statistical good per second and average particle velocity indicating that interference occurs and disrupts the number of good per second at a small stand-off distances (< 5 mm) but the average particle velocity remains constant. Black (GOOD/sec), Red (Average particle velocity)

The velocity distribution shows that introducing a substrate into the gas-particle flow has no significant impact on the measured particle velocity distribution (Figure 38). All of the distributions, from the point of laser measurement at the substrate interface to 20 mm from the substrate interface, peak at approximately 420 m/sec with approximately the same peak height. The percentage decreases as the distance decreases because there is a loss of good particles measured (as previously shown in Figure 37 thus causing a slight shift in the peak height as the number fraction modifies to cover all measured particles.

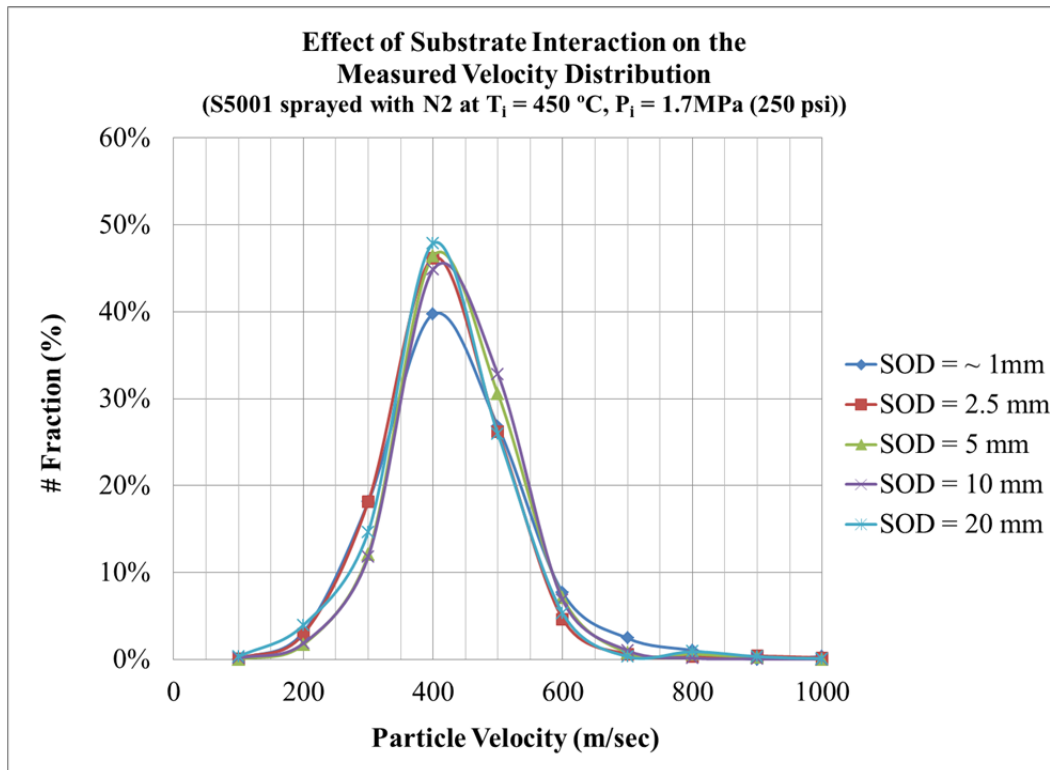


Figure 38. Substrate interaction effect on the measured velocity distribution for S5001 indicating no effect of the substrate interaction on the particle velocity distribution.

3. Simulation of Centerline (Windsor) UltiLife Nozzle

Prior to running a number of simulations with the model, it was first verified to be properly implemented in regards to fluid dynamics. This included an investigation of whether or not over the range of normal operation there would be any shocks in the nozzle that would alter the fluid dynamics from the standard compressible isentropic equations used to model the nozzle. Table 13 shows the results of this validation and indicates that the model was correctly predicting the gas pressure, temperature, and density relationships for helium and nitrogen based upon compressible isentropic flow relationships. Figure 39 shows that for the range of pressures, 0.34 to 2.07 MPa (50 to 300 psi) of the Centerline deposition system, the gas exit pressure is above the ambient pressure (0.5 kPa) in the cabinet. Because the exit pressure is higher than the ambient, it suggests that the model was implemented correctly, and it was not missing critical shocks that could occur in the nozzle.

	Helium		Nitrogen	
	Calculated	Simulated	Calculated	Simulated
Inlet				
Pressure (MPa)	1.7226	1.7226	1.7226	1.7226
Temperature (K)	503.15	503.15	503.15	503.15
Density (kg/m ³)	1.65	1.65	11.54	11.54
Outlet				
Pressure (MPa)	0.0064	0.0064	0.013	0.013
Temperature (K)	54.54	54.55	123.8	123.8
Density (kg/m ³)	0.057	0.057	0.347	0.347

Table 13. One-dimensional model validation results indicating model is correctly simulating the isentropic compressible flow of helium and nitrogen through the nozzle.

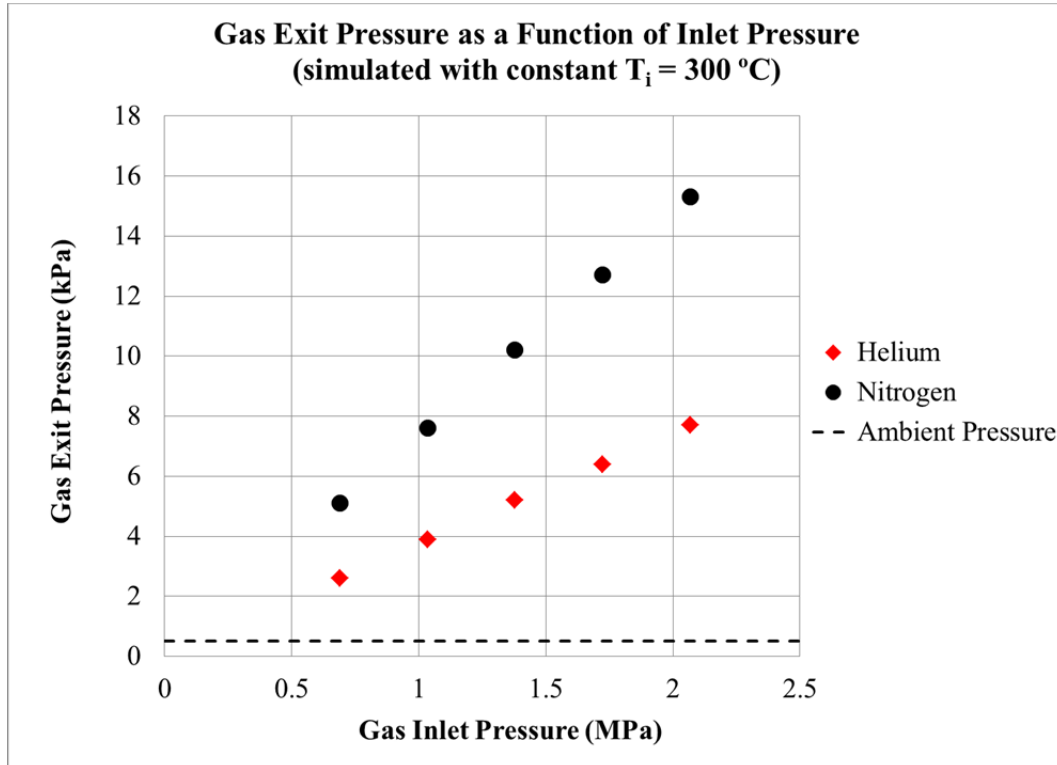


Figure 39. Gas exit pressure as a function of inlet pressure for helium and nitrogen, simulated at $T_i = 300\text{ }^{\circ}\text{C}$. Indicates that for the range of operation of the nozzle the gas exit pressure is always above ambient pressure. Red (helium), Black (nitrogen).

A single simulation of the Centerline (Windsor) UltiLife nozzle is shown in Figure 40. The plots represent the nozzle contour, gas pressure profile, gas and particle

velocity profiles, and gas and particle temperature profiles as a function of axial distance along the nozzle, for helium as the working gas with an inlet pressure and temperature of 1.7 Mpa (250 psi) and 230 °C, respectively. The particle size utilized was 20 μm . The physical geometry of the nozzle is shown in Figure 40-A. It is distinguished by a short, rapid decrease in radius up to the throat of the nozzle, followed by a long (120 mm) divergent section. As the gas approaches the throat in the convergent section, its pressure reduces slightly (Figure 40-B). As the gas is expanded through the throat, its pressure decreases rapidly almost as a step decrease, and continues to decrease, to approximately ambient pressure at the nozzle exit, albeit at a slower rate than in the throat section. As the gas approaches the throat of the nozzle its velocity increases slightly, as does its Mach number (Figure 40-C). As the gas expands through the nozzle throat its velocity has a jump increase and it reaches Mach 1. Attaining Mach 1 at the throat is critical to creating supersonic flow and also allows for the gas to continue accelerating through the divergent section of the nozzle. If sonic speed had not been attained in the throat then as the nozzle area got larger in the divergent section, the gas would actually decelerate. The gas velocity continues to increase through the divergent section of the nozzle, exiting at approximately 2100 m/sec and Mach number 5. The particles, introduced after the throat of the nozzle, also increase in velocity along the divergent section of the nozzle with much the same shape as the gas velocity, although with particle lag due to significant difference in density between the particle and entrainment gas. Figure 40-D shows the gas and particle temperature profiles along the nozzle. The gas temperature follows much the same trend as the gas pressure, reducing slightly in the converging section of the nozzle, sharply decreasing as the gas is expanded through the throat of the nozzle, and continuing to decrease along the divergent section of the nozzle until exiting below 100 K. The particle temperature profile follows the same trend as the gas temperature profile and decreases at almost the same rate as the gas temperature profile. Upon exit of the nozzle the particle temperature decreases to well below 200 K.

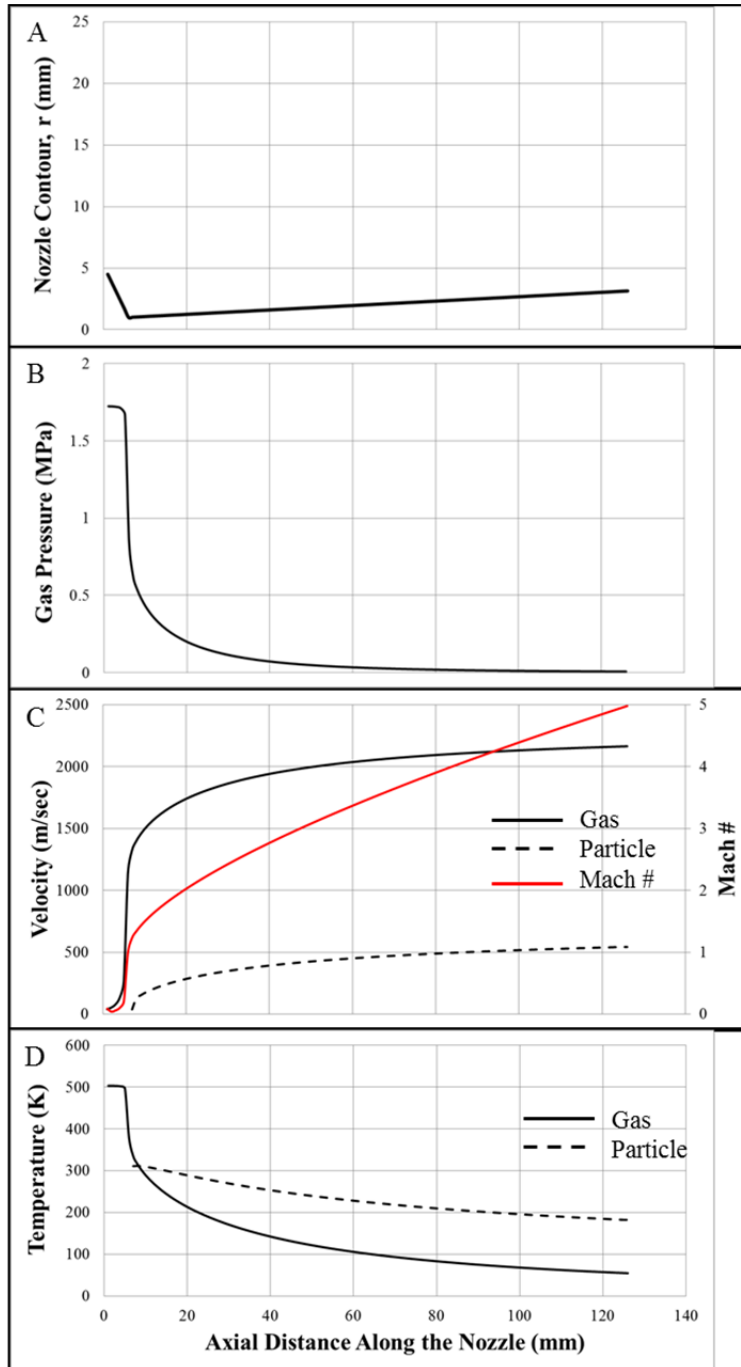


Figure 40. Fluid dynamics and particle transport MATLAB® model of the Centerline (Windsor) UltiLife nozzle. Simulated with helium gas at $P_i = 1.7$ Mpa (250 psi), $T_i = 230$ °C and particle size, $D_p = 20$ μ m. A.) nozzle contour radius, B.) gas pressure, C.) gas and particle velocity, D.) gas and particle temperature.

The gas pressure and temperature profiles along the nozzle show that because helium has a much lower molecular weight than nitrogen, it more rapidly expands through the throat of the nozzle resulting in both a lower exit pressure and exit temperature (Figure 41). Due to this more rapid expansion, the helium gas is accelerated more through the nozzle throat and attains nearly 2.5 times the exit velocity of the nitrogen gas, Figure 42. The particles, with a diameter of 20 μm , introduced into the flow for each of these gases exit the nozzle at 500 m/sec for helium-driven particles and 400 m/sec for nitrogen-driven. This equates to roughly 25 % of the helium gas and 45% of the nitrogen gas exit velocities. This suggests that using nitrogen as the working gas tends to have more of an effect on the particle velocity, because of the higher density of nitrogen, but because the helium is traveling at such a higher velocity, particles introduced into the helium travel at a much higher velocity due to the increased drag force.

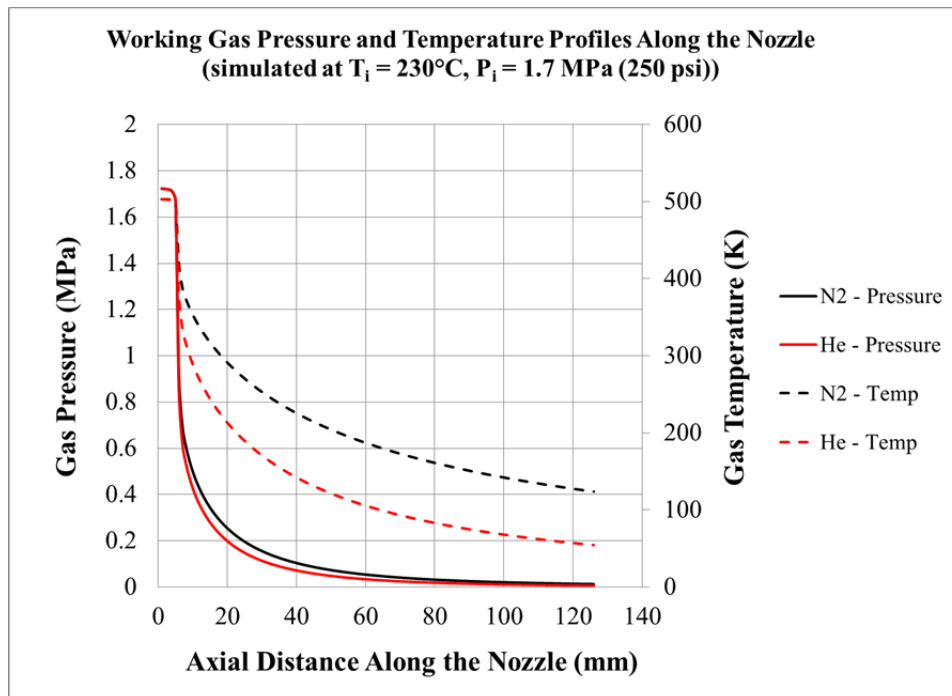


Figure 41. Working gas pressure and temperature profiles along the nozzle for simulated at $T_i = 230^\circ\text{C}$ and $P_i = 1.7 \text{ MPa}$ (250 psi) for both nitrogen and helium as the working gases. Indicates that helium expands faster through the nozzle throat causing a larger decrease in both gas temperature and pressure.

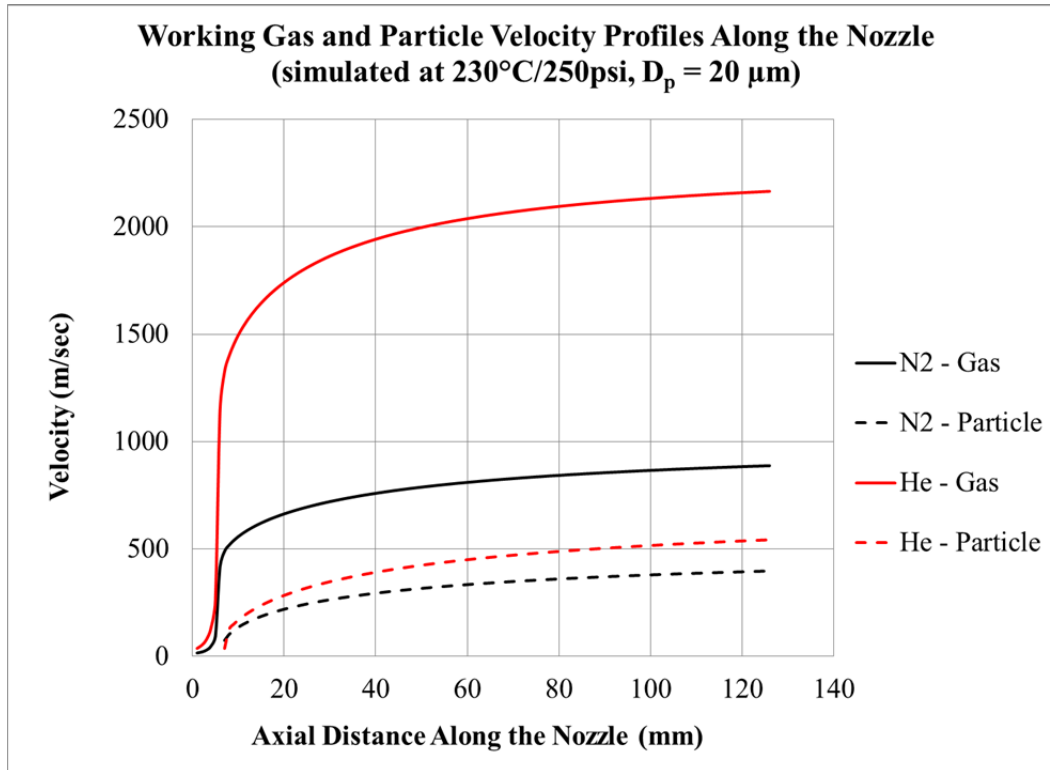


Figure 42. Working gas and particle velocity profiles along the nozzle simulated with helium and nitrogen at $T_i = 230\text{ }^{\circ}\text{C}$ and $P_i = 1.7\text{ MPa}$ (250 psi). Indicates that helium velocity is much greater than nitrogen velocity due to a much more rapid expansion of the gas in the throat, causing the particle velocity to be greater in helium than nitrogen.

For a given particle, gas type, and physical set up (nozzle geometry and stand-off distance), it is crucial to understand the effects of the only other adjustable parameters in the cold spray process, gas inlet temperature and gas inlet pressure. Figure 43 suggests that gas inlet temperature has a significant effect on gas exit velocity, but it does not have a great impact on the particle exit velocity. Over the range of 100 to 600 $^{\circ}\text{C}$, the helium gas exit velocity increases by nearly 1000 m/sec, from 1864 to 2852 m/sec, a 50 % increase, while the helium-driven particle nozzle exit velocity increases only by approximately 100 m/sec, from 509 to 616 m/sec, a 20 % increase. Likewise, the nitrogen gas exit velocity increases by just over 400 m/sec, approximately a 50 % increase, while the nitrogen-entrained particle exit velocity increases by roughly 100 m/sec, roughly a 25 % increase.

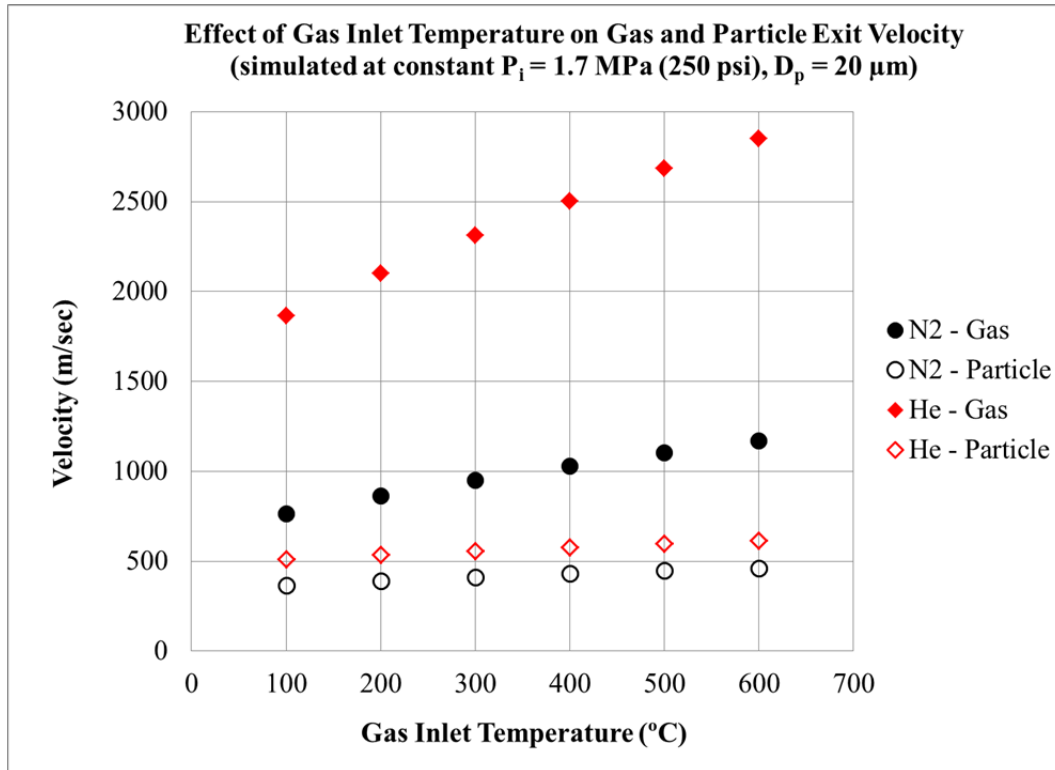


Figure 43. Effect of gas inlet temperature on gas and particle nozzle exit velocities simulated at a constant $P_i = 1.7$ MPa (250 psi), and $D_p = 20$ μm . Indicates that gas inlet temperature has significant effect on gas exit velocity, but not as significant on particle exit velocity. Red is helium, black is nitrogen, solid is gas, and open symbol is particle.

The second simulation of modification of gas parameters was conducted with a constant gas inlet temperature, 300 °C, and modifying gas inlet pressure. The results suggest that gas inlet pressure has no effect on gas exit velocity, but a substantial effect on the particle exit velocity, Figure 44. The particle velocity for the helium entrained particles increases just over 200 m/sec, from 376 to 589 m/sec, while the nitrogen-driven particles increase in exit velocity approximately 150 m/sec, from 283 to 431 m/sec, as pressure is increased over the range 0.34 to 2.07 MPa (50 to 300 psi), both approximately a 50 % increase. Each nozzle is designed to achieve a specific Mach number for the gas flowing through it, and therefore the gas velocity will remain constant regardless of the inlet pressure as long as the sonic condition is met at the throat. The Mach number values for the Centerline nozzle, as determined from simulation, are Mach 5 and Mach 4, for helium and nitrogen, respectively. As the gas density increases, so too does its ability

to accelerate the metal particles, which is why the increased particle exit velocities are predicted and observed.

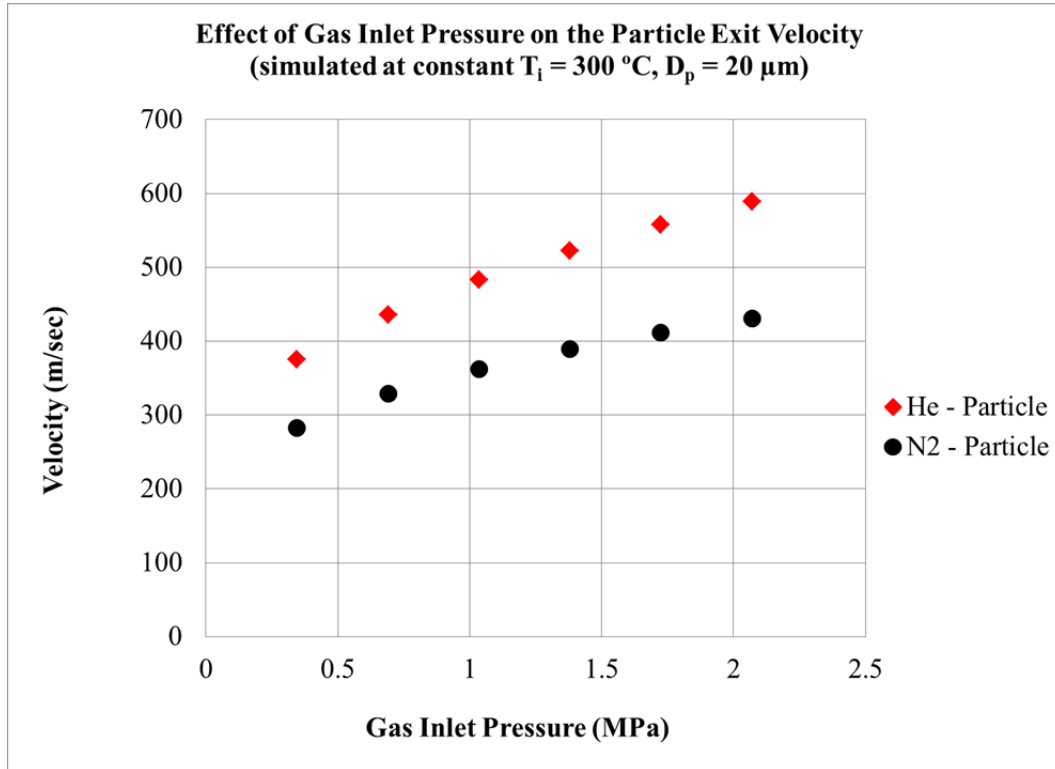


Figure 44. Effect of gas inlet pressure on the particle nozzle exit velocity (simulated at a constant $T_i = 300\text{ }^{\circ}\text{C}$, $D_p = 20\text{ }\mu\text{m}$). Indicates that gas inlet pressure has as significant effect on particle exit velocity. Helium (red diamonds), Nitrogen (black circles)

Another key piece to understanding the particle transport characteristics of the cold spray process is the effect particle size and particle morphology on particle velocity, and to also establish if the effect is the same for both nitrogen and helium. As particle size increases, the simulation shows that the particle velocity decreases. However, the sensitivity of the particle's velocity to its size becomes much less as the particle size increases (Figure 45).

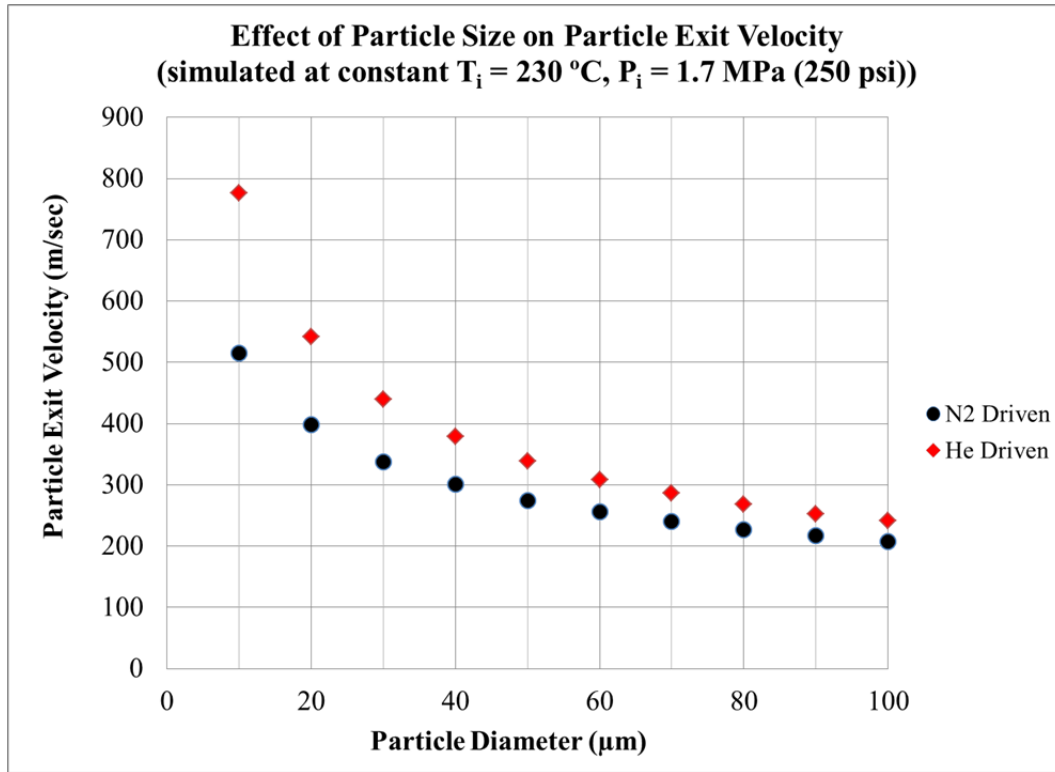


Figure 45. Effect of particle diameter on particle nozzle exit velocity. Simulated with helium and nitrogen at constant $T_i = 230\text{ }^{\circ}\text{C}$ and $P_i = 1.7\text{ MPa (250 psi)}$. Indicates that as particle size increase, particle velocity decreases, but as particle size increases the effect on velocity decreases. Indicates that nitrogen driven particles are less affected by particle size differences than helium driven ones. Black (nitrogen-driven), Red (helium-driven).

The last important characteristic of the particle transport properties of the low pressure cold spray process is the particle morphology. The results of the drag coefficient simulation suggest that as the particles becomes less spherical in shape the exit velocity of the particle increases, Figure 46. The results also suggest that this effect is more prevalent in helium as its exit particle velocity increased by 72 % versus the approximately 30 % increase in particle velocity attained by nitrogen-driven particles.

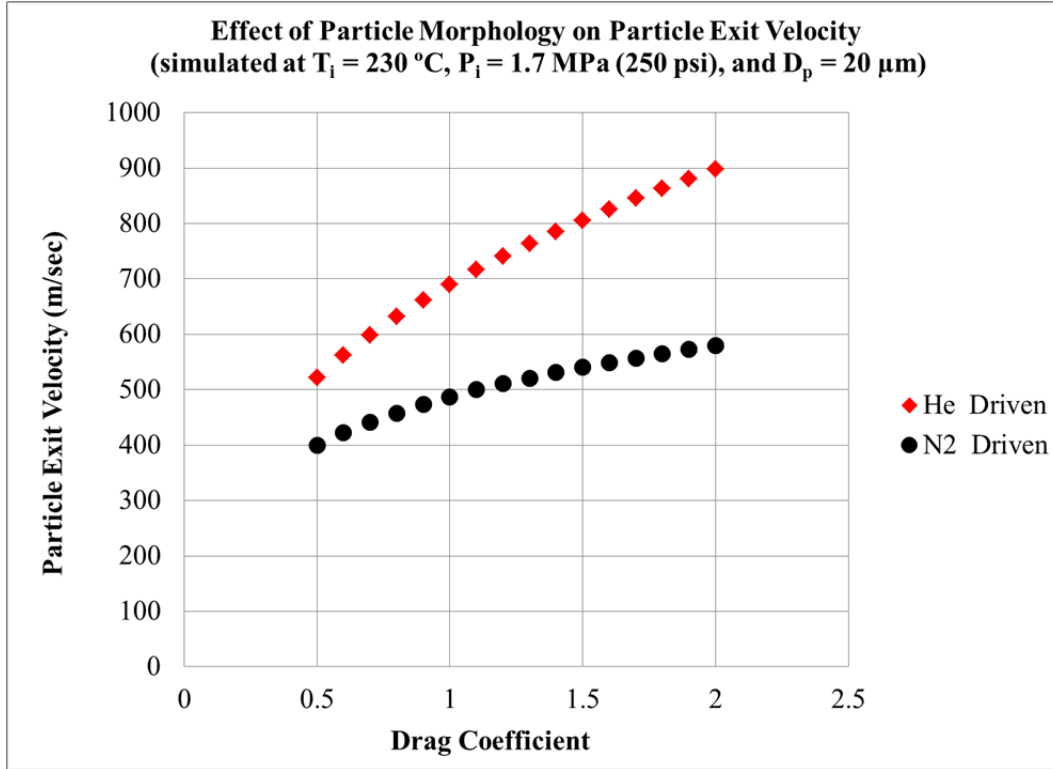


Figure 46. Effect of particle morphology on particle exit velocity. Simulated at $T_i = 230\text{ }^{\circ}\text{C}$, $P_i = 1.7\text{ MPa (250 psi)}$, and $D_p = 20\text{ }\mu\text{m}$. Indicates that as particle becomes less spherical (coefficient of drag increase), the particle exit velocity increases. Suggests that helium-driven particles are more affected by this than nitrogen-driven ones. Red (helium), Black (nitrogen).

4. Comparison of Laser Velocimetry Measurements Utilizing the One-Dimensional Model Simulation

Contrary to the normal convention of experiment being utilized to validate simulation, there is no way to precisely say that laser velocimetry is accurately reflecting the actual particle velocity during experimentation. That is to say, there is no experimental set-up of laser conditions and physical parameter conditions that could be done to accurately calibrate the laser so that it would be known that the measured particle velocities are accurate. Because of this, the one-dimensional model was utilized to validate the accuracy of the laser velocimetry measurements by comparing the simulation to nozzle exit velocities measured by laser velocimetry.

The simulated and measured particle velocities utilizing nitrogen as the working gas with inlet conditions of $T_i = 450^\circ\text{C}$ and $P_i = 1.7 \text{ MPa}$ (250 psi) shows that simulation and measured peaks both occur near 420 m/sec (Figure 47). Both the simulation and the measured particle velocity distributions follow the same trend with roughly the same slope up to the peak and after the peak. The peak height is different because of the difference in the number of bins. There are 10 bins in the simulated vice 8 in the measured. The measured data has a longer tail at higher velocities that is not seen in the simulated data. This is likely due to the binning that the Horiba Particle Analyzer does. The smallest diameter value utilized from the particle size measurements does not necessarily mean that is the smallest diameter present, it means that all diameters below that value were binned up to the value shown by the particle size analyzer and used in the simulation. The same effect can also be seen in the lower velocity range as the measured values reach lower velocities than the simulated ones due to the same binning effect only with the larger particles being binned down to the last relevant value.

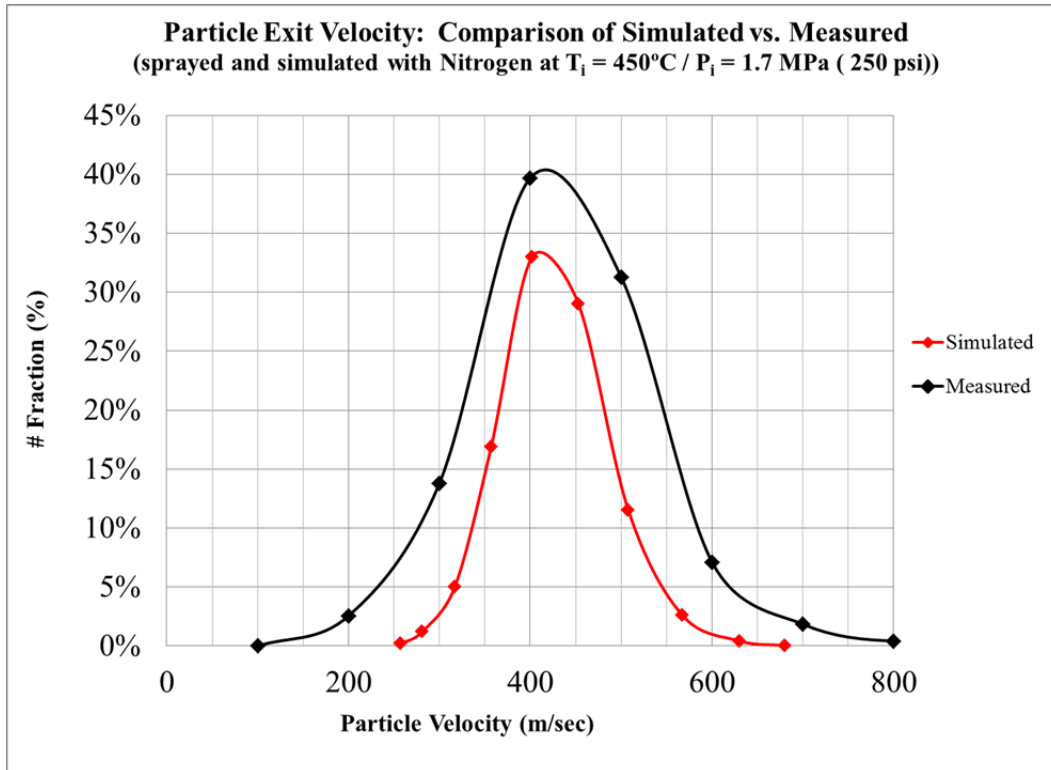


Figure 47. Comparison of simulated (red) and measured (black) particle velocity distributions utilizing nitrogen gas with inlet conditions of $T_i = 450^\circ\text{C}$ and $P_i = 1.7\text{ MPa}$ (250psi). Indicates approximately the same particle velocity at the peak and the same shape for each. Measured particle velocity shows a long tail toward higher velocities and more lower velocity values suggesting that the particle size bins did now show all available particle diameters.

Figure 48 represents the simulated and measured nozzle exit particle velocities utilizing helium as the working gas with inlet conditions of $T_i = 325^\circ\text{C}$ and $P_i = 1.2\text{ MPa}$ (175 psi). It shows that simulation and measured peaks occur at approximately the same particle velocity, 470 m/sec and 490 m/sec, respectively. Peak height again differs due to the number of bins being used. In this case, the simulated velocities do contain a tail toward higher values, but once again do not reach the higher and lower values attained by the measured particle velocity distribution.

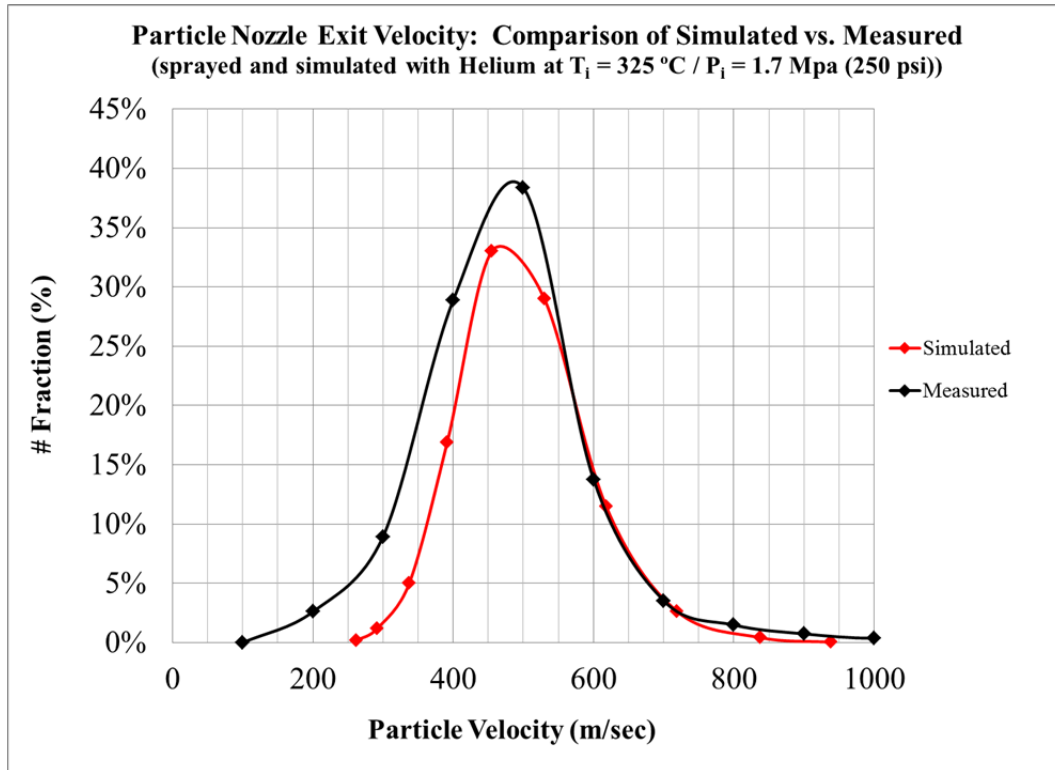


Figure 48. Comparison of simulated (red) and measured (black) particle velocity distributions utilizing helium gas with inlet conditions of $T_i = 325\text{ }^{\circ}\text{C}$ and $P_i = 1.2\text{ MPa}$ (175psi). Indicates approximately the same particle velocity at the peak and the same shape for each.

The comparison of the simulation with the nozzle exit velocities suggests that they are in good agreement and that the laser measured velocities are within the range expected. Because there are a number of assumptions utilized in the simulation, such as no particle interaction and perfectly spherical particles it is expected that they do not exactly match. Another key note is that the simulation is only valid up to the nozzle exit while the exit velocity measured by the laser was accomplished as close as possible to the exit but reasonably at approximately 1 mm from the nozzle exit. This extra distance from the nozzle exit effects the gas and particle velocities as the gas is allowed to rapidly expand to ambient pressure outside the nozzle and increase the particle velocity further.

5. Laser Measured Particle Velocity of S5001 and PG-AMP-10

A number of different cold spray conditions were measured utilizing laser particle velocimetry to investigate the effects of gas type, gas inlet pressure, gas inlet temperature,

and stand-off distance on the average particle velocity and velocity distributions for S5001 and PG-AMP-10. The conditions were also utilized in conjunction with the deposition efficiency in an attempt to determine the critical velocity for each material.

As shown in the particle velocity distributions, helium-entrained particles attained higher velocities than nitrogen-entrained ones (Figure 49). The velocity distribution for the helium driven gas particles peaked at 600 m/sec versus the 500 m/sec peak of the nitrogen driven particle velocity distribution. The curve was also significantly shifted toward higher velocities when utilizing helium. This is likely due to the much higher gas velocity attained by helium as it is expanded through the converging-diverging nozzle.

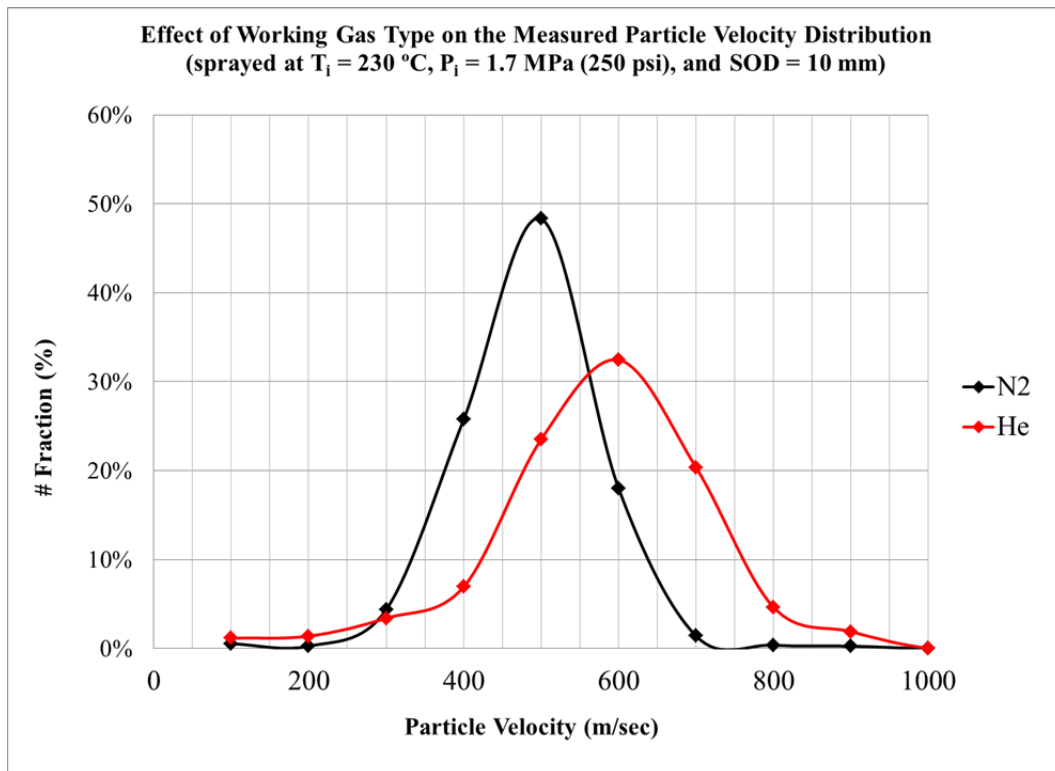


Figure 49. Effect of working gas type on particle velocity distribution for PG-AMP-10 sprayed at $T_i = 230\text{ }^{\circ}\text{C}$, $P_i = 1.7\text{ MPa}$ (250 psi), and SOD = 10 mm. Indicates that helium entrained particles travel at higher velocities for the same gas conditions.

The effect of inlet temperature modification on the particle velocity distribution for S5001 sprayed with helium gas at a constant inlet pressure, $P_i = 1.2\text{ MPa}$ (175 psi)

and stand-off distance of 10 mm shows that the particle velocity distribution is not significantly changed by increases in working gas inlet temperature, Figure 50. It should be noted that 325 °C is the maximum temperature achievable at this inlet pressure due to power limitations of the heater.

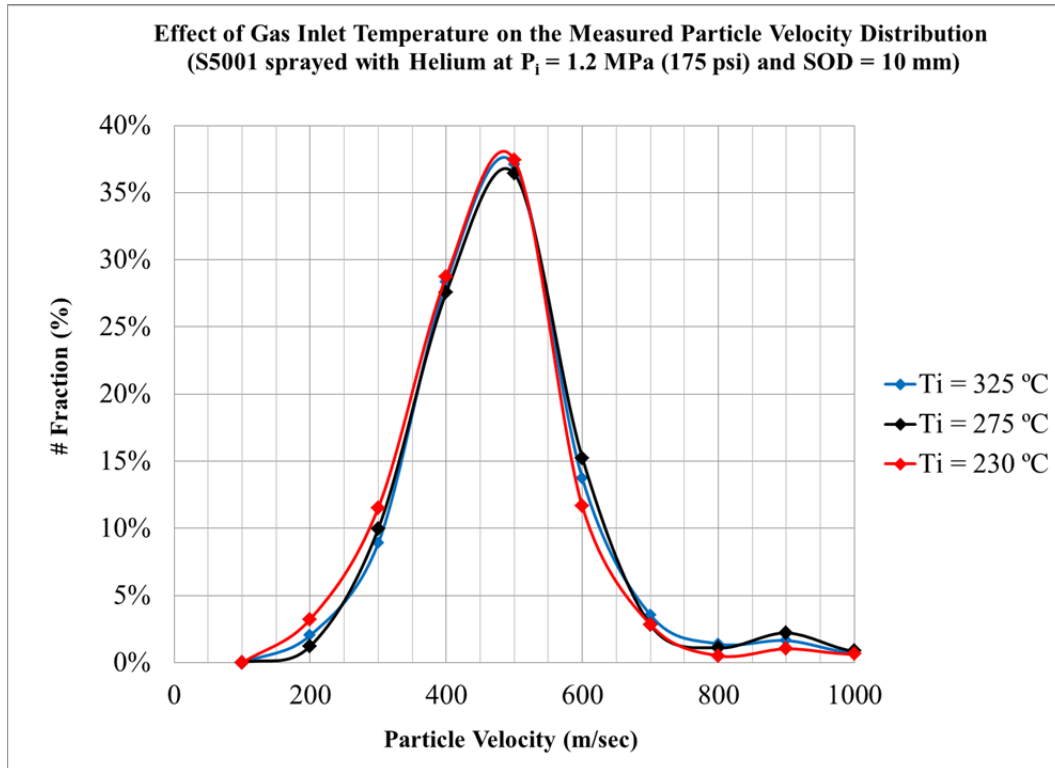


Figure 50. Effect of gas inlet temperature on the measured particle velocity distribution for S5001 sprayed with helium gas at a constant $P_i = 1.7$ MPa (250 psi) and stand-off distance of 10 mm. Indicates that at all temperatures the peak is at the approximately the same particle velocity. Suggests that gas inlet temperature has very little impact on particle velocity distribution.

The effect of modification of gas inlet pressure on the measured particle velocity distribution for PG-AMP-10 sprayed with helium gas at a constant inlet temperature, $T_i = 230$ °C and stand-off distance of 20 mm shows that as gas inlet pressure is increased from 1.2 to 1.7 MPa (175 to 250 psi) the particle velocity distribution peak shifted 500 to 610 m/sec (Figure 51). It also shows that the higher pressure curve is above and to the right for all higher velocity values. This suggests that gas inlet pressure has a significant

impact on particle velocity and increasing the gas inlet pressure increases particle velocity.

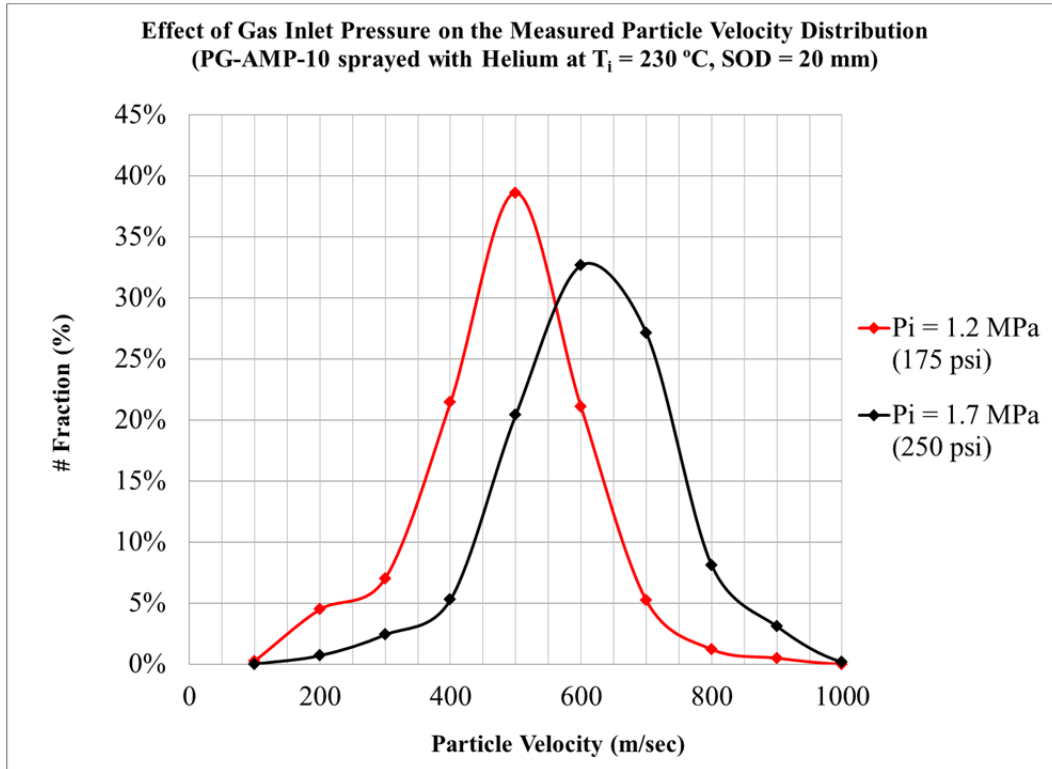


Figure 51. Effect of gas inlet pressure on the measured particle velocity distribution for PG-AMP-10 sprayed with helium gas at a constant $T_i = 230^\circ\text{C}$ and stand-off distance of 20 mm. Indicates a significant shift to higher velocities at higher pressure suggesting gas inlet pressure has a significant impact on particle velocity.

S5001 and PG-AMP-10 measurements from the nitrogen testing were utilized to show the effect of particle size and morphology on particle velocity (Figure 52). Utilized in conjunction with the characterization analysis from Chapter II, it can be seen that the PG-AMP-10 velocity distribution mirrors its particle size analysis, suggesting that the larger particles (where the hump appears in the particle size data of Figure 5) are moving at lower velocities (where the hump appears at low velocities, Figure 52), thus indicating that larger particles attain slower velocities than smaller ones. Also shown is the effect of particle morphology on velocity distribution. Again utilizing the characterization data, it is known that S5001's aspect ratio was closer to 1 (i.e. more spherically shaped). The

particle velocity distribution for the PG-AMP-10 powder is shifted toward higher velocities peaking at roughly 20 m/sec greater than S5001 suggesting that more irregularly shaped particles attain higher velocities than spherically shaped ones. The characterization data also established that the S5001 powder is significantly smaller than the PG-AMP-10 powder (with well over 50 % of the PG-AMP-10 powder being larger than the largest S5001 particles). This would suggest that the S5001 particles should be attaining higher velocities than the PG-AMP-10; however, the figure shows that PG-AMP-10 particle velocity is higher suggesting that particle morphology has more of an effect on particle velocity than particle size.

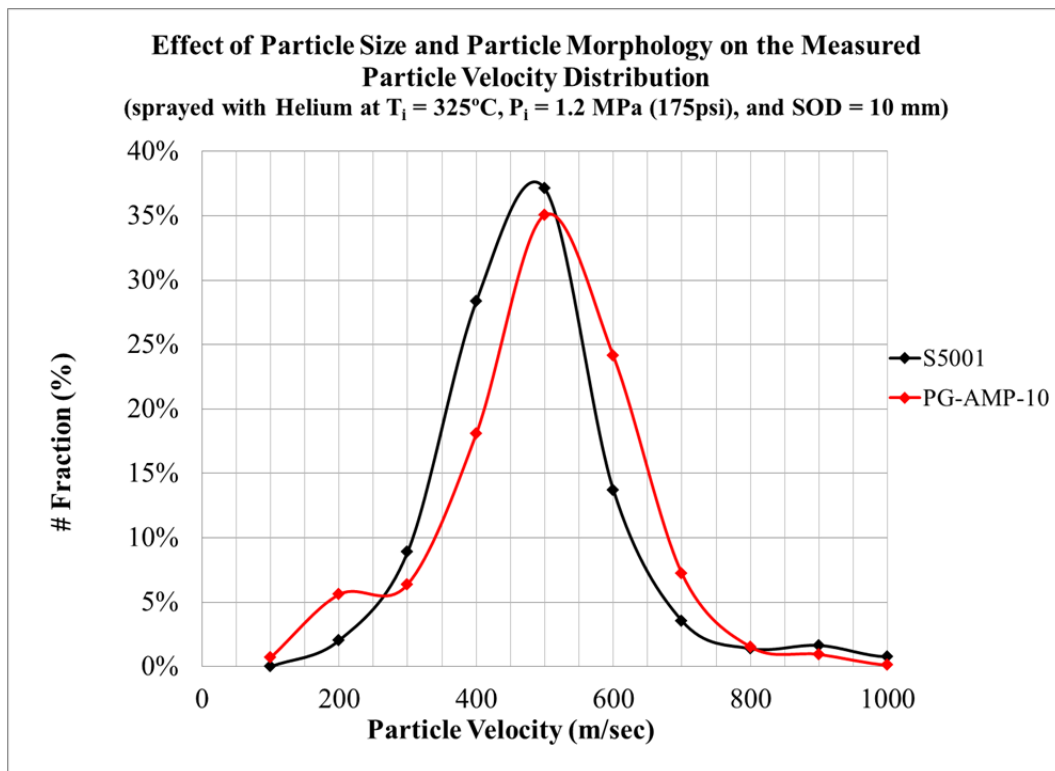


Figure 52. Effect of particle size and particle morphology on the measured particle velocity distribution. S5001 (black) and PG-AMP-10 (red) sprayed with helium at $T_i = 325^\circ\text{C}$, $P_i = 1.2 \text{ MPa}$ (175 psi), and SOD = 10 mm. Indicates, in conjunction with the characterization data for both powders that larger particles move at lower velocities and less spherical particles accelerate to higher velocities.

The measured particle velocity distributions for the $P_i = 1.7$ MPa (250 psi) conditions show that particle velocity increases as stand-off distance increases. This is likely due to the gas velocity increasing because it is still expanding to ambient pressure outside the nozzle, thus causing the particle to continue to accelerate.

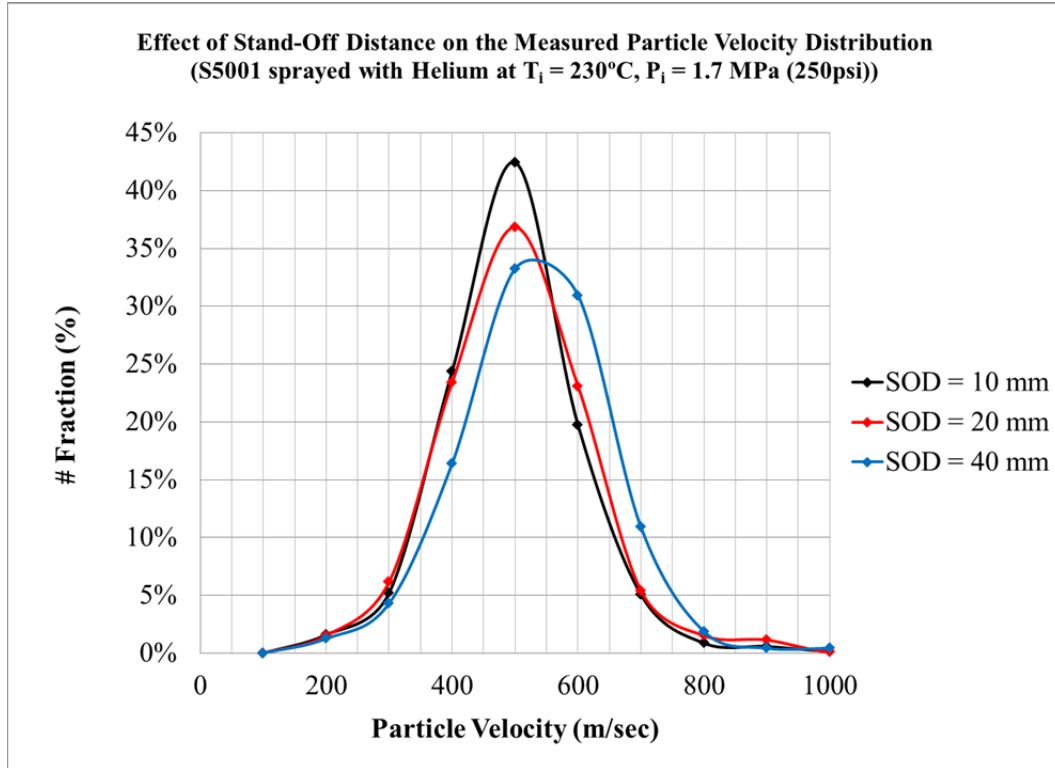


Figure 53. Effect of stand-off distance on the measured particle velocity distribution for S5001 powder sprayed with helium at $T_i = 230$ °C and $P_i = 1.7$ MPa (250 psi). Indicates that particle velocity increases from a stand-off distance of 10 mm (black) to 20 mm (red) to 40 mm (blue).

6. Determination of the Critical Velocity for S5001 and PG-AMP-10 Austenitic Stainless Steel

A full table of the average particle velocity, critical velocity, deposition efficiency, and coating thickness per pass results can be found in Appendix B for both S5001 and PG-AMP-10. Table 14 and Table 15 provide a summary of the results for S5001 and PG-AMP-10, respectively. The data shows the average particle velocity, critical velocity, and deposition efficiency for the powders sprayed with helium gas at a

constant stand-off distance of 10 mm. As expected, the average velocity at a given pressure does not tend to be affected drastically by changes in temperature at that pressure, but the critical velocity does tend to change (decrease as temperature is increased) thus leading to higher deposition.

Gas Inlet Temperature (°C)	Gas Inlet Pressure (MPa)	Average Particle Velocity (m/sec)	Critical Velocity (m/sec)	DE (%)
200	1.7	448	600	13
230	1.7	450	575	18.8
230	1.2	445	630	5.3
275	1.2	448	625	6.1
325	1.2	450	615	6.7
450	0.6	365	580	0.4

Table 14. Summary of S5001 average particle velocity, critical velocity, and deposition efficiency. Sprayed with helium gas at stand-off distance of 10 mm.

Gas Inlet Temperature (°C)	Gas Inlet Pressure (MPa)	Average Particle Velocity (m/sec)	Critical Velocity (m/sec)	DE (%)
200	1.7	510	640	33.9
230	1.7	515	630	35.1
230	1.2	445	595	21.6
275	1.2	448	590	24.8
325	1.2	450	580	26.9
450	0.6	330	550	2.3

Table 15. Summary of PG-AMP-10 average particle velocity, critical velocity, and deposition efficiency. Sprayed with helium gas at stand-off distance of 10 mm.

Figure 54 represents a qualitative approximation of the critical velocity of PG-AMP-10 utilizing the velocity distribution curves all sprayed at a stand-off distance of 10 mm with helium. It shows that a critical velocity of roughly 650 m/sec fits the observed

data quite well. The curve representing the 2.3 % deposition is almost entirely below the value, while there lies approximately 25 % of the distribution above the critical velocity for the curve representing a deposition efficiency of 24.8 % and approximately a third of the distribution lies above the critical velocity for the curve representing a deposition efficiency of 35.1 %. It should be noted that although this visual approximation of the critical velocity appears to fit the data well, the value of critical velocity that fits the data is higher than any critical velocity attained during the curve fit-integration process used.

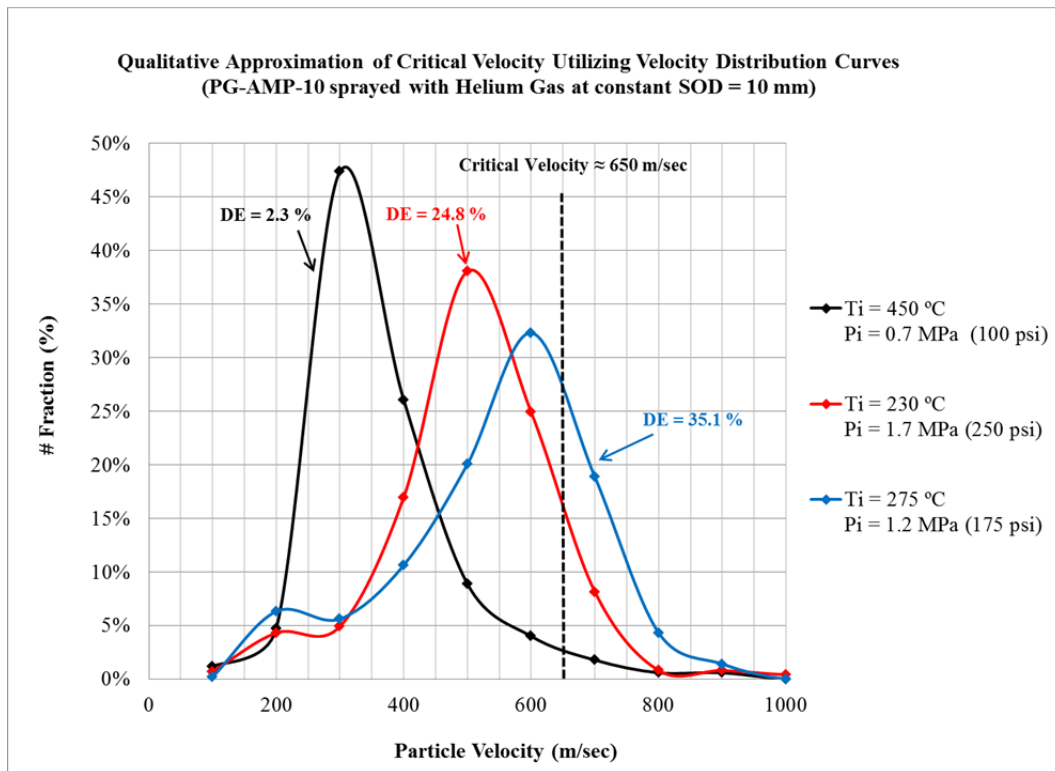


Figure 54. Qualitative approximation of critical velocity utilizing velocity distribution curves. PG-AMP-10 sprayed with helium at SOD = 10 mm. Indicates a critical velocity of approximately 650 m/sec fits the observed data well.

In general, the data suggests that as average particle velocity increases, for a given stand-off distance, the deposition efficiency increases, Figure 55 and Figure 56. We also see that the highest deposition efficiencies are attained at the 10 mm and 20 mm stand-off distances.

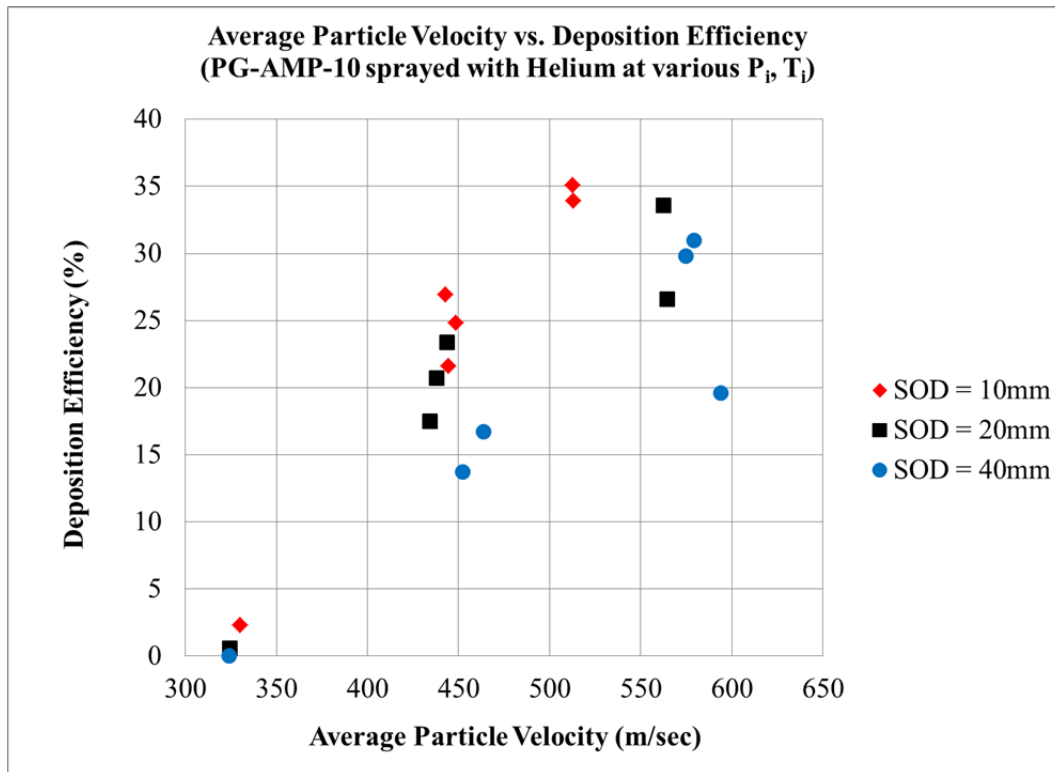


Figure 55. Average particle velocity versus deposition efficiency for PG-AMP-10 sprayed with helium at various gas inlet parameters. Suggests that for a given stand-off distance as the average particle velocity increases, the deposition efficiency increases.

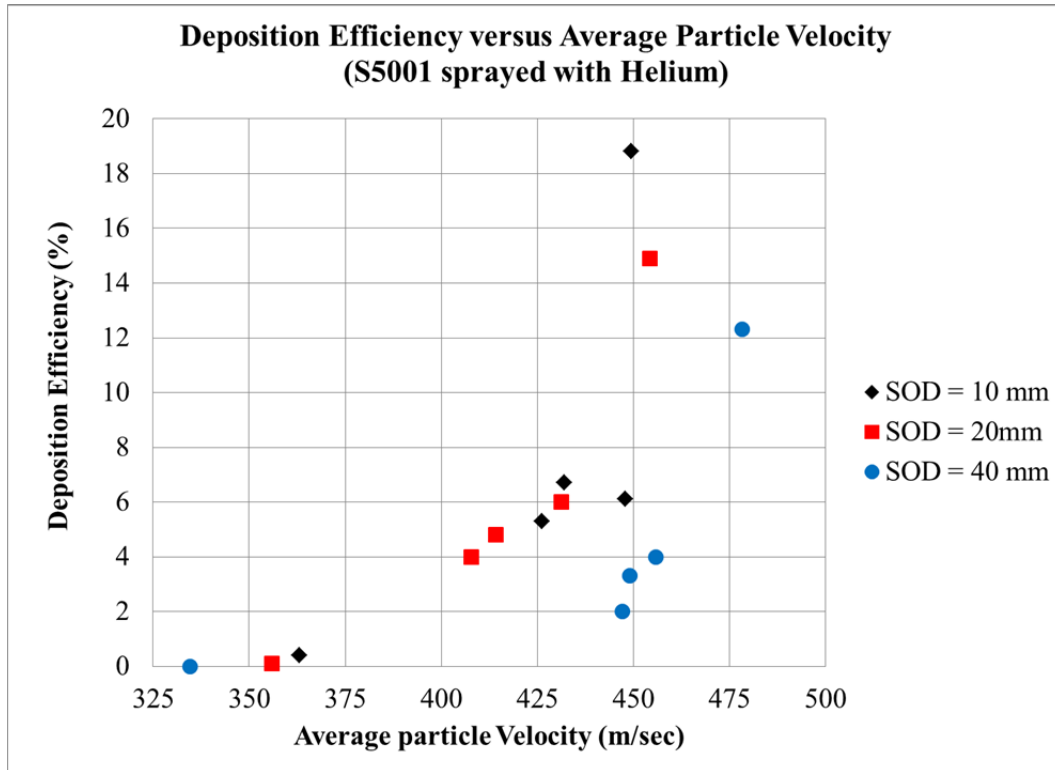


Figure 56. Average particle velocity versus deposition efficiency for S5001 sprayed with helium at various gas inlet parameters. Suggests that for a given stand-off distance as the average particle velocity increases, the deposition efficiency increases.

The critical velocity results show that in all cases, for a given pressure, and stand-off distance, as the temperature is increased, the critical velocity decreases (Figure 57). This is likely due to the softening effect that the higher gas temperature has on the particle thus making the plastic deformation easier. The results of the critical velocity data also suggest that the critical velocity varies as stand-off distance varies. This may be a result of further expansion of the gas and subsequent decrease in temperature of the gas and particle. As shown above, the average particle velocity tended to increase as stand-off distance was increased which should ultimately lead to higher deposition; however, the deposition efficiency tended to be lower, which indicates that critical velocity grew at a higher rate than average particle velocity (Figure 58).

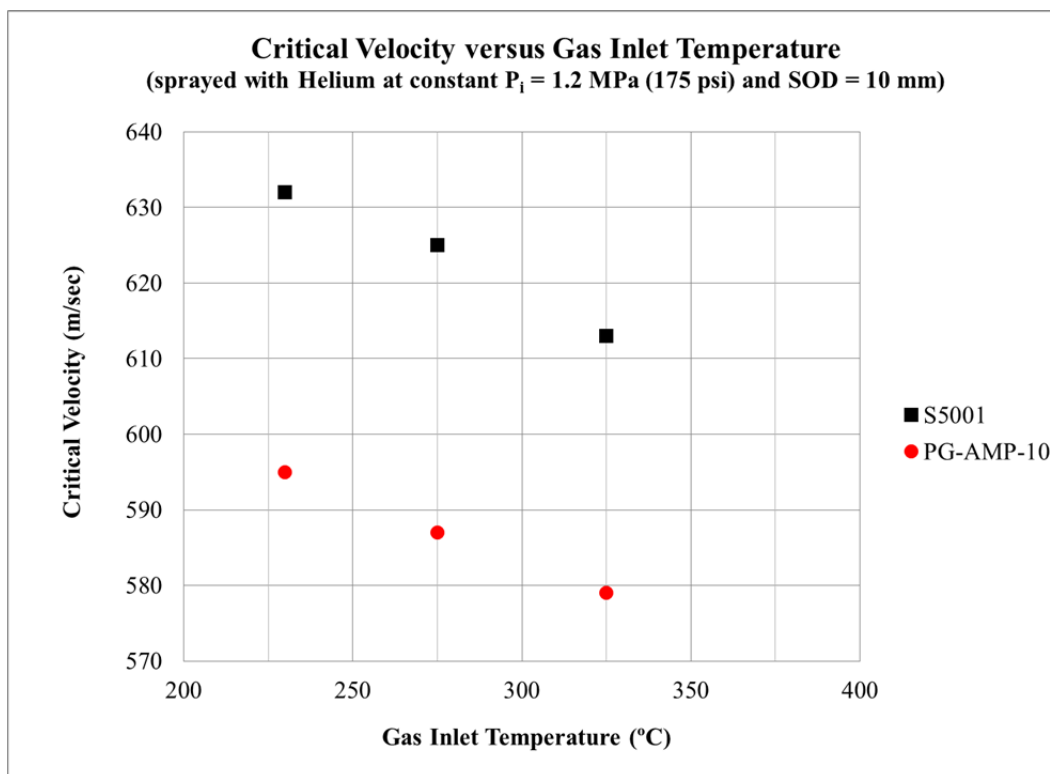


Figure 57. Critical velocity versus gas inlet temperature for S5001 (black) and PG-AMP-10 (red) sprayed with helium gas at a constant $P_i = 1.2$ MPa (175 psi) and SOD = 10 mm. Indicates that critical velocity is a function of gas inlet temperature, and powder.

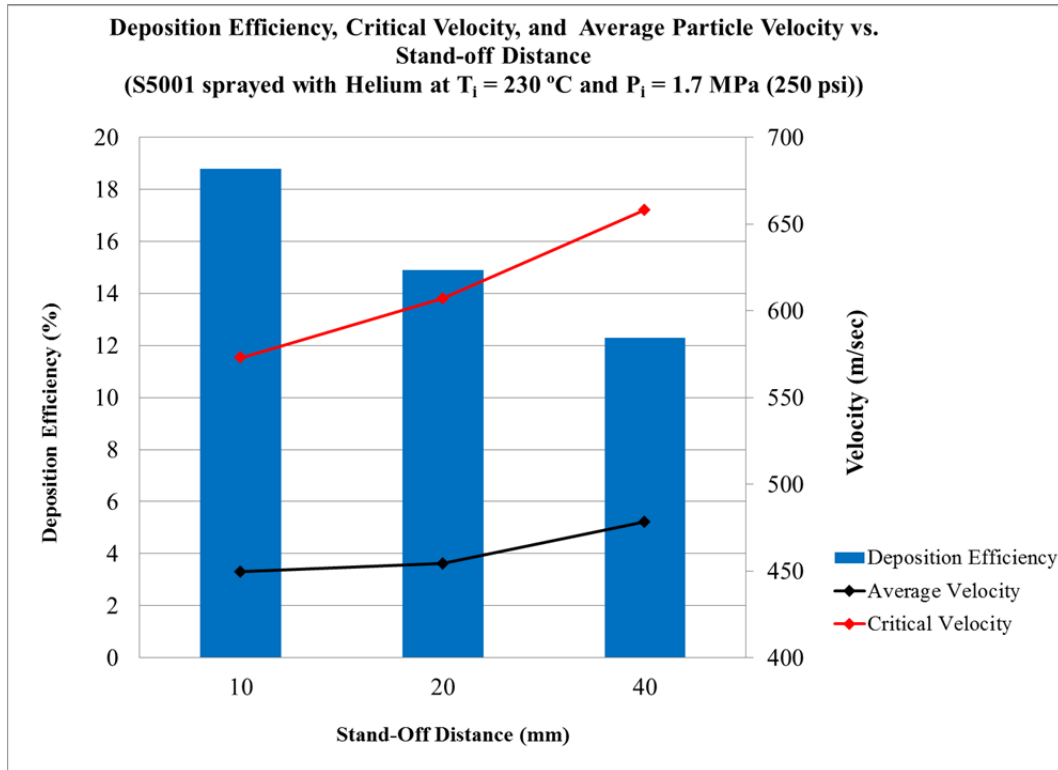


Figure 58. Deposition efficiency and average particle velocity as a function of stand-off distance for S5001 sprayed with helium at $T_i = 230\text{ }^{\circ}\text{C}$, $P_i = 1.7\text{ MPa}$ (250 psi). Suggests that average particle velocity increases as stand-off distance increases, but deposition efficiency decreases.

Utilizing all the results from the laser velocimetry and deposition efficiency experiments, it is clear that no one value for the critical velocity value for austenitic stainless steel was found based upon the powder, or the gas parameters utilized, however one can qualitatively approximate a critical velocity by overlaying the velocity distribution curves. There also appears to be certain trends that manifest themselves, such as higher temperatures, for a given pressure, tend to lower critical velocity and critical velocity tends to increase as stand-off distance is increased.

D. DISCUSSION

1. The Effect of Particle Size and Morphology on Particle Velocity and Deposition Efficiency

It is important to understand the effects of particle size and particle morphology on the particle velocity and deposition efficiency. The powder size and morphology are

controlled by the manufacturing process for the powder and can vary significantly between powders, as was shown in II.C of this thesis. The results of the simulation and laser measured velocity showed that smaller particles achieved higher particle velocities thus resulting in more particles attaining critical velocity and increasing deposition efficiency. This effect can also be seen in the study conducted by Huang et al. which showed that two stainless steel powders manufactured by MicroMelt, both spherical in shape, have different particle velocity distributions based upon their size alone [26]. For the same gas conditions, the smaller particles, 5 – 22 μm in diameter, attained higher velocities and higher deposition efficiencies than the larger particles, 16 – 45 μm in diameter.

The results of the simulation and laser measured velocities also show that particle morphology is of critical importance in particle velocity as well. Less spherical particles attain higher velocities than more spherical ones due to a larger accelerating gas drag coefficient. Again Huang et al. also showed this trend with their experimentation comparing the spherical MicroMelt (16 – 45 μm particles) with a multi-angular Praxair FE-101 powder with the same particle size range. They reported that not only did the Praxair powder attain higher velocities than the equivalent size spherical powder, but also higher than the smaller, 5 – 22 μm diameter, spherical powder. In all cases the deposition efficiency increased as a function of particle velocity. In 2007, Ning et al. also found similar results with both spherical and non-spherical copper powder, suggesting that the multi-angular particles attained velocities 20-50 m/sec higher than the spherical powders for the same particle size [58].

2. Critical Velocity Determination in the Low-Pressure Cold Spray Deposition Process

The critical velocity of a material utilized in the low-pressure cold spray deposition process is a theoretical value that if surpassed by a particle will result in the deposition of that particle. One of the objectives of this work was to determine if a critical velocity exists for austenitic stainless steel and if it does, is it the same for both powders studied. Clearly the results indicate that a range of critical velocities exists depending on a number of different factors, starting first with the powder being utilized

and then the conditions of spray (gas inlet temperature, pressure, and average particle velocity).

Schmidt et al. found that critical velocity tends to decrease with increases in particle size and developed a simple formula for estimating the critical velocity of a material based upon its diameter [59]. They attribute this effect to increased heat conduction or strain hardening.

We saw that critical velocity varied with temperature, actually lowering as temperature was increased. It was also seen that critical velocity increased with increases in average particle velocity, and deposition efficiency decreased with increased average particle velocity. Both of these results seem counterintuitive, as the faster the particles are moving the more that should be deposited. One possible explanation is that the gas dynamics of further expansion (at the higher stand-off distances) caused the temperature of both the gas and the particle to lower even more causing the critical velocity to increase for the same reasons that a higher temperature causes it to be lower. Schmidt et al. found that increasing particle temperature tends to lower the critical velocity and increase the deposition efficiency in the cold spray process [59]. Assadi et al. propose that critical impact velocity can ultimately be expressed as a function of the powder particle properties (i.e., specific heat, density, yield stress, and size) and the particle temperature [59, 60].

3. The Effect of Powder Feed Rate and Substrate Interaction on Achieving Statistically Significant and Consistent Particle Velocity Measurements

Utilizing the results from the feed rate experiment, it can reasonably be assumed that powder feed rate (over the range utilized in this experiment) has no effect on the measurement statistical consistency and accuracy. This in-turn means that less powder can be utilized during velocity experiments (in which the powder is lost for deposition use) and also means that velocity can be measured over the full range of feed rates utilized for deposition. This finding is important as not all powders have the same feeding characteristics and therefore some have to be fed at 10 % while others need to be fed at 80 % to achieve significant depositions.

This result is consistent with Gilmore et al.'s previous research conducted with copper particles [20]. Their experimentation showed that as powder feed rate increases, the average particle velocity actually decreases (indicating particle interaction slowing the particles down). However, over the range of powder feed rates utilized in this study (0.1 – 0.5 g/sec) the mean particle velocity remained at a constant value just as well (Figure 59). More experimentation would need to be conducted with other powders, which feed differently and would thus change the g/sec feed rate, in this unit to determine if the relationship holds true for all the powders utilized in research at the Naval Postgraduate School.

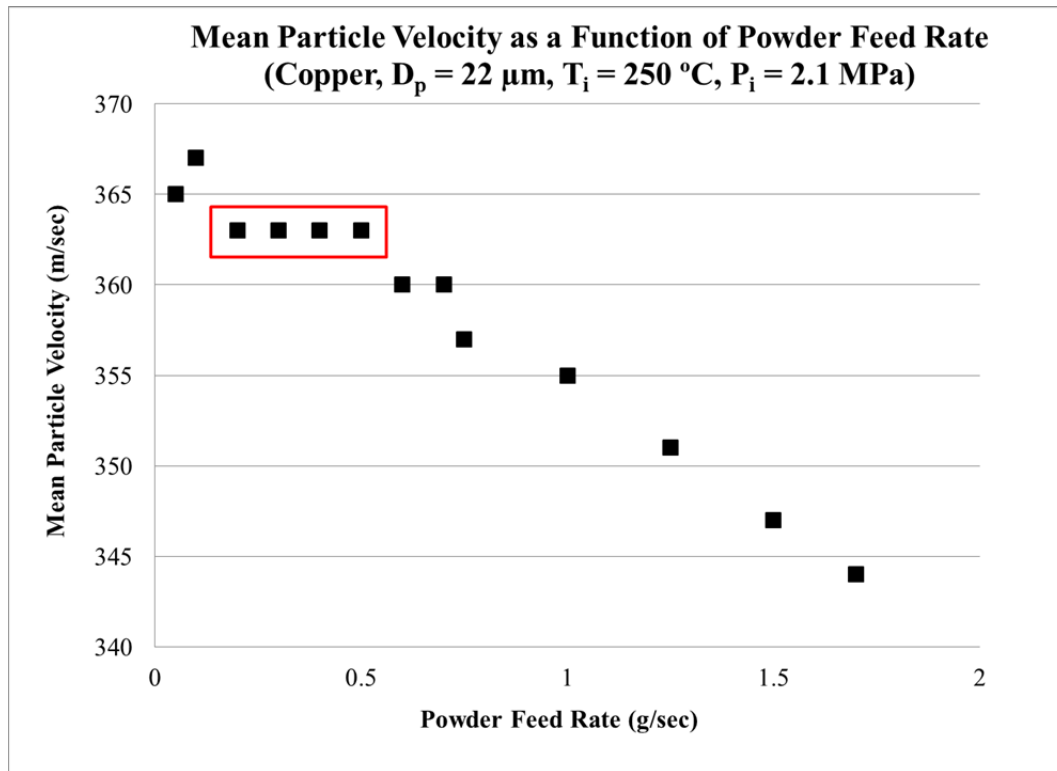


Figure 59. Effect of powder feed rate on mean particle velocity, after [20]. Red boxed area indicates the range over which S5001 experimentation was conducted.

The results of the substrate interaction experiment show that the presence of a substrate has a significant impact on the noise of the measurement thus lowering the number of good particle measurements per unit time, but did not have a significant

impact on the actual velocity measurement, for these parameters used. This result is also consistent with the findings by Gilmore et al. in their research on the velocity of copper powders in the cold spray process [20]. Because shock waves induced by the bow shock phenomenon or stagnation of the gas occur so closely to the substrate there is little time to significantly affect the velocity of the particles traveling through it prior to impacting the substrate. This also suggests that because the gas is expanded to nearly atmospheric at the point of substrate interaction, that the shock would be too weak to affect the momentum of the solid particles as they pass through it. This indicates that measuring the particle velocity without the presence of a substrate is suitable for finding the impact velocity of the particles during deposition.

4. The Effect of Working Gas Type, Pressure, and Temperature on Particle Velocity and Deposition Efficiency

Choosing a gas type is the first critical choice when attempting to increase particle velocity and attain higher deposition. Both the results and simulation show that using helium results in substantially higher particle velocities. This result has been seen in two previous research studies conducted by Dykhuizen and Smith, and Gilmore et al. [20, 49]. They first modeled the gas dynamics of both helium and nitrogen to determine the optimal nozzle design, then used the models and particle velocimetry to conclude that air has a greater effect on the particle velocity because of its higher density, but because helium is moving at such a higher rate the drag on the particle is significantly higher and overcomes the density effect.

In addition to control over the type of gas used in research and industry, the other adjustable parameters are the gas inlet temperature and pressure. The next logical parameter to change is the gas inlet pressure as changes in gas pressure tend to effect particle velocity more than changes in gas temperature. Initially, this result seems counterintuitive because changing the gas pressure had no effect on the gas velocity and if gas velocity remains constant then particle velocity should be unchanged as well, but because particle acceleration is driven by gas density, a gas pressure increase causes a gas density increase, therefore causing the entrainment gas drag force on the particle to increase, resulting in a higher velocity. Huang et al. found similar results in their work

with stainless steel powders showing their peak shifts from just greater than 600 m/sec to almost 800 m/sec for their high pressure – high temperature system [26]. Also similar to these findings, Gilmore et al.'s experimentation with copper powder showed the same trend for both the predicted and measured particle velocities [20]. The gas inlet pressure showed to have a much greater impact on the particle velocity than the gas inlet temperature.

The final parameter that can be modified is gas inlet temperature. The results of the simulation and experiment suggest that it has minimal effect on particle velocity, but it does increase deposition efficiency and therefore should be maximized as well. Gilmore et al. showed similar results while spraying copper particles with air and helium. Figure 60 indicates that over the range 230 °C to 325 °C, the predicted and measured particle velocities increase very little (for helium, approximately 740 m/sec to 760 m/sec) [20]. Huang et al. also reported particle velocity increasing as gas inlet temperature was increased in their study of the effect of particle velocity on stainless steel [26].

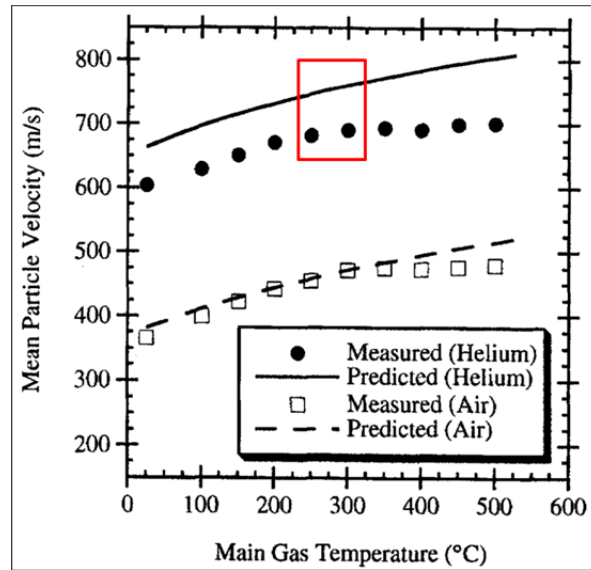


Figure 60. Mean particle velocity versus temperature plot for spray of 22 μm copper powder at constant inlet pressures, $P_i = 2.0 \text{ MPa}$ (300 psi) with helium or air as the driving gas, after [20]. Red boxed area represents range of austenitic stainless steel research conducted in this research showing minor increase in particle velocity due to temperature increase.

THIS PAGE INTENTIONALLY LEFT BLANK.

IV. LOW-PRESSURE COLD SPRAY DEPOSITION OF AUSTENITIC STAINLESS STEEL

This chapter will explore the low-pressure cold spray deposition of commercial austenitic stainless steel powders. In particular, we will examine the effects of the low-pressure cold gas dynamic process on their deposition characteristics and coating properties, such as hardness and porosity. A number of different spray gas conditions modifying the entrainment gas type, pressure, and temperature will be investigated to identify the suitable range of conditions for successful deposition. Section A contains an introduction and literature review of previous austenitic stainless steel experiments accomplished, while Section B delineates the experimental setup for these experiments. During the experiment, deposition efficiency and coating thickness per pass were measured as a function of spray gas type, pressure and temperature for each feedstock powder used. The experimental results are discussed in Section C, while Section D contains the discussion of these results.

A. INTRODUCTION

While this study aims to demonstrate the feasibility of austenitic stainless steel deposition at relatively low temperatures and low pressures, it is important to note that a number of studies have already shown that deposition of austenitic stainless steel in the cold spray deposition process is achievable, albeit at high-temperature-high pressure combinations or with the similar process of kinetic metallization [5, 11, 28, 29]. AL-Mangour et al. successfully demonstrated the deposition of 316L on mild steel with nitrogen at $P_i = 4$ MPa and $T_i = 700$ °C, with deposition efficiency ranging from 9 to 77 % and coating thickness ranging from 0.47 to 3.4 mm [5]. Han et al. deposited 304SS on interstitial free steel with air at $P_i = 3$ MPa and $T_i = 550$ °C [11], while Borchers et al. utilized nitrogen at $P_i = 2.5$ MPa and $T_i = 500$ °C and helium at $P_i = 3$ MPa and $T_i = 400$ °C to deposit 316L [29]. Villa et al. also deposited 316L stainless steel on aluminum alloy 7075 utilizing nitrogen at a range of inlet pressure and temperature conditions, $P_i = 2 - 4$ MPa and $T_i = 600 - 800$ °C, reporting deposition efficiencies in the range of approximately 20 – 90 %. All of these inlet conditions, however, are unobtainable using

the Centerline (Windsor) SST Model Series C deposition systems utilized in this experimentation. Because our aim is to one day utilize low pressure cold spray process as a field repair option, it is critical to understand its entire operating spectrum and determine the necessary conditions for achieving high quality deposits with a low pressure-low temperature portable cold spray unit as it is much more portable than a high pressure-high temperature system. Figure 61 depicts the range of previous stainless research as compared to the current work. The current work in this thesis was accomplished at much lower pressure and temperature combinations.

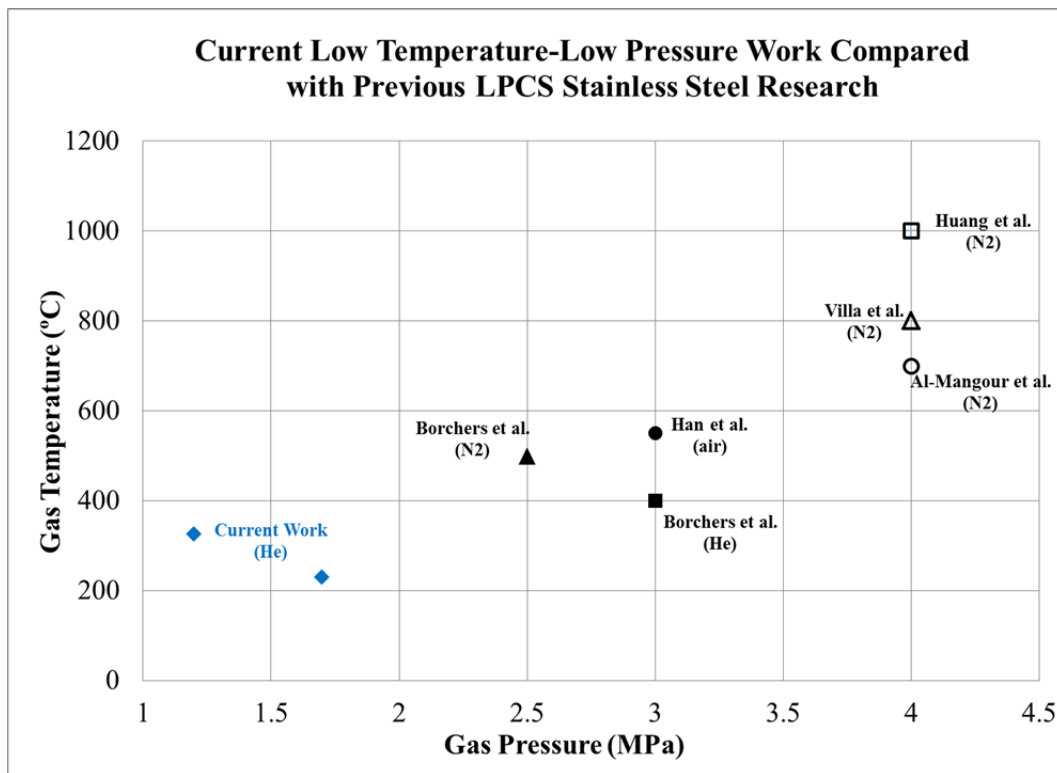


Figure 61. Current low temperature-low pressure stainless steel cold spray research compared against previous low pressure cold spray research. Current work (blue) is at much lower pressure and temperature.

Previous studies have also examined the porosity and mechanical properties of cold spray coatings. Meng et al. studied the influence of gas temperature on 304SS coatings depositing coatings utilizing nitrogen as gas inlet temperature ranging from 450 to 550 °C and inlet gas pressure of 3.0 MPa. Their findings suggest that an increase in

gas temperature tends to reduce porosity and increase particle-substrate bond cohesive strength, but has little effect on the microhardness of the coating [25]. Contrary to this result, Huang et al. found that increasing gas temperature also increases microhardness of the coating. They also found that increasing gas pressure tended to increase hardness of the coating, attributing these findings to the decrease in porosity of the coatings. They attribute the decrease in porosity to the increase in particle velocity, not to the increase in gas pressure [26]. Elongation to fracture, tensile strength, fatigue behavior, and wear resistance of stainless steel coatings has also been investigated [5, 12, 23, 28]. AL-Mangour et al. found the coatings to be extremely brittle, exhibiting no necking prior to fracture during tensile testing [5]. Similar to this, Meng et al. also found that the original coating had an unmeasurable elongation to fracture and an extremely low ultimate tensile strength of approximately 100 MPa, and suggested that a post-processing annealing treatment could help improve those properties [12]. AL-Mangour et al. also studied the fatigue behavior of the coatings and found that given the same fatigue loading (6000 N at 5×10^{-3} cycles/second) the coating experienced failure at one-tenth the number of cycles of the bulk material (600,000 versus 6,000,000), and attributed this reduction in fatigue strength to the high density of porosity and oxide inclusions which initiated cracks [23]. Villa et al. studied the abrasive wear rate of the coatings and found that that the wear resistance was 300 % greater than the aluminum substrate, suggesting that cold spray deposited, stainless steel coatings can be utilized as a wear resistant coating [28].

With all that said, all of those previous stainless steel cold spray investigations have been accomplished utilizing high-temperature, high-pressure conditions, leaving the question of what is the effect on the coating microstructure and properties of utilizing a low-pressure, low-temperature system that would ultimately deposit the austenitic stainless steel powders at lower velocities than previously studied.

B. EXPERIMENTAL METHODS

Using the powders described in II.C, low-pressure cold spray deposition was performed varying type, inlet temperature, and inlet pressure of the entraining gas. All four powders were utilized to complete a matrix of working gas conditions utilizing the

automatic spray robot parameters found in Table 17. The coatings were deposited onto previously grit-blasted, grey cast iron substrates at a stand-off distance of 16 mm. Deposition efficiency and coating thickness per pass were measured and calculated as described in II.B.

Gas Type	Gas Inlet Temperature (°C)	Gas Inlet Pressure (MPa)
Nitrogen	450	1.7
	600	0.7
	600	1.2
Helium	230	0.7
	230	1.2
	230	1.7
	325	0.7
	325	1.7
	450	0.7
	600	0.7

Table 16. Matrix of entrainment gas conditions utilized for complete comparison of cold spray deposition effect on austenitic stainless steel.

Spray Parameters	Setpoint
Gun Type	automatic
Gun Stand-off Distance (mm)	16
Gun Traverse Speed (mm/s)	40
Gun Step Over per Pass (mm)	1.2
Spray Time per Pass (sec)	22.4
# of Passes	2

Table 17. Automatic robot parameters utilized on the Centerline (Windsor) SST Model Series C.

The S5001 and PG-AMP-10 coatings produced in the III.B velocimetry experiments were also utilized in this chapter to complete a thorough examination of the effects of gas temperature, pressure, and stand-off distance modifications on the resultant coating porosity, hardness, coating-substrate interface bonding, and interparticle bonding.

Metallography preparation was conducted in much the same manner as chapter II.B with the exception of the final vibratory polishing stage with colloidal silica. Optical microscopy was conducted for each sample utilizing a Nikon OPTIPHOT 200 Series microscope and digital camera. Images were taken at 25x, 100x, and 500x magnification to detail the microstructure of the deposited coatings.

The hardness of the feedstock powder particles was measured utilizing an Agilent Technologies Inc. G200 Series nano-indenter, with a Berkovitch diamond indenter tip. 10 to 20 powder sample hardness points were obtained from each powder in an attempt to measure the powder particle hardness with high statistical confidence. The parameters utilized for the analysis are summarized in Table 18. As these particles were embedded in an epoxy matrix, the overall system compliance was relatively large and had to be corrected for each data point. Following the approach of Buchheit and Vogler, the compliance of each sample measurement points was corrected by utilizing the available plot of stiffness squared over load (Figure 62) [61]. The plotted line was adjusted to as horizontal as possible by adjusting the frame stiffness and harmonic stiffness correction factors. The hardness data was then taken from the average of the measurement over the 100 to 200 nm depth into the surface of the powder.

Nano-Indentation Parameter	Value
Indenter Tip	Diamond, Berkovich
Poisson's Ratio	0.30
Depth Limit (nm)	500
Measurement Depth (nm)	100-200
Allowable Thermal Drift Rate (nm/s)	0.05
Surface Approach Distance (nm)	1000
Surface Approach Velocity (nm/s)	10
Strain Rate (1/s)	0.05

Table 18. Parameters utilized for nano-indentation measurements of feedstock powder hardness.

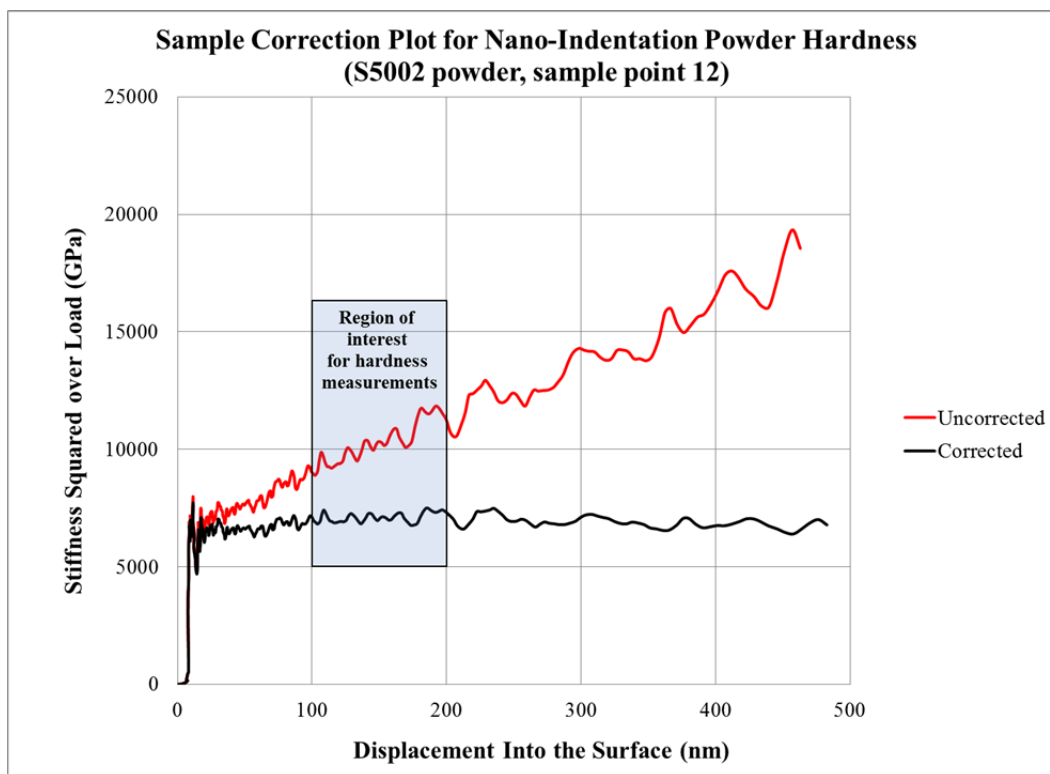


Figure 62. Sample plot of correction accomplished on nano-indentation powder hardness. Shows the uncorrected (red) and corrected (black), with the corrected being flat. The area of interest for the hardness measurement averaging was 100 – 200 nm into the surface of the powder.

Measurement of Vicker's microhardness of the coatings was accomplished utilizing a HVS-1000 Digital Micro Hardness Tester. A 1.96 N force was applied for a hold time of 15 seconds. Each coating was sampled a minimum of 10 times and from that data an average and standard deviation was determined.

C. RESULTS

1. Deposition Efficiency and Coating Thickness per Pass

a. Nitrogen Testing

Of the four austenitic stainless steel powders sprayed, only two, KM316 and PG-AMP-10, were deposited with a thick enough coating to gather both deposition efficiency and coating thickness per pass results (Table 19). The S5001 showed minor coating thickness at two conditions but no measurable deposition efficiency (within the precision

of the digital scale), and S5002 successfully deposited with a deposition efficiency result, but no measurable coating thickness.

Of the three gas inlet conditions utilized, the inlet condition of $P_i = 1.7$ MPa (250 psi) and $T_i = 450$ °C achieved the highest deposition efficiencies for both KM316 and PG-AMP-10 at 12.5 % and 4.1 %, respectively. The KM316 powder was also successfully deposited at the $T_i = 600$ °C, $P_i = 1.2$ MPa (175 psi) achieving a deposition efficiency of 6.3 %. The PG-AMP-10 powder achieved the highest coating thickness per pass of 0.26 mm.

Test No.	1	2	3	4	5	6
Powder Material	S5001	S5001	S5001	S5002	S5002	S5002
Gas (N2 or He)	N2	N2	N2	N2	N2	N2
Substrate Material	Grey Cast Iron	Grey Cast Iron	Grey Cast Iron	Grey Cast Iron	Grey Cast Iron	Grey Cast Iron
Gas Temperature (°C)	450	600	600	450	600	600
Gas Pressure (MPa)	1.7	0.7	1.2	1.7	0.7	1.2
Powder Feed Rate (g/min)	60.4	60.4	60.4	54.8	54.8	54.8
Deposition Efficiency (%)	unm	unm	unm	unm	unm	0.2
Coating Thickness per Pass (mm)	0.03	unm	0.02	unm	unm	unm
Test No.	7	8	9	10	11	12
Powder Material	KM316	KM316	KM316	PG-AMP-10	PG-AMP-10	PG-AMP-10
Gas (N2 or He)	N2	N2	N2	N2	N2	N2
Substrate Material	Grey Cast Iron	Grey Cast Iron	Grey Cast Iron	Grey Cast Iron	Grey Cast Iron	Grey Cast Iron
Gas Temperature (°C)	450	600	600	450	600	600
Gas Pressure (MPa)	1.7	0.7	1.2	1.7	0.7	1.2
Powder Feed Rate (g/min)	2.4	2.4	2.4	19.6	19.6	19.6
Deposition Efficiency (%)	12.5	unm	6.3	4.1	unm	unm
Coating Thickness per Pass (mm)	0.06	unm	0.04	0.26	unm	unm

Table 19. Summary of nitrogen cold spray deposition results.

Indicates that S5001 and S5002 did not successfully deposit and achieve both a measurable deposition efficiency and coating thickness. Shows that KM316 deposited the best in terms of deposition efficiency but PG-AMP-10 deposited the best in terms of coating thickness per pass. (highlights: yellow = gas parameters, green = measureable depositions, red = unmeasurable depositions)

b. Helium Testing

Full summary tables of the results of deposition efficiency and coating thickness per pass for all four powders can be found in Appendix C.

All of the stainless steel powders were successfully deposited utilizing the low pressure cold spray deposition process with helium as the entrainment gas, but not all of the entrainment gas inlet conditions deposited measurable deposits. For instance, S5001, KM316, and PG-AMP-10 did not have measurable deposits for the inlet gas conditions of $T_i = 230\text{ }^{\circ}\text{C}$ and $P_i = 0.7\text{ MPa}$ (100 psi). The gas inlet conditions of $T_i = 230\text{ }^{\circ}\text{C}$ and $P_i = 1.7\text{ MPa}$ (250 psi) proved to be the best overall condition producing the highest deposition efficiency and coating thickness per pass for all the powders (Table 20). In fact all of the powders achieved greater than 10 % deposition efficiency utilizing this condition. The second best condition for deposition was gas inlet conditions of $T_i = 325\text{ }^{\circ}\text{C}$ and $P_i = 1.2\text{ MPa}$ (175 psi), Table 22. It should be noted that for a given pressure, there is a maximum temperature achievable with the Centerline model and current nozzle design. Due to the limitations of the heater, there is always a limit to the pressure, and therefore limit the mass flow-rate, of gas that can be used due to the cooling effect the gas has on the nozzle as it attempts to maintain temperature. The worst inlet gas condition found, for helium, was $T_i = 230\text{ }^{\circ}\text{C}$ and $P_i = 0.7\text{ MPa}$ (100 psi), Table 21. This condition resulted in an unmeasurable amount of deposition in all but one powder, S5002.

Test No.	1	2	3	4
Powder Material	S5001	S5002	KM316	PG-AMP-10
Gas (N2 or He)	He	He	He	He
Substrate Material	Grey Cast Iron	Grey Cast Iron	Grey Cast Iron	Grey Cast Iron
Gas Temperature (°C)	230	230	230	230
Gas Pressure (MPa)	1.7	1.7	1.7	1.7
Powder Feed Rate (g/min)	60.4	54.8	2.4	19.6
Deposition Efficiency (%)	11.8	12.3	41.8	29.4
Coating Thickness per Pass (mm)	0.67	0.71	0.15	0.93

Table 20. Summary of deposition efficiency and coating thickness per pass results for all four powders at $T_i = 230$ °C, $P_i = 1.7$ MPa (250 psi), and SOD = 16 mm. This condition provided the best overall deposition efficiency and coating thickness per pass. All powders achieved greater than 10 % deposition efficiency. (highlight indicates the measured DE and coating thickness measurements)

Test No.	1	2	3	4
Powder Material	S5001	S5002	KM316	PG-AMP-10
Gas (N2 or He)	He	He	He	He
Substrate Material	Grey Cast Iron	Grey Cast Iron	Grey Cast Iron	Grey Cast Iron
Gas Temperature (°C)	230	230	230	230
Gas Pressure (MPa)	0.7	0.7	0.7	0.7
Powder Feed Rate (g/min)	60.4	54.8	2.4	19.6
Deposition Efficiency (%)	unm	0.13	unm	unm
Coating Thickness per Pass (mm)	unm	0.01	unm	unm

Table 21. Summary of deposition efficiency and coating thickness per pass results for all four powders at $T_i = 230$ °C, $P_i = 0.7$ MPa (100 psi), and SOD = 16 mm. This condition provided the least overall deposition efficiency and coating thickness per pass. All powders, with the exception of S5002, did not achieve measurable deposition. (highlight indicates the measured DE and coating thickness measurements)

Test No.	1	2	3	4
Powder Material	S5001	S5002	KM316	PG-AMP-10
Gas (N2 or He)	He	He	He	He
Substrate Material	Grey Cast Iron	Grey Cast Iron	Grey Cast Iron	Grey Cast Iron
Gas Temperature (°C)	325	325	325	325
Gas Pressure (MPa)	1.2	1.2	1.2	1.2
Powder Feed Rate (g/min)	60.4	54.8	2.4	19.6
Deposition Efficiency (%)	4.8	2.6	38.3	23.9
Coating Thickness per Pass (mm)	0.5	0.57	0.15	0.76

Table 22. Summary of deposition efficiency and coating thickness per pass results for all four powders at $T_i = 325$ °C, $P_i = 1.2$ MPa (175 psi), and SOD = 16 mm. This condition provided the second best overall deposition efficiency and coating thickness per pass. All powders achieved greater than 2 % deposition efficiency. KM316 and PG-AMP-10 both achieved greater than 20 % deposition efficiency. (highlight indicates the measured DE and coating thickness measurements)

Figure 64 shows the effects of gas inlet pressure on the deposition efficiency of all four austenitic stainless steel powders. As can be seen none of the powders achieved a measurable deposition at the lowest pressure condition of 0.7 MPa. All of the powders, with the exception of S5002, then achieved an increasing amount of deposition for each subsequent increase in gas inlet pressure. S5002 did initially deposit well with the first pass, but the second pass removed almost the entire first pass, leaving only a couple flakes for the 1.2 MPa inlet gas condition (Figure 63). This test was repeated numerous times to verify the result. KM316 deposited with the highest overall deposition efficiency of 41.8 %, albeit at an extremely low coating thickness per pass of 0.15 mm, Figure 65. In all cases KM316 achieved the highest deposition efficiency; however the PG-AMP-10 powder deposited with high efficiency and coating thickness per pass, achieving coating thicknesses per pass, on average, 6 times larger than the KM316 powder (Figure 65).



Figure 63. Photograph of S5002 sprayed with helium at $T_i = 230\text{ }^{\circ}\text{C}$, $P_i = 1.2\text{ MPa}$, and $\text{SOD} = 16\text{ mm}$. The spray pattern is 25 mm by 40 mm. This photograph shows that the second pass completely removed the first with the exception of a few flakes of metal that remained.

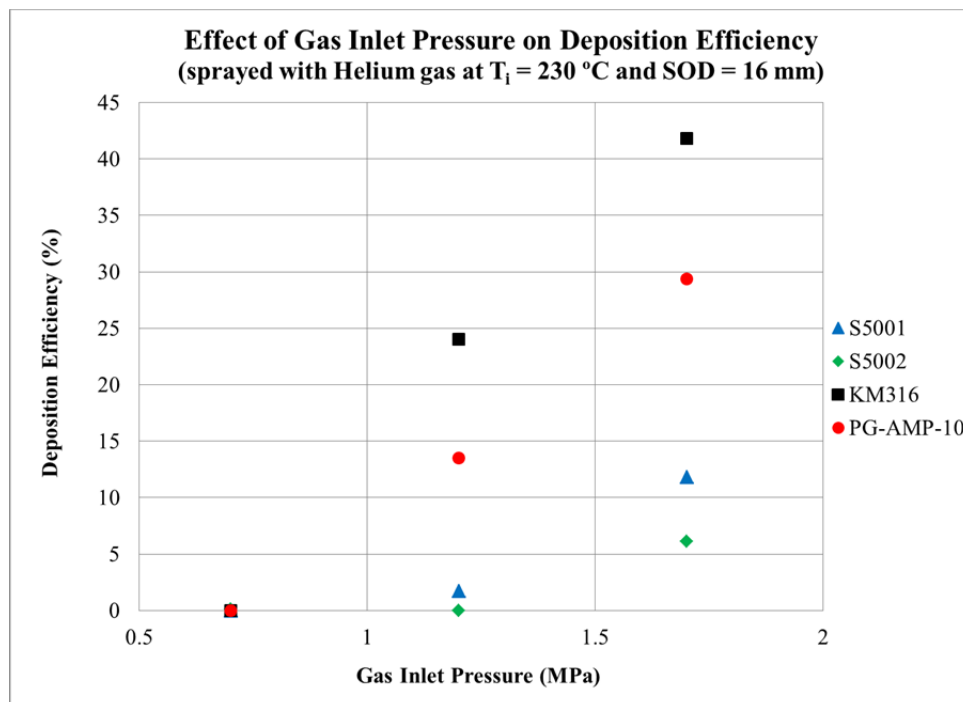


Figure 64. Effect of gas inlet pressure on deposition efficiency. Indicates all four powders deposition were immeasurable at the 0.7 MPa condition and increased in deposition efficiency as gas inlet pressure was increased from 0.7 MPa to 1.7 MPa. (with the exception of S5002 at 1.2 MPa).

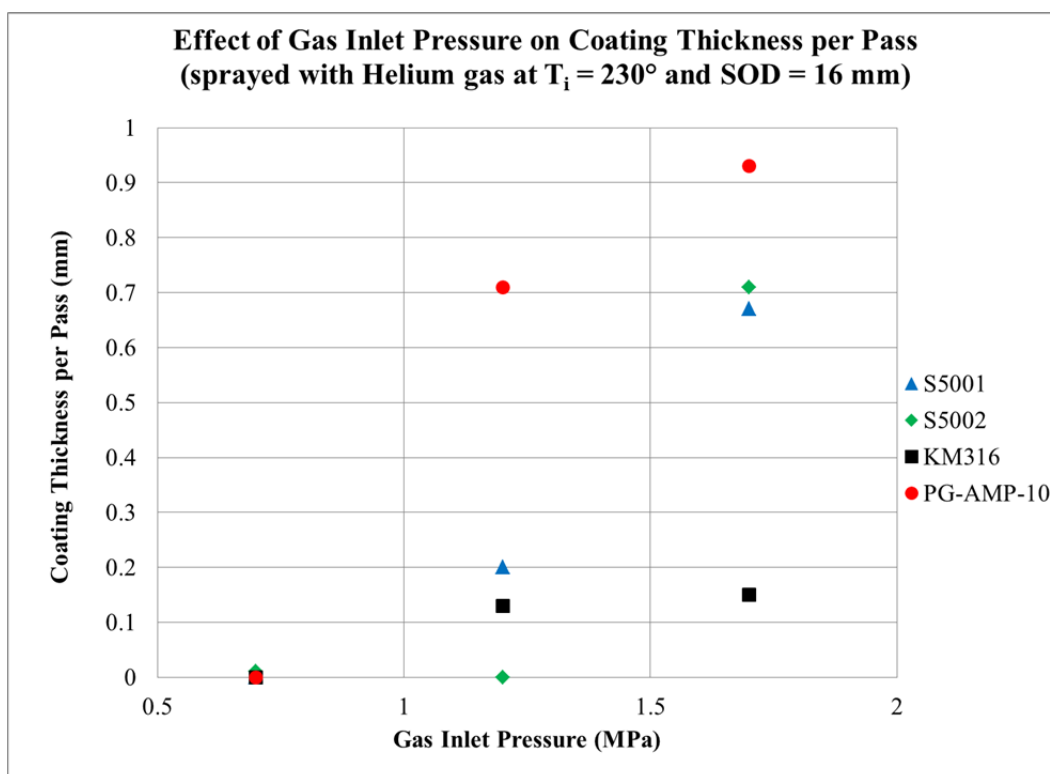


Figure 65. Effect of gas inlet pressure on coating thickness per pass. Indicates all four powders coating thickness was immeasurable at the 0.7 MPa condition and increased in thickness as gas inlet pressure was increased from 0.7 MPa to 1.7 MPa. (with the exception of S5002 at 1.2 MPa).

As gas inlet temperature was increased from 230 °C to 600 °C for a fixed gas inlet pressure of 0.7 MPa, the deposition efficiency increased for all four powders (Figure 66) KM316 showed the most increase achieving almost 10 % deposition efficiency at the highest temperature condition while both S5001 and S5002 achieved the lowest, approaching 0.5 % deposition efficiency. The coating thickness per pass for all four powders followed the same trend (Figure 67). It should be noted that at this low inlet pressure condition none of the powders achieved a coating thickness per pass of 1 mm, but the PG-AMP-10 powder still achieved the highest, at least double every other powders' coating thickness per pass.

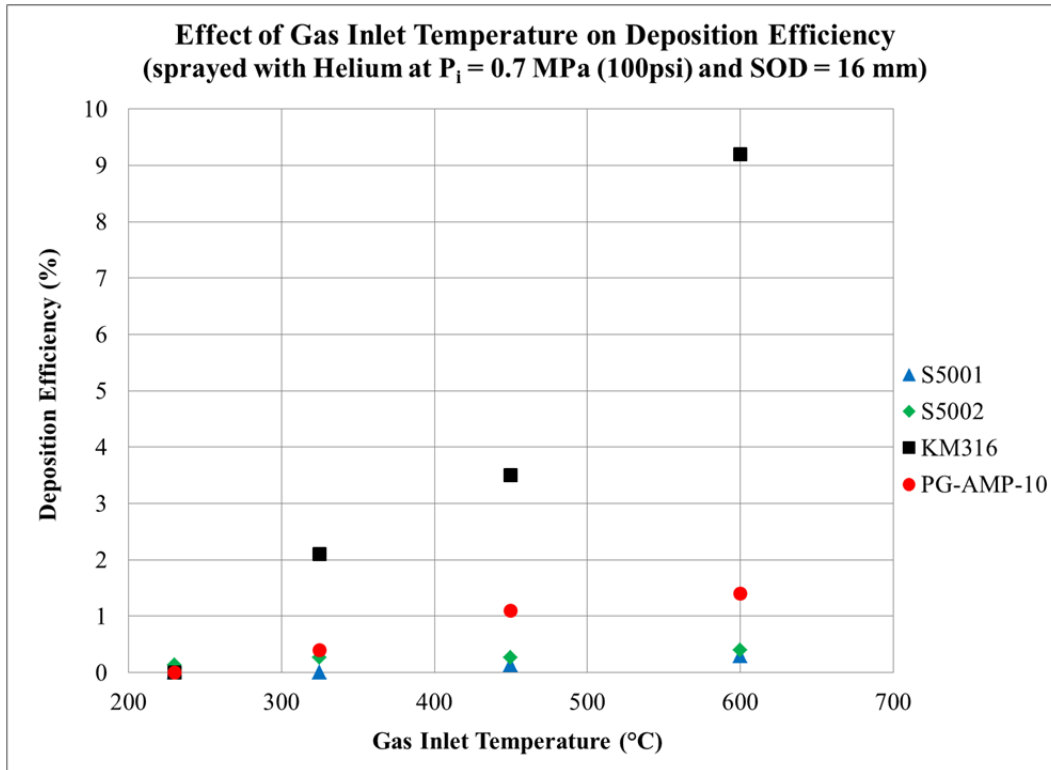


Figure 66. Effect of gas inlet temperature on deposition efficiency. Indicates an increase in deposition efficiency as gas inlet temperature is increased for all powders. Low inlet pressure was utilized to have enough comparison points and therefore deposition efficiency is low.

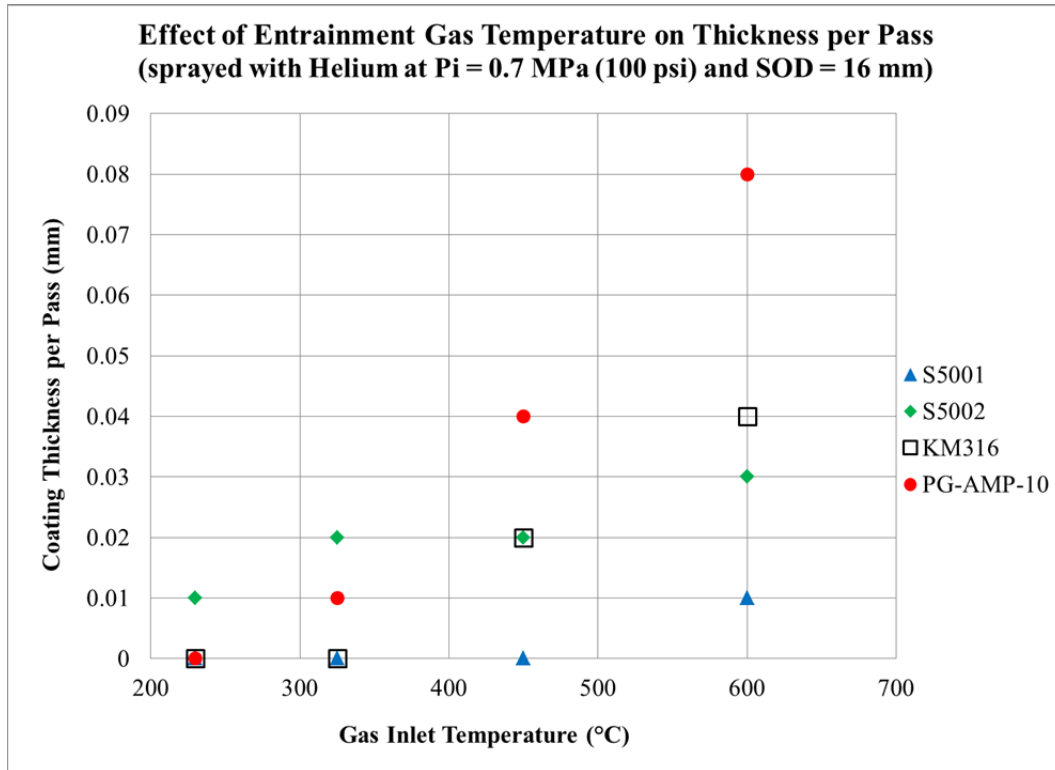


Figure 67. Effect of gas inlet temperature on coating thickness per pass. Indicates all four powders coating thickness increased as gas inlet temperature was increased from 230 – 600 °C. Shows PG-AMP-10 powder achieved the largest coating thickness at 0.08 mm, doubling or more all the other powders.

2. Coating Microstructure

A low magnification view of the cross-sections of all four commercial powders sprayed at the same condition (helium at $T_i = 230$ °C, $P_i = 1.7$ MPa (250psi)) revealed qualitatively higher porosity levels in the KM316 and PG-AMP-10 coatings versus the S5001 and S5002 powders (Figure 68). The S5001 coating (Figure 68-A) appears to have developed a brittle crack throughout its entire thickness. The S5001 and PG-AMP-10 coatings appear to have the thickest coatings, while the S5002 and KM316 have the smallest thickness. It should be noted that the KM316 coating was sprayed with twice as many passes as the other three in order to obtain a thick enough coating for optical microscopy and hardness measurements.

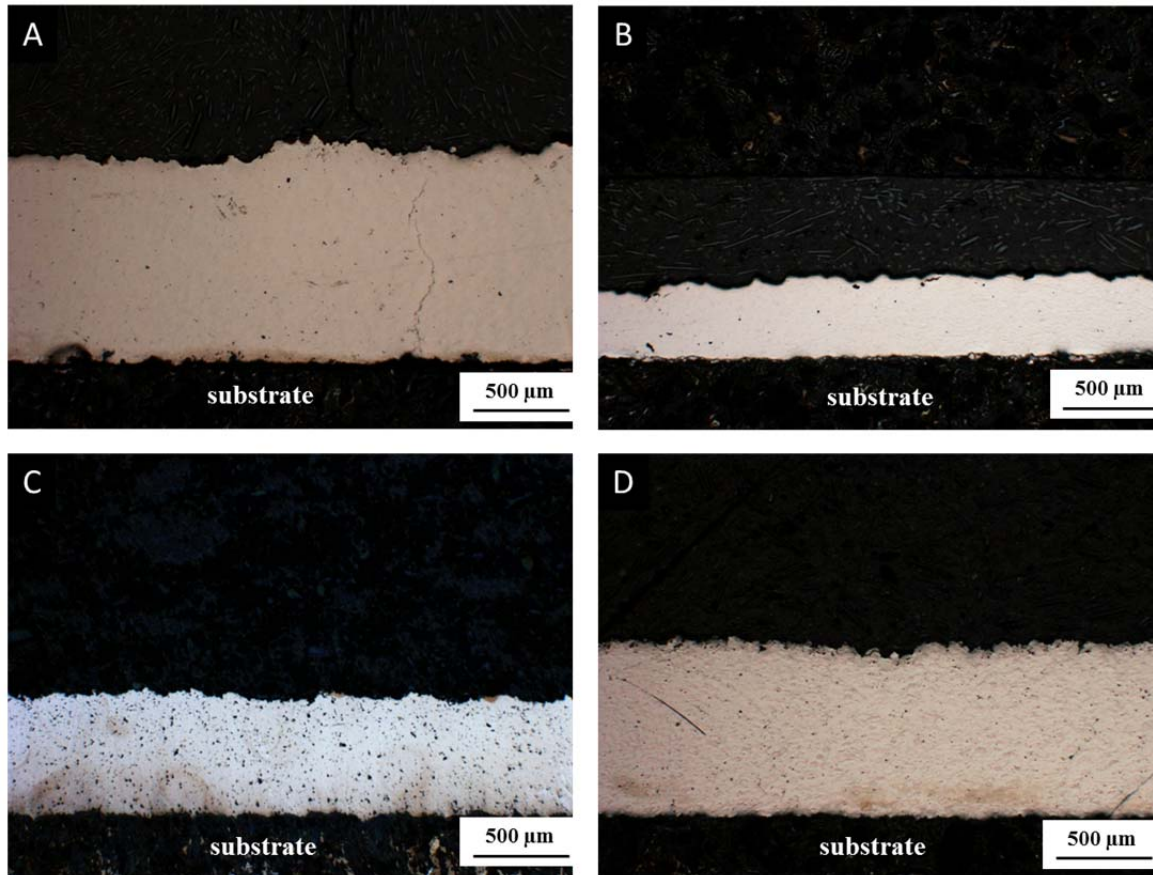


Figure 68. Low magnification optical microscopy images of coating cross-sections of all four powders sprayed with helium at $T_i = 230\text{ }^{\circ}\text{C}$, $P_i = 250\text{ psi}$ and $\text{SOD} = 16\text{ mm}$. Qualitatively more porosity in the KM316 and PG-AMP-10 coatings. Crack through the thickness of the S5001. A.) S5001, B.) S5002, C.) KM316, D.) PG-AMP-10.

The difference in porosity of the coatings is clearly evident at higher magnification levels, as the S5001 and S5002 appear to have very limited porosity at the particle-particle boundaries, while the KM316 and PG-AMP-10 show signs of significant porosity in the optical micrographs (Figure 69). Likely due to its structure of small and large particles sintered together, the PG-AMP-10 coating had large amounts of porosity at the particle-particle boundaries. Also clearly visible in the S5002 and PG-AMP-10 was a mixture of phases (ferrite and austenite) denoted by the different shades of the particles (darker and lighter). At the particle-substrate boundary, S5001 and PG-AMP-10 both show substantial amounts of cracking (Figure 70). This cracking was not visible in

the S5002 or KM316. There also appears to be a larger amount of porosity in the particle-substrate boundary in the S5001 and S5002 than the other two coatings.

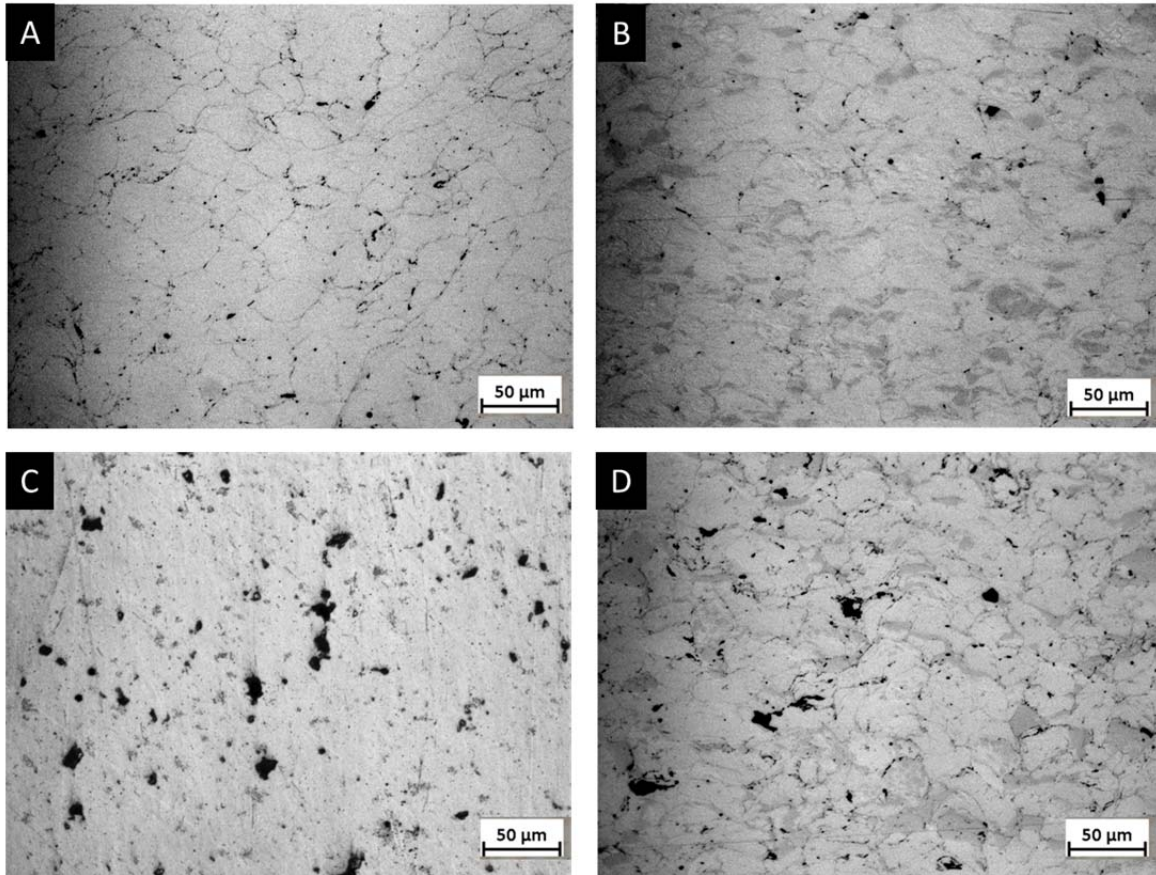


Figure 69. High magnification (200x) cross-section optical microscopy images of all four powders' coatings sprayed with helium at $T_i = 230\text{ }^{\circ}\text{C}$, $P_i = 250\text{ psi}$ and $\text{SOD} = 16\text{ mm}$. S5001 and S5002 have limited porosity. Different phases are observable in S5002 and PG-AMP-10. PG-AMP-10 has large amounts of porosity at the particle-particle boundary. A.) S5001, B.) S5002, C.) KM316, D.) PG-AMP-10.

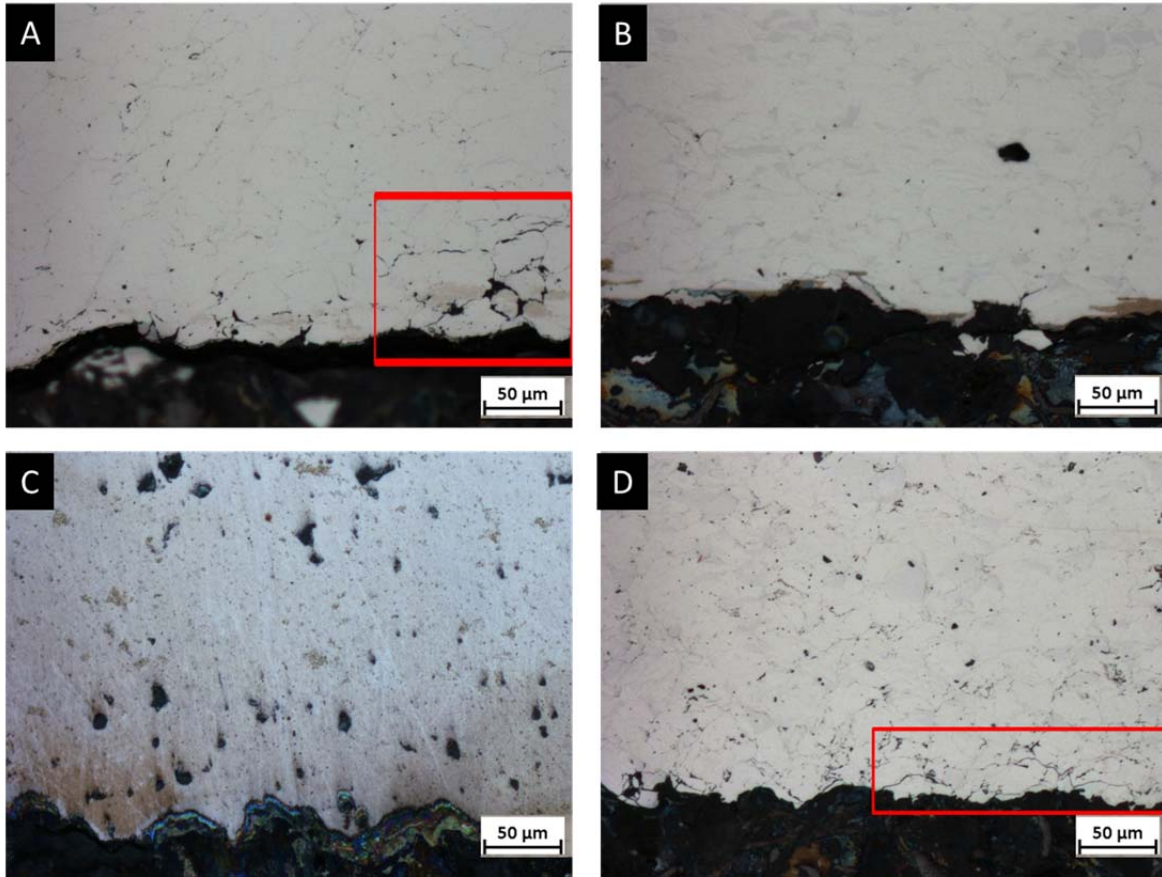


Figure 70. High magnification (200x) optical microscopy images of particle-substrate boundary for all four commercial powders sprayed with helium at $T_i = 230\text{ }^{\circ}\text{C}$, $P_i = 250\text{ psi}$ and $\text{SOD} = 16\text{ mm}$ onto grey cast iron. Cracking observable in S5001 and PG-AMP-10 near the particle-substrate boundary (boxed in red) that is not prevalent in the main coating microstructure. A.) S5001, B.) S5002, C.) KM316, D.) PG-AMP-10

The PG-AMP-10 coatings were further investigated to study the effects of stand-off distance. The low magnification images (Figure 71) show qualitatively the same amount of porosity at all stand-off distances, suggesting that stand-off distance had no effect on the coating porosity, even though previous velocimetry suggested that average particle velocity increased as stand-off distance increased. Interestingly, the particle-substrate boundary bond quality appears to have increased at the further stand-off distance (Figure 71-C). The amount of porosity at the boundary appears to have reduced significantly, but further testing would need to be accomplished to ensure the result is

repeatable. This same effect can be seen in the higher magnification optical micrographs of the particle-substrate boundary, Figure 72.

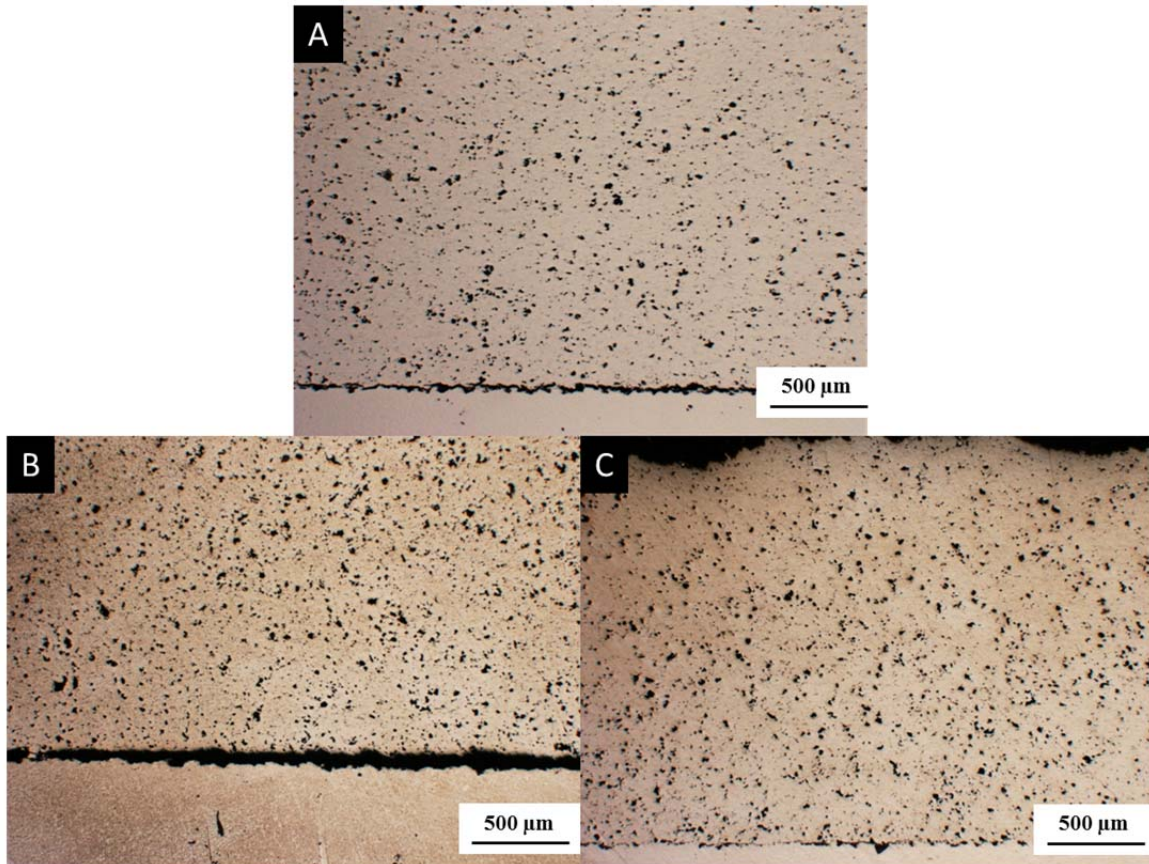


Figure 71. PG-AMP-10 low magnification optical microscopy images of the coating and particle-substrate boundary at varying stand-off distances, sprayed with helium at $T_i = 230\text{ }^{\circ}\text{C}$, $P_i = 250\text{ psi}$. Suggests that stand-off distance has no significant effect on coating porosity, but does have an effect on particle-substrate boundary porosity and bond. As stand-off distance increased from 10 mm to 40 mm the boundary porosity reduced significantly. A.) SOD = 10 mm, B.) SOD = 20 mm, C.) SOD = 40 mm.

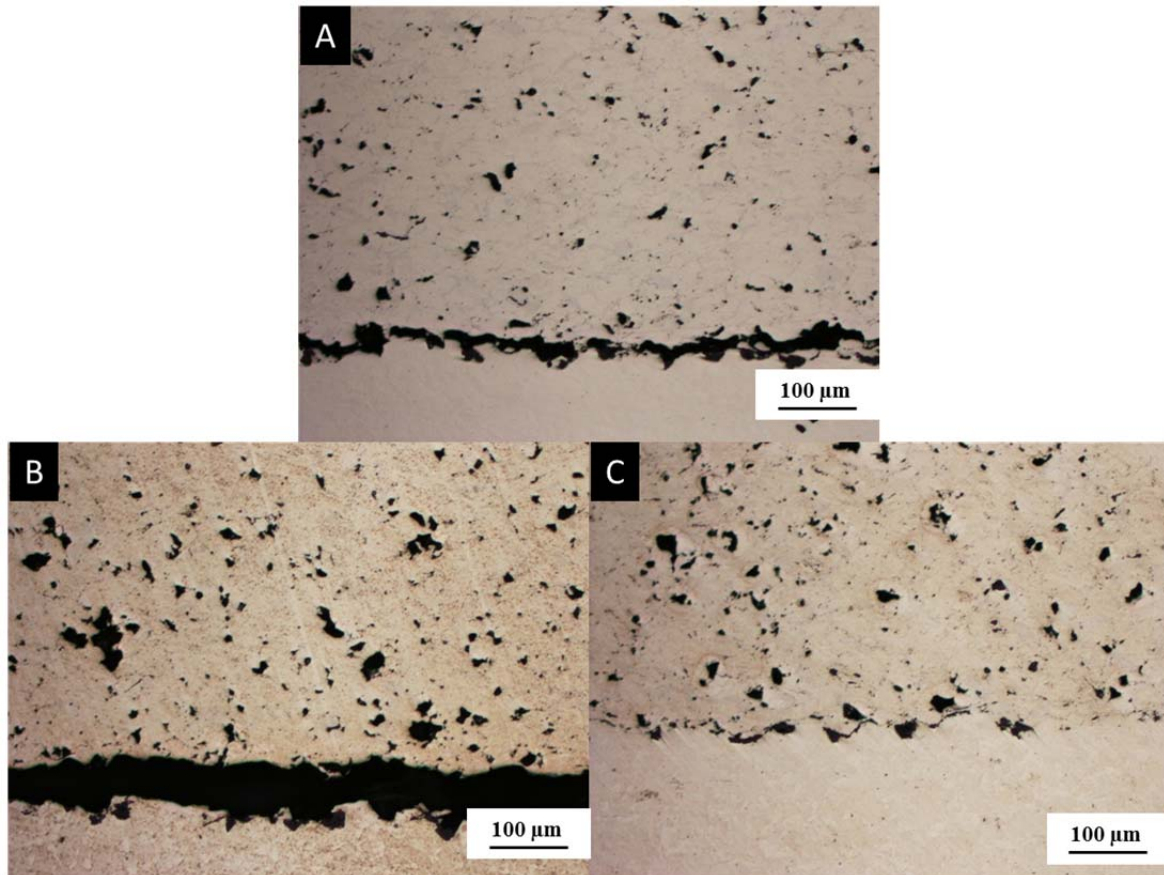


Figure 72. PG-AMP-10 high magnification optical microscopy images of the particle-substrate boundary at varying stand-off distances, sprayed with helium at $T_i = 230\text{ }^{\circ}\text{C}$, $P_i = 250\text{ psi}$. Suggests that stand-off distance does have an effect on particle-substrate boundary porosity and bond. As stand-off distance increased from 10 mm to 40 mm the boundary porosity reduced significantly. A.) SOD = 10 mm, B.) SOD = 20 mm, C.) SOD = 40 mm.

As gas inlet temperature was increased for the PG-AMP-10 coating, the amount of porosity in the coating was reduced (Figure 73). Sprayed with helium at a constant $P_i = 1.2\text{ MPa}$, as the gas inlet temperature was varied from $275\text{ }^{\circ}\text{C}$ (Figure 73-A) to $325\text{ }^{\circ}\text{C}$ (Figure 73-B), there was a significant reduction in the porosity of the coating especially in the second pass of the $325\text{ }^{\circ}\text{C}$ condition. This is likely due to the higher temperature of the gas annealing the surface. It also appears that the particle-substrate boundary porosity was reduced. A higher magnification view of the particle-substrate boundary can be seen in Figure 74. This figure shows the transition from $235\text{ }^{\circ}\text{C}$ (Figure 74-A) to $275\text{ }^{\circ}\text{C}$

(Figure 74-B) and finally 325 °C (Figure 74-C). In each case, the qualitative amount of porosity at the particle-substrate boundary was reduced (boxed in red) and the bond seems to have increased. This suggests that gas inlet temperature is a key factor in improving coating quality from a porosity stand-point and improving the quality of particle-substrate bond.

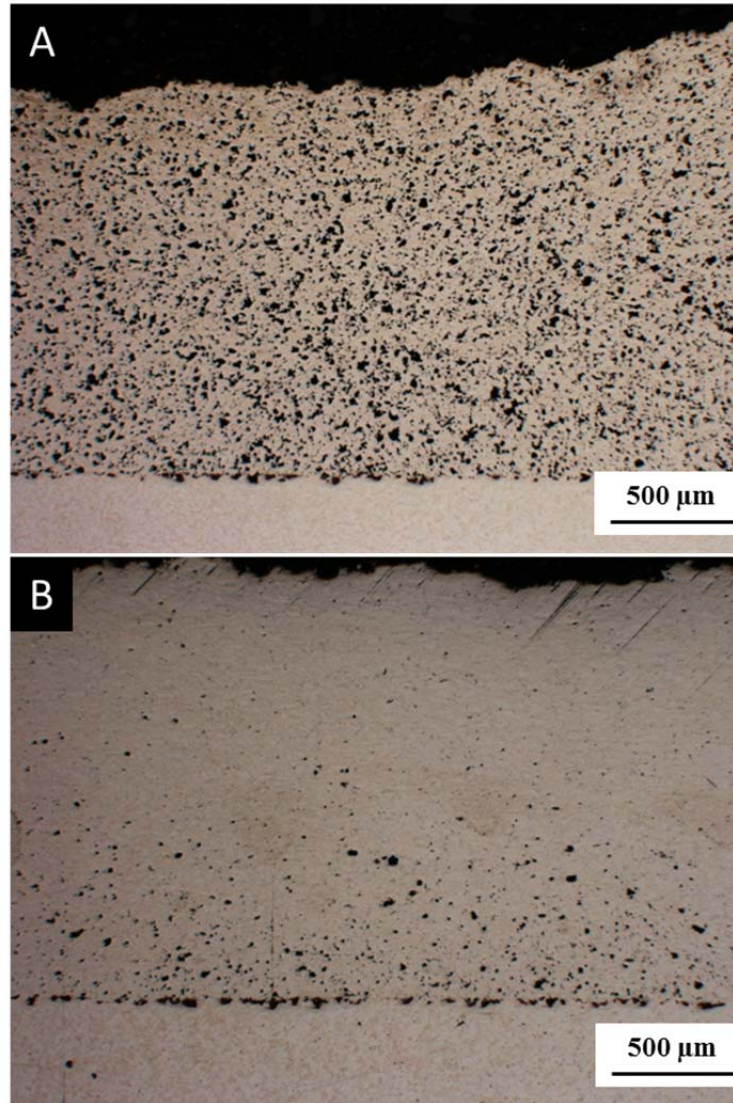


Figure 73. Gas inlet temperature effect on PG-AMP-10 coating microstructure indicating that as temperature is increased the coating porosity is reduced and the particle-substrate boundary porosity is reduced. Also shows that the second pass at higher temperature is less porous than the first. Sprayed with helium at $P_i = 1.2$ MPa (175 psi) and SOD = 10 mm. A.) $T_i = 275$ °C, B.) $T_i = 325$ °C.

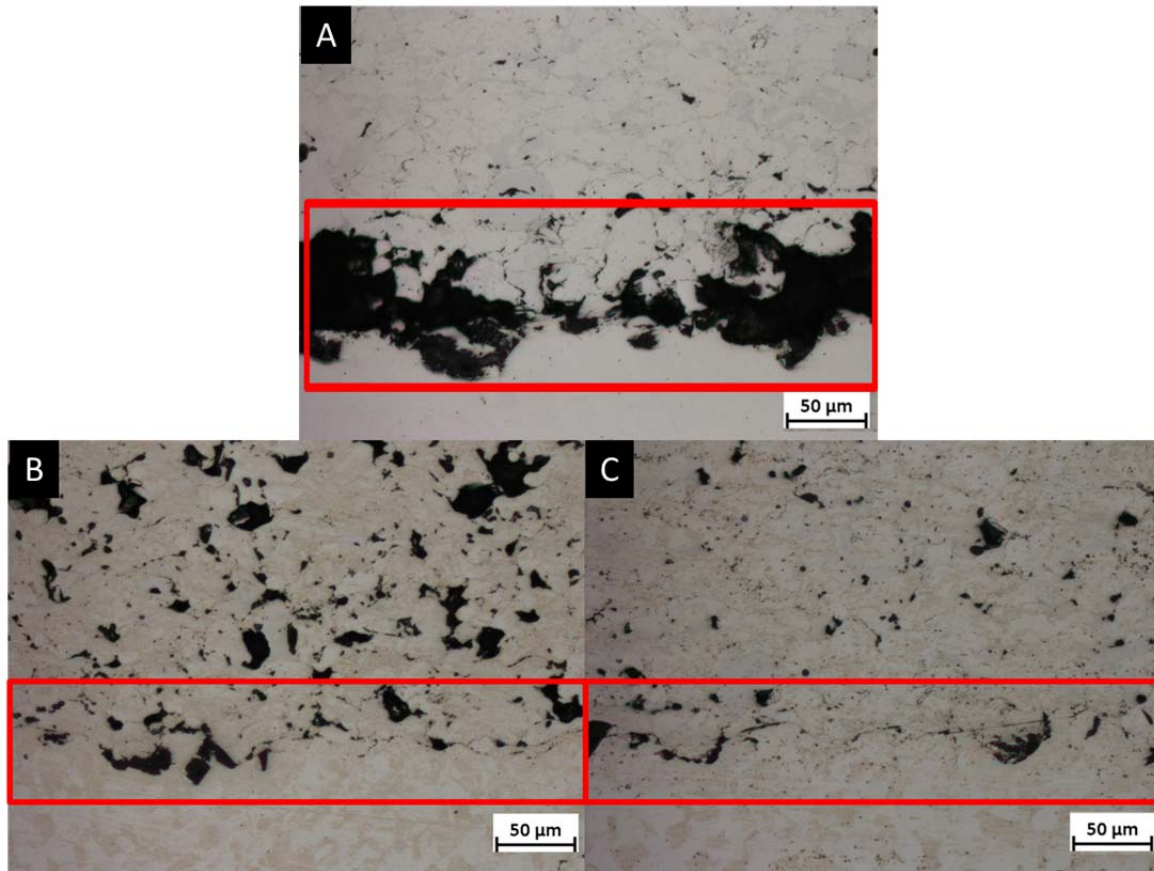


Figure 74. Gas inlet temperature effect on particle-substrate boundary porosity and bond. Indicates that as gas inlet temperature is increased the boundary porosity decreases and bond quality increases. PG-AMP-10 sprayed with helium at constant $P_i = 1.2$ MPa (175 psi) and SOD = 10 mm. A.) $T_i = 230$ °C, B.) $T_i = 275$ °C, C.) $T_i = 325$ °C. (red boxed area is the particle-substrate interface)

As gas inlet pressure was increased from 1.2 MPa (175 psi) to 1.7 MPa (250 psi) with a constant inlet temperature of 230 °C, the coating porosity remained approximately the same, but the particle-substrate interface porosity and bond quality may have increased, but not substantially, for the PG-AMP-10, Figure 75.

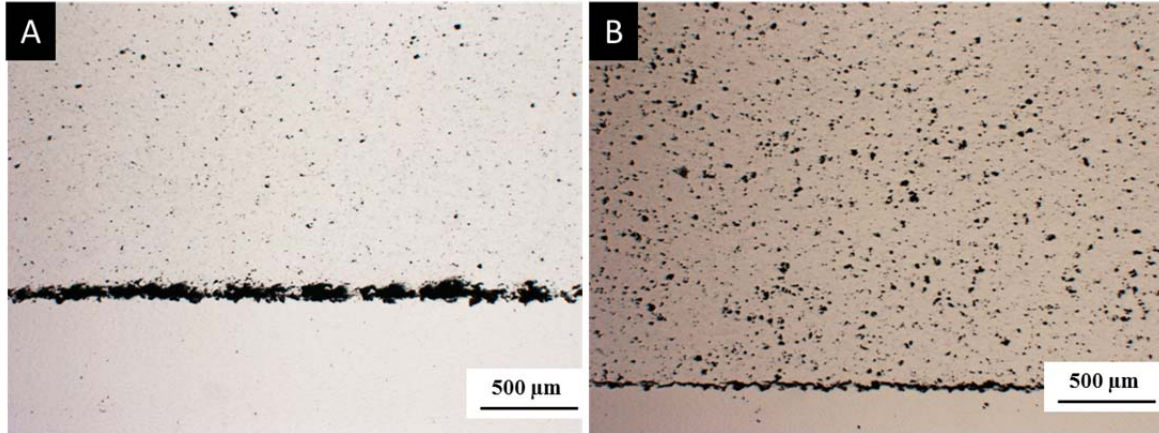


Figure 75. PG-AMP-10 optical microscopy images, sprayed with helium at $T_i = 230\text{ }^{\circ}\text{C}$ and $\text{SOD} = 10\text{ mm}$. Suggest pressure has limited effect on improving coating quality, but may have a minor effect on improving the particle-substrate bond quality. A.) $P_i = 1.2\text{ MPa}$ (175 psi), B.) $P_i = 1.7\text{ MPa}$ (250 psi).

3. Hardness

Powder hardness, as obtained from nanoindentation, suggests that the S5001 and S5002 powders were the hardest and the KM316 was the softest (Figure 76). The S5001 results contained the smallest amount of variability in its measurements, while the KM316, having the overall softest mean, had a large amount of variability. PG-AMP-10 is the second softest and has lower variability than KM316, which could suggest that most of its particles are softer than KM316. It should be noted that the nanoindentation measurement process on micron sized particles is extremely difficult which could lead to the large amounts of variability seen in the results.

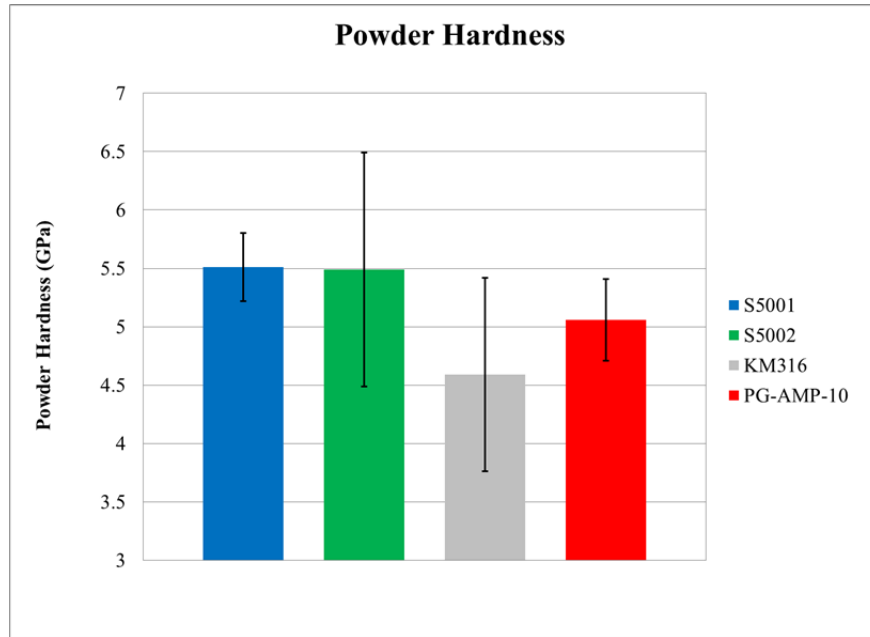


Figure 76. Powder hardness as corrected from nano-indentation measurements. S5002 is hardest with small variability. KM316 is the softest but with vary large variability.

Coating hardness results of all four commercial powders sprayed with helium at $T_i = 230\text{ }^{\circ}\text{C}$, $P_i = 250\text{ psi}$, and at a stand-off distance of 16 mm show that the S5001, S5002, and KM316 had the highest hardness values and were basically indistinguishable, 317 Hv, 314 Hv, and 29 Hv, respectively; while the PG-AMP-10 coating was by far the lowest in hardness at 231 Hv, Table 23. It should be noted that the base metal (SS316L) Vicker's microhardness was 172 Hv \pm 4 indicating that all coatings are, as expected, significantly harder than the base metal. It should also be noted that in the majority, (~75 %), of the indents that inter-splat cracking occurred was observed due to the force of the indent, Figure 77, suggesting that the coatings, and in particular the particle-particle boundaries, are brittle.

Vicker's Micro-Hardness Results	
Powder	Hardness (GPa)
S5001	317 ± 19
S5002	314 ± 44
KM316	295 ± 27
PG-AMP-10	231 ± 23

Table 23. Vicker's micro-hardness results of all four commercial powder coatings sprayed with helium at $T_i = 230\text{ }^{\circ}\text{C}$, $P_i = 250\text{ psi}$, SOD = 16 mm. PG-AMP-10 had the lowest hardness.

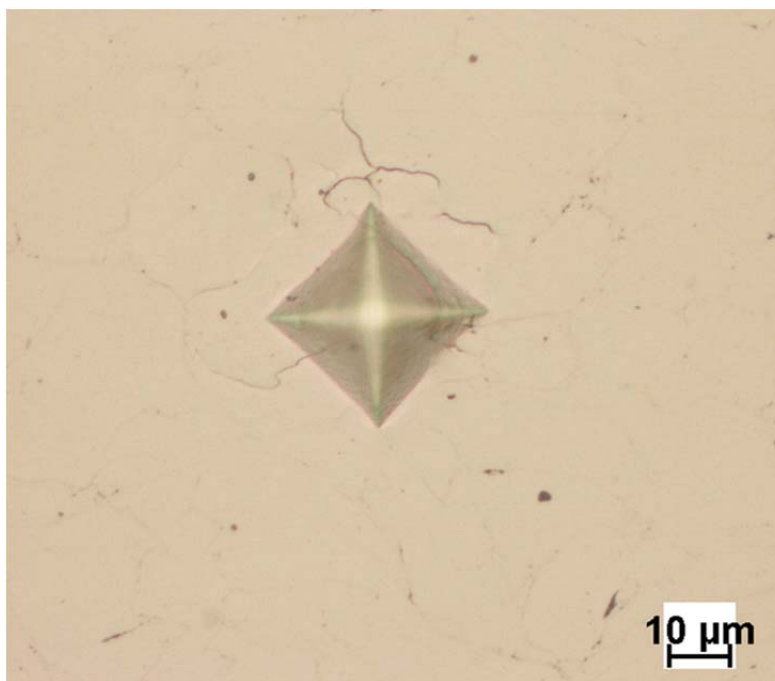


Figure 77. Inter-splat cracking of S5001 coating as a result of taking Vicker's microhardness indents. Suggests that the coatings, and in particular the particle-particle boundaries are brittle.

Based upon the results of the hardness measurements taken on S5001 and PG-AMP-10, it is difficult to determine if gas inlet temperature has an effect on the coating hardness. Although a minor change in the mean coating hardness for S5001 can be seen, because of the large range of scatter of the data, it can safely be concluded that gas inlet temperature did not have an effect on its coating hardness (Figure 78). The same however cannot be said for PG-AMP-10 as there is scatter in the data, but there is a large

change in the mean hardness between 275 °C and 325 °C. Although not conclusive, the results suggest that increasing the working gas inlet temperature softened the coating.

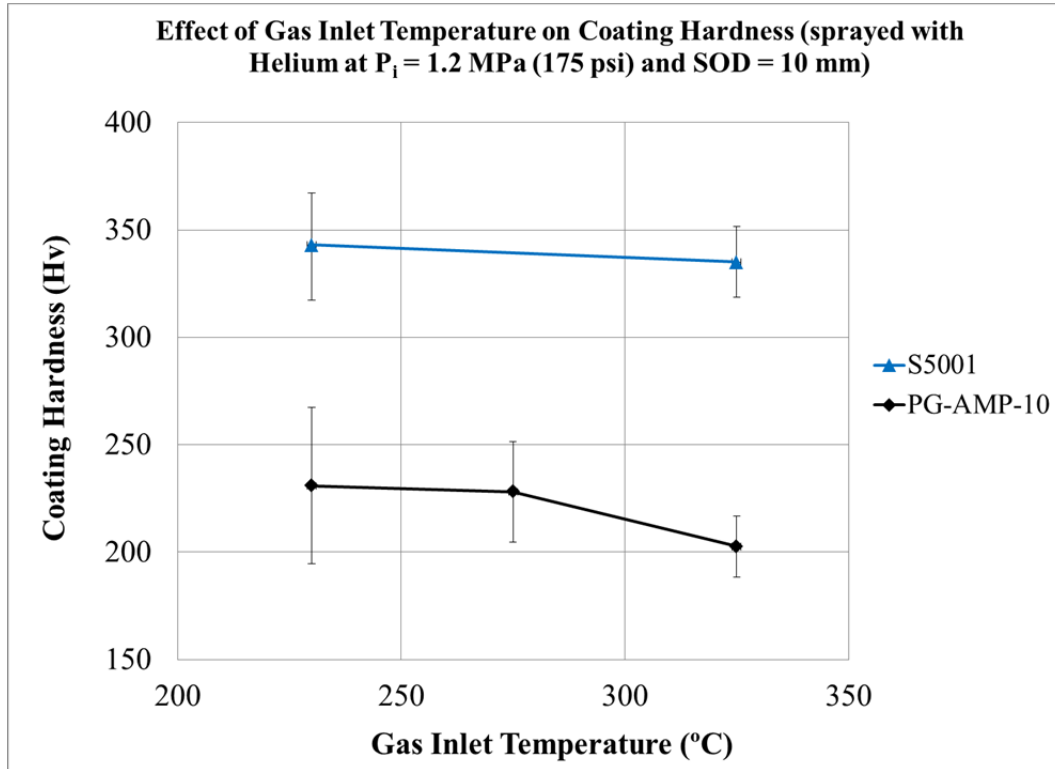


Figure 78. Gas inlet temperature effect on coating hardness. S5001 and PG-AMP-10 sprayed with helium at constant $P_i = 1.2$ MPa (175 psi) and varying temperature. Suggests that increasing gas inlet temperature may have reduced coating hardness but due to scatter in the results it is difficult to definitely say.

PG-AMP-10 and S5001 hardness results were also utilized to investigate if gas inlet pressure plays a role in the resultant coating hardness (Table 24). Both S5001 and PG-AMP-10, sprayed with helium at a constant $T_i = 230$ °C and varying pressure, showed no change in the coating hardness, suggesting that gas pressure does not play a role in determining the hardness of the coating at these conditions. It should be noted that a different load had to be used for the lower pressure condition as the coating was thickness was small that the higher load produced indents larger than the coating itself.

Vicker's Micro-Hardness Results		
Powder	Hardness (GPa)	
	$P_i = 1.2 \text{ MPa}$ (175 psi)	$P_i = 1.7 \text{ MPa}$ (250 psi)
S5001	335 \pm 26	317 \pm 19
PG-AMP-10	231 \pm 36	231 \pm 23

Table 24. Vicker's micro-hardness results for S5001 and PG-AMP-10 as a function of gas inlet pressure. Sprayed with helium at constant $T_i = 230 \text{ }^\circ\text{C}$. Suggest gas inlet pressure has no significant effect on coating hardness.

The final correlation, varying stand-off distance, was investigated with PG-AMP-10 sprayed with helium at $T_i = 230 \text{ }^\circ\text{C}$ and $P_i = 1.7 \text{ MPa}$ (250 psi). Although the average hardness tended to increase from 231 Hv at 16 mm to 265 Hv at 40 mm, the scatter of the results suggests that increasing stand-off distance had little impact on coating hardness.

D. DISCUSSION

1. Deposition Efficiency versus Coating Quality

Deposition efficiency is utilized as a major measuring stick for how well the low pressure cold spray process is performing, but as shown in this work, and the work of others, it is not the best or only measure that should be utilized. PG-AMP-10 and KM316 had by far the highest deposition efficiency, with KM316 attaining over 40 % deposition. In most cases, KM316 and PG-AMP-10 attained at least twice the deposition efficiency of the S5001 and S5002 coatings; however, upon investigating the quality of the microstructure, the S5001 and S5002 tend to have less porosity and better particle-substrate bonding.

Similar to this, Villa et al. reported deposition efficiencies ranging from 19 to 89 %, but upon further investigation of the coating microstructure, they also noted that several coatings contained large amounts of porosity and poor particle-substrate bonding. Specifically, low-temperature conditions that produced reported deposition efficiencies

from 19 to 60 % had a coating in which thickness was not even able to be obtained due to its large amount of porosity and lack of bonding.

2. The Relationship between Porosity and Coating Hardness

The results of this research suggest that coatings with higher levels porosity (KM316 and PG-AMP-10) tend to have lower hardness than coatings produced with less porosity (S5001 and S5002). This finding is consistent with other research conducted with stainless steels. Huang et al. found that as particle velocity increased so too did the densification of their coatings which led to higher microhardness values [26]. Meng et al. also recognized that the coatings were brittle and thus studied the influence of post-processing annealing treatment on the coatings. Their findings suggest that with no annealing treatment, the coating elongation to fracture is immeasurably small and the ultimate tensile strength is on the order of 75 MPa, but that annealing treatments can significantly increase both to 3 % and 325 MPa, respectively [12]. AL-Mangour et al. also found similar results when conducting tensile testing of their coatings, finding no visible sign of necking prior to fracture for the as-sprayed coatings [5].

It should be noted that at first glance, it seemed that the coatings were not as hard as the initial powders. This result seemed counterintuitive because the cold spray process is based upon plastic deformation and basic work-hardening of the powder particles and therefore the coatings should be harder than the original particles. This supposed decrease in hardness can be attributed to the fact that the powders themselves are extremely hard and the nano-indentation measures specifically that powder hardness, Contrary to that, the Vicker's microhardness measurements were taken over a large number of powders and thus the hardness measurement averaged the powder hardness, the strength of the bond between them, and the porosity in the coating. This ultimately led to a coating value which was lower than the initial particle hardness.

3. Powder Design

One of the major findings with this research is the difference between deposition efficiency and deposition rate. The ability of a powder to feed through a system is dependent on the system being utilized and the powder that is trying to be fed. Because

each system's powder feeding mechanism is different, no one powder can satisfy all of those requirements for every system available and this plays a large role in the deposition rate. It is quite common for deposition efficiency and coating thickness per pass to be measured and reported in the literature but what it is not always commented on is that there could be drastically different values of each for different powders. DE and thickness should trend in the same direction for a given powder (i.e. deposition efficiency increases therefore coating thickness per pass increases) but when observing two separate powders it is critically important to understand both the deposition efficiency and rate. In this research the KM316 powder achieved by far the highest deposition efficiency but it did not feed well in this system and therefore led to an extremely low deposition rate. Contrary to this, the S5001 or S5002 powders, manufactured for the Centerline unit, had significantly lower deposition efficiencies but resulted in higher quality, thicker coatings, suggesting that those powders fed well through the system and although their deposition efficiency wasn't as high, their overall performance was much better. This poor flow characteristic has been seen in research before when the particle size gets too small by Spencer and Zhang [2]. It should be noted that the KM316 was the smallest in mean size and overall particle size distribution and was manufactured for the Inovati Kinetic Metallization System.

Particle morphology also plays a critical role in the design and manufacture of feedstock powders. We found that PG-AMP-10 deposited significantly better than the S5001 and S5002 powders, likely due to achieving much higher velocities due to PG-AMP-10's multi-angular morphology, but the coating was wrought with porosity and poor quality bonding. The porosity and poor bonding is likely due to the structure of the PG-AMP-10 feedstock powder. Because it was formed with larger and small particles conglomerated together the coating was left with a large amount of porosity. Had the particles been separate larger and smaller particles, Spencer and Zhang, showed that the porosity of the coating can be significantly reduced while maintaining the optimal flow characteristics of each [2].

As shown by our results, the softer the feedstock powder, such as KM316, attained the highest deposition efficiency, followed by PG-AMP-10, the second softest,

and then S5001 and S5002, the hardest of the feedstock powders. These results suggest that powder hardness may play a key role in its deposition and that softer particles may deposit better than harder ones. Ning et al. also found that an annealing pretreatment of their C-Cu powder tended to increased deposition efficiency suggesting that the softer powders deposit more readily [58].

For these reasons, we propose a combination of the good feedstock powder properties to create a suitable austenitic stainless steel powder for low pressure – low temperature cold spray deposition. The particles should have a multi-angular morphology, be of mixed particle size, and be relatively soft. This design should maximize velocity of the particles, increase deposition efficiency, and decrease porosity in the coatings; creating higher quality coatings.

THIS PAGE INTENTIONALLY LEFT BLANK

V. CONCLUSION

In this thesis research, austenitic stainless steel was successfully deposited utilizing the low-pressure, low-temperature cold spray deposition process. The viable working gas option for use in the low-pressure cold spray deposition of austenitic stainless steels is helium. A key finding was that the characteristics of commercial feedstock powders can vary greatly. The average particle size alone ranged from 17 to 60 microns. The particle morphology also ranged from relatively spherical powders to multi-angular, conglomerated masses of large and small particles. Lastly, the phase content of the powders varied from a phase-pure austenitic stainless steel to duplex stainless steels with a ferrite fraction up to 50 %. These differences in powders led to substantial variation in deposition efficiency and coating quality.

We also successfully demonstrated the use of laser particle velocimetry during cold spray deposition; its first use at the Naval Postgraduate School. We found through simulation and actual measurement that particle morphology may be the dominant factor in determining the in-flight velocity obtainable by a powder. It was also found that critical velocity, although a conceptually simple idea, is actually very complex and is dependent on a number of factors including particle size, temperature, and hardness. It was consistently observed; however, that as the gas inlet temperature was increased, the critical velocity for deposition decreased.

Each of the four commercial powders had different coating characteristics. The harder, spherical powders resulted in lower deposition efficiencies but the resultant coatings were of higher quality with low porosity and good particle-substrate bonding. To the contrary, the softer powders attained significantly higher mass deposition efficiencies but the coating quality was poorer, with porosity and poor interface bonding. The ideal powder particles would have a multi-angular morphology, be softer in nature, and have a mixed particle size distribution.

THIS PAGE INTENTIONALLY LEFT BLANK

APPENDIX A: ONE-DIMENSIONAL MODEL SIMULATION MATLAB CODE

A. HELIUM EXAMPLE

```
%%%%%%%%%%%%%%%%%%%%%%%%%%%%%%%%%%%%%%%%%%%%%%%%%%%%%%%%%%%%%%%%%%%%%%%%%
%
%       Centerline Nozzle One-Dimensional Model
%
%%%%%%%%%%%%%%%%%%%%%%%%%%%%%%%%%%%%%%%%%%%%%%%%%%%%%%%%%%%%%%%%%%%%%%%%%

% This model uses the area ratio of the nozzle to predict the gas
% pressure, temperature, and velocity along the nozzle up to the nozzle
% exit, utilizing the isentropic expansion equations.

% This model also predicts the particle velocity and particle temperature
% along the nozzle, up to the nozzle exit.

% Parameters that can be modified

% Gas Inlet Conditions
% P_go: inlet gas pressure [psi]
% T_go: inlet gas temperature [degC]
% U_gi: inlet gas velocity [m/sec]

% Gas Type Constants
% kappa: specific heat ratio for the gas
% R_h: specific gas constant

% Particle Properties
% Dp: the particle diameter [m]
% T_pi: initial temperature of particle [K]
% rho_p: density of particle [kg/m^3]
% Cp: specific heat of particle [J/kg-K]
% Up_i: initial particle velocity [m/sec]

clear all
close all
clc

% Nozzle Characteristics

length = 126;
nozzle = linspace(0,126,126);
for j=1: length;

    if j<=5
        r(j,1)= -3.5/5*(j-1)+4.5;
```



```

elseif j>5
    r(j,1)=2.15/120*(j)+0.8925;
end
end

NozzleArea = pi.*r.^2;

A_throat = NozzleArea(6);

aratio = NozzleArea./A_throat;

% Gas Inlet Properties

P_go = 175;           % [psi] inlet pressure
P_gi = P_go*6894.75729; % [Pa] inlet pressure
T_go = 230;           % [deg C] inlet temp
T_gi = T_go+273.15;   % [K] inlet temp
U_gi = 10;            % [m/s] initial velocity

% Helium Properties
kappa = 1.66;         % specific heat ratio
R_h = 2.077;          % gas constant
rho_gi = P_gi/(1000*R_h*T_gi); % set initial gas density

% Particle Properties (copper)
Dp = 20e-6;           % diameter of particle [m]
T_pi = 300;           % initial temperature of particle [K]
rho_p = 8000;         % density of particle [kg/m^3]
Cp = 500;             % specific heat of particle [J/kg-K]

% Outputs of Model (as a function of length along the nozzle)
% Pg: Gas Pressure [Pa]
% Tg: Gas Temperature [K]
% Ug: Gas Velocity [m/sec]
% rho_g: Gas Density [kg/m^3]
% Up: Particle Velocity [m/sec]
% Tp: Particle Temperature [K]

% All other thermodynamic values can also be obtained but not are not
% outputted to the "createfigure" plot

% calculates constant in the gas velocity equation
Cnit= 2*(kappa/(kappa-1))*R_h*T_gi*1000;

% Manually Entered Values of the pressure ratio as a function of area ratio
% as Solver couldn't solve the exponential function and find the roots

Pratio1=[ .999358317; .998737359; .997145176; .992016005429711;
0.967559989427262; 0.488084943132466; 0.359127920170656; 0.310200003980210;
0.275259784181674; 0.247764607032805; 0.225107532475300; 0.205917151497742;
0.189360087557498; 0.174882435844313; 0.162092820026253; 0.150702167193243;
0.140489687746872; 0.131282274076478; 0.122941328310629; 0.115353964780749;
0.108426919914473; 0.102082208362417; 0.096253945448567; 0.0908859717935833;
0.085930043842133; 0.081344433061167; 0.077092825583738; 0.073143446813573;

```

```

0.069468357203175; 0.0660428797527548; 0.062845130644178; 0.059855630733058;
0.057056982177513; 0.054433596971072; 0.051971467672090; 0.0496579730284701;
0.047481711726954; 0.045432360106761; 0.043500549287789; 0.041677759083642;
0.039956225685067; 0.0383288611983731; 0.036789183342719; 0.035331253667411;
0.033949623142243; 0.032639284172274; 0.031395628156039; 0.0302144076238522;
0.029091702882145; 0.028023891856827; 0.027007623555420; 0.026039793957921;
0.025117524628255; 0.0242381433493700; 0.023399166717793; 0.022598284397934;
0.021833345058447; 0.021102343386980; 0.020403408484383; 0.0197347933359821;
0.019094865114476; 0.018482096538080; 0.017895057766986; 0.017332409200586;
0.016792894742944; 0.0162753357781050; 0.015778625608683; 0.015301724214751;
0.014843653661604; 0.014403493731683; 0.013980377929290; 0.0135734898791433;
0.013182059930296; 0.012805361960177; 0.012442710640023; 0.012093458630353;
0.011756994206475; 0.0114327389684121; 0.011120145739417; 0.0108186965716827;
0.0105279008844743; 0.0102472938960565; 0.00997643499960203; 0.00971490626976290;
0.00946231110004981; 0.00921827302606644; 0.00898243440768678; 0.00875445546019458;
0.00853401308891893; 0.00832080010210796; 0.00811452417147227; 0.00791490700643299;
0.00772168360610464; 0.00753460158970589; 0.00735342029841805; 0.00717791044925272;
0.00700785319751374; 0.00684303983721456; 0.00668327116123197; 0.00652835689970110;
0.00637811538002266; 0.00623237298461940; 0.00609096374543653; 0.00595372902022256;
0.00582051699311404; 0.00569118245731430; 0.00556558648031084; 0.00544359594917421;
0.00532508342963159; 0.00520992687834970; 0.00509800926392109; 0.00498921844651164;
0.00488344688009397; 0.00478059142854200; 0.00468055314990850; 0.00458323701855389;
0.00448855194056857; 0.00439641032292972; 0.00430672808437605; 0.00421942445714449;
0.00413442178584863; 0.00405164547409070; 0.00397102374922936; 0.00389248760537308;
0.00381597068494368; 0.00374140909760348];

```

```
% Solves for Pg, Tg, Ug, rho_g
```

```
for k=1:126;
```

```

    Pg(k,1)=P_gi.*Pratio1(k,1);
    Tg(k,1)=T_gi.*(Pratio1(k,1)^((kappa-1)/kappa));
    Ug(k,1)=sqrt(Cnit*(1-Pratio1(k,1)^((kappa-1)/kappa))+U_gi^2);
    rho_g(k,1)=rho_gi.*(Pratio1(k,1)^(1/kappa));

```

```
end
```

```
% Finding thermodynamic and hydrodynamic values utilizing linear
```

```
% interpolation based upon temperature of the gas
```

```
% Prandtl Number
```

```
% Dynamic Viscosity (www.nist.gov)
```

```
% Thermal Conductivity (www.nist.gov)
```

```
for k=1:126;
```

```
    if Tg(k,1)<=800 && Tg(k,1)>=700
```

```

        Pr(k,1)=((Tg(k,1)-700)/(800-700)).*(.654-.654)+.654;
        visc(k,1)=(1/1e7)*(((Tg(k,1)-700)/(800-700)).*(394.2-358.6)+358.6);
        therm(k,1)=(1/1e3)*(((Tg(k,1)-700)/(800-700)).*(307-292)+292);

```

```
    elseif Tg(k,1)<=700 && Tg(k,1)>=600
```

```

        Pr(k,1)=((Tg(k,1)-500)/(700-500)).*(.654-.668)+.668;
        visc(k,1)=(1/1e7)*(((Tg(k,1)-600)/(700-600)).*(358.6-321.7)+321.7);
        therm(k,1)=(1/1e3)*(((Tg(k,1)-600)/(700-600)).*(292-247)+247);

```

```

elseif Tg(k,1)<=600 && Tg(k,1)>=550
    Pr(k,1)= ((Tg(k,1)-500)/(700-500))*(.654-.668)+.668;
    visc(k,1)=(1/1e7)*(((Tg(k,1)-550)/(600-550))*(321.7-302.7)+302.7);
    therm(k,1)=(1/1e3)*(((Tg(k,1)-550)/(600-550))*(247-229)+229);

elseif Tg(k,1)>=500 && Tg(k,1)<=550
    Pr(k,1)= ((Tg(k,1)-500)/(700-500))*(.654-.668)+.668;
    visc(k,1)=(1/1e7)*(((Tg(k,1)-500)/(550-500))*(302.7-283.2)+283.2);
    therm(k,1)=(1/1e3)*(((Tg(k,1)-500)/(550-500))*(229-211.4)+211.4);

elseif Tg(k,1)>=450 && Tg(k,1)<=500
    Pr(k,1)= ((Tg(k,1)-450)/(500-450))*(.668-.6715)+.6715;
    visc(k,1)=(1/1e7)*(((Tg(k,1)-450)/(500-450))*(283.2-263.15)+263.15);
    therm(k,1)=(1/1e3)*(((Tg(k,1)-450)/(500-450))*(211.4-194.7)+194.7);

elseif Tg(k,1)>=400 && Tg(k,1)<=450
    Pr(k,1)= ((Tg(k,1)-400)/(450-400))*(.6715-.675)+.675;
    visc(k,1)=(1/1e7)*(((Tg(k,1)-400)/(450-400))*(260.7-242.7)+242.7);
    therm(k,1)=(1/1e3)*(((Tg(k,1)-400)/(450-400))*(194.7-179.5)+179.5);

elseif Tg(k,1)>=350 && Tg(k,1)<=400
    Pr(k,1)= ((Tg(k,1)-350)/(400-350))*(.675-.6775)+.6775;
    visc(k,1)=(1/1e7)*(((Tg(k,1)-350)/(400-350))*(242.7-221.35)+221.35);
    therm(k,1)=(1/1e3)*(((Tg(k,1)-350)/(400-350))*(179.5-164.9)+164.9);

elseif Tg(k,1)>=300 && Tg(k,1)<=350
    Pr(k,1)= ((Tg(k,1)-300)/(350-300))*(.6775-.680)+.680;
    visc(k,1)=(1/1e7)*(((Tg(k,1)-300)/(350-300))*(221.35-199.2)+199.2);
    therm(k,1)=(1/1e3)*(((Tg(k,1)-300)/(350-300))*(164.9-149.9)+149.9);

elseif Tg(k,1)>=250 && Tg(k,1)<=300
    Pr(k,1)= ((Tg(k,1)-250)/(300-250))*(.680-.682)+.682;
    visc(k,1)=(1/1e7)*(((Tg(k,1)-250)/(300-250))*(199.2-176.0)+176.0);
    therm(k,1)=(1/1e3)*(((Tg(k,1)-250)/(300-250))*(149.9-133.8)+133.8);

elseif Tg(k,1)>=200 && Tg(k,1)<=250
    Pr(k,1)= ((Tg(k,1)-200)/(250-200))*(.682-.675)+.675;
    visc(k,1)=(1/1e7)*(((Tg(k,1)-200)/(250-200))*(176.0-151.4)+151.4);
    therm(k,1)=(1/1e3)*(((Tg(k,1)-200)/(250-200))*(133.8-115.1)+115.1);

elseif Tg(k,1)>=150 && Tg(k,1)<=200
    Pr(k,1)= ((Tg(k,1)-150)/(200-150))*(.675-.676)+.676;
    visc(k,1)=(1/1e7)*(((Tg(k,1)-150)/(200-150))*(151.4-124.9)+124.9);
    therm(k,1)=(1/1e3)*(((Tg(k,1)-150)/(200-150))*(115.1-95.0)+95.0);

elseif Tg(k,1)>=100 && Tg(k,1)<=150
    Pr(k,1)= ((Tg(k,1)-100)/(150-100))*(.676-.686)+.686;
    visc(k,1)=(1/1e7)*(((Tg(k,1)-100)/(150-100))*(124.9-95.29)+95.29);
    therm(k,1)=(1/1e3)*(((Tg(k,1)-100)/(150-100))*(95.0-73.0)+73.0);

elseif Tg(k,1)>=50 && Tg(k,1)<=100
    Pr(k,1)= ((Tg(k,1)-50)/(100-50))*(.686-.686)+.686;
    visc(k,1)=(1/1e7)*(((Tg(k,1)-50)/(100-50))*(95.29-60.66)+60.66);
    therm(k,1)=(1/1e3)*(((Tg(k,1)-50)/(100-50))*(73.0-46.23)+46.23);

```

```

elseif Tg(k,1)>=5 && Tg(k,1)<=50
    Pr(k,1)= ((Tg(k,1)-1)/(50-1))*(.759-.768)+.768;
    visc(k,1)=(1/1e7)*(((Tg(k,1)-1)/(50-1))*(60.66-12.24)+12.24);
    therm(k,1)=(1/1e3)*(((Tg(k,1)-1)/(50-1))*(46.23-2.69)+2.69);
end

end

% Solving for particle velocity

% Initializing all the vectors

Up=zeros(126,1);
Up(7,1)=1; % initialize the inlet velocity of powder
Cd=zeros(126,1);
Cd(7,1)=0.005; % initialize the drag coefficient
Re=zeros(126,1);

% Starts at point 7 (1 mm after nozzle throat)

for l=7:125

    % find acceleration, velocity, drag, and Reynolds number
    % iterates to constantly solve for new Reynolds and drag based upon
    % previous difference in particle and gas velocity

    accel(l,1)=(3/4)*(Cd(l,1)*rho_g(l,1))/(Dp*rho_p)*(Ug(l,1)-Up(l,1))*(abs(Ug(l,1)-Up(l,1)));
    Up(l+1,1)= Up(l,1)+accel(l,1)*.001/Up(l,1);
    Up(l,1)= Up(l+1,1);
    Re(l,1)= rho_g(l,1)*(Ug(l,1)-Up(l,1))*Dp/visc(l,1);
    Cd(l+1,1)=(2.25*(Re(l,1)^(-0.31))+0.36*(Re(l,1)^0.06))^3.45;
    Cd(l,1)=Cd(l+1,1);
    Re(126,1)=rho_g(126)*Dp/visc(126)*(Ug(126)-Up(126));

end

% Solving for thermal properties of powder

Tp=zeros(126,1);
Tp(7,1)=300;

for k=1:126;
    Nu(k,1)=2+(0.6*(Re(k,1)^(1/2))*Pr(k,1)^(1/3));
    h(k,1)=Nu(k,1)*therm(k,1)/Dp;
end

for j=7:125;
    gradT(j,1)=(Tg(j,1)-Tp(j,1))*6*h(j,1)/(Cp*rho_p*Dp);
    Tp(j+1,1)=Tp(j,1)+gradT(j,1)*.001/Up(j,1);
    Tp(j,1)=Tp(j+1,1);
end

% Plotting the results

createfigure(nozzle, r, Pg, Ug, Up, Tg, Tp);

```

B. NITROGEN PRESSURE RATIO VECTOR

```

Pratio1=[ 0.9994279595105772743646312428877; 0.99887435804436752964573646595476;
0.99745463655132887725565348695391;      0.99287981249687136257655774869606;
0.97103275286803830029446802699067;      0.5283; 0.40240266632812843194967804189092;
0.35343092882868206328564980112933;      0.31794783304570457455229560759642;
0.28967941028141737037885585557185;      0.26612587873236539347265694996295;
0.24597123594883147390450439146987;      0.22841464443794684325445974308422;
0.2129227603949677578008149286229;      0.19911779116803491407596200834576;
0.18671987997249248167656775661942;      0.17551457577927223647871571092489;
0.1653331409851762216368735557473;      0.15603996298895793316788215911412;
0.14752414657858485640761984400972;      0.13969369280634815614342264329864;
0.13247134555677816161379353588601;      0.12579155149193422946252496233256;
0.11959818573250105398610181718068;      0.11384281787664477675508913156606;
0.10848336793797999073335048453607;      0.10348304925088123115973259563124;
0.098809526287852167307728849978138;      0.094434235945774788476715761378926;
0.090331834914473737836791135324143;      0.086479745518153817737033682195938;
0.082857779343070578106066221630894;      0.079447822946475703549524691541319;
0.076233573579956515760539641560571;      0.073200315553209656826925681185372;
0.070334729882437401789898330270304;      0.067624731397354786258719978609731;
0.065059328652699300783865524169458;      0.062628502896674488743764236089683;
0.06032310305640444337645425567187;      0.058134754257541794793221840885933;
0.056055777837164002142316101235464;      0.054079121162363422425940256540263;
0.052198295851248744013505797246744;      0.050407323223366890874459273705184;
0.048700685994226012969224195851993;      0.047073285382410021419079787138611;
0.045520402924516341432179716706884;      0.044037666398112111454313066684003;
0.042621019340250575764220189244167;      0.041266693722105212982765725722841;
0.039971185401579349318500153358456;      0.038731232027420986386269837719438;
0.037543793112099424380860695669701;      0.036406032027838407031589735025349;
0.035315299711854606680179875115618;      0.034269119893917834548102133528305;
0.03326517568257186923570836011631;      0.032301297366336021711345691403496;
0.031375451303450971922287301777853;      0.030485729788655267727432404505275;
0.029630341798426468637795683127225;      0.028807604527383357629055603411432;
0.02801593563836777193942375675462;      0.027253846157308463124916798477773;
0.026519933951490074168913284430867;      0.025812877736451610420621956059556;
0.02513143156254745495434269677483;      0.024474419737323978252656988053416;
0.023840732144386055521945525479426;      0.023229319923429719496041964698327;
0.022639191479664152306089536565266;      0.022069408793995230343696107776137;
0.021519084008145152598948658144099;      0.020987376261378114734845006155524;
0.020473488757729546924163267755228;      0.019976666044626563518353402452414;
0.019496191485568719121816262954054;      0.019031384911135146472363818726422;
0.018581600434016449254443259728943;      0.018146224415058176407692323316599;
0.017724673568461417355374807693515;      0.017316393195330058027236075041536;
0.016920855535696502738849326710998;      0.016537558230008662903844463392574;
0.016166022881829772789496314960073;      0.01580579371419997047080261227905;
0.015456436312739048576122577249225;      0.015117536449143115658819888509253;
0.014788698979247658191933900204849;      0.014469546810302405725124357486959;
0.014159719932534134159629030248113;      0.013858874510464950371697598828256;
0.013566682029811542236836181307549;      0.013282828496116933794461954352111;
0.013007013681564055188235156251798;      0.012738950416693253833648621225554;
0.012478363923994788803188153259385;      0.012224991190575990122225704032076;
0.011978580377311785223451802717851;      0.011738890262079279157947306750562;
0.011505689714853611284171642365004;      0.011278757202603737097053237270212;
0.011057880322076051403838775420048;      0.010842855358690660928975616973931;

```

0.010633486869901112244958153519404;	0.010429587291484766209796769316922;
0.010230976565338211365789575388018;	0.010037481787450811401428219427101;
0.0098489368748210392404424710495587;	0.0096651822501644652076873836911835;
0.0094860645433403864589022106082385;	0.009311436308496152410650360074452;
0.0091411557559951450723744321857468;	0.0089750864982562235237267360676588;
0.0088130973086898290884850469604848;	0.008655061892969116276597343058913;
0.0085008586719238260141495344344908;	0.0083503705753905710026289588838098;
0.0082034848463955838021856252121661;	0.0080600928550857474559018468819958;
0.0079200899218604470842457123286782;	0.0077833751491910048495637464011399;
0.0076498512616464301079062106847039;	0.0075194244536738485531381255425642;
0.0073920042447096989470953111447489;	

C. CREATEFIGURE CODE

```
function createfigure(nozzle, r, Pg, Ug, Up, Tg, Tp)
% Plotting results
% Create figure
figure1 = figure;

% Create subplot
subplot1 = subplot(4,1,1,'Parent',figure1,'YTick',[0 5 10 15 20],...
    'XTickLabel',{' ',' ',' ',' ',' '});
box(subplot1,'on');
grid(subplot1,'on');
hold(subplot1,'all');

% Create plot
plot(nozzle,r,'Parent',subplot1);

% Create ylabel
ylabel('Nozzle Contour, r(mm)');

% Create subplot
subplot2 = subplot(4,1,2,'Parent',figure1,...
    'YTickLabel',{'0','1','2','3','4'},...
    'YTick',[0 1000000 2000000 3000000 4000000],...
    'XTickLabel',{' ',' ',' ',' ',' '});
box(subplot2,'on');
grid(subplot2,'on');
hold(subplot2,'all');

% Create plot
plot(nozzle,Pg,'Parent',subplot2);

% Create ylabel
ylabel('Pressure, P (MPa)');

% Create subplot
subplot3 = subplot(4,1,3,'Parent',figure1,'YTick',[0 200 400 600 800 1000],...
    'XTickLabel',{' ',' ',' ',' ',' '});
box(subplot3,'on');
grid(subplot3,'on');
hold(subplot3,'all');
```

```

% Create plot
plot(nozzle,Ug, nozzle, Up,'Parent',subplot3);

% Create ylabel
ylabel('Velocity [m/s]');
legend('Ug','Up', 'Location', 'southeast')
% Create subplot
subplot4 = subplot(4,1,4,'Parent',figure1);
%% Uncomment the following line to preserve the X-limits of the axes
% xlim(subplot4,[0 300]);
%% Uncomment the following line to preserve the Y-limits of the axes
% ylim(subplot4,[0 650]);
box(subplot4,'on');
grid(subplot4,'on');
hold(subplot4,'all');

% Create plot
plot(nozzle,Tg, nozzle, Tp,'Parent',subplot4);

% Create ylabel
ylabel('Temperature [K]');
legend('Tg', 'Tp')
% Create xlabel
xlabel('Axial Distance, x (mm)');

```

APPENDIX B: SUMMARY TABLES OF VELOCIMETRY EXPERIMENT RESULTS

Test No.	2	3	4	5	6
Powder Material	S5001	S5001	S5001	S5001	S5001
Gas (N2 or He)	He	He	He	He	He
Gas Temperature (°C)	250	250	250	250	250
Gas Pressure (MPa)	1.03	1.03	1.03	1.03	1.03
Powder Nominal Feed Rate (%)	40	40	40	40	40
Laser Stand-Off Distance (mm)	20	20	20	20	20
Capture Depth (μsec)	10	20	50	250	500
Trigger Level (mV)	200	200	200	200	200
# GOOD (sec ⁻¹)	12.9	3.4	5	2.1	0.5

Table 25. S5001 capture depth calibration results (highlight indicates the capture depth modification and resultant #good/sec).

Test No.	1	2	3	4	5
Powder Material	PG-AMP-10	PG-AMP-10	PG-AMP-10	PG-AMP-10	PG-AMP-10
Gas (N2 or He)	He	He	He	He	He
Gas Temperature (°C)	250	250	250	250	250
Gas Pressure (MPa)	1.03	1.03	1.03	1.03	1.03
Powder Nominal Feed Rate (%)	40	40	40	40	40
Laser Stand-Off Distance (mm)	20	20	20	20	20
Capture Depth (μsec)	10	20	50	250	500
Trigger Level (mV)	200	200	200	200	200
# GOOD (sec ⁻¹)	75.5	69.3	56.4	19	9.9

Table 26. PG-AMP-10 capture depth calibration results (highlight indicates the capture depth modification and resultant #good/sec).

Test No.	1	2	3	4
Powder Material	S5001	S5001	S5001	S5001
Gas (N2 or He)	He	He	He	He
Gas Temperature (°C)	250	250	250	250
Gas Pressure (MPa)	1.03	1.03	1.03	1.03
Powder Nominal Feed Rate (%)	40	40	40	40
Laser Stand-Off Distance (mm)	20	20	20	20
Capture Depth (μsec)	20	20	20	20
Trigger Level (mV)	50	100	150	200
# GOOD (sec ⁻¹)	21.2	22.5	18.8	17.6
Test No.	5	6	7	8
Powder Material	S5001	S5001	S5001	S5001
Gas (N2 or He)	He	He	He	He
Gas Temperature (°C)	250	250	250	250
Gas Pressure (MPa)	1.03	1.03	1.03	1.03
Powder Nominal Feed Rate (%)	40	40	40	40
Laser Stand-Off Distance (mm)	20	20	20	20
Capture Depth (μsec)	20	20	20	20
Trigger Level (mV)	250	500	1000	2000
# GOOD (sec ⁻¹)	18.6	20.1	11	1.5

Table 27. S5001 trigger level calibration results (highlight indicates the trigger level modification and resultant #good/sec).

Test No.	1	2	3	4
Powder Material	PG-AMP-10	PG-AMP-10	PG-AMP-10	PG-AMP-10
Gas (N2 or He)	He	He	He	He
Gas Temperature (°C)	250	250	250	250
Gas Pressure (MPa)	1.03	1.03	1.03	1.03
Powder Nominal Feed Rate (%)	40	40	40	40
Laser Stand-Off Distance (mm)	20	20	20	20
Capture Depth (μsec)	20	20	20	20
Trigger Level (mV)	50	100	150	200
# GOOD (sec ⁻¹)	109.2	107.7	70.7	66.6

Test No.	5	6	7	8
Powder Material	PG-AMP-10	PG-AMP-10	PG-AMP-10	PG-AMP-10
Gas (N2 or He)	He	He	He	He
Gas Temperature (°C)	250	250	250	250
Gas Pressure (MPa)	1.03	1.03	1.03	1.03
Powder Nominal Feed Rate (%)	40	40	40	40
Laser Stand-Off Distance (mm)	20	20	20	20
Capture Depth (μsec)	20	20	20	20
Trigger Level (mV)	250	500	1000	2000
# GOOD (sec ⁻¹)	88.4	92.6	57.6	8.6

Table 28. PG-AMP-10 trigger level calibration results (highlight indicates the trigger level modification and resultant #good/sec).

Test No.	1	2	3	4	5	6
Powder Material	S5001	S5001	S5001	S5001	S5001	S5001
Gas (N2 or He)	N2	N2	N2	N2	N2	N2
Gas Temperature (°C)	450	450	450	450	450	450
Gas Pressure (Mpa)	1.7	1.7	1.7	1.7	1.7	1.7
Powder Nominal Feed Rate (%)	2	5	10	20	40	80
Laser Stand-Off Distance (mm)	20	20	20	20	20	20
Statistical Measure (# good/sec)	47	41	39	41	43	39
Average Particle Velocity (m/s)	425	434	395	398	415	397

Table 29. Summary of results of the nominal powder feed rate experiment (highlighted values indicate the parameter changed, powder nominal feed rate, and the resultant statistical measure and average particle velocity).

Test No.	1	2	3	4	5
Powder Material	S5001	S5001	S5001	S5001	S5002
Gas (N2 or He)	N2	N2	N2	N2	N3
Substrate Material	316SS	316SS	316SS	316SS	316SS
Gas Temperature (°C)	450	450	450	450	450
Gas Pressure (MPa)	1.7	1.7	1.7	1.7	1.7
Powder Nominal Feed Rate (%)	40	40	40	40	40
Substrate Stand-Off Distance (mm)	40	30	25	22.5	~21
Laser Stand-Off Distance (mm)	20	20	20	20	20
Statistical Measure (# good/sec)	48.6	48.9	45.7	33.5	11
Average Particle Velocity (m/s)	422	438	439	432	471

Table 30. Summary of results of the substrate interaction experiment.

Highlighted values indicate the parameter changed (substrate stand-off distance) and the resultant statistical measure and average particle velocity.

Test No.	1	2	3	4	5	6
Powder Material	S5001	S5001	S5001	S5001	S5001	S5001
Gas (N2 or He)	He	He	He	He	He	He
Gas Temperature (°C)	200	200	200	230	230	230
Gas Pressure (MPa)	1.7	1.7	1.7	1.7	1.7	1.7
Powder Nominal Feed Rate (%)	40	40	40	40	40	40
Laser Stand-Off Distance (mm)	10	20	40	10	20	40
Average Particle Velocity (m/sec)	448.0	487.4	500.7	449.5	454.3	478.3
Critical Velocity (m/sec)	600.0	645.0	677.0	573.0	607.0	658.0
Deposition Efficiency (%)	13.0	12.3	10.4	18.8	14.9	13.3
Coating Thickness per Pass (mm)	0.22	0.21	0.17	0.31	0.21	0.19
Test No.	7	8	9	10	11	12
Powder Material	S5001	S5001	S5001	S5001	S5001	S5001
Gas (N2 or He)	He	He	He	He	He	He
Gas Temperature (°C)	230	230	230	275	275	275
Gas Pressure (MPa)	1.2	1.2	1.2	1.2	1.2	1.2
Powder Nominal Feed Rate (%)	40	40	40	40	40	40
Laser Stand-Off Distance (mm)	10	20	40	10	20	40
Average Particle Velocity (m/sec)	426.2	421.2	447.2	448.0	429.9	441.5
Critical Velocity (m/sec)	632.0	635.0	676.0	625.0	630.0	652.0
Deposition Efficiency (%)	5.3	2.4	2.0	6.1	3.4	2.8
Coating Thickness per Pass (mm)	0.08	0.06	0.05	0.11	0.06	0.03
Test No.	13	14	15	16	17	18
Powder Material	S5001	S5001	S5001	S5001	S5001	S5001
Gas (N2 or He)	He	He	He	He	He	He
Gas Temperature (°C)	325	325	325	450	450	450
Gas Pressure (MPa)	1.2	1.2	1.2	0.7	0.7	0.7
Powder Nominal Feed Rate (%)	40	40	40	40	40	40
Laser Stand-Off Distance (mm)	10	20	40	10	20	40
Average Particle Velocity (m/sec)	449.1	431.2	456.1	363.1	356.0	334.6
Critical Velocity (m/sec)	613.0	614.0	648.0	578.0	583.0	NA
Deposition Efficiency (%)	6.7	6.0	5.0	0.4	0.1	0.0
Coating Thickness per Pass (mm)	0.11	0.11	0.05	0.01	0.00	0.00

Table 31. Summary of all laser velocimetry, critical velocity, deposition efficiency, and coating thickness per pass results for S5001, from Chapter III.

Test No.	1	2	3	4	5	6
Powder Material	PG-AMP-10	PG-AMP-10	PG-AMP-10	PG-AMP-10	PG-AMP-10	PG-AMP-10
Gas (N2 or He)	He	He	He	He	He	He
Gas Temperature (°C)	200	200	200	230	230	230
Gas Pressure (MPa)	1.7	1.7	1.7	1.7	1.7	1.7
Powder Nominal Feed Rate (%)	40	40	40	40	40	40
Laser Stand-Off Distance (mm)	10	20	40	10	20	40
Average Particle Velocity (m/sec)	513.3	564.6	574.7	512.6	562.5	579.3
Critical Velocity (m/sec)	640.0	684.0	696.0	632.0	666.0	689.0
Deposition Efficiency (%)	33.9	26.6	29.8	35.1	33.6	31.0
Coating Thickness per Pass (mm)	1.32	1.26	1.07	1.36	1.26	1.13
Test No.	7	8	9	10	11	12
Powder Material	PG-AMP-10	PG-AMP-10	PG-AMP-10	PG-AMP-10	PG-AMP-10	PG-AMP-10
Gas (N2 or He)	He	He	He	He	He	He
Gas Temperature (°C)	230	230	230	275	275	275
Gas Pressure (MPa)	1.2	1.2	1.2	1.2	1.2	1.2
Powder Nominal Feed Rate (%)	40	40	40	40	40	40
Laser Stand-Off Distance (mm)	10	20	40	10	20	40
Average Particle Velocity (m/sec)	444.5	434.4	452.4	448.7	437.8	463.9
Critical Velocity (m/sec)	595.0	591.0	604.0	587.0	582.0	610.0
Deposition Efficiency (%)	21.6	17.5	13.7	24.8	20.7	16.7
Coating Thickness per Pass (mm)	0.83	0.67	0.53	1.07	0.78	0.64
Test No.	13	14	15	16	17	18
Powder Material	PG-AMP-10	PG-AMP-10	PG-AMP-10	PG-AMP-10	PG-AMP-10	PG-AMP-10
Gas (N2 or He)	He	He	He	He	He	He
Gas Temperature (°C)	325	325	325	450	450	450
Gas Pressure (MPa)	1.2	1.2	1.2	0.7	0.7	0.7
Powder Nominal Feed Rate (%)	40	40	40	40	40	40
Laser Stand-Off Distance (mm)	10	20	40	10	20	40
Average Particle Velocity (m/sec)	443.0	443.9	469.1	330.0	324.6	324.2
Critical Velocity (m/sec)	579.0	580.0	594.0	547.0	578.0	NA
Deposition Efficiency (%)	26.9	23.4	19.6	2.3	0.6	0.0
Coating Thickness per Pass (mm)	1.07	0.86	0.75	0.12	0.01	0.00

Table 32. Summary of all laser velocimetry, critical velocity, deposition efficiency, and coating thickness per pass results for PG-AMP-10, from Chapter III.

APPENDIX C: SUMMARY RESULTS OF ALL DEPOSITION EXPERIMENTS FROM CHAPTER IV

Test No.	1	2	3	4	5	6	7
Powder Material	S5001	S5001	S5001	S5001	S5001	S5001	S5001
Gas (N2 or He)	He	He	He	He	He	He	He
Substrate Material	Grey Cast Iron	Grey Cast Iron	Grey Cast Iron	Grey Cast Iron	Grey Cast Iron	Grey Cast Iron	Grey Cast Iron
Gas Temperature (°C)	230	230	230	325	325	450	600
Gas Pressure (MPa)	0.7	1.2	1.7	0.7	1.2	0.7	0.7
Powder Feed Rate (g/min)	60.4	60.4	60.4	60.4	60.4	60.4	60.4
Deposition Efficiency (%)	unm	1.7	11.8	unm	4.8	0.14	0.29
Coating Thickness per Pass (mm)	unm	0.2	0.67	unm	0.5	unm	0.01

Table 33. Summary of helium spray deposition results for S5001 powder.

Test No.	1	2	3	4	5	6	7
Powder Material	S5002	S5002	S5002	S5002	S5002	S5002	S5002
Gas (N2 or He)	He	He	He	He	He	He	He
Substrate Material	Grey Cast Iron	Grey Cast Iron	Grey Cast Iron	Grey Cast Iron	Grey Cast Iron	Grey Cast Iron	Grey Cast Iron
Gas Pressure (MPa)	230	230	230	325	325	450	600
Gas Pressure (psi)	0.7	1.2	1.7	0.7	1.2	0.7	0.7
Powder Feed Rate (g/min)	54.8	54.8	54.8	54.8	54.8	54.8	54.8
Deposition Efficiency (%)	0.13	unm	12.3	0.27	2.6	0.27	0.4
Coating Thickness per Pass (mm)	0.01	unm	0.71	0.02	0.57	0.02	0.03

Table 34. Summary of helium spray deposition results for S5002 powder.

Test No.	1	2	3	4	5	6	7
Powder Material	KM316	KM316	KM316	KM316	KM316	KM316	KM316
Gas (N2 or He)	He	He	He	He	He	He	He
Substrate Material	Grey Cast Iron	Grey Cast Iron	Grey Cast Iron	Grey Cast Iron	Grey Cast Iron	Grey Cast Iron	Grey Cast Iron
Gas Temperature (°C)	230	230	230	325	325	450	600
Gas Pressure (MPa)	0.7	1.2	1.7	0.7	1.2	0.7	0.7
Powder Feed Rate (g/min)	2.4	2.4	2.4	2.4	2.4	2.4	2.4
Deposition Efficiency (%)	unm	24	41.8	2.1	38.3	3.5	9.2
Coating Thickness per Pass (mm)	unm	0.13	0.15	unm	0.15	0.02	0.04

Table 35. Summary of helium spray deposition results for KM316 powder.

Test No.	1	2	3	4	5	6	7
Powder Material	PG	PG	PG	PG	PG	PG	PG
Gas (N2 or He)	He	He	He	He	He	He	He
Substrate Material	Grey Cast Iron	Grey Cast Iron	Grey Cast Iron	Grey Cast Iron	Grey Cast Iron	Grey Cast Iron	Grey Cast Iron
Gas Temperature (°C)	230	230	230	325	325	450	600
Gas Pressure (MPa)	0.7	1.2	1.7	0.7	1.2	0.7	0.7
Powder Feed Rate (g/min)	19.6	19.6	19.6	19.6	19.6	19.6	19.6
Deposition Efficiency (%)	unm	13.5	29.4	0.4	23.9	1.1	1.4
Coating Thickness per Pass (mm)	unm	0.71	0.93	0.01	0.76	0.04	0.08

Table 36. Summary of helium spray deposition results for PG-AMP-10 powder.

LIST OF REFERENCES

- [1] M. F. Smith, "Comparing cold spray with thermal spray coating technologies," in *The Cold Spray Materials Deposition Process: Fundamentals and Applications*, V. K. Champagne, Ed., Boca Raton, FL, Woodhead, 2007, pp. 43–61.
- [2] K. Spencer and M. -X. Zhang, "Optimisation of stainless steel cold spray coatings using mixed particle size distributions," *Surface and Coatings Technology*, vol. 205, no. 21, pp. 51355140, May 2011.
- [3] Y. Tao, T. Xiong, C. Sun, L. Kong, X. Cui, T. Li and G. Song, "Microstructure and corrosion performance of a cold sprayed aluminum coating on AZ91D magnesium alloy," *Corrosion Science*, vol. 52, no. 10, pp. 3191–3197, Oct. 2010.
- [4] B. S. DeForce, T. J. Eden and J. K. Potter, "Cold spray Al-5% Mg coatings for the corrosion protection of magnesium alloys," *Journal of Thermal Spray Technology*, vol. 20, no. 6, pp. 1352–1358, Dec. 2011.
- [5] B. AL-Mangour, R. Mongrain, E. Irissou and S. Yue, "Improving the strength and corrosion resistance of 316L stainless steel for biomedical applications using cold spray," *Surface and Coatings Technology*, vol. 216, pp. 297–307, Feb. 2013.
- [6] P. F. Leyman and V. K. Champagne, "Cold spray process development for the reclamation of the apache helicopter mast support," Army Research Laboratory, Aberdeen Proving Ground, MD, Tech. Rep. ARL-TR-4922, 2009.
- [7] J. Villafuerte and D. Wright, "Practical cold spray success: Repair of Al and Mg alloy aircraft components," *Advanced Materials and Processes*, vol. 168, no. 5, pp. 53–55, May 2010.
- [8] R. Jones, N. Matthews, C. A. Rodopoulos, K. Cairns and S. Pitt, "On the use of supersonic particle deposition to restore the structural integrity of damaged aircraft structures," *International Journal of Fatigue*, vol. 33, no. 9, pp. 1257–1267, Sept. 2011.
- [9] N. Matthews, R. Jones and G. C. Sih, "Application of supersonic particle deposition to enhance the structural integrity of aircraft structures," *Science China-Physics, Mechanics, and Astronomy*, vol. 57, no. 1, pp. 12–18, Jan. 2014.
- [10] W. Han, X. M. Meng, J. B. Zhang and J. Zhao, "Elastic modulus of 304 stainless steel coating by cold gas dynamic spraying," *Journal of Iron and Steel Research International*, vol. 19, no. 3, pp. 73–78, Mar. 2012.
- [11] W. Han, X. M. Meng, J. Zhao and J. B. Zhang, "Effect of heat treatment on microstructure and bending behavior of 304 stainless steel coating by cold gas

- dynamic spraying,” *Materials Research Innovations*, vol. 16, no. 2, pp. 109–114, Apr. 2012.
- [12] X. Meng, J. Zhang, W. Han, J. Zhao and Y. Liang, “Influence of annealing treatment on the microstructure and mechanical performance of cold sprayed 304 stainless steel coating,” *Applied Surface Science*, vol. 258, no. 2, pp. 700–704, Nov. 2011.
 - [13] J. Pattison, S. Celotto, R. Morgan, M. Bray and W. O'Neill, “Cold gas dynamic manufacturing: A non-thermal approach to freeform fabrication,” *International Journal of Machine Tools and Manufacture*, vol. 47, no. 3, pp. 627–634, Mar. 2007.
 - [14] A. Sova, S. Grigoriev, A. Okunkova and I. Smurov, “Potential of cold gas dynamic spray as additive manufacturing technology,” *International Journal of Advanced Manufacturing Technologies*, vol. 69, no. 9, pp. 2269–2278, Dec. 2013.
 - [15] K. Spencer, D. M. Fabijanic and M. -X. Zhang, “The influence of Al₂O₃ reinforcement on the properties of stainless steel cold spray coatings,” *Surface and Coatings Technology*, vol. 206, no. 14, pp. 3275–3282, Mar. 2012.
 - [16] G. Sundararajan, N. M. Chavan and S. Kumar, “The elastic modulus of cold spray coatings: Influence of inter-splat boundary cracking,” *Journal of Thermal Spray Technologies*, vol. 22, no. 8, pp. 1348–1357, Dec. 2013.
 - [17] V. K. Champagne, “Introduction,” in *The Cold Spray Materials Deposition Process: Fundamentals and Applications*, V. K. Champagne, Ed., Boca Raton, FL, Woodhead, 2007, pp. 17.
 - [18] J. Vicek, H. Huber, H. Voggenreiter, A. Fischer, E. Lugscheider, H. Hallen and G. Pache, “Kinetic Powder Compaction Applying the Cold Spray Process—A Study on Parameters,” presented at International Thermal Spray Conference (ITSC), Singapore, 2001.
 - [19] K. Sakaki, “Numerical simulation of the cold spray process,” in *The Cold Spray Materials Deposition Process: Fundamentals and Applications*, V. K. Champagne, Ed., Boca Raton, FL, Woodhead, 2007, pp. 118–126.
 - [20] D. Gilmore, R. Dykhuizen, R. Neiser, T. Roemer and M. Smith, “Particle velocity and deposition efficiency in the cold spray process,” *Journal of Thermal Spray Technologies*, vol. 8, no. 4, pp. 576–582, Dec. 1999.
 - [21] V. K. Champagne, *The Cold Spray Materials Deposition Process: Fundamentals and Applications*. Boca Raton, FL: Woodhead, 2007.

- [22] A. Sova, S. Grigoriev, A. Okunkova and I. Smurov, "Cold spray deposition of 316L stainless steel coatings on aluminum surface with following laser post-treatment," *Surface and Coating Technologies*, vol. 235, pp. 283–289, Nov. 2013.
- [23] B. AL-Mangour, R. Dallala, F. Zhim, R. Mongrain and S. Yue, "Fatigue behavior of annealed cold-sprayed 316L stainless steel coating for biomedical applications," *Materials Letters*, vol. 91, pp. 352–355, Jan. 2013.
- [24] C. Borchers, F. Gartner, T. Stoltenhoff and H. Kreye, "Microstructural bonding features of cold sprayed face centered cubic metals," *Journal of Applied Physics*, vol. 96, no. 8, pp. 4288–4292, Oct. 2004.
- [25] X. Meng, J. Zhang, J. Zhao, Y. Liang and Y. Zhang, "Influence of gas temperature on microstructure and properties of cold spray 304SS coating," *Journal of Material Science and Technology*, vol. 27, no. 9, pp. 809–815, Sept. 2011.
- [26] R. Huang, W. Ma and H. Fukanuma, "Effect of particle velocity on cold sprayed stainless steel deposits," in *Proceedings from the International Thermal Spray Conference and Exposition*, Houston, TX, 2012, pp. 594–599.
- [27] H. Gabel, "Kinetic metallization compared with HVOF," *Advanced Materials Processes*, vol. 162, no. 5, pp. 47–48, May 2004.
- [28] M. Villa, S. Dosta and J. M. Guilemany, "Optimization of 316L stainless steel coatings on light alloys using Cold Gas Spray," *Surface and Coatings Technologies*, vol. 235, pp. 220–225, Nov. 2013.
- [29] C. Borchers, T. Schmidt, F. Gärtner and H. Kreye, "High strain rate deformation microstructures of stainless steel 316L by cold spraying and explosive powder compaction," *Applied Physics A-Materials Science and Processing*, vol. 90, no. 3, pp. 517–526, Mar. 2008.
- [30] W. Han, X. Meng, J. Zhao and J. Zhang, "Fracture behavior of 304 stainless steel coatings by cold gas dynamic spray," *Acta Metallurgica Sinica-English Letters*, vol. 24, no. 3, pp. 249–254, June 2011.
- [31] Refractive index of stainless steel.(n.d.). Filmetrics. [Online]. Available: <http://www.filmetrics.com/refractive-index-database/Stainless+Steel>.
- [32] L. N. Brewer and C. C. Fields, "Mapping and assessing plastic deformation using EBSD," in *Electron Backscatter Diffraction in Materials Science*, A. J. Schwartz, M. Kumar, B. L. Adams and D. P. Fields, Eds., New York: Springer, , 2009, pp. 251–262.

- [33] B. D. Cullity, *Elements of X-Ray Diffraction*. Reading, MA: Addison-Wesley, 1978.
- [34] R. Wright, J. Bae, T. Kelly, J. Flinn and G. Korth, "The microstructure and phase-relationships in rapidly solidified type-304 stainless steel powders," *Metallurgical Transactions A-Physical Metallurgy and Materials Science*, vol. 19, no. 10, pp. 2399–2405, Oct. 1988.
- [35] H. Gabel, "Kinetic metallization compared with HVOF," *Advanced Materials Processes*, vol. 162, no. 5, pp. 47–48, May 2004.
- [36] A. Hall, D. Cook, R. Neiser, T. Roemer and D. Hirschfeld, "The effect of a simple annealing heat treatment on the mechanical properties of cold-sprayed aluminum," *Journal of Thermal Spray Technologies*, vol. 15, no. 2, pp. 233–238, June 2006.
- [37] A. C. Hall, L. N. Brewer and T. J. Roemer, "Preparation of aluminum coatings containing homogenous nanocrystalline microstructures using the cold spray process," *Journal of Thermal Spray Technologies*, vol. 17, pp. 352–359, Sept. 2008.
- [38] M. P. Dewar, A. G. McDonald and A. P. Gerlich, "Interfacial heating during low-pressure cold-gas dynamic spraying of aluminum coatings," *Journal of Materials Science*, vol. 47, no. 1, pp. 184–198, Jan. 2012.
- [39] G. Bae, K. Kang, J. Kim and C. Lee, "Nanostructure formation and its effects on the mechanical properties of kinetic sprayed titanium coating," *Materials Science and Engineering A-Structural Materials Properties, Microstructure, and Processing*, vol. 527, no. 23, pp. 6313–6319, Sept. 2010.
- [40] K. Kim, S. Kuroda and M. Watanabe, "Microstructural development and deposition behavior of titanium powder particles in warm spraying process: From single splat to coating," *Journal of Thermal Spray Technologies*, vol. 19, no. 6, pp. 1244–1254, Dec. 2010.
- [41] L. Ajdelsztajn, B. Jodoin, G. Kim and J. Schoenung, "Cold spray deposition of nanocrystalline aluminum alloys," *Metallurgical and Materials Transactions A-Physical Metallurgy and Materials Science*, vol. 36A, no. 11, pp. 657–666, Mar. 2005.
- [42] L. Ajdelsztajn, B. Jodoin and J. M. Schoenung, "Synthesis and mechanical properties of nanocrystalline Ni coatings produced by cold gas dynamic spraying," *Surface and Coatings Technology*, vol. 201, no. 3, pp. 1166–1172, Oct. 2006.

- [43] J. Liu, H. Cui, X. Zhou, X. Wu and J. Zhang, "Nanocrystalline copper coatings produced by cold spraying," *Metals and Materials International*, vol. 18, no. 1, pp. 121–128, Feb. 2012.
- [44] B. Jodoin, "Effects of shock waves on impact velocity of cold spray particles," presented at International Thermal Spray Conference (ITSC), Singapore, 2001, pp. 399-407.
- [45] H. Assadi, F. Gärtner, T. Stoltenhoff and H. Kreye, "Bonding mechanism in cold gas spraying," *Acta Materialia*, vol. 51, no. 15, pp. 4379-4394, Sept. 2003.
- [46] C. -J. Li, H. -T. Wang, Q. Zhang, G. -J. Yang, W. -Y. Li and H. L. Liao, "Influence of spray materials and their surface oxidation on the critical velocity in cold spraying," *Journal of Thermal Spray Technology*, vol. 19, no. 1, pp. 95–101, Jan. 2010.
- [47] J. Pattison, S. Celotto, A. Khan and W. O'Neill, "Standoff distance and bow shock phenomena in the Cold Spray process," *Surf. Coat. Technol.*, vol. 202, no. 8, pp. 1443-1454, Jan. 2008.
- [48] J. Park, M. Lee, S. S. Yoon, H. Kim, S. C. James, S. D. Heister, S. Chandra, W. Yoon, D. Park and J. Ryu, "Supersonic nozzle flow simulations for particle coating applications: Effects of shockwaves, nozzle geometry, ambient Pressure, and substrate location upon flow characteristics," *Journal of Thermal Spray Technology*, vol. 20, no. 3, pp. 514–522, Mar. 2011.
- [49] R. Dykhuizen and M. Smith, "Gas dynamic principles of cold spray," *Journal of Thermal Spray Technology*, vol. 7, no. 2, pp. 205–212, June 1998.
- [50] M. Grujicic, C. Zhao, C. Tong, W. Derosset and D. Helfrich, "Analysis of the impact velocity of powder particles in the cold-gas dynamic-spray process," *Materials Science and Engineering A-Structural Materials Processes.*, vol. 368, no. 1, pp. 222–230, Mar. 2004.
- [51] V. Kosarev, S. Klinkov, A. Alkhimov and A. Papyrin, "On some aspects of gas dynamics of the cold spray process," *Journal of Thermal Spray Technology*, vol. 12, no. 2, pp. 265-281, Jun. 2003.
- [52] H. Fukanuma, N. Ohno, B. Sun and R. Huang, "In-flight particle velocity measurements with DPV-2000 in cold spray," *Surface and Coatings Technology*, vol. 201, no. 5, pp. 1935–1941, Oct. 2006.
- [53] L. Pouliot, CSM eVOLUTION Product Manual. Canada: TECNAR Automation Ltd., 2013.
- [54] R. Clift, J. R. Grace and M. E. Weber, *Bubbles, Drops and Particles in Fluids*. Mineola, NY: Academic Press, 1987.

- [55] T. L. Bergman, A. S. Lavine, F. P. Incropera and D. P. Dewitt, *Introduction to Heat Transfer*. Hoboken, NJ: John Wiley & Sons, 2011.
- [56] The viscosity and thermal conductivity of pure monatomic gases from their normal boiling point up to 5000K in the limit of zero density and at 0.101325 MPa. (March 23, 1990). NIST. [Online]. Available: <http://www.nist.gov/data/PDFfiles/jpcrd401.pdf>.
- [57] F. M. White, "Compressible flow," in *Fluid Mechanics*, 7th ed. New York: McGraw-Hill, 2011, pp. 609–699.
- [58] X. Ning, J. Jang and H. Kim, "The effects of powder properties on in-flight particle velocity and deposition process during low pressure cold spray process," *Applied Surface Science*, vol. 253, no. 18, pp. 7449–7455, July 2007.
- [59] T. Schmidt, F. Gärtner, H. Assadi and H. Kreye, "Development of a generalized parameter window for cold spray deposition," *Acta Materialia*, vol. 54, no. 3, pp. 729–742, Feb. 2006.
- [60] H. Assadi, T. Schmidt, H. Richter, J. Kliemann, K. Binder, F. Gärtner, T. Klassen and H. Kreye, "On parameter selection in cold spraying," *Journal of Thermal Spray Technology*, vol. 20, no. 6, pp. 1161–1176, Dec. 2011.
- [61] T. E. Buchheit and T. J. Vogler, "Measurement of ceramic powders using instrumented indentation and correlation with their dynamic response," *Mechanics of Materials*, vol. 42, no. 6, pp. 599–614, June 2010.

INITIAL DISTRIBUTION LIST

1. Defense Technical Information Center
Ft. Belvoir, Virginia
2. Dudley Knox Library
Naval Postgraduate School
Monterey, California